IN-SITU SYNCHROTRON X-RAY IMAGING AND TOMOGRAPHY STUDIES OF THE EVOLUTION OF SOLIDIFICATION MICROSTRUCTURES UNDER PULSE ELECTROMAGNETIC FIELDS

being a Thesis submitted for the Degree of
Doctor of Philosophy
in the University of Hull

by

Wenjia Du (B.Sc, M.Sc, PGTS)

October 2018

Dedication

I would like to dedicate this thesis to my loved Mom (Li Zhang) and Dad (Guang Du) for their love, support and encouragement throughout my PhD study. I love them very much.

Declaration

I, Wenjia Du, hereby declare that this thesis and the associated datasets are the results of my own original work (under the guidance of Professor Jiawei Mi) carried out in the School of Engineering and Computer Science of the University of Hull during the period from September 2014 to October 2018.

Abstract

This research studies the dynamic evolution of dendritic structures and intermetallic phases of four Al based alloys during the solidification under pulse electromagnetic fields (PMFs). An advanced PMF solidification device was upgraded, built, commissioned for the research. The alloys used were Al-15Cu, Al-35Cu, Al-15Ni and Al-5Cu-1.5Fe-1Si. Systematic in-situ and real-time observation and studies were carried out at the TOMCAT beamline of Swiss Light Source, I13-2 beamline of Diamond Light Source and ID19 beamline of European Synchrotron Radiation Facility in the duration of this project. Synchrotron X-ray radiography and tomography were used primarily to observe and study the influence of PMFs on the nucleation and growth of primary dendritic structures and intermetallic phases under different magnetic flux and solidification conditions for the four alloys. More than 20 TB images and tomography datasets have been obtained throughout this research. Much effort and time was spent on segmenting, visualising and analysing these huge datasets using the Hull University supercomputer cluster, Viper, and the software, Avizo, ImageJ (Fiji), etc to explore and extract new insights and new science from those datasets. In particular, the skeletonisation function available from Avizo was customised and used to quantify the complex 3D microstructures and interconnected networks of different phases for the alloys. The important new findings of the research are:

(1) Fragmentation of primary Al dendrites in the Al-15%Cu alloy was found when the magnetic flux of PMF applied is above 0.75 T; similarly, the fragmentation of Al_3Ni intermetallic phases in the Al-15%Ni alloy was also observed when the

magnetic flux of PMF applied is above 0.8 T. The clear and real-time observation of the fragmentation events in both dendritic and intermetallic phases provide unambiguous evidence to demonstrate that PMFs play a dominant role in structure fragmentation and multiplication, which is one important mechanism for structure (grain) refinement.

(2) PMFs also produces pinch pressure gradient inside the semi-solid melt. Due to the different magnetic anisotropic properties between the liquid and solid phases, shear stresses due to the pinch pressure gradient may be produced. In the case of Al-15%Ni alloy, shear stresses of up to 30 MPa is created, which is sufficient to fracture Al_3Ni phases. For the first time, such fragmentation mechanism for the Al_3Ni phases in the Al-15%Ni alloy was revealed in this research.

(3) The transition (or change of growth modes) of Al columnar dendrites to seaweed type dendrites in Al-15Cu alloy; and the facet growth to dendritic growth of the Al_3Ni phases in the Al-15%Ni alloy were also observed in real-time when the magnetic flux is in the range of 0.75~0.8 T. Again, such dynamic changes in structure growth under PMFs are due to the enhanced melt flow caused by the applied fields.

(4) In-situ tomography observation of PMF processing of the Al-5Cu-1.5Fe-1Si alloy also shows the effect of PMF on the refinement of the Chinese script type Fe intermetallic phases. In addition, the true 3D morphologies of three different types of Fe intermetallic phases in this alloy were clarified, again for the first time, in this research.

Acknowledgments

First and foremost, I would like to express my sincere gratitude to my supervisor, Professor Jiawei Mi, for his academic guidance and strong support during my PhD research. Without his support and encouragement, it would be impossible for me to overcome many technical obstacles in the project. He inspires me to face up to any challenging issues in research and life.

I also would like to thank all my colleagues and friends for their stimulating and fruitful discussions, help and friendships. They are Dr Wei Zhang, Dr Chuangnan Wang, Dr Dongyue Tan, Dr Theerapatt Manuwong, Dr Jia Chuan Khong, Dr Tung Lik Lee, Mr Billy. Koe, Dr Jianlong Li, Dr Yuanda Cheng and Mr Yi Fan, etc, just name a few. Particularly, I appreciate the support from Mr Peter. Kazinczi for upgrading the 2nd version of pulse electromagnetic experimental apparatus. I appreciate very much the time spent with them during my PhD study.

Last, but not the least, I would like to thank the collaborators for their invaluable support before, during and after the beamline experiments. They are Dr Julie Fife from TOMCAT beamline of Swiss Light Source; Dr Silvia Cipiccia and Dr Andrew Bodey from Diamond-Manchester Imaging Branchline (I13-2) of Diamond Light Source; Dr Elodie Boller and Dr Alexander Rank from ID19 of European Synchrotron Radiation Facility. It is a great pleasure and honour to work with these dedicated scientists.

Publications and awards:

The journal and conference papers and awards from my PhD study are listed below:

Journal paper published

- Y. Zhao, **W. Du**, B. Koe, T. Connolley, D.G. Eskin, J. Mi, “3D Characterization of Fe-rich intermetallic phases in Al-5%Cu alloys by synchrotron X-ray microtomography”, Scripta Materialia, 146, pp:321-326

Conference papers

- **W. Du**, J. Mi, “Synchrotron X-ray Studies of the Evolution of Solidification Microstructures under Pulse Electromagnetic Field”, the 9th International Symposium on Electromagnetic Processing of Materials, Japan, Oct 2018.
- **W. Du**, S. Cipiccia, A. Bodey, J. Mi, Real-time tomography studies of microstructure evolutions of Al alloys solidified under pulse electromagnetic fields, 6th Decennial International Conference on Solidification Processing, UK, July 2017.
- Y. Zhao, **W. Du**, T. Connolley, D.G. Eskin, J. Mi, Synchrotron X-ray tomography studies of Fe-rich intermetallic phases in Al alloys, 6th Decennial International Conference on Solidification Processing, UK, July 2017.
- C. Wang, D. Tang, W. Zhang, **W. Du**, T. Connolley, J. Mi. High speed synchrotron X-ray imaging of ultrasonic bubble cloud in liquid metal, 9th International Symposium on Cavitation, Switzerland, Dec 2015. (DOI: 10.1088/1742-6596/656/1/012178)

Journal papers under preparation

- **W. Du**, W. Zhang, Z. Guo, T. Lee, J. Fife, J. Mi, “4D synchrotron X-ray tomography studies of microstructural evolution of an Al-15%Cu alloy solidified under pulse electromagnetic field”, aiming to Scripta Materialia.
- **W. Du**, S. Cipiccia, A. Bodey, C. Rau, J. Mi, “Real-time synchrotron X-ray studies of the dynamic evolution of intermetallics during solidification under pulse electromagnetic fields”, aiming to Acta Materialia
- S. Wang, Z. Guo, **W. Du**, J. Mi, Ultrafast high fidelity phase field modelling of multi-dendrites evolution in solidification and validation by synchrotron X-ray tomography, aiming to Acta Materialia

Awards

- 2017 Research Travel Grant for 147th TMS Annual Meeting in USA;
- 2016 Best Poster Prize (Real-Time Synchrotron X-ray Tomography of Intermetallic Phases Solidified under Pulse Electromagnetic Field) awarded at the Diamond Light Source (DLS) Synchrotron User Meeting;
- 2016 Synchrotron Radiation School (via extremely competitive application in UK/EU), University of Oxford and Diamond Light Source;
- 2015 ISIS Neutron Training Course (via extremely competitive application in UK/EU), Science and Technology Facilities Council;

Table of Contents

Chapter 1: **Introduction**

1.1 Background

Metal alloys are very important structural and functional materials in human society since civilization began many thousands of years ago; and continue to be the indispensable materials in man-made products, vehicles and infrastructure in the modern world.

The physical, functional and mechanical properties of metal alloys are determined mainly by chemistry, nano and micrometre scale structures (grain size) and defects (voids and/or inclusions), and their characteristic distributions within the alloys. Generally, the smaller the grain size, the stronger and tougher the alloys, as defined by the classical Hall-Petch relationship [1]. How to achieve an optimal morphology, size and distribution of grains and those of defects to maximize alloy's mechanical properties are the main driving force for metal alloy research activities.

Grain nucleation and subsequent microstructural evolution are important steps in determining the properties and performance of metal alloys. Many techniques and industrial practices have been developed to refine and control the grain size of metal alloys through solidification processes. Conventional methods of adding external grain refiners to refine the solidification structures of metal alloys have been used in industry for many decades [2, 3]. To reduce negative environmental impact and develop sustainable and green manufacturing strategies, in the past twenty years or so, many studies have been carried out to develop new technologies. The most important developments so far have been the uses of

external physical fields such as ultrasonic fields [4] and magnetic fields [5] to control the nucleation and grain growth during metal solidification. They are generic physical methods irrespective of the chemistry of alloys involved. For example, electric current pulse [6] has been shown to be effective in grain refinement. However, some experiments involved the uses of dangerously high electric current or voltage in order to apply sufficient fields uniformly in a relatively large volume of melt. Hence, safe and energy efficient methods are needed to be developed. Most previous studies used the 'quench-and-look' methods where a completely solid alloy sample is analysed post-mortem after experiments. Generally, the 2D sectional images methods (electron or X-ray based imaging methods) cannot provide 3D information that is often needed to understand fully the complex 3D morphologies and structures of dendrites and intermetallic phases often found in solidified metal alloys. Some researchers used serial sectioning by focused ion beam (FIB) milling plus electron microscopy imaging to generate 3D datasets, but this cannot be used in real-time processing conditions. Findings of previous research on solidification under pulse electric current (PEC) and pulse magnetic field (PMF) are often restricted to or based on isolated experiments and post–mortem analyses. Results and interpretations are often inconsistent, and sometimes contradictory to one another (Details are reviewed in Chapter 2).

In my PhD research, I used a new pulse generator with the low input voltage (usually below 240 V) and real-time Synchrotron X-ray radiography and tomography technique to observe and quantify microstructural evolution in

different pulse magnetic field conditions. Binary (Al-15%Cu, Al-35%Cu, Al-15%Ni) and quaternary (Al-5%Cu-1.5%Fe-1%Si) alloys were used. The higher spatial and temporal resolution of synchrotron X-ray make it possible to acquire the primary dendritic patterns, intermetallic patterns and Chinese script-like patterns of Fe phases in different solidification conditions under pulse electromagnetic fields.

1.2 Objectives

The main objective of my thesis is to develop in-situ experimental approaches and to do more systematic studies with the aims of obtaining the in-depth and quantitative understanding of the inherent multi-physical problems in solidification processes under pulsed magnetic fields, including:

1. Upgrading of the pulse electromagnetic field solidification apparatus, including a new cooling system, a new and robust casing, capacitors, firmware, safety interlock, and hall sensor;
2. Designing and building of bespoke small-scale furnaces that are suitable for the physical environment of different beamlines in different synchrotron X-ray facilities for conducting real-time pulse magnetic field solidification experiments;
3. Studying of the nucleation, growth and morphology changes of primary phases (α–Al), primary and secondary intermetallic phases (Al_3Ni, Al_2Cu, α–AlFeSi and β–AlFeSi) of metal alloys under different pulse electromagnetic fields during solidification;
4. Analysing of the huge amount of image datasets and interpreting the

phenomena found in the experiments, providing more quantitative insight on understanding the mechanism of nucleation and crystal growth under electromagnetic pulse fields during metal solidification process.

1.3 Thesis structure

This thesis consists of 8 chapters:

Chapter 1 is a brief introduction, including the background, objectives and the structure of the thesis.

Chapter 2 is a comprehensive literature review relevant to this project. It is grouped into three sections: 1) a review on the historical and up-to-date research of nucleation and crystal growth (e.g. primary dendritic phase, intermetallic phase, eutectic phase, Chinese-script phase formation) during metal solidification, and solidification microstructures under magnetic fields; 2) The basic theories and practice of X-ray radiography and tomography; 3) the uses of synchrotron X-ray techniques in metallurgical and solidification processing.

Chapter 3 describes, in details, the upgrading of the in-situ solidification apparatus with an external pulse magnetic field (the improvement of electromagnetic pulse kit, thermal controllers, furnaces etc.) and the sample environment. The measurements of discharging currents, voltage and the resulting magnetic pulse densities via Gaussian meter and oscilloscope are presented.

Chapter 4 describes the sample making and experimental preparation (phase diagrams, X-ray attenuations) and key parameters (spatial and temporal resolution, X-ray energy, camera selection and exposure time, etc) for the experiment carried out at the X-ray beamlines of Diamond Light Source (DLS), Swiss Light Source (SLS), and European Synchrotron Radiation Facility (ESRF).

Chapter 5 studies the formation of primary Al_3Ni intermetallic phases of Al-15wt%Ni alloy during solidification process in PMF. The phase fragmentation induced by magnetic pulses and the nucleation and growth behaviours are in-situ observed and quantified by theoretical calculation.

Chapter 6 presents the mechanisms controlling the formation of primary *α*-Al dendrites during solidification and coarsening in an Al-15wt%Cu alloy. The fragmentation induced by the PMF as well as its nucleation and subsequent growth behaviours that are characterized via fast 4D synchrotron X-ray tomography at SLS and quantified by skeletonization.

Chapter 7 briefly presents the preliminary synchrotron results of *α*-intermetallic (Chinese-script) and β-intermetallic (plate-like) phase evolution during directional solidification in an Al-5%Cu-1.5%Fe-1%Si alloy with the PMF via ultrafast 4D imaging at ESRF.

Chapter 8 is a suggestion of future direction of the research in this field.

Chapter 2: **Literatures Reviews**

In this chapter, the relevant and key literatures are critically reviewed, including (1) solidification under external magnetic fields; (2) basic theories and practice of X-ray radiography and tomography, and their application in solidification process. The review is focusing on solidification research under external magnetic fields and the recent advances of using synchrotron X-ray imaging and tomography to study the solidification process.

2.1 Solidification under external magnetic fields

Magnetic fields are classified into (1) static magnetic field, (2) travelling magnetic field and (3) pulse electromagnetic field based on their physical setup. During solidification, magnetic fields can be applied either axially or transversely with respect to the samples. The magnitude of a magnetic field is an important factor, but it is ambiguous to say whether it is ‘strong’ or ‘weak’. Generally, when a magnetic field is strong enough to influence crystal growth, then it can be considered as a ‘strong magnetic field’ [7]. The fundamental principles and the historical development of using PMF to control the solidification microstructures are reviewed in this chapter.

2.1.1 Solidification under static magnetic field

There are numerous literatures regarding the effect of static fields on microstructure [8-11]. Here, I briefly review the alteration of Al_3Ni (it is space group Pmna) morphology by the action of static fields during solidification.

In 2008, X. Li *et al*. [12] study Influences of a high magnetic field (up to 14 T) on the alignment behavior of the primary Al_3Ni phase in three hypereutectic Al–Ni alloys. He found that the plane alignment perpendicular to the magnetic field has formed under a certain condition as shown in Figure 2.1. He investigated the alignment-influencing factors (1) the magnetic field intensity, (2) solidification temperature and (3) the alloy composition has played great roles during the alignment process as shown in Figure 2.2. Indeed, it is observed that under a certain magnetic field intensity there exists a critical solidification temperature, and above this temperature the alignment degree increases with the increase of the solidification temperature, and that under a certain solidification temperature there exists a critical magnetic field intensity, and above this magnetic field intensity the alignment degree increases with the increase of the magnetic field intensity. In Figure 2.2a, he also found that with the increase in the Ni content of the alloy the alignment degree decreases.

In 2016, similar results are found by X. Li *et al.* [13] again with more temperature and magnetic intensity conditions under an axial static magnetic field up to 14 T. Moreover, the orientation of the preferred growth direction of the Al_3Ni eutectic phases depended mainly on the solidification direction and the alignment of the primary Al_3Ni phase.

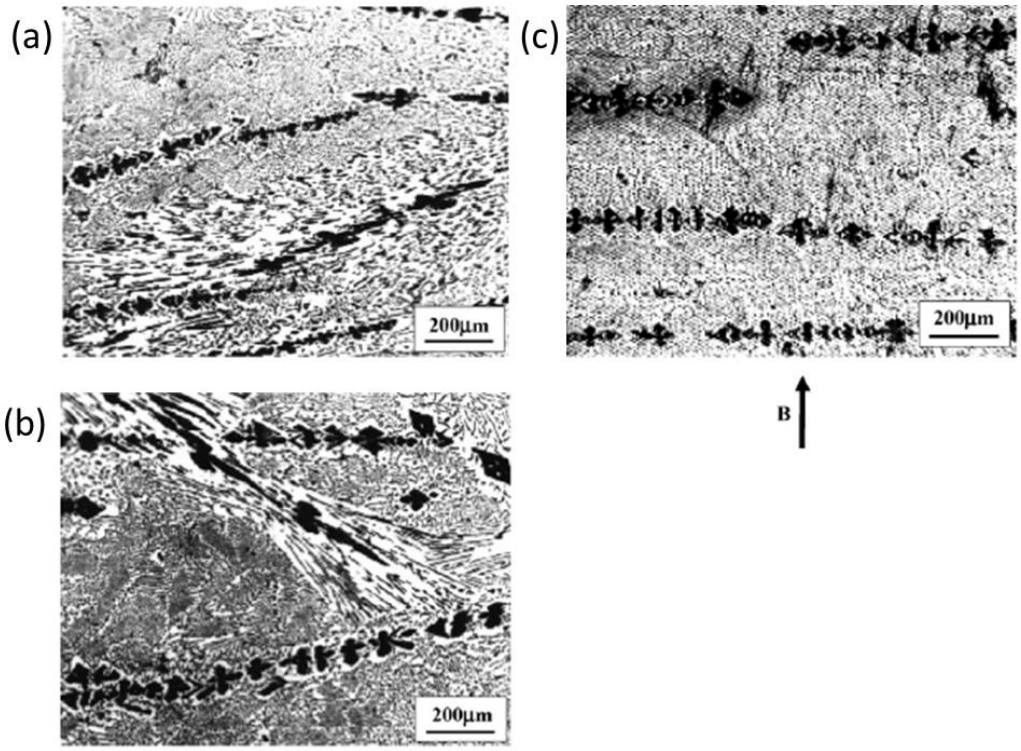

Figure 2.1 Microstructure of the Al–8 wt%Ni alloy solidified from 750 °C at a cooling rate of 18 K/min under various magnetic field intensities: (a) 1 T; (b) 1.5 T; (c) 2 T.

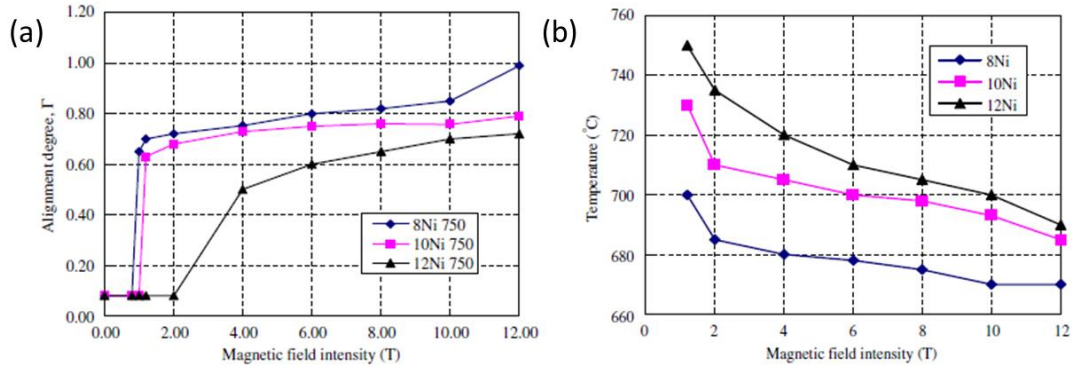

Figure 2.2(a) Dependences of the alignment degree of the primary Al_3Ni phases on the magnetic field during the solidification from 750 °C; (b) The critical alignment temperature of the Al_3Ni against the magnetic intensities for the Al–8Ni, Al–10Ni and Al–12Ni alloys.

His EBSD analysis in Figure 2.3, the crystal orientation results show that with 2 T, the aligned structure began to deviate from the solidification direction. When the magnetic intensity exceeded 6 T, the longer axis of the Al_3Ni phase (i.e., the <010>) became oriented perpendicular to the solidification direction and ultimately formed a layer-like structure [13]. This is discussed based on the magneto crystalline anisotropy of the Al_3Ni crystal and the rotating alignment of the primary phase under a high magnetic field.

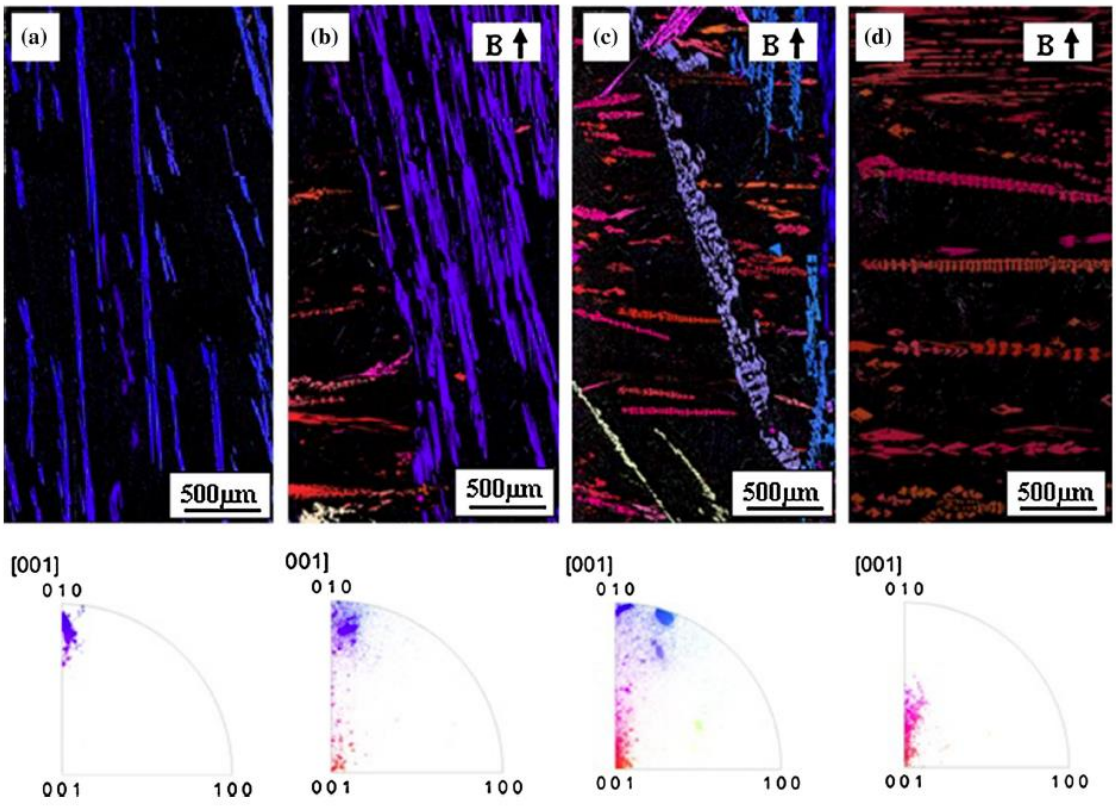

Figure 2.3 EBSD maps and the corresponding pole figures for the Al_3Ni phases in the longitudinal structures in directionally solidified Al-12wtNi alloys at a growth speed of 50 μm/s under various magnetic fields: (a) 0 T; (b) 4 T; (c) 6 T; (d) 12 T.

2.1.2 Electromagnetic field

The Lorentz force ($\boldsymbol{F}$) generated by the interaction between an imposing current ($\boldsymbol{I}$) and the magnetic field ($\boldsymbol{B}$) is calculated by $\boldsymbol{F} = \boldsymbol{I} \times \boldsymbol{B}$.

Takahashi [14] classified the electromagnetic field (EF) into 6 types: (1) stationary magnetic field only; (2) alternating current only; (3) alternating magnetic field only; (4) travelling magnetic field; (5) simultaneously applying the direct current and stationary magnetic field and (6) simultaneously applying the alternating current and alternating magnetic field.

Two main basic approaches have been implemented for achieving grain refinement [15]: (1) passing an electric current directly into the melt via contacting electrodes and interacting with a magnetic field; (2) producing an induced current into the melt and allowing it interact with a magnetic field. The advantages and disadvantages of the two methods are briefly discussed below.

2.1.2.1 Direct contact current

Figure 2.4 shows the direction of the Lorentz force induced by the interaction of an electric current (input via direct-contact electrode) with a magnetic field (induced or stationary magnetic field). It follows the right-hand rule (Figure 2.4a).

Figure 2.4b presents the technique called electromagnetic vibration (EMV). The externally imposed horizontal electric and magnetic fields are perpendicular in a

parallelepipedic tank during solidification. The externally imposed stationary magnetic field B_o interacts with the sinusoidal electric current of density j and gives rise to a vertically directed periodic electromagnetic force $j \bullet B_o$ of frequency N, which in turn forces the solidifying melt into vibration [16].

The direct electric current pulse (ECP) with parallel electrodes mode is schematically illustrated in Figure 2.4c. The ECP gives rise to induction pulse magnetic field in the melt. The periodic Lorenz force ($F = J \times B$) resulted from the interaction between ECP and induction pulse magnetic field produces the periodic agitation on the upper surface, which can be observed during the experimental process. Subsequently, under the action of Lorenz force, a large number of growing nuclei move down and enter into the undercooled melt [17].

Figure 2.4d shows the arrangement of, in a contact manner, applying pulse electric current into a stationary magnetic field created by a permanent magnet. A permanent magnet was placed very close to the melt sample, with field lines running approximately normally in and out of the sample surface. Hence, a pulsed Lorentz force horizontally acted on the sample.

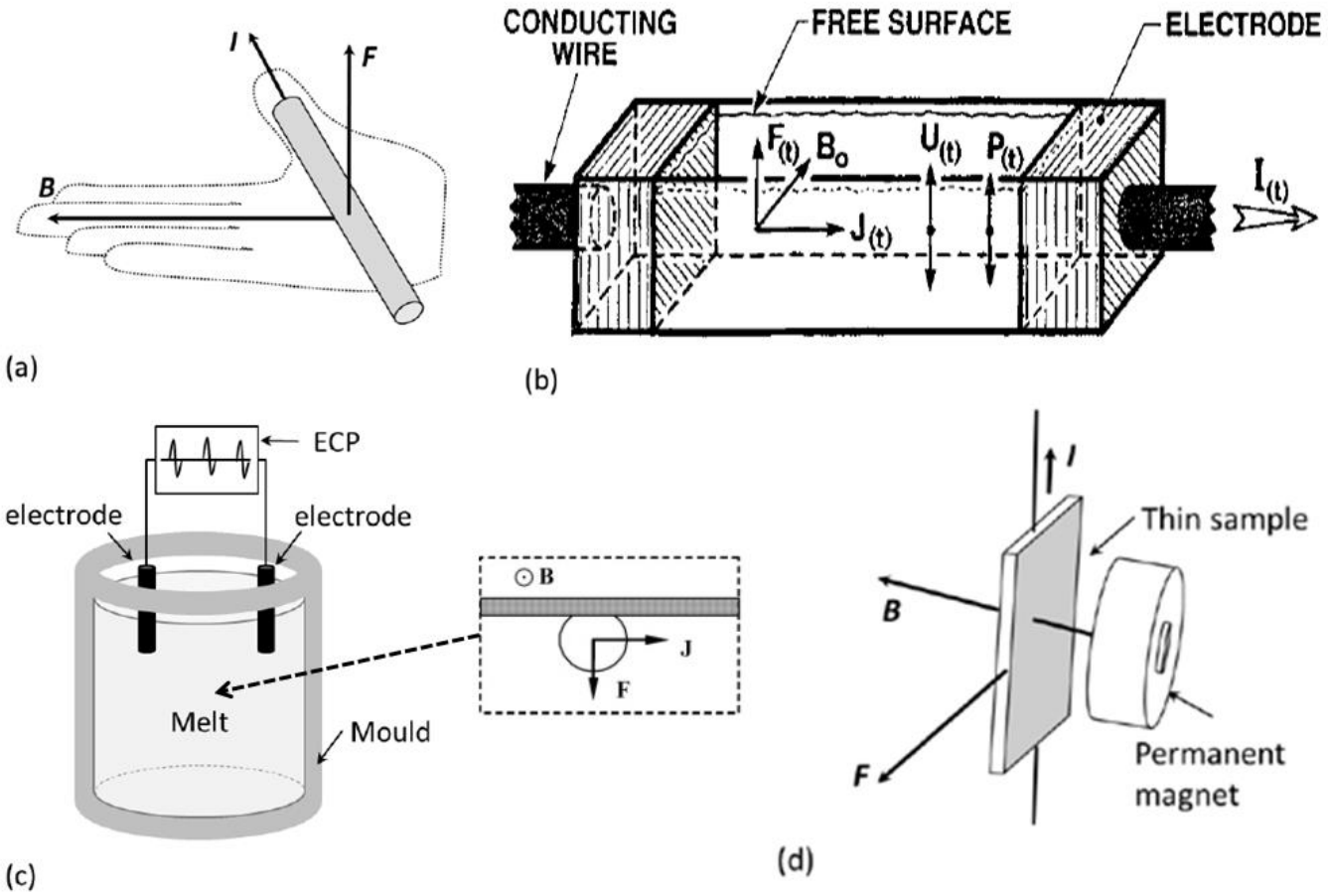

Figure 2.4 (a) The right-hand rule; (b) the Lorentz force generated in an electromagnetic vibration (EMV) technique; (c) the direct-contact electric current pulse (ECP) technique and (d) the contact pulse electric current (PEC) technique.

2.1.2.2 Induced current

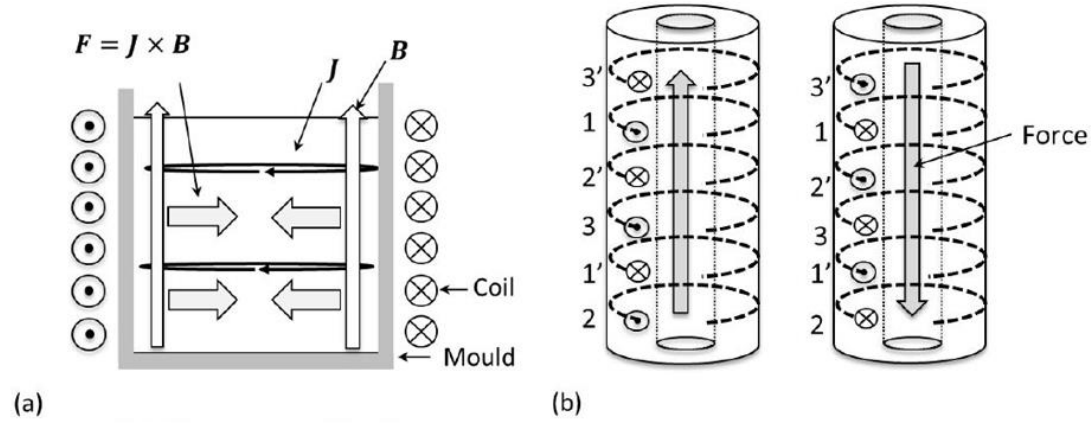

Figure 2.5 (a) The Lorentz force generated by the interaction between an induced current and the induced magnetic field; and (b) schematic view of the travelling magnetic field, and its Lorentz force directions.

When electric current passes through a solenoid coil, induced current occurs inside the conductive liquid metal materials surrounded by the coil. Due to the conductivity difference between the melt and the solidifying crystals, the induced current density across those two phases is therefore quite different, leading to the different electromagnetic force acted on them. The electromagnetic force (also called **pinch force**) is produced by the interaction of this induced current and the induced magnetic field as shown in Figure 2.5a. Hence, the pinch force is generated with its direction pointing towards the centre of the system according to the right-hand rule, producing the radial compressive stresses. J. P. Barnak proposed that the pinch force squeezes the liquid metal, which could reduce heterogeneous nucleation at the mold wall and disperse any nuclei which may

have formed at or near the mold wall [18]. He found the stress is sufficient enough to shear-off dendritic arms and to shear (stir) the molten metal whose viscosity reaches the specific values (i.e. 2.4 mPa-s).

Figure 2.5b shows the principle of travelling magnetic field, this technique is quite unique due to Lorentz force direction is different from other techniques [19, 20].

2.1.3 Solidification under electromagnetic fields

From the 1930s to 1970s, research and applications of electromagnetic processing of materials were mainly on using electromagnetic induction for heating or melting metal alloys, stirring melt for temperature and chemical homogenization, applying electromagnetic force for levitating against gravity, applying electromagnetic brake for controlling liquid metal flow or reducing turbulence [21, 22].

In the 1970s, the researcher and engineer at Iron and Steel Institute of Japan (ISIJ) started realized the huge potentials and benefits of electromagnetic fields in steel manufacturing and since then the term ‘Electromagnetic Metallurgy’ was established.

In 1989, it was coined as ‘Electromagnetic Processing of Materials (EPM)’ by Asai [23]. Since then, eight series of international Symposiums had been dedicated to the development in this field [24], and the ninth Symposium (EPM2018) will be held in Awaji Island, Hyogo, Japan on 14-18 Oct 2018 [http://www.epm2018.org/].

In this chapter, the historical and recent research and technological development on electromagnetic fields are reviewed below with a focus on their applications to the solidification processes.

2.1.2.1 Under electromagnetic vibration (EMV)

Electromagnetic vibration (EMV) is generated by simultaneous imposition of a direct magnetic field and an alternating electric field into a conducting liquid as schematically shown in Figure 2.4b.

This technique was applied to refine the microstructure of Al alloys in 1975 by Nishimura [25] and it attracted gradually increasing interest from researchers in this field. The vibrating electromagnetic force is generated inside the liquid, with a frequency equal to that of the applied electric field and a direction perpendicular to the plane of the two fields [26]. Nishimura of Osaka Prefectural Industrial Research Institute and Kawano of Kyoto University, Japan [25] reported the effects on grain refinement of metal alloys by applying an alternating electromagnetic field into solidifying melts using the apparatus schematically showed in Figure 2.4b. Pure Al, Al-Cu and Al-Zn alloys were investigated. The maximum magnetic flux density of the magnetic field imposed was about 0.27 Tesla, while the electric currents applied were from 0 to 20 A with an increasing step of 5 A for the different experiments [25]. They found that the grain refinement effect was roughly proportional to the applied current intensity, *i.e.* the vibration amplitude.

In 1996, Vives of the University of Avignon, France reported systematic studies [16, 27]. The forced vibration was produced by applying simultaneously a sinusoidal electric current (intensity: $i = I \sin\omega t$, frequency: N) and a stationary magnetic field, B_o inside alloy melt contained in a parallel tank as schematically shown in Figure 2.4b. Such an arrangement is very similar to that used Nishimura's experiment in 1975 [25].

The stationary magnetic field B_o interacts with the electric current of density j and gives rise to a vertically directed periodic electromagnetic force $J \times B_o$ of frequency N, which in turn forces the solidifying melt into vibration. The resultant vertical electromagnetic force applied to the whole melt volume is given by $F = B_o I L \sin\omega t$ and generates an electromagnetic vibrating pressure $P = B_o I L \sin\omega t / (L \times a) = B_o I \sin\omega t / a$.

Figure 2.6 show two typical pressure amplitudes and the corresponding microstructures of an A356 alloy.

Figure 2.6c shows coarse refined dendritic structures at P = 0.3 bar. While in the presence of an EMV with the pressure amplitude profile as that showed in Figure 2.6d (P = 0.52 bar), globular grains with an average diameter of ~120 μm were formed, which are predominantly caused by the shearing effects generated by the vertical velocity (a peak value > 1 m/s [16]) during vibration. This shearing process breaks dendritic particles and deforms them into a spheroidal shape which is quite similar to those encountered in the rheocasting techniques [16, 27]. The results exhibited that the higher electric amplitude fields, the finer of the grain size of alloys.

Grain nucleation is enhanced by either the increase in the equilibrium temperature (hence the effective undercooling) caused by the pressure spike during the collapse of the cavitation bubbles, or as a result of cooling the surface of the bubbles by evaporation during its growth. Hence, cavitation renders grain refinement by (1) increasing grain nucleation rate and (2) increasing grain multiplication effect by disrupting and fragmenting growing phases. The effects of cavitation resulted in much finer grains (50 μm mean size) and less globular than those produced by the shearing effect in the absence of cavitation (Figure 2.6b, e). Moreover, it is seen that the cavitation effects result in the total disappearance of the numerous large clusters. Similar significant reduction in the grain size under the cavitation was also obtained in a 2024 alloy and a 1050 alloy, which is characterized by a relatively narrow solidification temperature range [16, 27].

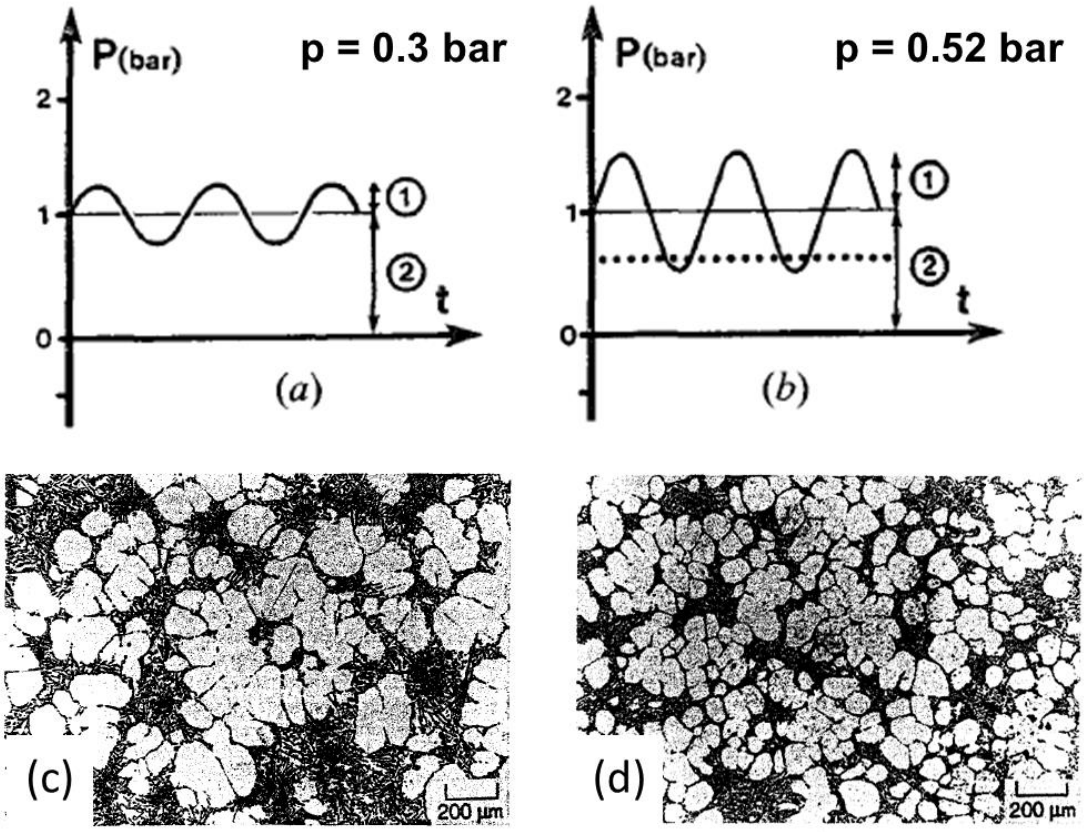

Figure 2.6 The pressure waves generated by the interaction between the magnetic field and the electric field with the amplitude of (a) P = 0.3 bar and (b) P = 0.52 bar. The refined microstructures of an A356 Al alloy by the electromagnetic vibration: (c) the coarse refined dendritic structures at P = 0.3 bar and (d) globular grains with an average diameter of ~120 μm at P = 0.52 bar [16, 27].

Compared to the cases of mechanically vibrated melts, the electromagnetically irradiated semisolid alloy mixtures exhibit uniform grain refinement across the entire section. The EMV method can remarkably decrease micro porosities, but the segregation of a solute element near the interface of precipitates was not eliminated. This is due to the electromagnetic forces which induce oscillating motion act uniformly throughout the semisolid melt. Moreover, it should be noted that the cavitation provoked by the electromagnetic pressure fluctuations, are not

likely to be present in the mechanically vibrated melts (excluding those by applying ultrasound into the melt mechanically). They stated that the mechanism of grain refinement by this method is not clear, but may be due to the accelerated nucleation effect and by a detachment of dendrite tips due to thermal fluctuations [25]. However, from the industrial application point of view, such process has a serious drawback. Because, for the large-scale ingot castings, substantial energy consumption is required to reach the cavitation threshold. It is not easy to apply relatively intense steady magnetic-field strength inside an air gap on the order of 30 cm width and to inject current intensity of about 40,000 A [16].

2.1.2.2 Under electric current pulse (ECP)

The electrodes of the electric current pulse (ECP) are submerged into the liquid metal as shown in Figure 2.4c. Generally, ECP consists of electrodes and a current generator to generate the electromagnetic field when the current passing through the electrode into the molten metal.

When ECP is directly applied into the liquid metal, the shock wave or the pressure gradient interrupts the growth of dendrite, fracturing dendrite arms by the discharged pulse [17]. High pulse voltage can be generated by using a capacitor bank [28]. The electric current discharged from the capacitor bank is a short pulse, and after the discharge current instantaneously reached its peak value, the amplitude declined with time rapidly.

In 1974, Vashchenko, *et al*. [29] were probably the first to report the application of electric current in a cast iron during the process of solidification. They found that the electric current could suppress the occurrence of impurities and increase the mobility of carbon in cast iron [29]. The refinement effect was most appreciable in pure Al but not pronounced in the alloys containing a higher amount of an alloying element, nor in the titanium-treated alloys.

In 1985, Misra of Indian Institute of Technology reported that, in a short communication [30], applying a direct electric potential to the solidifying melt contained inside a glass tube (5 mm in diameter and 100 mm long) can change the normal process of nucleation and growth of equilibrium phases. A Pb-15%Sb-7%Sn alloy was used in the experiment [30] and part of the results is reproduced here and showed in Figure 2.7. Unfortunately, Misra did not give any explanation on the mechanism for the changes of microstructures [30]. In 1986, Misra [31] applied the similar method (a direct current of -50 mA/cm^2 at ~20 V) to a high temperature alloy, Ni-Mg bearing cast iron during solidification. Again, clear microstructural changes were found. But no explanation on the refining mechanism [31].

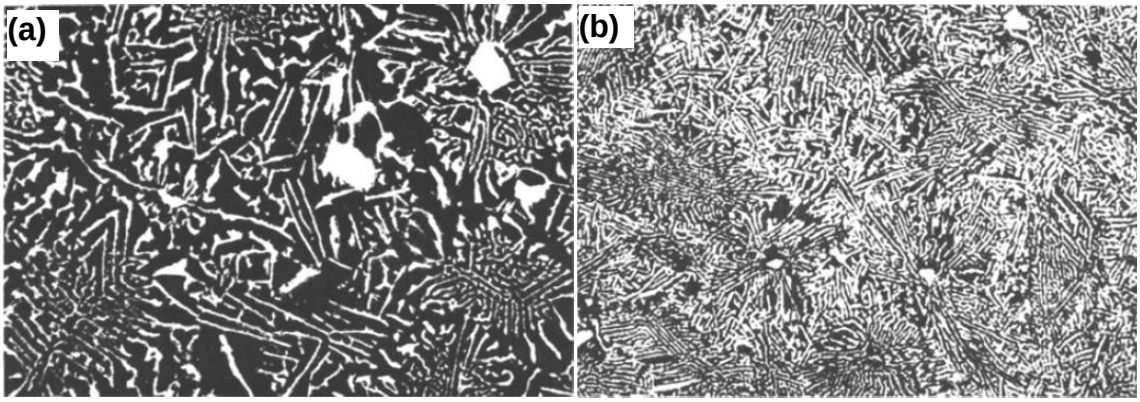

Figure 2.7 The microstructure of a Pb-15%Sb-7%Sn alloy solidified (a) without applied potential; (b) with a direct current (30~40 mA/cm^2 at ~30 V) passed through the melt [30].

In 1990, Nakada and Flemings of Massachusetts Institute of Technology, USA reported systematic experiments [28, 32]. The schematic of the experimental apparatus is shown in Figure 2.4c. The capacitor bank has 320 μF capacitance and could be charged to a pre-defined voltage of up to 5000 V by using a regular AC electric source.

A Sn-15wt%Pb hypoeutectic alloy was used in the experiment [28]. This alloy has a liquidus temperature of ~488 K, and solidification is complete at the eutectic temperature of 456 K. The alloy samples were melted in the electric furnace and heated to 553 K (65 K of superheating), and then cooled at different cooling rates of 18, 11, and 6 K/min respectively. The onset of solidification (nucleation of primary Sn phase) took place at ~480 K. The pulse electric discharging (PED) was then carried out with different initial capacitor bank voltages, and different capacitor triggering times after the onset of solidification. Multi-capacitors were also used for discharging [28]. The voltage drops across the specimen during

PED was measured using a digital oscilloscope. From the voltage drop, the discharge time and the oscillating frequency could be determined.

Figure 2.8a is an example of the measured voltage drop (oscillated with a frequency of ~3 kHz and the discharging interval was 1 ms) across the specimen after discharging the capacitor bank with an initial voltage of 2500 V.
They found that (1) the time of triggering after the onset of solidification, (2) cooling rates, and (3) the initial capacitor bank voltage are the dominant control factors on determining the microstructure change from dendritic to transient to globular morphology.

For example, Figure 2.8b indicated that, at a cooling rate of 11 K/min, how the transition from dendritic to global structure occurred with the increasing of capacitor bank voltage and shortening of the time of trigger of PED. In addition, the voltage required for exact structural transition increased with increasing time of trigger after the onset of solidification.

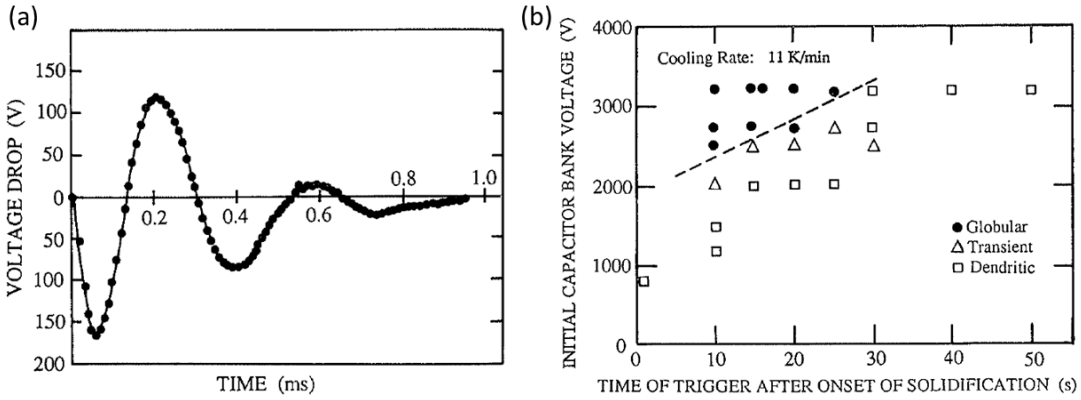

Figure 2.8 (a) An example of the measured voltage drop across a specimen during discharging with an initial capacitor bank voltage of 2500 V. (b) The relationship between microstructures, initial capacitor bank voltages and time of trigger after onset of solidification (single) at a cooling rate of 11 K/min [32].

The typical examples of the dendritic, transient and global structures obtained in the experiments are showing Figure 2.9. Actually, the fraction of the solid phase presented in the solidifying melt at the instant of triggering PED is critical for the transition from dendritic to globular microstructures. Figure 2.10a shows the relationship between the calculated fraction of solid and time of triggering PED after the onset of solidification for three different cooling rates [28].

In Figure 2.10a, the critical upper limit of the fraction of solid in the melt in order to obtain globular microstructures were highlighted with shaded areas for three different initial capacitor bank voltages, 2500, 2700, and 3200 V respectively. Figure 2.10b shows the relationship between the upper limit of the fraction of solid at which the globular microstructure was obtained and initial capacitor bank voltages.

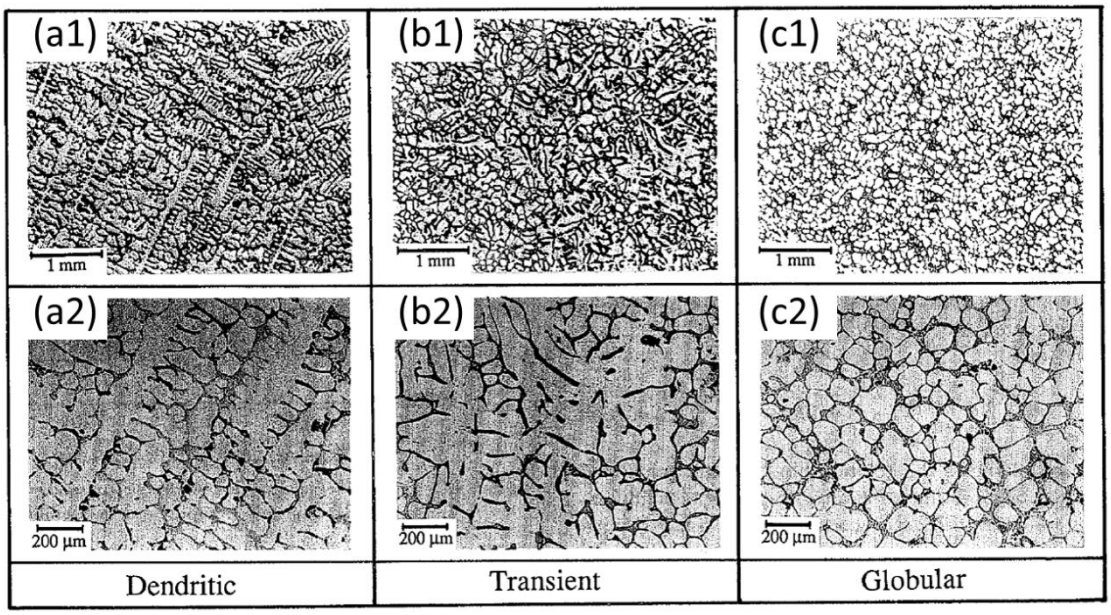

Figure 2.9 Typical examples of (a) the dendritic (the one below is the enlarged image), (b) transient and (c) globular microstructures obtained in the experiments [28].

Figure 2.10 shows more clearly that the limit of the fraction of solid depends on the initial capacitor bank voltage, and is independent of cooling rate [28]. Nakada, *et al.* argued that when PED was conducted, the shock wave induced by discharging was observed on the surface of the molten metal. This is supposed to be the result of the pinch force at the moment of discharge. The strength of the pinch force can be calculated at any arbitrary position in the specimen and at any time during the discharging. Because the magnetic flux density and current density vary at each point of the specimen, which give rise to a pinch force gradient and cause local velocity differences in the molten metal, generating shear stresses. When the shear stress is high enough, dendrites are expected to be broken into globular fragments. However, in this paper, Nakada did not calculate the shear stresses inside the specimen at PED [28].

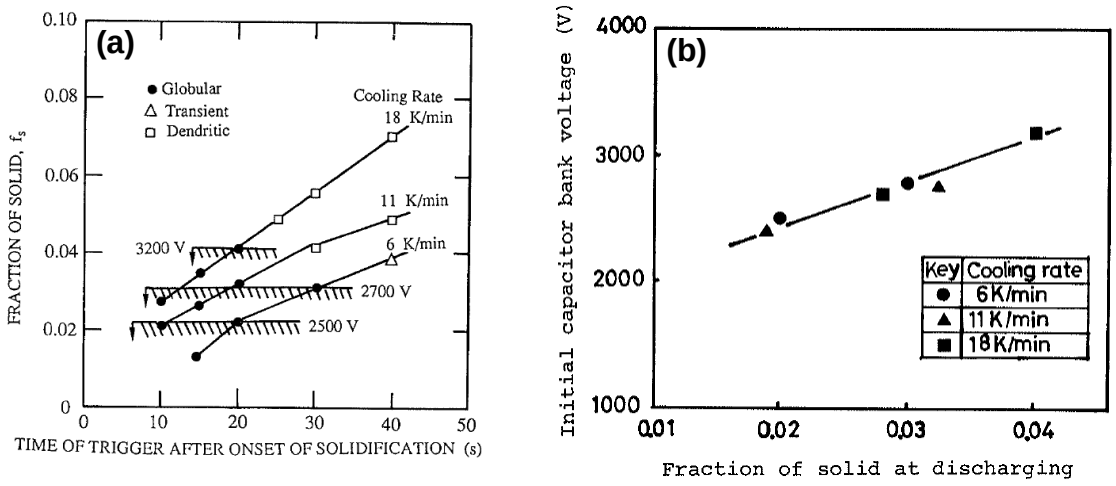

Figure 2.10 In the conditions of forming globular microstructures, (a) the upper limit for the solid fraction in the melt when different cooling rates and initial discharging voltages were used. (b) The relationship between the upper limit for the solid fraction and the initial discharging voltage [28].

In 1994, Bamak, Sprecher and Conrad of North Carolina State University, USA published a short communication in Scripta Metallurgica, attempted to provide more evidence on explaining the mechanisms of grain refinement caused by applying electric current pulses into melts [18].

Their results showed that when applied an electropulsing of 1426 A/cm^2, the undercooling was increased to 9~13 °C as compared to just ~0.5 °C for the case without electropulsing (Figure 2.11a). Figure 2.11b showed that the size of the eutectic colony decreased with the increase of current density, even though the pulsing frequency was decreased. With a current density of 1000-1500 A/cm^2 applied at a frequency of 1.5~5 pulses per second during the whole solidification process, the eutectic colony size was reduced to approximately an order of

magnitude smaller. However, no big difference for the eutectic lamellae was observed.

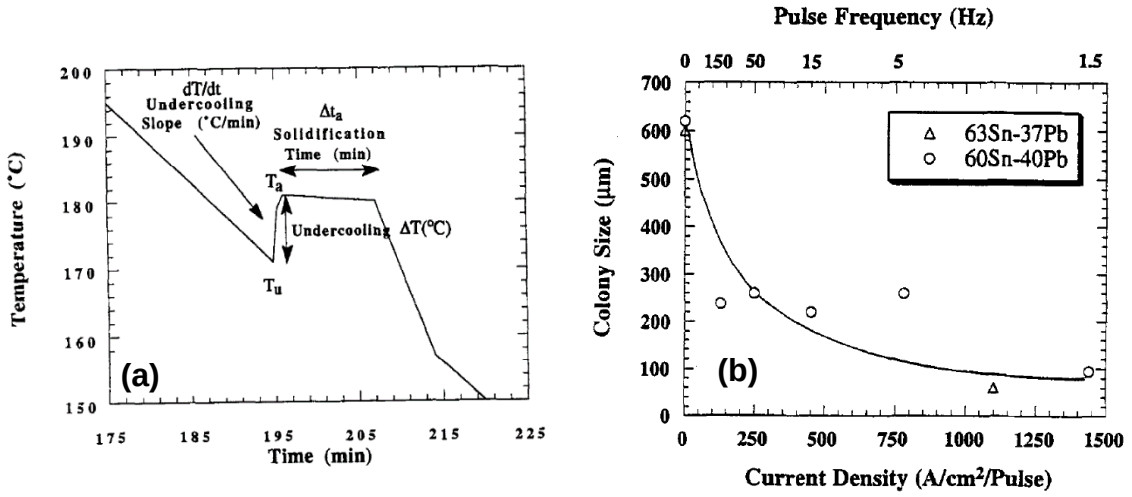

Figure 2.11 (a) The cooling curve during the solidification of a Sn-40%Pb with concurrent electropulsing of 1426 A/cm^2 and 1.5 pulses per second; (b) The effect of electropulsing current density and frequency on the eutectic colony size in Sn-40%Pb and Sn-37%Pb alloys [18].

In contrast to results from Nakada, *et al* in [28], in all cases they studied, the dendrites in the electropulsed specimens were of the same form and size as those without electropulsing, indicating that the dendrites had not been broken [18]. They argued that, because the lamellae spacing was not reduced, the electropulsing applied mainly influence the nucleation of the eutectic colonies rather than their rate of growth. They also discussed the possible reasons that cause the increase in undercooling by the electropulsing, and excluded the skin and pinch effect, and the possibility of decreasing liquid diffusivity by the applied electropulses. Then it is down to whether the electropulsing could decrease the Gibbs free energy or increase the liquid-solid interfacial energy. Unfortunately,

they did not have sufficient experimental evidence to determine which one is more important in the observed increase in undercooling and in turn the nucleation rate with electropulsing [18].

After entering the new millennium, research in this field has become very active in China, and researchers in Zhai's and Ren' group in Shanghai University, China have done a systematic study on using pulse electric current (they called electric current pulse, hence the acronym "ECP" is used here) to refine the grain structures of metal alloys [13, 33]. Some of their important work and findings are summarized and critically reviewed here.

In 2007, Liao, *et al* designed a series of experiments using a similar experimental approach as that in Nakada' s work showed in Figure 2.4c. The electrodes were instead arranged in an up-down manner inside the melt contained inside a sand mould. One electrode was at the bottom of the crucible and the other at the top of the crucible. The ECP with a peak value of 2000 A, and a frequency of 1000 Hz was applied into pule Al melt. The melt was poured at 1113 K into the sand mould of room temperature. Four specimens were cast at the same time, the macrostructures with an applied ECP on different solidification stages are presented in Figure 2.12a. Liao [6] made a strong claim that the solidification structure cannot be refined when ECP is applied to the pure Al in the liquid state or during crystal growth period. ECP has no inoculation effect on the liquid melt. Hence, grain refinement occurred when applying ECP during the nucleation

stage [17]. However, Liao, *et al* did not give any detailed theoretical analyses, for example, as that did by Nakada *et al* in [28], to support their strong argument.

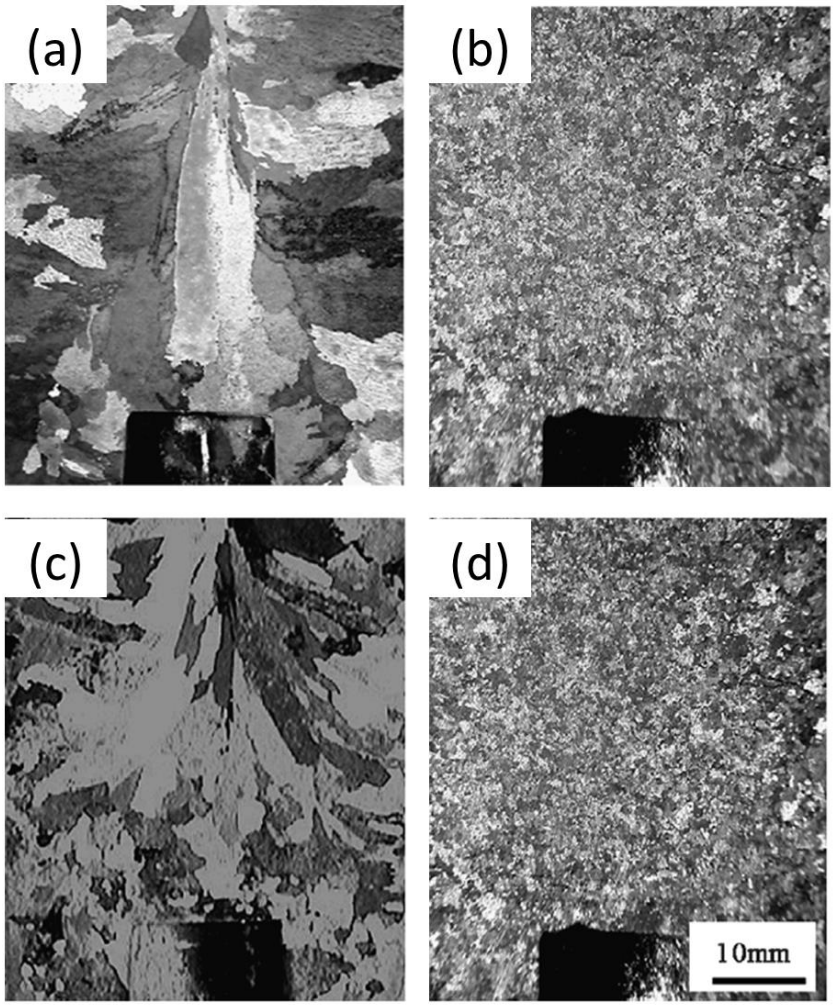

Figure 2.12 Pure Al macrostructures with an applied ECP at different solidification stages: (a) after pouring, apply ECP until the molten metal is cooled down to 938 K; (b) after pouring, apply ECP until the nucleation is finished; (c) apply ECP for the whole stage of crystal growth; (d) apply ECP for the whole stage of solidification [6].

In 2008, Li, *et al.* used parallel electrodes to apply ECP in pure Al melt during solidification and observed the similar phenomena, i.e. grain refinement effect was significant when the ECP was applied in the nucleation stage, but no effect when the ECP was applied in the liquid state [6, 17]. Under the same cooling

condition and ECP parameters, the grain refinement efficiency of parallel electrodes arrangement is better than that of the up-down arrangement. They also argued that ECP with high frequency would increase the atom vibration frequency and enhance the adsorption probability. In addition, ECP also changes the Gibbs free energy of liquid and solid, and the diffusion activation energy [17]. All these effects promote heterogeneous nucleation.

Li, *et al.* [17] proposed the crystal rain effect due to the action of the ECP. After liquid Al is poured into the mould, a small thermal undercooling is generated at the upper surface, leading to the formation of a thin solidified shell or an oxide layer, which provides an appropriate substrate for heterogeneous nucleation. The atomic clusters locating at or near the surface have more opportunities to collide with each other and agglomerate into the stable nucleus under the action of the ECP. At the same time, the ECP also induce a pulse magnetic field within the melt, producing periodic Lorenz force that is acting on the surface. Such force creates shock waves that breaks up the thin solidified shell and makes the nuclei to separate from the mould surface and move into the undercooled melt. This can be viewed as crystal rain. Some of them grow into equiaxed crystals, and some impinge continuously the tip of the primary columnar crystal growing from the mould wall. Such impingement prevents the primary columnar crystal from growing into the coarse columnar crystal. Hence, an overall fine-equiaxed solidification structure is formed [17].

Yin, *et al.* [34] studied the effects of electrode's materials and dimension on the grain refinement. They used three different types of parallel electrodes that were

made of (1) carbon steel, (2) carbon steel with the water-cooling capability, and pure copper. The cross-sections of the electrodes are 15 mm × 2 mm, and 30 mm × 2 mm respectively. They found that, with the same ECP parameters, the electrode with the cross-section of 15 mm × 2 mm had the negligible effect on grain refinement of pure Al, while that of the 30 mm × 2 mm had markedly grain refinement effect [34]. They argued when the electrode of a small cross-section was used, more Joule heat was produced in a small area, resulting in the decrease in the undercooling in the upper surface (where the electrode was acting on) and therefore suppressed grain nucleation, leading to no obvious grain refinement [34]. In the case when pure copper or water-cooled steel electrode (both have cross section of 30 mm × 2 mm) was used, the Joule heat generation was reduced and heat transfer was quicker, leading to a shorter solidification time. ECP also has no effect on the refinement because the grains at the upper surface grew too quickly to be melted or shaken off by the applied pulses [34].

For the Lorentz force generated in this way, the direction of the force will change relative to the change of the electric current vector. In the case of using AC current, the electric current of a sine wave will lead to a sine wave of force. In addition, the amplitude of the force is dependent on the amplitude of the electric current passing through the sample.

2.1.2.3 Under travelling electromagnetic field (TMF)

The travelling magnetic field (TMF) is a direct technique to introduce an electromagnetic force (body force) to the sample in the direction related to gravity. The force is created by means of applying out-of-phase currents to a number of coils. Three phases current applied as shown in Figure 2.5b, the three phases (1–1'), (2–2'), (3–3') are fed by three alternating currents shifted in time. The Lorentz force is induced inside of a conducting melt [35] in the cylinder container and the force direction acts in the axial directions, against gravity or parallel to gravity. This force induces the liquid flows during crystal formation, the flows disturb the growth of grain and stir the nuclei distributes in the direction of flow. The effect of the TMF enhances the nucleation and the growth of equiaxed grains. The force direction depends on the travelling field created from the current path. Metan, *et al*. [36] studied the influence of the travelling fields on Al-Si alloys. In Figure 2.13, the electromagnetic stirring using a TMF with a sufficient field strength provides a homogenous distribution of fine grains of the solidified samples. Zaidat, *et al*. [37] obtained the equiaxed grains in Al-Ni alloys during directional solidification under a TMF.

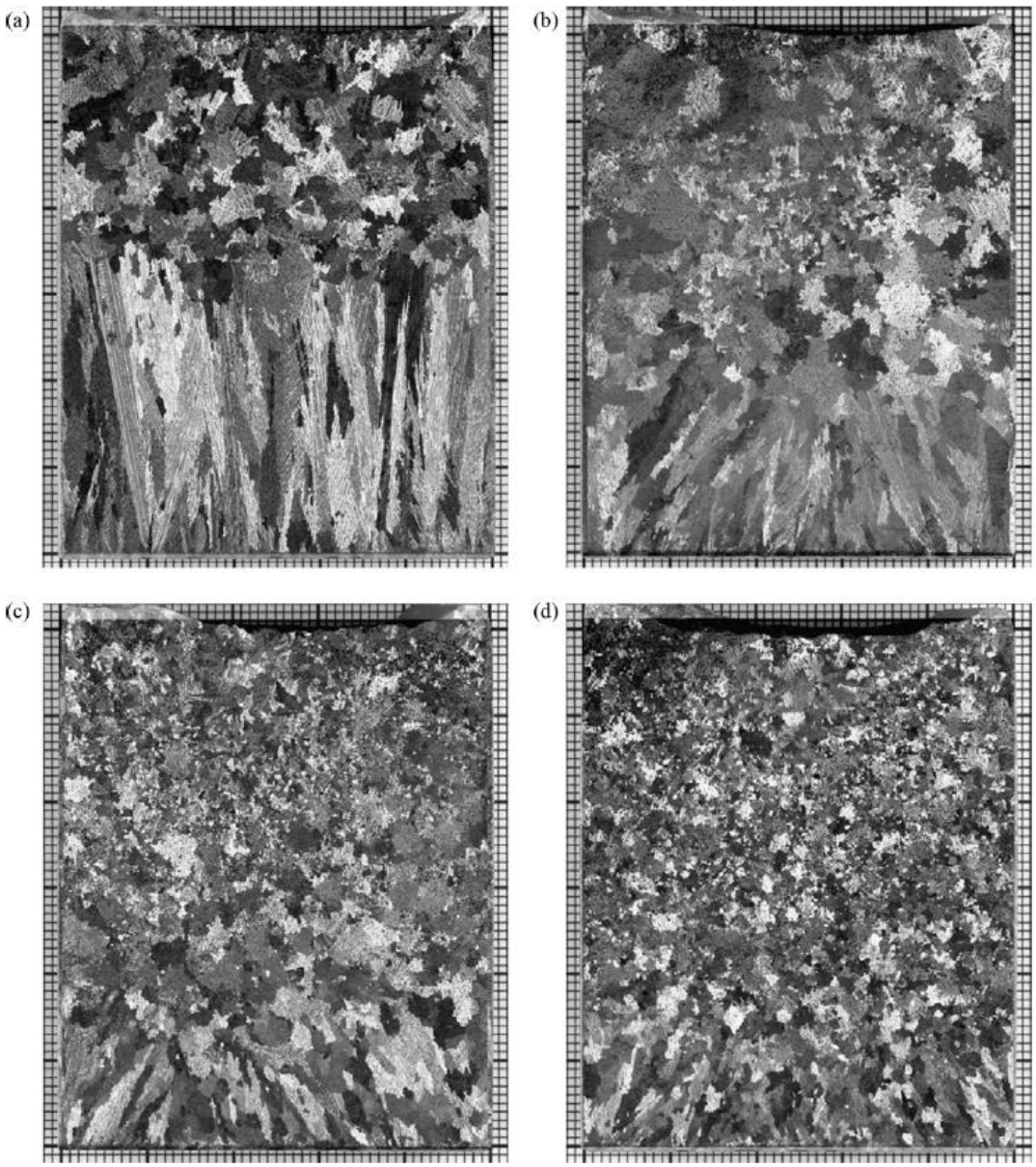

Figure 2.13 Macrostructure of Al–7 wt% Si samples without grain refining particles: (a) without electromagnetic stirring; (b) upward TMF, 6 mT; (c) upward TMF 12 mT; (d) upward TMF 18mT.

2.1.2.4 Under pulse magneto oscillation (PMO)

Recently, a novel, non-contact technique has been developed and named as pulse magneto oscillation (PMO). However, in this thesis, we use the term “pulse

electromagnetic field (PMF)" in order to reflect the physical nature of this technique. PMO stores electric power using a high capacitance capacitor, then discharges the pulse current into a coil which induces a pulse Lorentz force. The Lorentz force causes the vibration of the liquid metal due to the coil contact the outer surface of a sample container. The inner melt will be shocked by the pulse oscillating wave so that the structure can be refinement.

In 2008, Gong, *et al.* [38] developed a pulse magneto-oscillation (PMO) method to refine the solidification structures of pure Al, They used a capacitor bank of 200 μF to store electricity of voltage as high as 8000 V, and then discharged it into a copper coil of 2500 V. The experimental setup is showed in Figure 2.5a. In some experiments, they placed a stainless-steel mesh with the sieve number of 60 inside the mould to protect any nucleus outside from entering the mesh.

Figure 2.14 shows the effects of the PMO on the refinement of the solidification macrostructures. Without PMO, it was coarse columnar grains (Figure 2.14a). When PMO was applied the macrostructure is divided into two parts by the mesh. Only the structures outside the mesh were refined (Figure 2.14b). While that inside the mesh, the structures are still coarse grains.

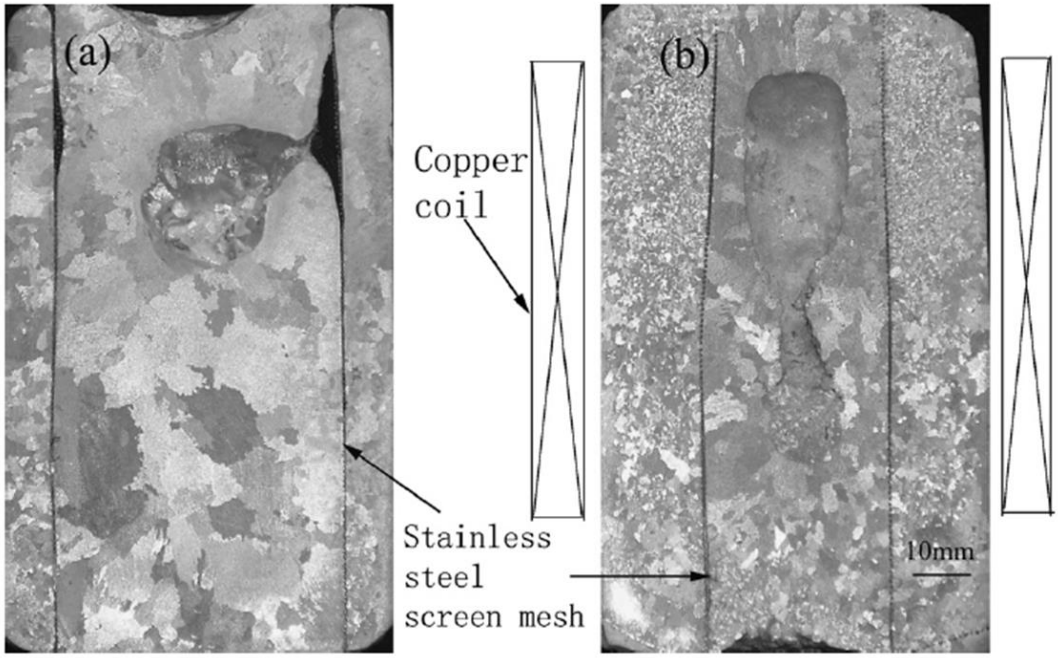

Figure 2.14 The macrostructures of the pure Al specimens with vertically placed stainless steel mesh (a) without PMO; (b) with PMO [38].

From those experimental evidence, Gong, *et al* argued that the PMO has the similar effect on the pure Al as that of the ECP in terms of grain refinement. The mechanism is that the nuclei formed on the mould wall fall off and drift into the melt under the action of PMO, leading to the refinement of the solidification structure. The best refinement effect due to PMO and ECP treatment can only be achieved during the nucleation stage and the first half period of crystal growth.

If pulse electric current induced by PMO has the same pulse width and intensity to those of the ECP generated by electrodes, their refinement effects on the melt should be identical since the distribution of the electromagnetic field in the melt is the same [38]. However, contact electrodes are needed in the ECP treatment. Such arguments are actually contradictory because the induced current inside the melt due to PMO is not the same as that due to the ECP. In addition, Gong,

et al also discussed how PMO sound wave pressure helped to move nuclei clusters inside the melt [38]. Such an argument was without evidence and quite confusing.

In 2012, Yin, *et al* reported a surface pulsed magneto-oscillation (SPMO) method for refining the solidification structures of metals and alloys [39]. An example of a flexible arrangement by using a special flat spiral type coil made by a pure copper tube (can be cooled with flowing water). The experimental apparatus (Figure 2.15a) is consisting of a pulse generator, an oscilloscope for monitoring the electropulse, and an electric resistance furnace. The direction of the Lorentz force is given by the “left hand” rule. The magnetic field is not perpendicular to the liquid surface, being at an angle of θ to the eddy current, thus the Lorentz force's direction is changing constantly with the electropulse varying, making the melt oscillate up and down.

Under normal solidification conditions without SPMO, the surface chill zone was clearly observed, forcing the surface crystals grew downwards and impinged on the crystals below, resulting in a clear boundary as showed in Figure 2.15b. While with SPMO, the SPMO-induced free crystals on the top tended to drift away towards the centre and then piled up on the bottom by the forced convection (Figure 2.15c). In addition, the macro-shrinkage cavity became smaller after the SPMO treatment. Because of the increase in the area of the equiaxed grains, and the induct Joule heating on the upper surface, which is favourable for the decrease in the shrinkage cavity [39].

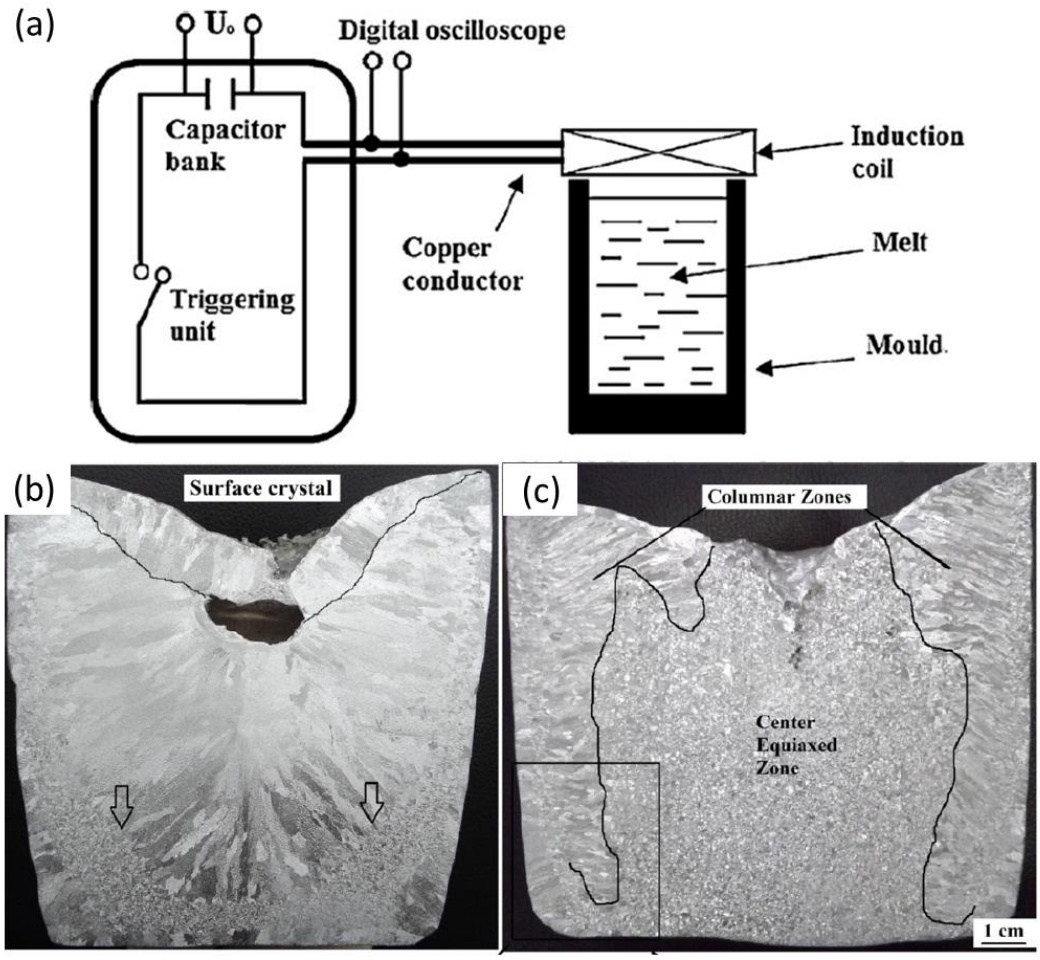

Figure 2.15 (a) the schematic of the experimental setup. The macrostructures of two pure Al ingots: (b) without SPMO, (c) treated with SPMO.

In 2014, Liang, *et al* [40] studied the effects of PMO on thermal undercooling. They found that, for pure Al melt, the thermal undercooling of the melt increases and the temperature gradient from the mould wall to the centre of the casting decreases due to melt convection induced by the PMO treatment. Increasing thermal undercooling largely promotes nucleation of pure Al grains while decreasing the temperature gradient to low levels means that most of the melt is slightly undercooled preventing remelting thus improving the survivability of the nucleated grains and allowing these grains to grow. Therefore, when PMO

treatment produced these casting conditions, very fine grain structures could be achieved [40].

2.1.4 Summary

External physical fields, e.g. ultrasound or magnetic fields can generate force inside the semi-solid melt, affecting the growth of grains or dendrites, or breaking the dendrite arms to act as “embryonic nuclei” for the subsequent growth [41, 42]. This force has the effect on dendrite fragmentation process. The force also enhances convection to disperse the newly formed fragments throughout the solidifying melt, therefore uniform grain growth is produced inside the entire volume, resulting in a refined grain structure.

For all electromagnetic field techniques reviewed so far, the main advantages are: (1) they are sufficient electromagnetic expulsive force can be generated to act on the solidifying melt. The PMF or the PMO techniques even offers a clean process in environmental perspective since there is no contact between the melt and the power source; (2) they are generic methods. The effect of the electromagnetic force is dependent on the difference in electric conductivity and those between the different elements or phases in the melt.

However, the electromagnetic field techniques also have disadvantages depending on the setup and its characteristics: (1) for the direct-contact techniques, e.g. neither EMV nor ECP method, the parts or probes of those apparatus have to submerge or attach to the melt to transmit the currents into the melt. The submerged part of the device is contacting the molten sample which causes contamination of the melt and damage of the device; (2) the direct-contact

techniques are effective for refinement of small volume of melt, but have limitation in applying the current into a large volume of melt; (3) For contactless techniques, there is a need of high electric current or voltage (a huge consumption of energy) to generate huge amount of force into the melt in order to break up the grain structure during solidification, therefore it is also difficult for large volume of melt. This grain refinement volume by non-contact method needs further investigation.

Based on the above reviews and analyses, an energy efficient pulse electromagnetic fields (PMF) device was designed and developed in this research with the aim of combining the above advantages together. The principle, design and the manufacturing of this device is described in Chapter 3.

2.2 X-ray and synchrotron X-ray

X-ray and neutron beam can “see” through opaque materials, such as liquid metals. And they are powerful tools to study in–situ and in real–time the solidification structures. The fundamentals of lab-based X-rays and synchrotron X-rays are described below, with an emphasis on the difference between synchrotron X-rays and lab-based X-rays, and why the synchrotron X-rays imaging is needed in this project.

2.2.1 A brief history of X-rays

In November 1895, Rontgen discovered X-rays in his laboratory at the University of Würzburg, Germany. He examined the radiations associated with the

discharged electrodes in an evacuated glass tube. The Figure 2.16 shows the stunning image of displaying bones of his colleague Albert von Kölliker's hand.

Figure 2.16 X-ray radiogram made by Wilhelm Conrad Rontgen (1845–1923) of a hand of a colleague in 1896. He was awarded the first Nobel Prize for physics in 1901.

It was about 100 years ago that W. Coolidge developed the Coolidge X-ray tube at General Electric Research Laboratories in New York. The Coolidge tube served as the standard X-ray tube for many decades with only marginal improvements in the design and making, and a gradual increase in the X-ray flux until the arrival of synchrotron X-rays that provide the exponential improvement in the X-ray brilliance, coherence, spatial resolution, etc.

Figure 2.17 shows the brilliance of 1st generation synchrotron light source, the electron-positron colliding machine, became available in the 1970s. The 2nd generation with the use of large storage ring and bending magnets started from the 1980s. The 3rd generation of synchrotron radiation (SR) facilities have a remarkable improvement in flux and intensity of the X-rays produced, and are available for research in almost all disciplines of sciences [43]. Nowadays, the 4th generation light source, called X-ray free-electron lasers (XFEL), produce flashes of X-ray light with angstrom-level wavelengths — small and coherent enough to image individual atoms. The European XFEL, the world's largest X-ray laser staring in 2017, generates ultrashort X-ray flashes — 27, 000 times per second and with a brilliance that is a billion times higher than that of the best conventional X-ray radiation sources.

Several aspects of an X-ray source determine the quality of the X-ray beam. These aspects can be combined into a single quantity (called the brilliance) which allows users to compare the beams from different sources [43]: $Brilliance = \frac{Photons/second}{(mrad)^2(mm^2\ source\ area)(0.1\%\ BW)}$

First of all, there is the number of *photons emitted per second*. Next, there is the collimation of the beam. This describes how much the beam diverges, or spreads out, as it propagates. The collimation of the beam is given in *milli-radian* (both for the horizontal and for the vertical direction). Thirdly, it may be of importance how large the *source area* is (usually given in mm^2). Finally, there is the issue of the spectral distribution. Some X-ray sources produce very smooth spectra, others have peaks at certain photon energies. When making comparisons, what range of photon energies contribute to the measured intensity. The convention is

therefore to define the photon energy range as a fixed relative energy *bandwidth* (BW), which has been chosen to be 0.1% [43].

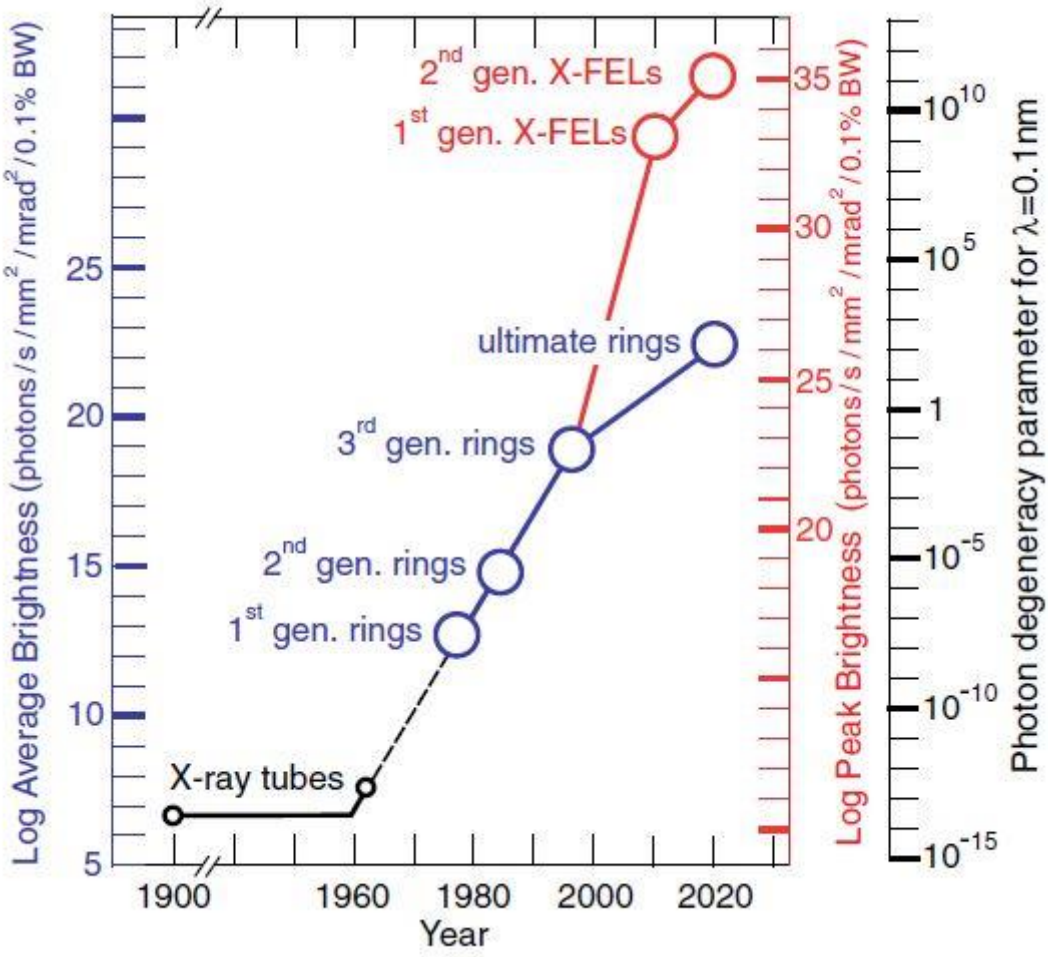

Figure 2.17 The brilliance of X-ray sources as a function of time [43, 44].

2.2.2 X-ray sources

Figure 2.18 illustrates the principle of generating X-ray from the Coolidge tube. When a filament, also called cathode, is heated up by using a high voltage normally in the range of 20-150 kV, electrons are emitted and then accelerated

in a vacuum by a high electric field towards to a metal target, such as W, Cu, Mo, Ag, etc., which being positive is called the anode and it is normally cooled by using a circulation of water. In medical X-ray tubes, the target is usually tungsten or a more crack-resistant alloy of rhenium (5%) and tungsten (95%), but sometimes molybdenum for more specialized applications, such as when softer X-rays are needed as in mammography. In crystallography, a copper target is most common [43]. In 1960s, rotating anode generator was invented with the use of a higher power as the heat could be dissipated over a much larger volume than in a standard tube (Figure 2.18b).

Figure 2.18c shows that the spectrum of X-rays generated from electrons impinging on a metal anode has two distinct components. The first is a broad and continuous spectrum, commonly known as Bremsstrahlung radiation. It has a maximum energy that corresponds to the high voltage applied to the tube. The second is sharp line spectra with characteristic energies superimposed on top of the broad spectrum. The sharp line spectra are produced by the collisions of the incident electrons with the atoms in the target material. When an incident electron collides onto an atom, it may also cause an electron to be removed from one of the inner shells of the atom, creating a vacancy. The subsequent relaxation of an electron from an outer shell into this vacancy produce an X-ray with a characteristic energy equal to the difference in energy between the two shells. For example, Figure 2.18d shows that the electrons at K shell are knocked off and then the vacancies are filled by the electrons from L and M shell. During this process, the extra energy of the electrons on L and M shells will be released in the way of emitting X-ray with the energy at K_α and K_β with an intensity few orders

higher than the Bremsstrahlung spectrum (especially K_α), and this is called characteristic X-ray. For experiments requiring a monochromatic beam, the K_α line is often used, which is several orders of magnitude more intense (bright) than the Bremsstrahlung spectrum. The energy of characteristic X-ray mainly depends on the atomic structure of the target materials, and some of the commonly used targets are listed in Table 2.1.

Table 2.1 The common anode materials and characteristic X-rays [45].

Anode material	Atomic number	Photon energy (keV)		Wavelength (nm)	
		K_α	K_β	K_α	K_β
W	74	59.3	67.2	0.0209	0.0184
Mo	42	17.5	19.6	0.0709	0.0632
Cu	29	8.05	8.91	0.157	0.139
Ag	47	22.2	24.9	0.0559	0.0497
Ga	31	9.25	10.26	0.134	0.121
In	49	24.2	27.3	0.0512	0.455

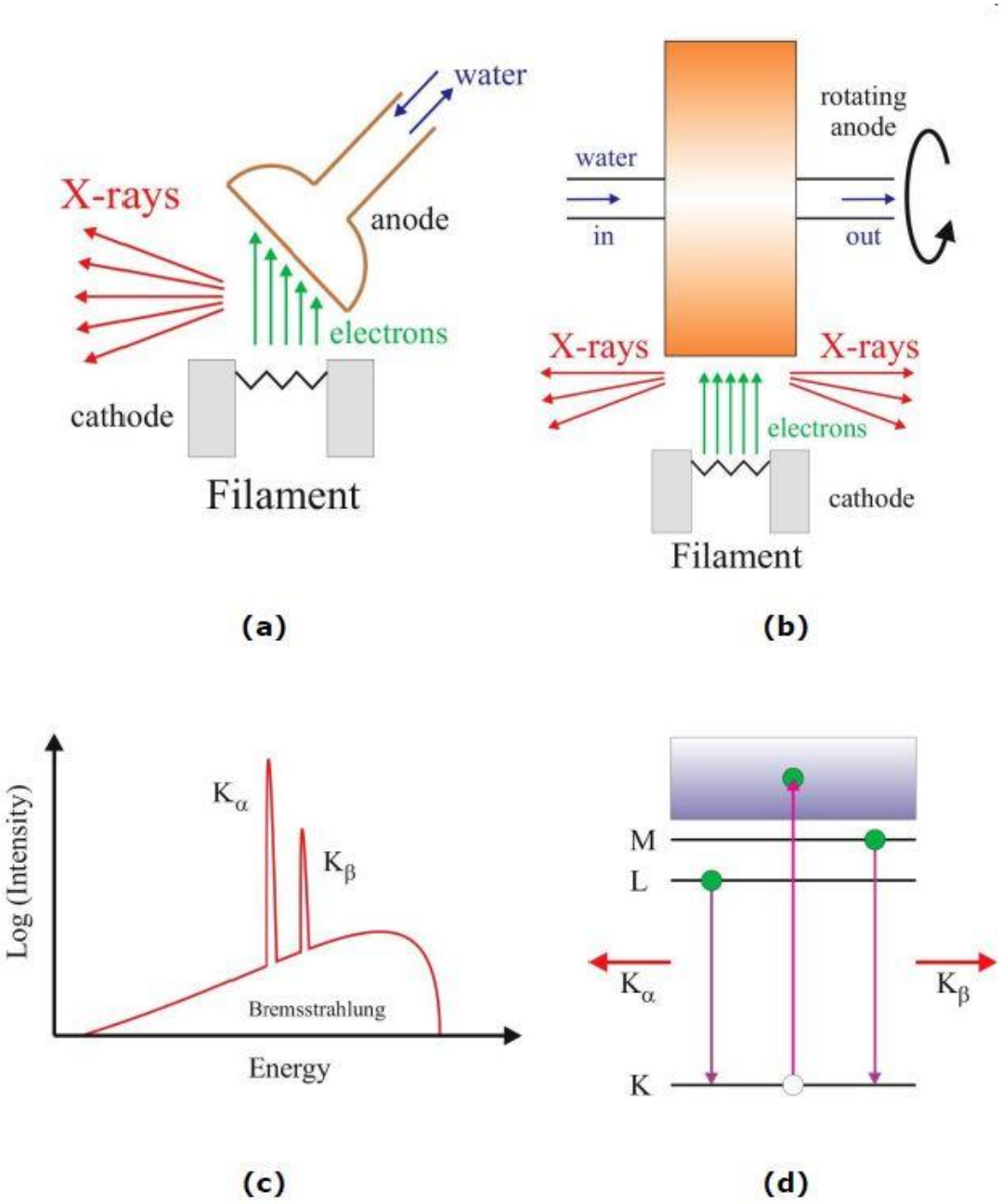

Figure 2.18 (a) the standard X-ray tube was developed by Coolidge around 1912. The intensity limitation is set by the maximum power a cooled metal anode can withstand; (b) the power can be increased by dissipating it over a larger volume which is achieved by rotating the anode; (c) the spectrum from an X-ray tube has discrete fluorescent lines superimposed on the continuous bremsstrahlung radiation; (d) schematic atomic energy level diagram: the K_α line results from transitions between an L and K shell, whereas the K_β comes from an M to K transition [43].

2.2.3 Synchrotron radiation

2.2.3.1 Introduction of synchrotron radiation

Synchrotron radiation (SR) takes its name from a specific type of particle accelerator. Presently, there are about 90 SR facilities (e.g. the Diamond light source, the Swiss Light Source, and the European Synchrotron Radiation Facility) around the world serving a wide variety of fundamental and applied research fields [45, 46].

SR has following advantages for metal research:

(1) the very high brilliance of the X-ray (very high photon flux) make it possible to perform time-resolved research in-situ to visualise the dynamic events of materials at micron or even submicron length scale, and in a timescale down to microsecond; (2) the high energy can penetrate thick materials for imaging internal structure non-destructively, e.g. superalloy [47].

Synchrotron facilities provides a wide energy range. For instance, Figure 2.19 shows the average brightness against the photon energy for typical synchrotron radiation sources, in comparison to conventional X-ray tubes in lab. The brilliance of X-ray produced by an undulator (10^{21}) is higher than that from a wiggler (10^{18}), and both produce X-rays with much higher brilliance than those produced by traditional lab-based X-ray tube (up to 10^{11}) and bending magnet (10^{16}). This could significantly reduce the noises and the beam hardening. However, the narrow bandwidth of the radiation spectrum is resulted in discontinued energy spectrum in an undulator, while the X-ray from wiggler has a continuous energy.

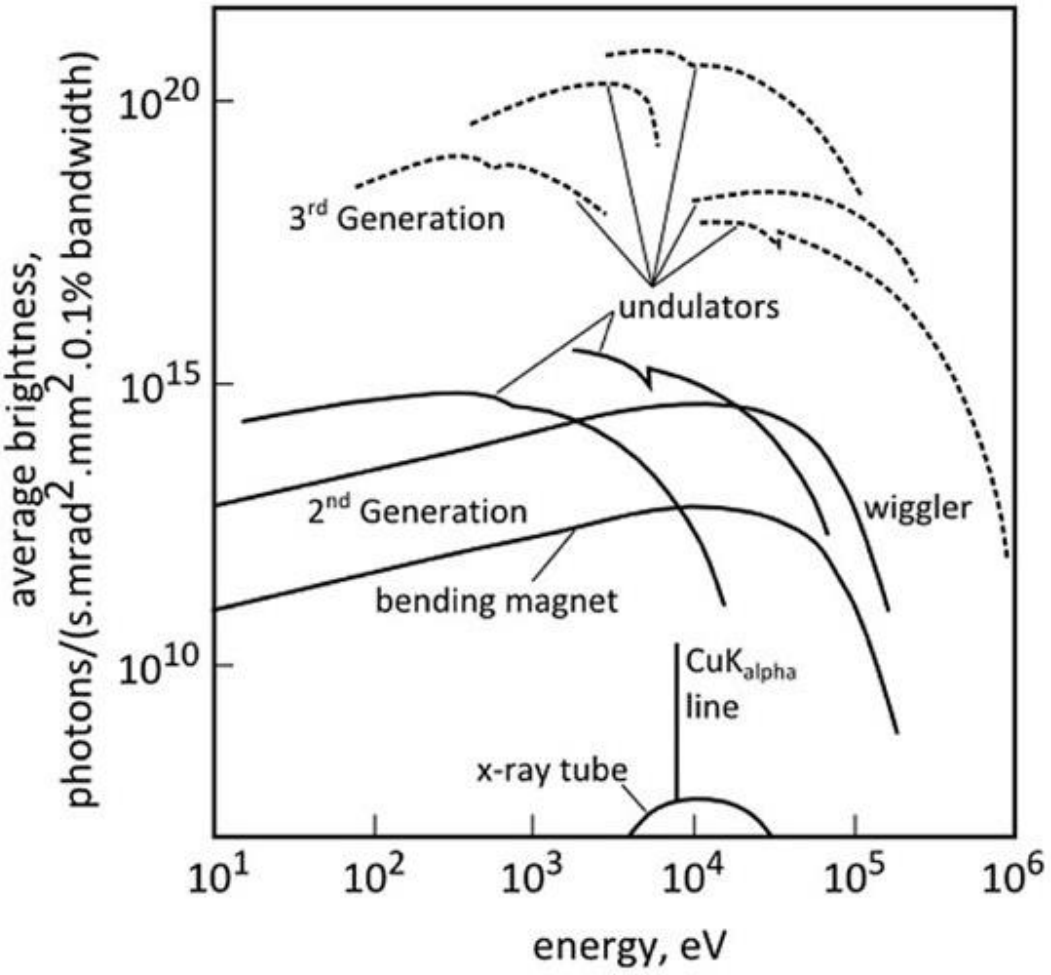

Figure 2.19 Average spectral brilliance (brightness) against photon energy for typical synchrotron light sources compared with conventional X-ray laboratory sources. It is obvious to see that synchrotrons provide high fluxes over a wide energy spectrum [48].

2.2.3.2 Diamond Light Source

All 3rd generation synchrotron X-ray facilities around the world are operated in the same principles. Diamond Light Source (DLS) as shown in Figure 2.20a is used here to describe the basic theory, essential configurations and functions. DLS is the UK's national synchrotron source which has 31 beamlines with the range of

energy from 1.2 eV to 150 keV. It works as a giant microscope, producing bright light (10 billion times brighter than the sun) and helping scientists and researchers to study anything from fossils to jet engines to viruses and vaccines.

As shown in Figure 2.20b, an X-ray beam at the DLS begins with electrons that produced in electron gun, and electrons are accelerated by high-voltage alternating electric fields in a linear accelerator (linac). Selective phasing of the electric field accelerates the electrons to 100 million volts (MeV). At 100 MeV, electrons are traveling nearly at (>99.999%) the speed of light, which is 299,792,458 meters/ second (186,000 miles/second) [45].

Next, electrons are injected into the booster synchrotron, a racetrack-shaped ring of electromagnets, and accelerated from 100 MeV to 3 billion electron volts (3 GeV) in one-half second, and they could travel around the entire world 7.5 times in a single second. The accelerating force is supplied by electrical fields in four radio frequency (RF) cavities. In order to maintain the orbital path of the electrons, bending and focusing magnets are used to increase the electron field strength in synchronization with the RF field [45].

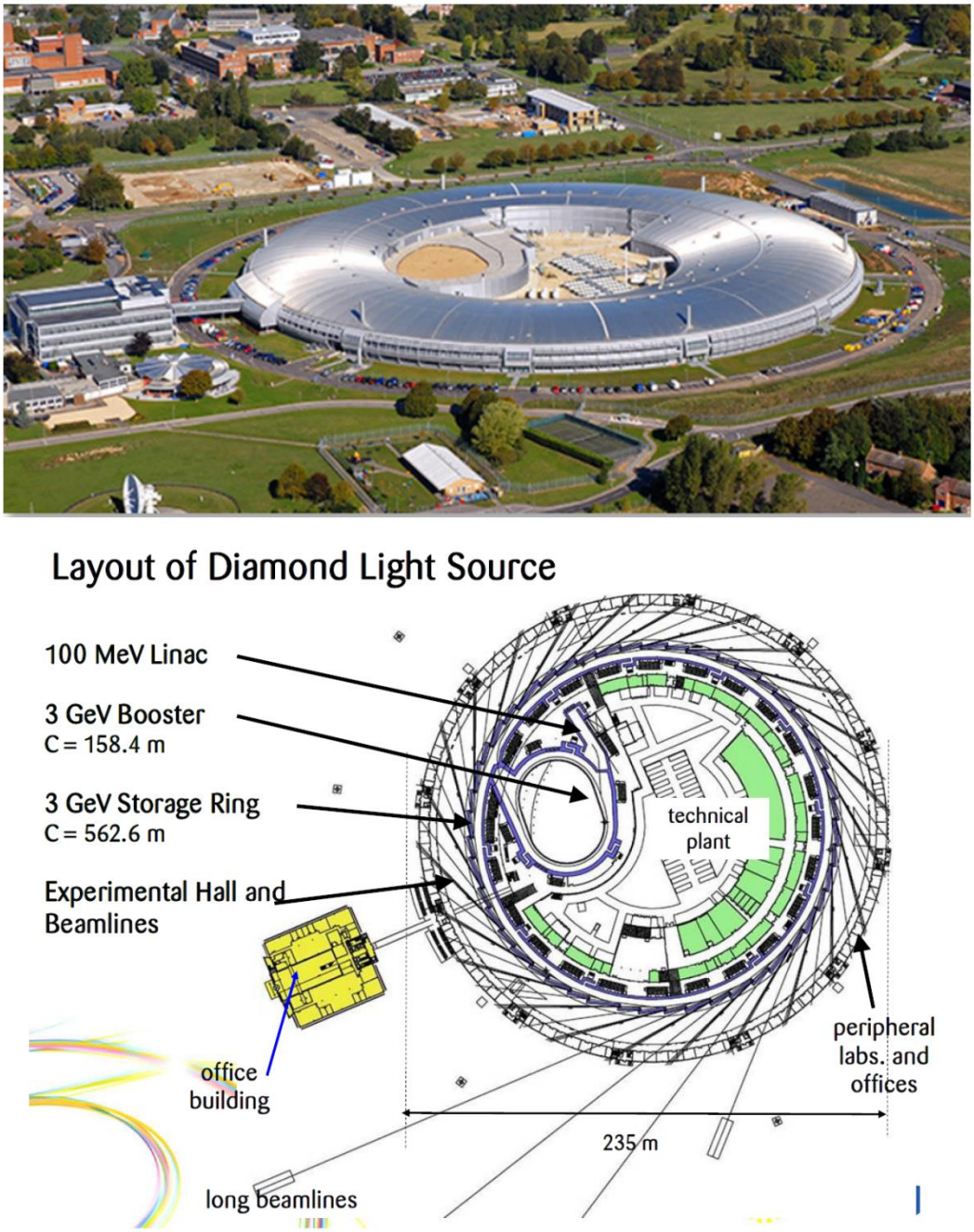

Figure 2.20 (a) The aerial view of Diamond Light Source, UK; (b) A schematically diagram of a typical 3rd generation SR source composed of (1) a linear accelerator (Linac); (2) a booster ring; (3) a storage ring with wiggler or undulator; (4) beamline hutches (office building) [45].

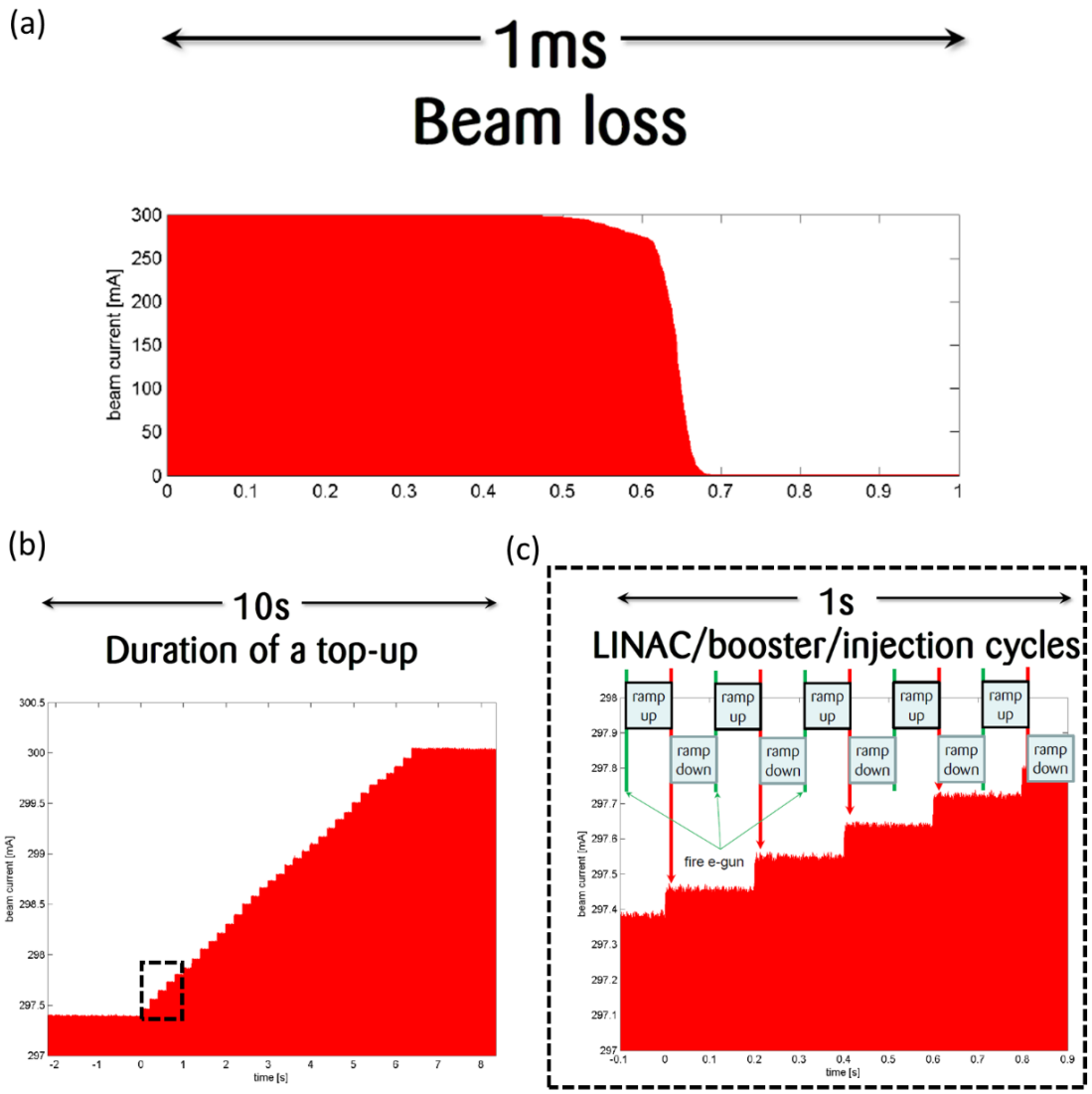

Figure 2.21 The beam current on various timescales and when to top-up the electrons.

The 3 GeV electrons are injected into the 562.6 m circumference storage ring. However, the storage ring is not a true circle, but a type of polygon called a tetracontakaioctagon, made of 48 straight sections angled together with 48 bending magnets, and this magnetism is used to steer the electrons around the ring. A powerful electromagnetic field focuses the electrons into a narrow beam

that is bent on a circular path as it orbits within aluminium tube vacuum chambers running through the centres of the electromagnets.

As the electrons circulate in the storage ring they collide with each other, and with the few gas molecules that remain in the vacuum are lost. To make up for this loss, new electrons are added to the ring every 10 minutes in a process known as “top-up” shown in Figure 2.21. The advantage of top-up, compared to the previous method of injecting electrons only twice per day, is that the light beams delivered to the beamlines are more stable and remain at maximum intensity at all times.

2.2.4 Synchrotron X-ray radiography and tomography

The word ‘tomography’ is derived from the Greek words ‘tomos’ meaning ‘to slice’ and ‘graph’ meaning ‘image’ [49].

Basically, tomography generates a three-dimensional image by collecting transmission radiographic dataset. This data often called “projection images” is shown in Figure 2.22, it contains the entire microstructures information. However, it cannot be directly used since all of the information along the beam path is superimposed. To deconvolute the information along the beam path, the sample need rotate over 180 ^{o}. In addition, the more projections are acquired, the closer the summation of them resembles the original information (higher quality of the data) during the rotation. The microstructural information can be calculated from the projection data via a reconstruction method.

Nowadays, a synchrotron based non–destructive computed tomography (CT) microscopy technique with a high resolution down to micron range ($< 1\ \mu\mathrm{m}$) often

called μ–SR tomography. The SR has high fluxes which significantly improve the speed of data acquisition. Hence, it is possible to record entire tomogram in a few seconds or even, in favourable circumstances, on the subsecond timescale (< 1 s) [50]. This time-resolved materials processing studies using μ–SR tomography of processes such as solidification are becoming popular [51-54]. Theoretically, tomography experiments can be conducted at almost any SR facility. Table 2.2 shows a selection of beamlines located at the synchrotron radiation facilities.

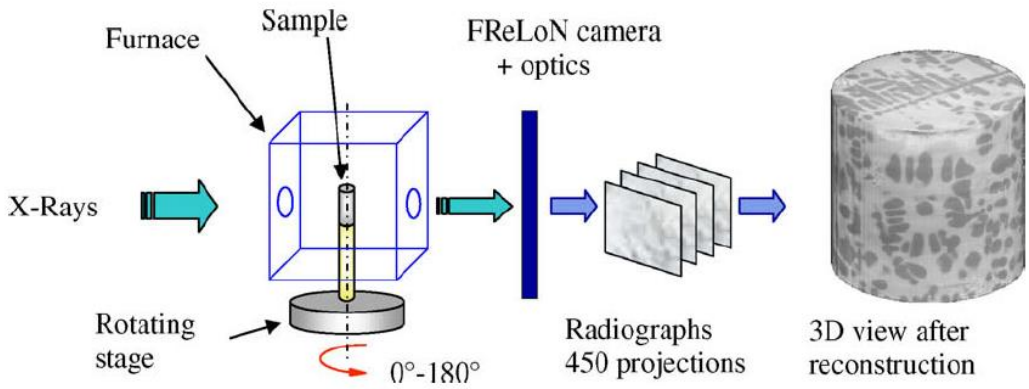

Figure 2.22 The schematic setup for high-resolution tomography experiments at ID 19 (ESRF) [55].

Figure 2.23 show the development of famous SR facilities with respect to the spatial and temporal resolutions across the world. The energy ranges specified should be seriously considered. Researchers are also advised to consult the local beamline scientist, and to search the beamline manuals and extreme limits before any experiments. In most cases, the tomography experiments will be performed in a narrower energy range because the beam intensity is much higher and the

charge coupled device (CCD) systems are optimised to a fairly narrow energy range. For example, we quote the beamline ID19 at ESRF: The beamline can work in the energy range 8 to 250 keV, however most of the materials related experiments are performed in the range of 10 – 35 keV.

Recently, researchers are now combining bespoke heating furnace, and/or mechanical testing rigs with micro- synchrotron tomography to carry out in-situ experiments. In next section, a few applications of ultrafast or high-speed micro-synchrotron tomography to study metallic materials will be reviewed.

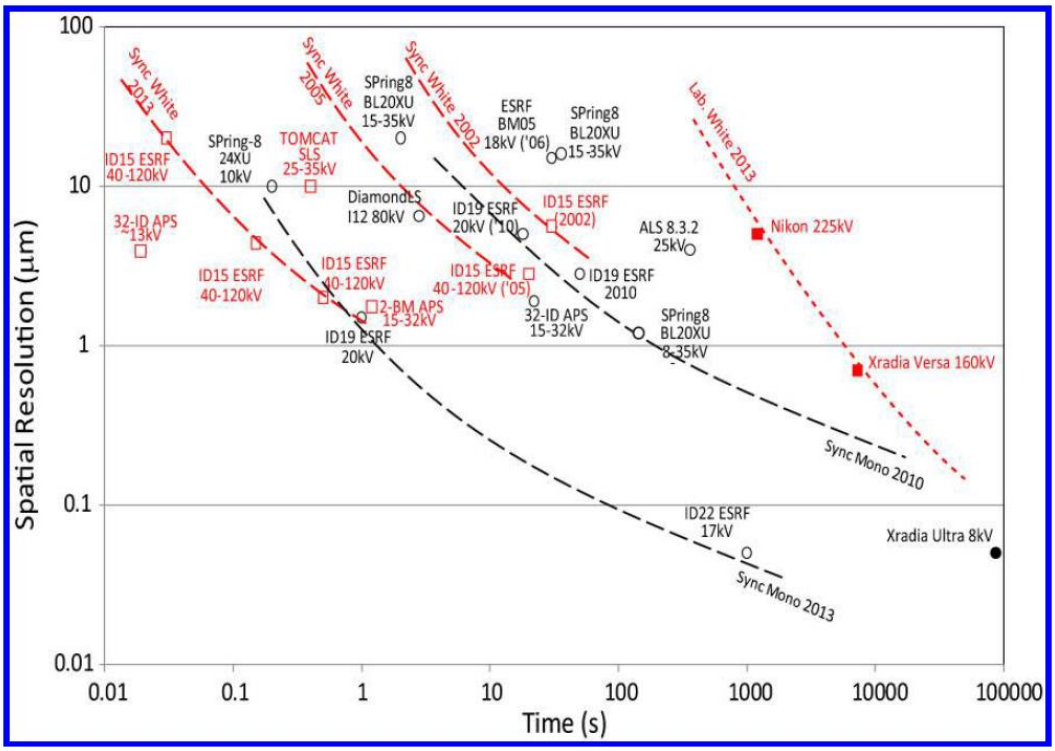

Figure 2.23 The spatial resolution against the temporal resolution for different beamlines in different X-ray facilities [50].

Table 2.2 Synchrotron beamlines that can perform tomography experiments

Facilities	Country	Ring energy (GeV)	beamline	Energy range (keV)	source
APS	USA	7	2-BM-B	3 – 33	Bending magnet
DLS	UK	3	I13	8 – 30	Undulator
SLS	Switzerland	2.4	TOMCAT	9 – 45	Wiggler
ESRF	France	6	ID19	10 – 250	Undulator & Wiggler
Spring-8	Japan	8	BL20XU	8 – 113	Undulator

2.3 In-situ synchrotron X-ray study of metal solidification

Synchrotron radiation is widely used for materials science and engineering studies (For example, mechanical properties of materials, organic or metal solidification, catalysts and additive manufacturing) [56-61].

The very recent successful examples have been briefly reviewed regarding in-situ study the solidification dynamic via synchrotron radiations.

Firstly, in the period of 1993-2014, Professor John Campbell, *et al* [62, 63] use lab-based X-ray to study the entrained air bubbles during liquid filling of the casting; (2) Professor Ragnvald Mathiesen and Professor Lars Arnberg of Norwegian University of Science and Technology were the first to use synchrotron X-ray radiography to study dendrite growth in metal alloy at ESRF using radiography in 1999 [64].

Currently, there two research groups who did a few very advanced 4D tomography studies on metal alloys are: (1) In the UK, Professor Peter Lee's group at University of Manchester and Diamond Light Source; (2) In the US, Professor Peter Voorhees's group at Northwestern University. Research groups in France, Japan did and are doing tomography as well.

2.3.1 Solidification

In 1999, Mathiesen use the very intensive coherent monochromatic synchrotron radiation beam (23.88 ~ 25 keV) with a fast readout low noise detector for in situ studies of solidification of Sn-Pb alloys. Temporal and spatial resolutions down to ~0.7 s and ~2.5 mm, respectively and with a field of view up to 1 mm^2 were obtained [64]. In Figure 2.24, the columnar dendritic growth and the cellular growth of Sn crystals in Sn–10 wt%Pb and the equiaxed Pb dendritic growth in Sn–52 wt%Pb were observed respectively, for the first time.

His experimental approach provides a new method to study the time-resolved solidifying metal microstructures in real-time, and open a new area for the in-situ solidification studies, and also provide strong evidences for validating the numerical simulations and theoretical modelling.

However, limited information was described might be attributed to the limitation of beamline resolution and the immature data processing software at that time.

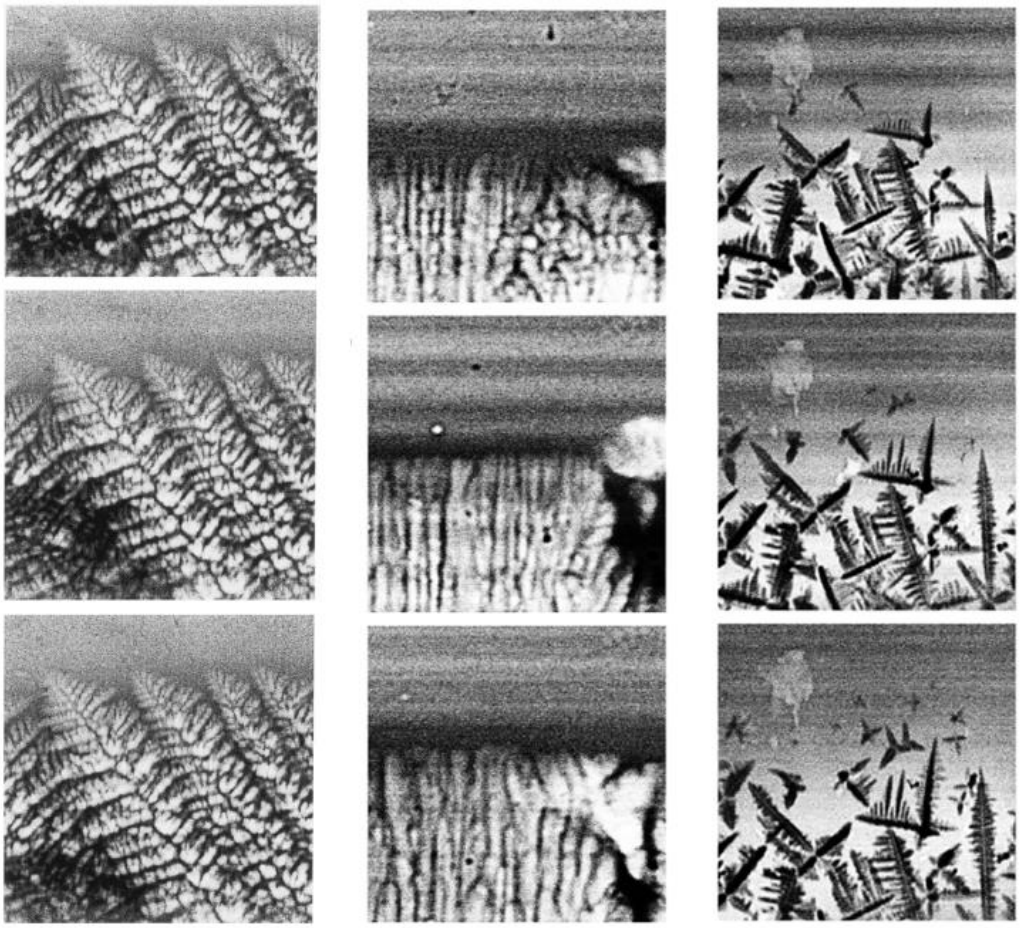

Figure 2.24 The time-resolved microstructures via synchrotron X-ray radiography, showing the columnar dendritic growth (left column) and cellular growth (middle column) of Sn crystals in Sn–10wt%Pb alloy and the equiaxed dendritic growth (right column) of Pb crystals in Sn–52wt%Pb alloy [64].

In 2009, Limodin *et al*. [65] used synchrotron fast X-ray microtomography to study in situ the microstructural evolution of an Al–Cu alloy during solidification at a constant cooling rate of 3 K/min. In Figure 2.25, the evolution of the dendritic

microstructure with solidification time was fully characterised with a spatial resolution of 2.8 µm.

The time-resolved of solid fraction, the specific surface area of the solid-liquid interface, and the distribution of local curvature were quantified. In addition to solidification growth, two coarsening mechanisms were observed to act upon the dendrite arms. The first mechanism involves remelting of small secondary dendrite arms to the benefit of bigger adjacent arms. The second is the coalescence of adjacent secondary arms, with progressive filling of the inter-arm spacing and coalescence at the tips. In situ X-ray tomography allows revisiting the various models which have been proposed to account for dendrite coarsening during solidification [65].

However, same solidification experiments at different cooling rates are needed to study the influence of this parameter on the coarsening mechanisms observed. It suggested that at higher cooling rates the coarsening mechanisms have probably less influence on the dendrite morphology. Also, it would be necessary to further reduce the acquisition time of a tomographic scan in order to carry out in situ observations of dendritic solidification at higher cooling rates.

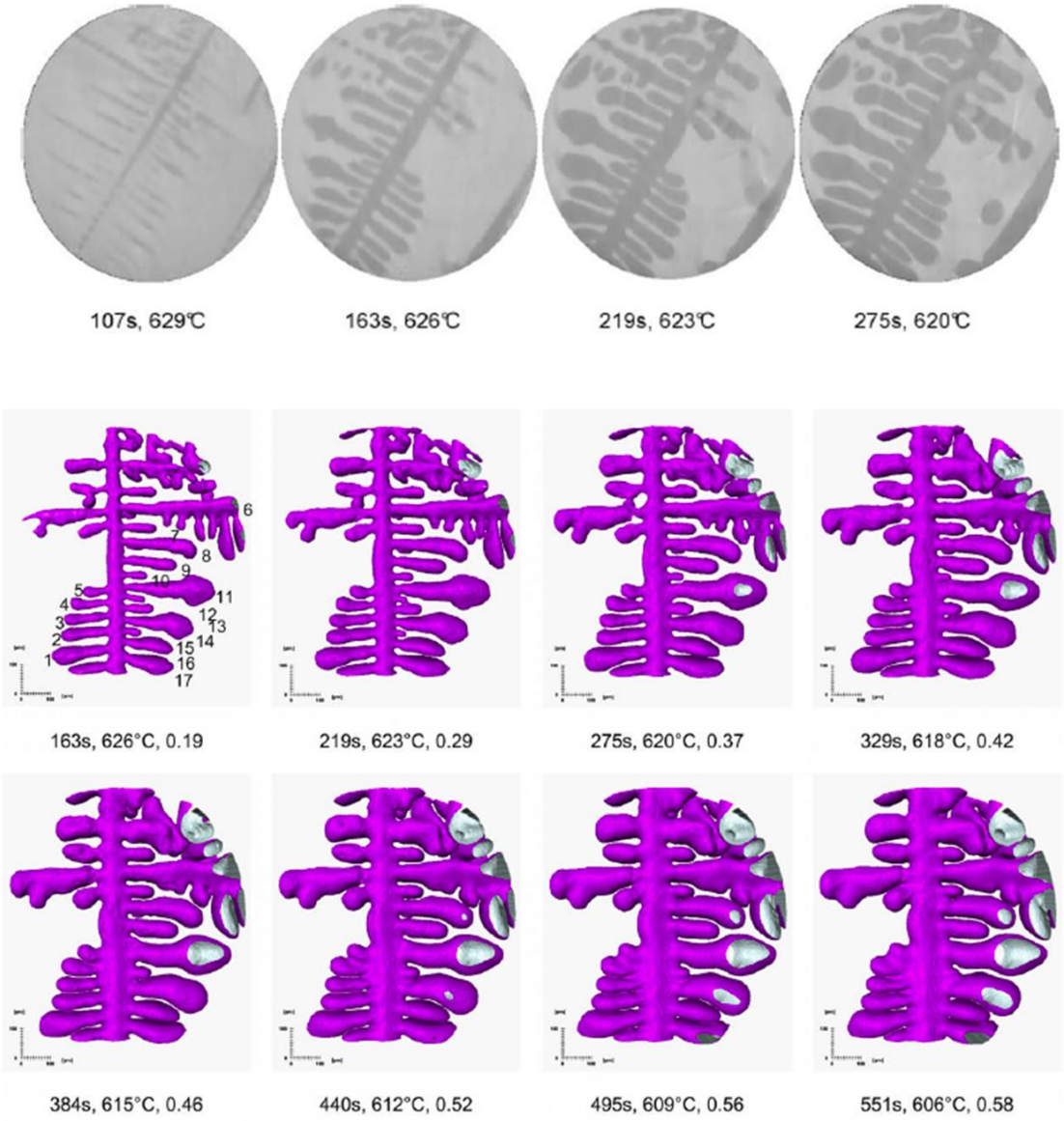

Figure 2.25 2-D slices show the microstructural evolution (top) and three-dimensional dendritic evolution with time during solidification (bottom parts) in an Al-15wt%Cu alloy. The cooling rate at a constant of 3 ^{o}C/min [65].

Iron (Fe) is a common impurity in aluminium alloys and is usually considered detrimental to casting quality and production yield. Because of the solubility of Fe in liquid Al is high (≈1.8 wt.%), Fe can enter molten aluminium in many ways either from the dissolution of Fe from steel casting tools during the casting process or from recycled Al scraps where Fe concentration is often higher than 0.5%. This amount of Fe is sufficient to produce various forms of secondary Fe-rich intermetallic phases [66]. Normally, the presence of a small quantity of Fe can induce the formation of hard and brittle intermetallic iron-rich plates which have deleterious effects on cast ability, machinability and mechanical properties [67]. In most cases, these Fe-phases, especially when the needle-like or plate-like phases, e.g. β-Al_7Cu_2Fe phase, are detrimental to the alloys [68].

In 2010, S. Terzi *et al.* [69] investigated the β-Al_5FeSi phase formation during solidification of an Al-Si-Fe alloy via in-situ synchrotron X-ray tomography. He observed that after formation of the primary Al dendrites, the β phase forms as an irregular eutectic together with eutectic α-Al. In Figure 2.26, only four plates were nucleated in the sample, and all nucleated in the very early stage of the eutectic reaction and subsequently developed into complex connected three-dimensional plates. The plates display very rapid lateral growth and slow thickening, which, together with the observation of imprints of dendrites and ridges in the plates, suggesting a very weakly coupled eutectic in this case [69]. However, the formation of α and β Fe-rich phases during solidification under external phases has not been reported in open literatures.

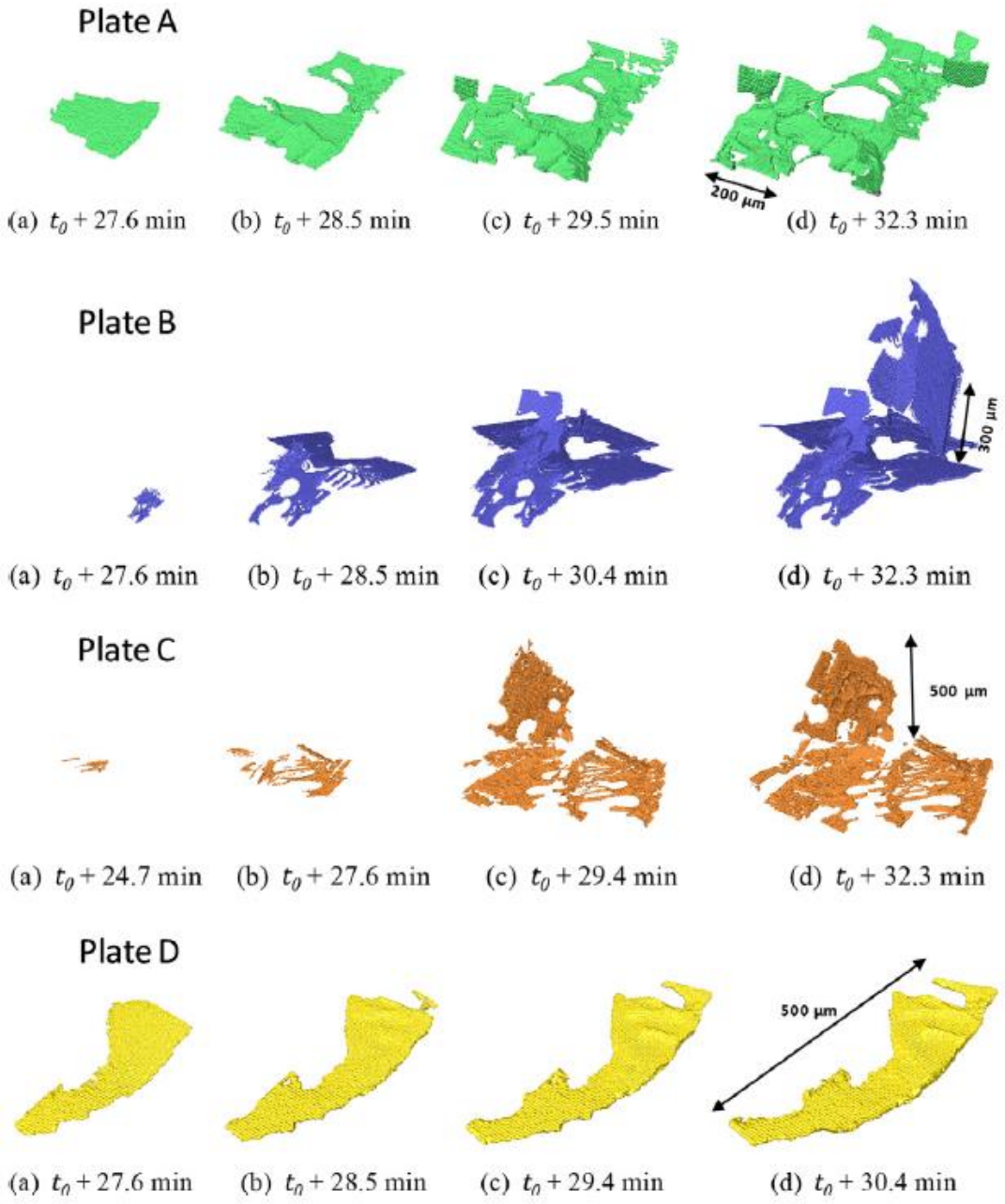

Figure 2.26 A series of reconstructed images from the four independently nucleated complex β plates, taken at several time steps during their growth.

In 2016, Cai *et al* [70] used a 53 keV monochromatic beam to investigate the formation of cellular structures, growth, the cellular-to-dendrite transition, and then to established columnar dendrites (shown in Figure 2.27) in an Al-15%wtCu alloy via 4D synchrotron X-ray tomographic imaging. The cellular morphology was found to be highly complex, with frequent lateral bridging as shown in Figure 2.27. Protrusions growing out of the cellular front with the onset of morphological instabilities were captured, together with the subsequent development of these protrusions into established dendrites.

They also observed dendrite fragmentation, and the mechanisms were due to the combination of stress induced by buoyancy and the Gibbs – Thomson effect, and the failure accelerated by a transgranular liquation cracking (TLC) mechanism. The results demonstrate that 4D imaging can provide new data to both inform and validate solidification models [70].

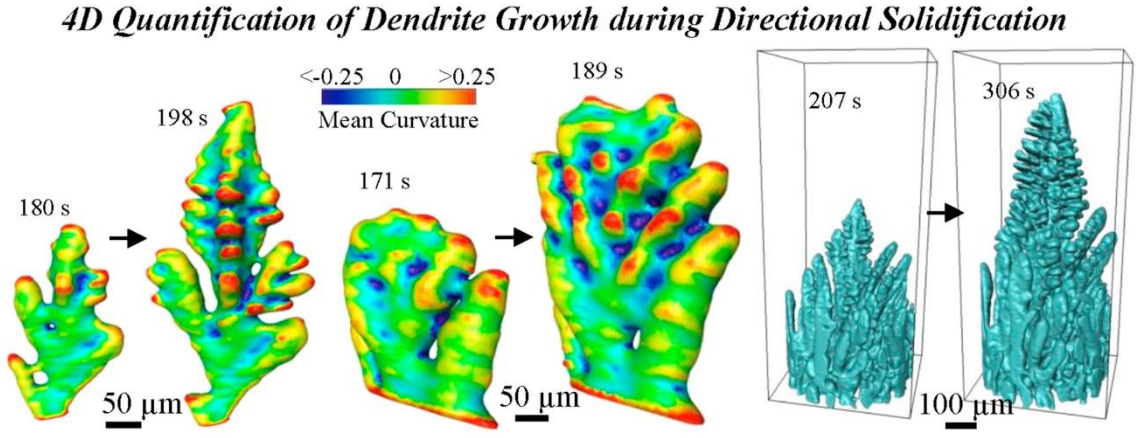

Figure 2.27 (1) Initial growth evolution (coloured by its mean curvature) of dendritic structure at 180 and 198 s and the coralline-like morphology at 171 and 189 s, respectively; (b) The 3D morphology of dendrite structure at t = 207 and 306 s, respectively [70].

In 2016, Ashwin *et al*. [71] investigated the growth behaviour of an irregular eutectic alloy via fast 4D synchrotron tomography as shown in Figure 2.28.

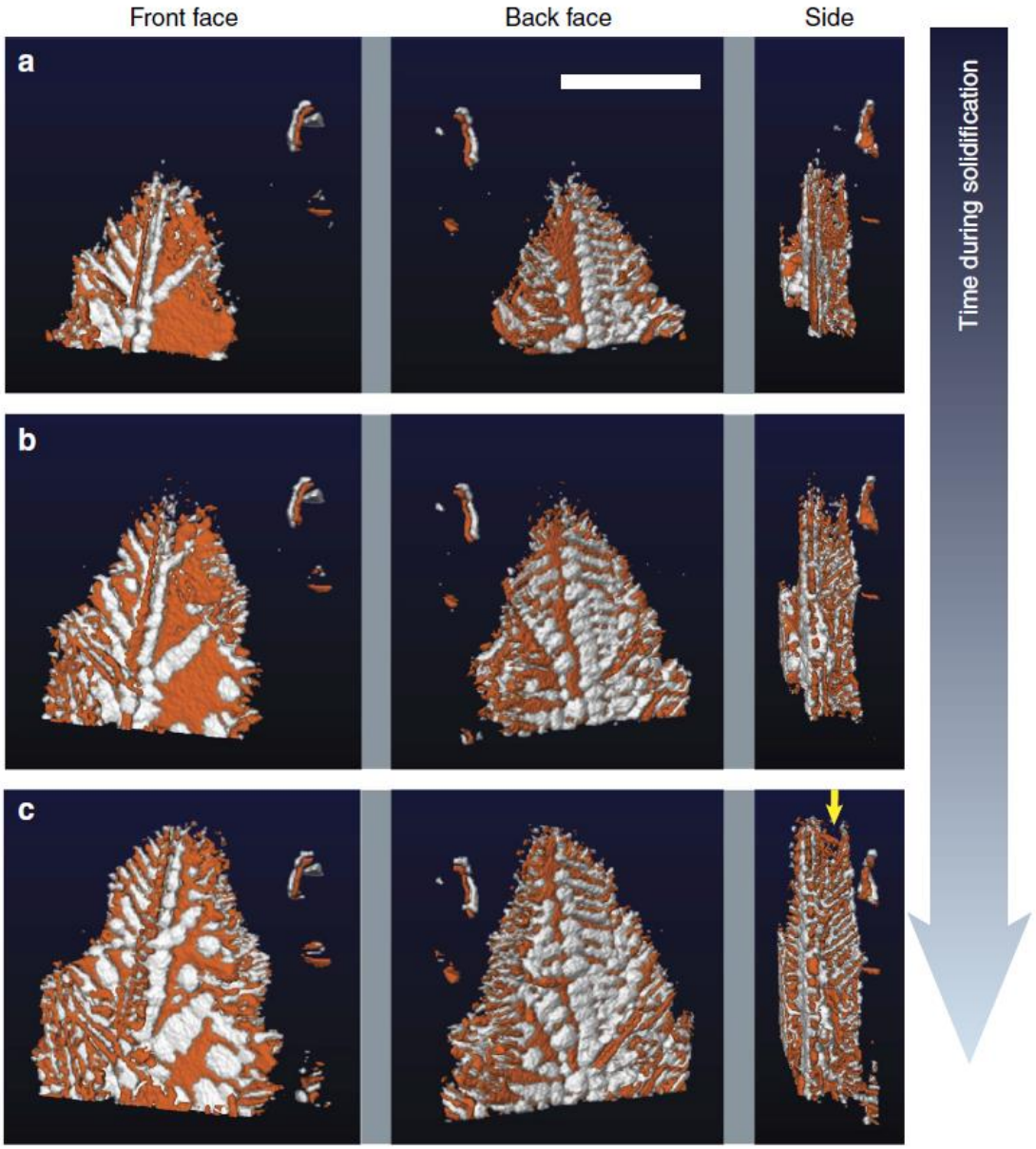

Figure 2.28 Morphology of the eutectic colony during the growth process. Frames given at (a) 100, (b) 140, (c) 180 s since start the solidification. Shown are three views per time-step, corresponding to the front, back and side of the eutectic colony [71].

They performed in-situ experiment at sector 2–BM of Advanced Photon Source (APS) by using very high spatial (pixel sizes of 0.65 μm) and temporal (27 ms exposure time) resolution. They resolved a longstanding controversy in the field, and demonstrate that none of the existing models are fully adequate for describing the rich variety of anisotropic patterns that arise during crystallization. They also found that defects play a critical role in the growth of the eutectic, in which pockets of metal engulf the exposed facets and control the overall growth rate of a eutectic colony. These experimental results identify a new mechanism for the growth of an irregular eutectic, and provide the key insights needed to model the crystallization of these technologically complex materials [71].

2.3.2 Solidification under electric current pulse fields

In 2014, Liotti, *et al.* of Oxford University, UK [72] reported the experiments of using synchrotron X-ray imaging to study the effect of dendrite fragmentation by a passing a pulse electric current through a thin Al-15wt%Cu sample. The sample melt was placed inside a static magnetic field. Hence, the alloy melt was subject to a pulse electromagnetic field (PEMF) during solidification. A special solidification apparatus (Figure 2.29a) was designed and built for such experiments. This schematic of setup is based on Figure 2.4d. The two plate heaters were aligned vertically in the vertical plane and separated by an adjustable gap through which X-rays can pass through. Between the gaps, a 200 μm thick foil sample was placed in close contact with both heaters. This entire sample holder arrangement could be moved vertically under computer control for imaging the solid-liquid interface by the X-ray beam and the imaging camera. A

permanent ring magnet was placed 3 mm from the foil sample, with field lines running approximately normally in and out of the sample surface. By applying an electric current (I) from a signal generator through the plane of the sample in the presence of the static magnetic field (B), a pulsed Lorentz force (*F*) acted on the sample can be generated ($F = B\ I\ \mathrm{Sin}(\theta)\ L$, $\theta = 90°$ is the angle between the electric and magnetic field and L is the active length of the sample). The current pulse magnitude, waveform and frequency were generated and controlled by a signal generator. A common trigger signal was used to synchronize the measured thermal data with corresponding video images, so that specific events observed in the images could be linked directly to thermal data and any pulse events. Al-15 wt%Cu alloy foil samples were used and the experiments were carried out at the B16 beamline of the Diamond Light Source, UK [72].

Figure 2.29b showed that, in consistency with previous studies, the “bulk” movement of liquid, i.e. convection, close to the dendrite front caused temperature and solute perturbations, which is the primary source for dendritic arm fragmentation in this type of alloy. Without PEMF, the dendrite fragmentation rate was 0.26×10^9 fragments $m^{-3}\ s^{-1}$ (Figure 2.29b). However, it raised to 1.18×10^9 fragments $m^{-3}\ s^{-1}$ with a PEMF applied (Figure 2.29c-d). They suggested that PEMF induced an enhanced movement of solute-rich inter-dendritic liquid, and caused relatively small-scale movement of liquid between both the primary and the secondary dendrite arms. The movement transports comparatively solute-rich liquid from within the dendrite network to more dilute regions, causing dendrite arm remelting [72].

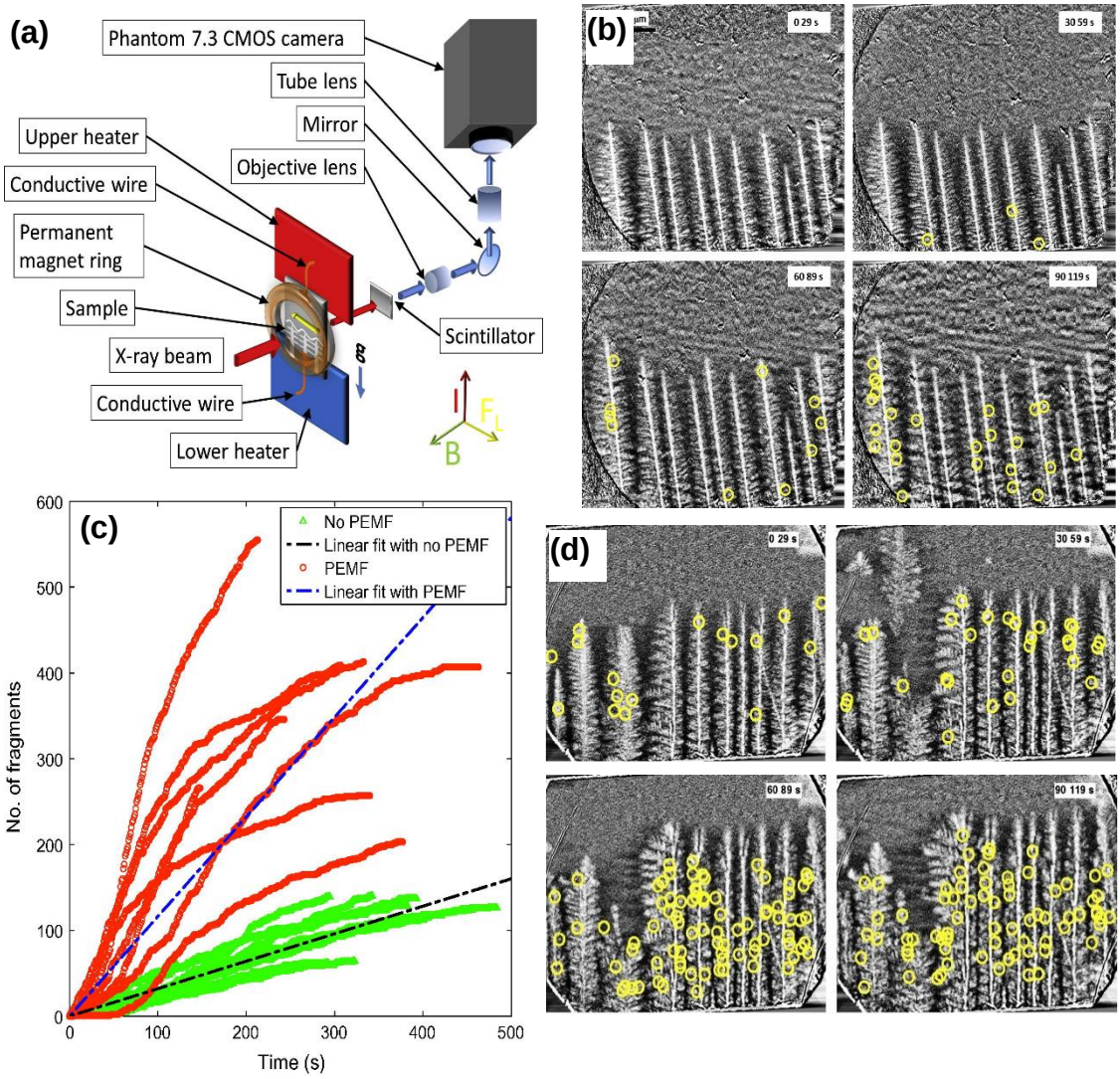

Figure 2.29 (a) A schematic of the sample arrangement and experimental set-up; (b) The growing Al–15wt%Cu dendrite array and the locations where fragmentation occurred (marked by yellow circles) during the solidification (thermal gradient G = 48 K/mm and no external PEMF); (c) The cumulative fragmentation number curves without and with the PEMF; (d) The fragmentation events occurred under the action of a PEMF (marked by a yellow circle) [72].

In a further study, Liotti, *et al* [73] also demonstrated that the stronger the applied PEMP, the greater the induced flow and the higher the fragmentation rate. However, there was no compelling evidence for any change in fragmentation mechanism or the distribution of fragmentation events in their experiments.

2.4 The simulation of solidification under external fields

A number of experimental approaches of solidification under external magnetic fields have been reported as described above. The magnetic fields lead the microstructures change significantly. These changes can be attributed to convective transport of solute by thermoelectric magneto hydrodynamics (TEMHD). A detailed description of TEMHD is given by Shercliff [74].

In summary, TEMHD describes fluid flow generated by a Lorentz force that is formed through the interaction of thermo electric currents and a magnetic field. Thermo electric currents are generated by spatial variations in temperature and Seebeck Coefficient (absolute thermo electric power). The diagram of TEHMD is shown in Figure 2.30a. During the solidification process, these conditions are satisfied by the externally driven thermal gradient and through ejection of solute at the liquid/solid interface respectively.

A. Kao *et al*. [75] studied the mechanism of macrosegregation and modification to dendrite size and spacing from a transverse magnetic field via imaging based numerical simulation. He found the primary driver for this mechanism was identified as a strong Lorentz force formed in the interdendritic region, which leads to a large-scale flow circulation as shown in Figure 2.30b. To satisfy continuity a large-scale flow circulation forms that passes through the interdendritic network, changing direction at the wall and passing back over the dendrite tips. The microstructure evolution is modified by convective transport of solute (Figure 2.30c&d) and the predicted morphological features compare favourably to experimental data in the literature. His modelling results cannot be obtained by experiments and it give an insight into the magnitude of flow

velocities within the interdendritic region [75]. However, he suggested that introducing the contactless forces (i.e. pulse electromagnetic fields) deep within the mushy zone is of considerable interest both scientifically and industrially. Because this technique has the potential to provide an additional control mechanism to the microstructure formation through tailored design of the magnetic field, if the PMF is fully understood.

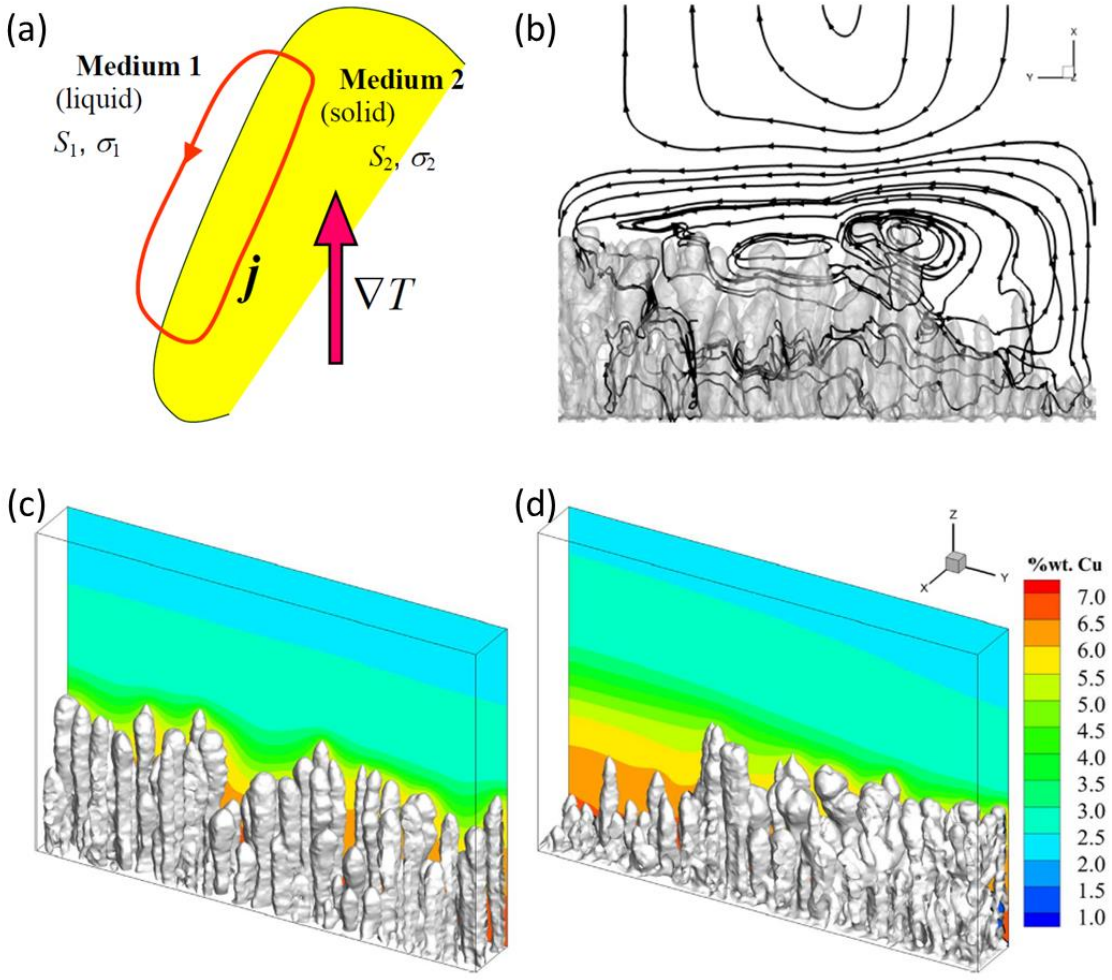

Figure 2.30 (a) Sketch of the thermo-electric current distribution near the interface between two media; (b) Streamlines of TEMHD; Three-dimensional microstructure and concentration profile: (c): B = 0 T and (d) B = 0.1 T.

Chapter 3: **Upgrading of the pulse electromagnetic field solidification equipment**

This chapter describes the upgrading of the pulse magnetic field solidification equipment (previously designed and built by T. Manuwong [47]), including the design, building and optimisation of different versions of bespoke furnaces, pulse generator and pulse coils and the upgrading of PID temperature controllers. The purpose of the upgrading is to develop relevant mechanical, electric and control system into a more robust, flexible and automatic system, allowing the equipment to be suitable for the physical and technical environment in Beamline I13 of Diamond Light Source, TOMCAT of Swiss Light Source and ID19 of ESRF. In addition, a number of measuring circuits and ports were added in the pulse generator to facilitate the measurement of discharging current, voltage and the resulting magnetic pulse via Gaussian meter and oscilloscope in our university lab.

3.1 The solidification apparatus

3.1.1 Furnaces

For doing in-situ synchrotron X-ray environments, the furnace needs to have the following functions or characteristics: (1) capable of heating to a higher temperature (in our experiments ~1000 ºC) and cooling quickly with a stable and automatic temperature control during experiments; (2) having a window and clear path for X-ray beam to pass through, (3) geometrically accommodating

ultrasound probe or the magnetic pulse coils, (4) simple and flexible operations for changing samples.

I have participated in five beamline experiments during my PhD and each beamline has its own setup environment, therefore four different version of furnaces were designed and commissioned for each experiment. The detailed information of each experiment is listed in Table 4.2. Four different versions of furnaces were upgraded to suit each experiment.

In the 2015 DLS experiment, the 1st version of the furnace was designed and built by Tan et al. This furnace consists of Duratec 750 materials and six cartridge heaters, which can deliver a heat power of 1.8 kW and heat the samples to 1073 K [45]. However, it was time-consuming to assemble all components, temperature and thermal gradient control (it was also not easy to realise the temperature gradient control).

Hence, I designed and upgraded the 2nd, 3rd and 4th version of furnaces with the help and inputs from my supervisor and Dr Wei. Zhang. The upgrade allowed me to perform the planned research tasks at the beamline experiments.

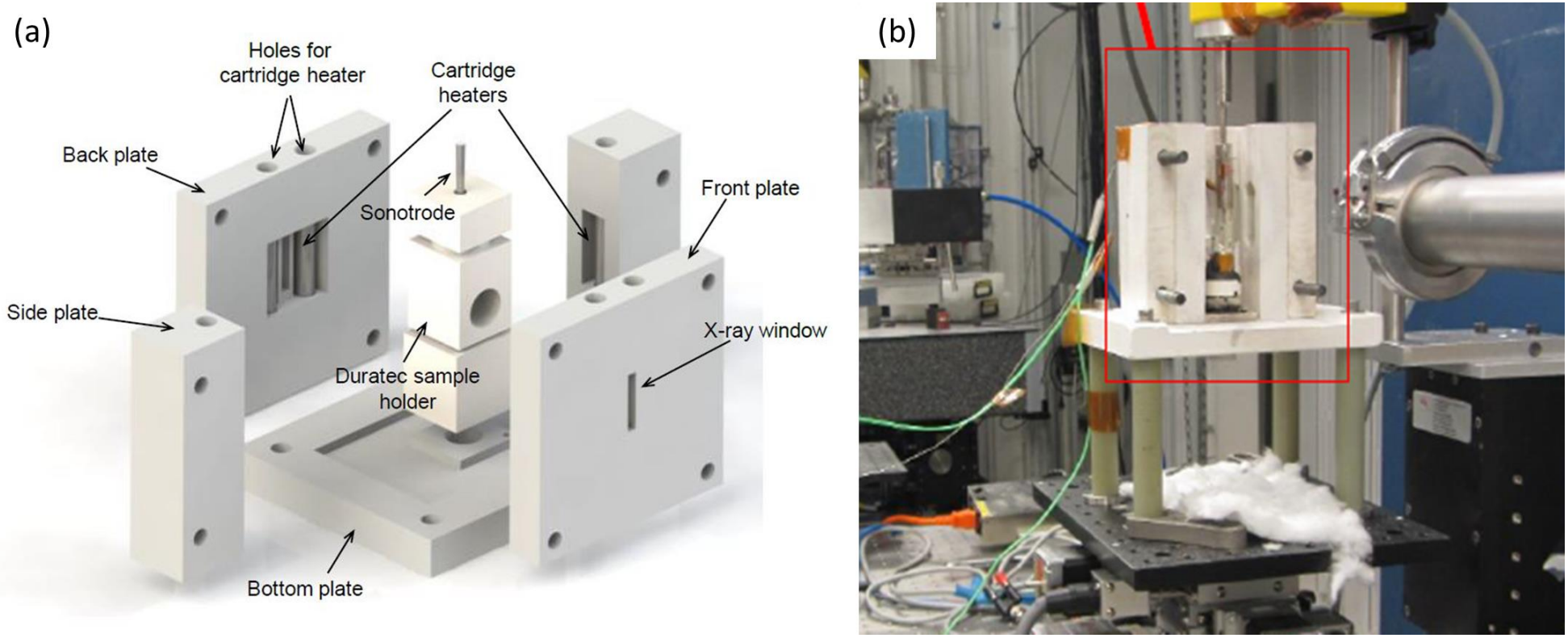

Figure 3.1 (a) the 1st CAD rendering of the furnace and (b) the corresponding actual furnace and setup at APS.

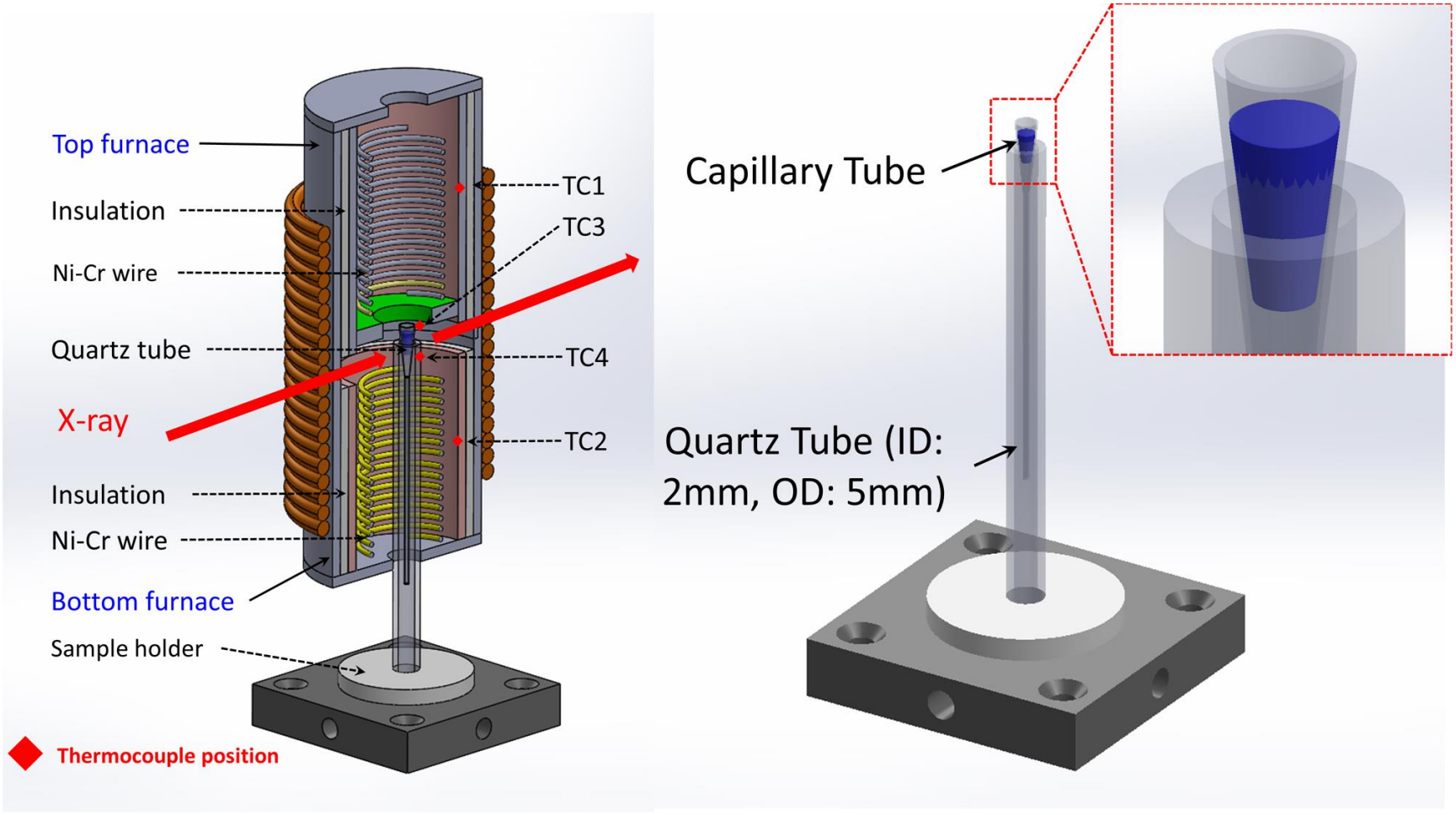

Figure 3.2 The Bridgeman type furnace (two small-scale furnaces were stacked together and positioned inside a copper coil) for I13-2, DLS experiment design by Du.

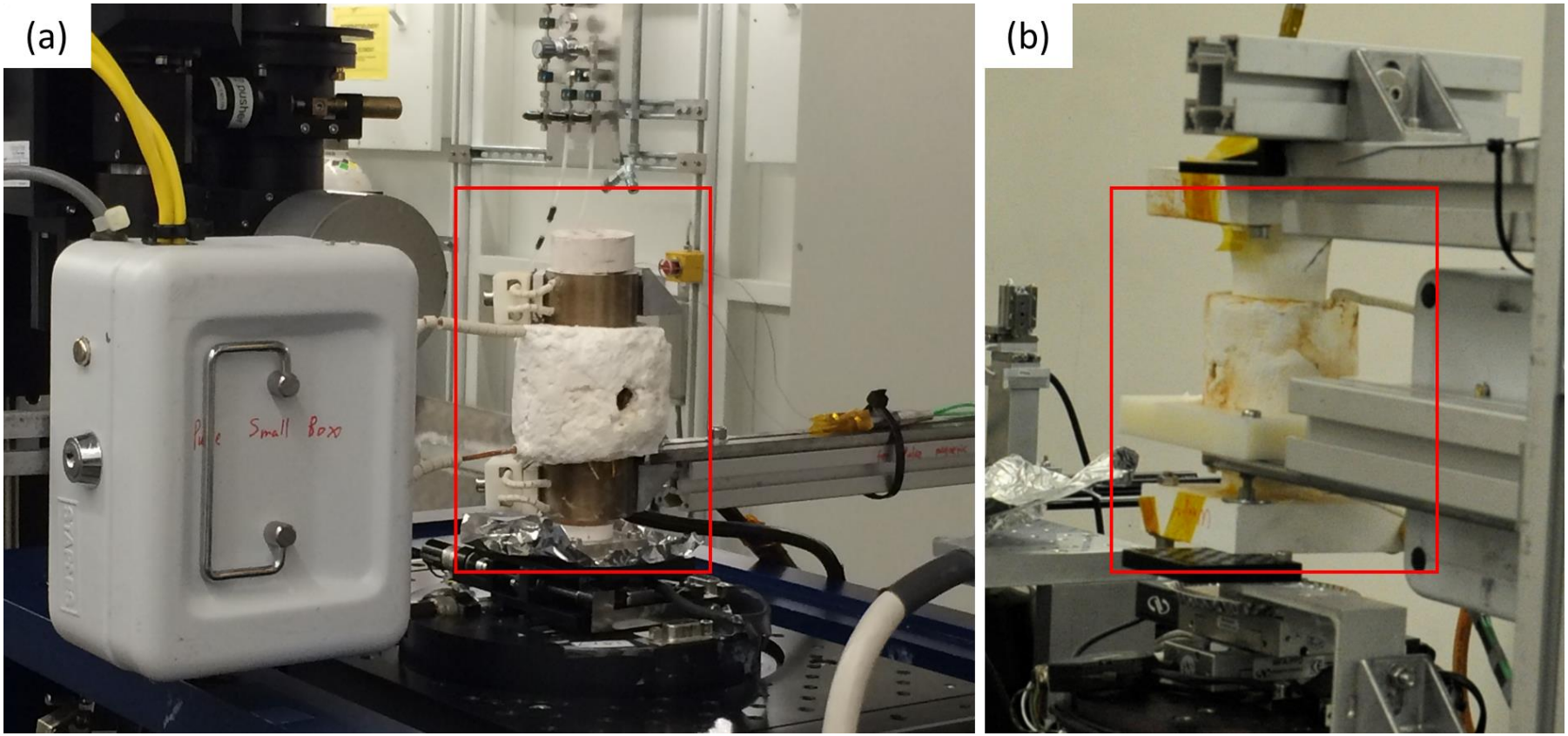

Figure 3.3 The actual 2nd & 3rd version furnaces (corresponding design in Figure 3.2) used at (a) TOMCAT and (b) I13-2 beamline.

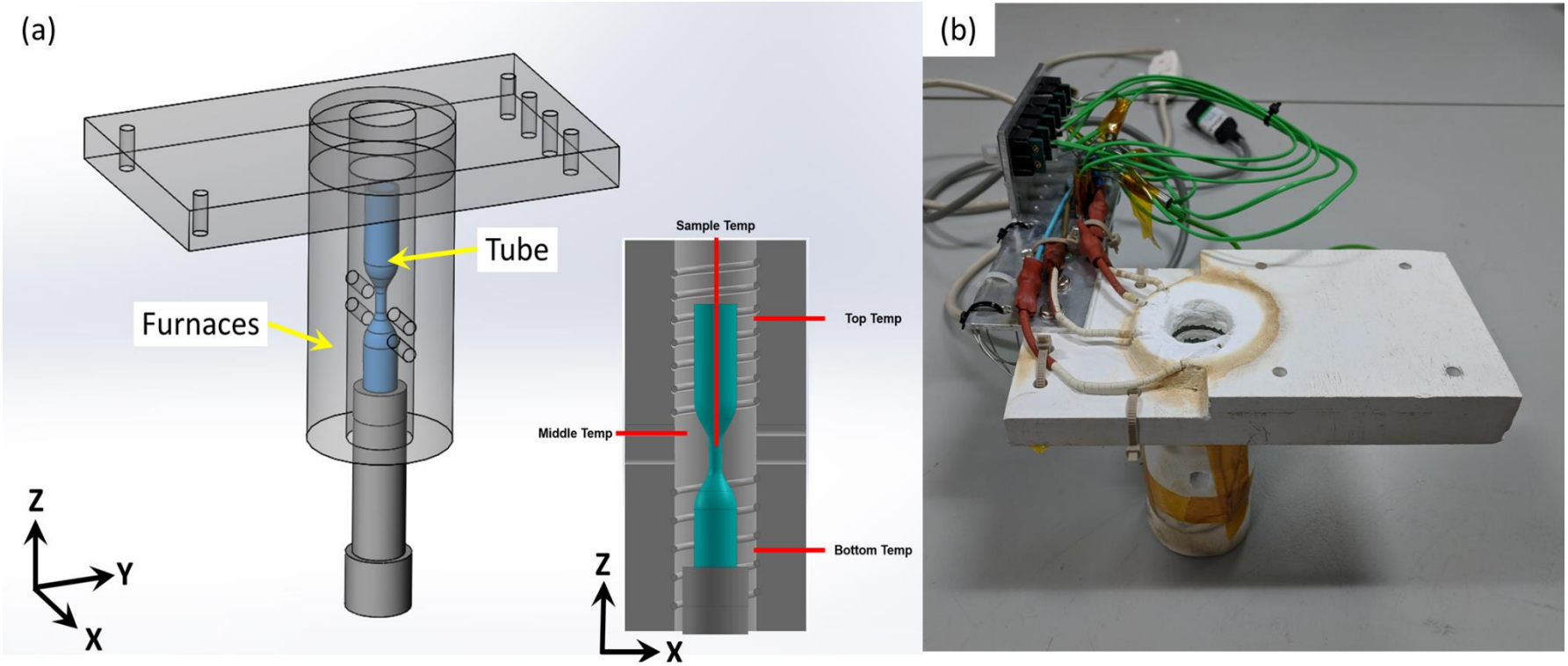

Figure 3.4 (a) The left figure shows Bridgeman type furnace (two independent heating wires were built into a single furnace) for ID19, ESRF synchrotron experiment design by Du. Four thermocouples are used for measuring the top, middle, bottom zoon and sample; (b) The actual 4th version furnace (corresponding design in Figure 3.4a).

Small-scale electrical-resistance furnaces were designed to melt sample. High-resistivity nickel-chromium wire was used as the heating element (diameter of 0.25 mm, KANTHAL, UK), which can go up to 1250 °C. Approximately 10 metre wire was winded into a helical heating element with a radius of 1.5 mm, fibre mastic and ceramic wool were used to hold the helical element in place. The calculation details of heating wire selection can find in Appendix 1.

From the design point of view, the 2nd and 3rd versions have little difference. 2nd version used stainless steel as the furnace outside wall, while the insulation material (fibre mastic) was used as the outside cover in the 3rd version, providing a safe environment when change thermocouples or other manual action.
The design concept is based on a compact Bridgeman furnace containing two temperature zones (each zone has an independent temperature control system) to allow us to control the solidifying microstructures.

For TOMCAT (using the 2nd version) and I13-2 (using the 3rd version) experiment, I use two K-type thermocouples (KMTSS-IM050U-150; Omega, UK), 2 mm apart, were positioned very close to the quartz tube (at the locations marked by TC 3 and TC 4 in Figure 3.2) to measure the temperatures at the location where X-ray images were taken.

However, the 4th version of the furnace avoids mechanical assemble during the in-situ experiment, and save the beamline preparation time. The alignment between furnace and pulse coil is much easier than 2nd and 3rd version. Moreover,

I fixed three thermocouples at the position shown in Figure 3.4. Using this TCs setup, it is not necessary to switch TCs or TC re-position. Moreover, the temperature is absolutely repeatable.

For ID 19 experiment, three K-type thermocouples were used (406-482, 0.5mm diameter x 250mm long, TC Direct, UK) for measuring top, middle, and bottom zoon of the furnace, the details setup is shown in Figure 3.4a.

Generally, another thermocouple is inserted into the sample before tomography experiment to understand the real temperature difference between furnace and sample. Tomographic solidification experiment is usually performed after withdrawing the thermocouple where inserted in the melt. Because of (1) the sample and quartz tube kept rotating during the experiment, the TC wires will entangle each other; (2) The diameter of wire is 0.5 mm, and it is too big if I put it into a thin tube (consider the inner diameter of tube is 2 mm).

All temperatures were recorded using a data logger (TC-08; Pico Technology, UK) connected to a PC during the experiments. TC-08 has fast and accurate acquisition rate, it provides eight channels measuring a wide range of temperature (from -270 to +1820 °C) at the same time. The Graphical user interface (GUI) is shown in Figure 3.9. All the temperature profiles are presented in Chapter 4.3.

3.1.2 Temperature controller

The proportional–integral–derivative (PID) temperature controller, using an accurate and stable control loop feedback mechanism (Figure 3.5), is used to control temperature, mainly without extensive operator involvement. The temperature control system of PID will accept a temperature sensor such as a thermocouple (TC) as input and compare the actual temperature to the desired control temperature or set point (SP). It will then provide an output to a control element, continuously calculating an error value *e(t)* as the difference between a desired SP and a measured process variable (PV) and applies a correction based on proportional, integral, and derivative terms (denoted P, I, and D respectively). In this model:

Term **P** is proportional to the current value of the SP − PV error *e(t)*. If the error is large and positive, the control output will be proportionately large and positive, taking into account the gain factor "K". Using proportional control alone in a process with compensation such as temperature control, will result in an error between the SP and the actual PV, because it requires an error to generate the proportional response. If there is no error, there is no corrective response;

Term **I** accounts for past values of the SP − PV error and integrates them over time to produce I term. If there is a residual SP − PV error after the application of proportional control, the integral term seeks to eliminate the residual error by adding a control effect due to the historic cumulative value of the error. When the error is eliminated, the integral term will cease to grow. This will result in the proportional effect diminishing as the error decreases, but this is compensated for by the growing integral effect;

Term **D** is a best estimate of the future trend of the SP − PV error, based on its current rate of change. It is called "anticipatory control", as it is effectively seeking to reduce the effect of the SP − PV error by exerting a control influence generated by the rate of error change. The more rapid the change, the greater the controlling or dampening effect [76].

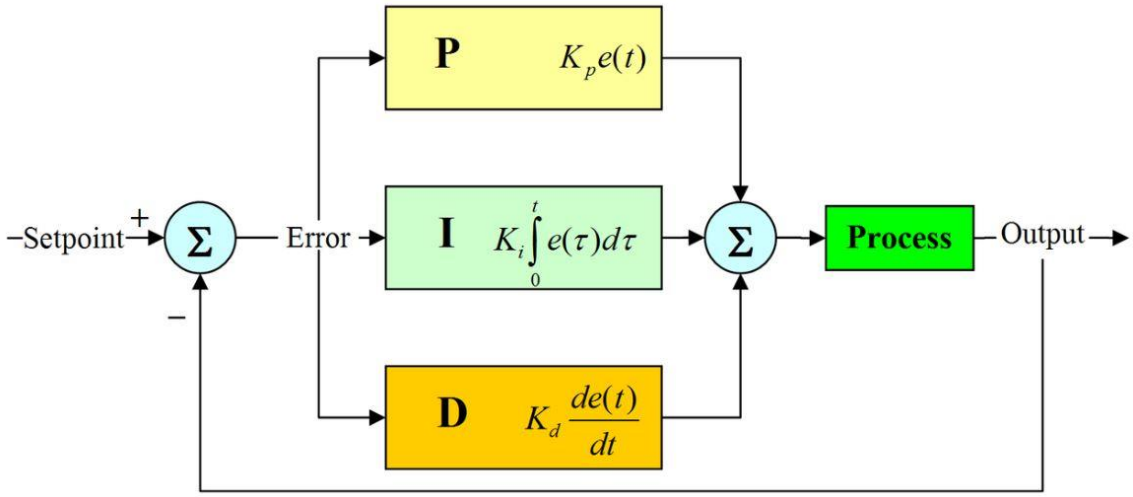

Figure 3.5 A block diagram of a PID controller in a feedback loop. r(t) is the desired process value or setpoint (SP), and y(t) is the measured process value (PV).

I upgraded the temperature controllers. Generally, each thermal controller consists of a proportional–integral–derivative (PID) controller and a solid–state relay with a heat sink together.

The 1st version controller is an edition that needs manual inputs as shown in Figure 3.6a. When the more complex cooling or heating procedure is needed, it is difficult for one user to tune the button for two controllers all time at same time.

Hence, at 2016 DLS experiment, it is the first time that the advanced thermal controller is used to generate our temperature profiles. The example of the heating-cooling cycles for different alloy systems can be found in Chapter 4.3. The real photo for 2nd version controller is shown in Figure 3.6b.

The Platinum Configurator software provides a straightforward solution that communication between user and PID, it is much easier to control than before via a USB channel in Figure 3.6b1. The snapshot of the graphical user interface (GUI) is shown in Figure 3.7.

This control software enables us to tune the multi-controllers easily. In addition, each thermal controller has a built-in program that can be used to realise the multi-stage ramp and soak steps for precisely controlling the temperature profile as shown in Figure 3.8.

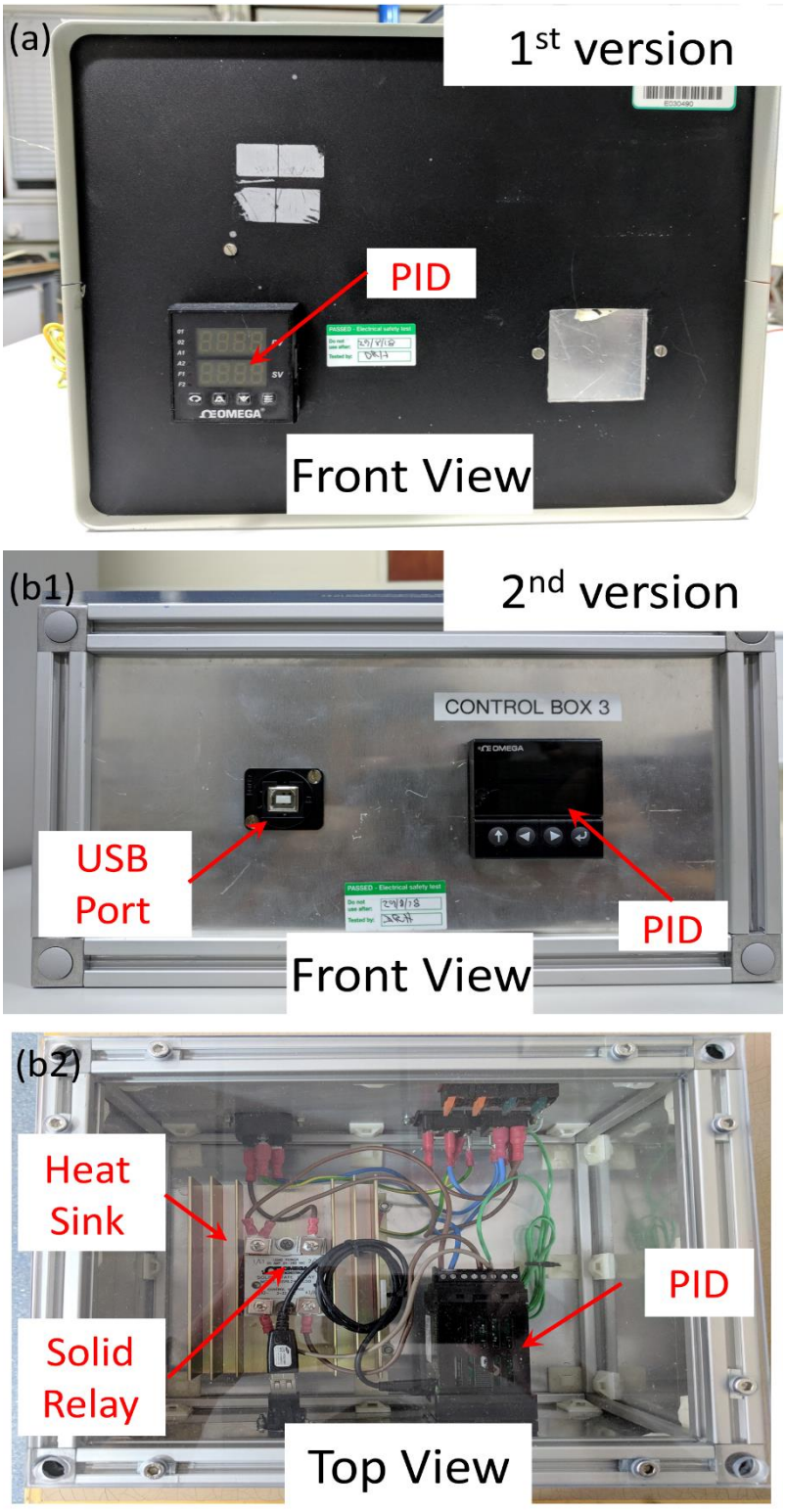

Figure 3.6 The actual bespoke temperature controller (a) the 1st version and (b) the 2nd version with a transparent lid and USB port to connect to a PC.

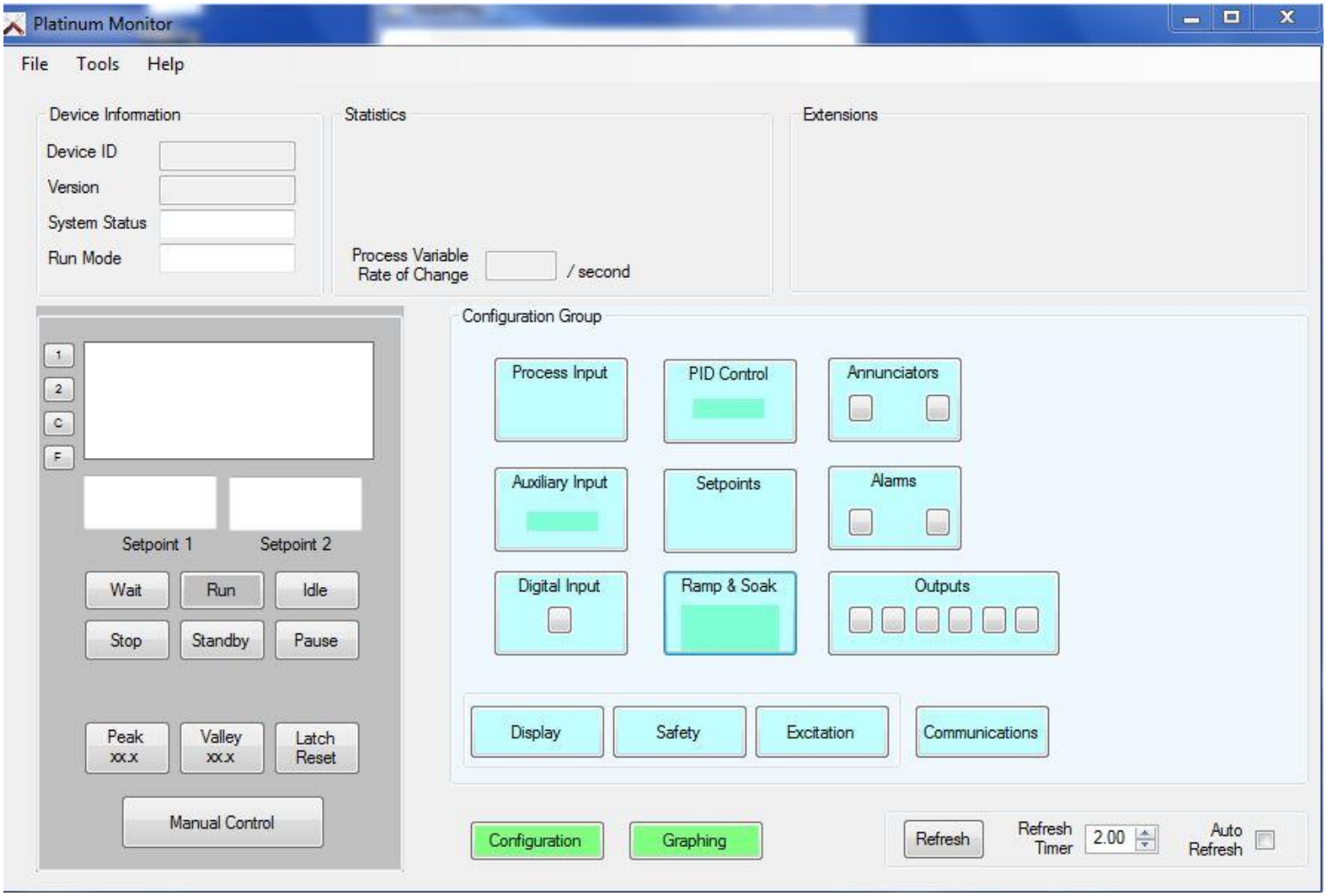

Figure 3.7 The snapshot of graphical user interface (GUI) for the 2nd thermal controller.

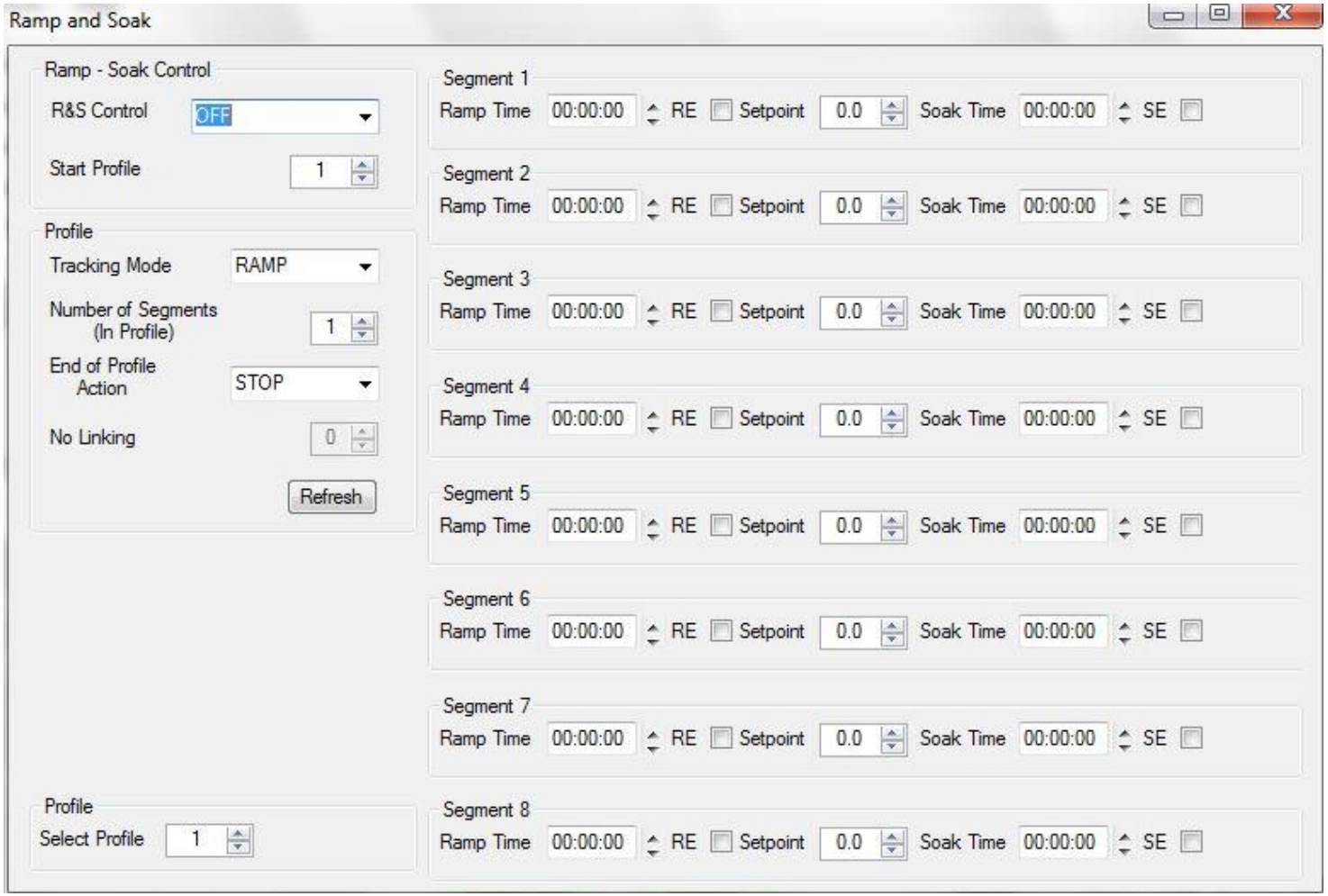

Figure 3.8 The snapshot of ramp & sock time setup interface for precise temperature control during melting and solidification process.

Table 3.1 The tuned PID parameters for the 3rd version of the furnace at I13.

	Top furnace	**Bottom furnace**	
Set point (°C)	800	750	800
P	3.2	2.6	2.1
I	0.1	0.5	0.3
D	18.2	3.6	3.1

Another crucial issue is to tune the parameters of the PID controller to match the characteristics of furnaces. Calibration is needed for different furnaces and different alloy systems (due to the different heating requirements). If improper numbers were used it would lead to either over shot of the heating elements or the system is out of control. I use the auto tune plus semi-empirical methods to find values based on loads of tests. After an AUTOTUNE cycle, the values are used as a reference. Next, we slightly modify them to find the best P, I, and D values. An example summarized in Table 3.1.

The reading fluctuation from data logger is common, especially when high temperature alloys (higher than 700 deg) were melted. To overcome this noise issue, I use the Inconel thermocouple instead of using general k-type thermocouple for signal communicating between the 4th version furnace and data logger during the ESRF experiment and the results looks better. Next, using the algorithm of Savitzky-Golay [77] filter (in either Matlab or Origin) to preserve shapes of peaks while removing the background noise and creating smoothed profiles.

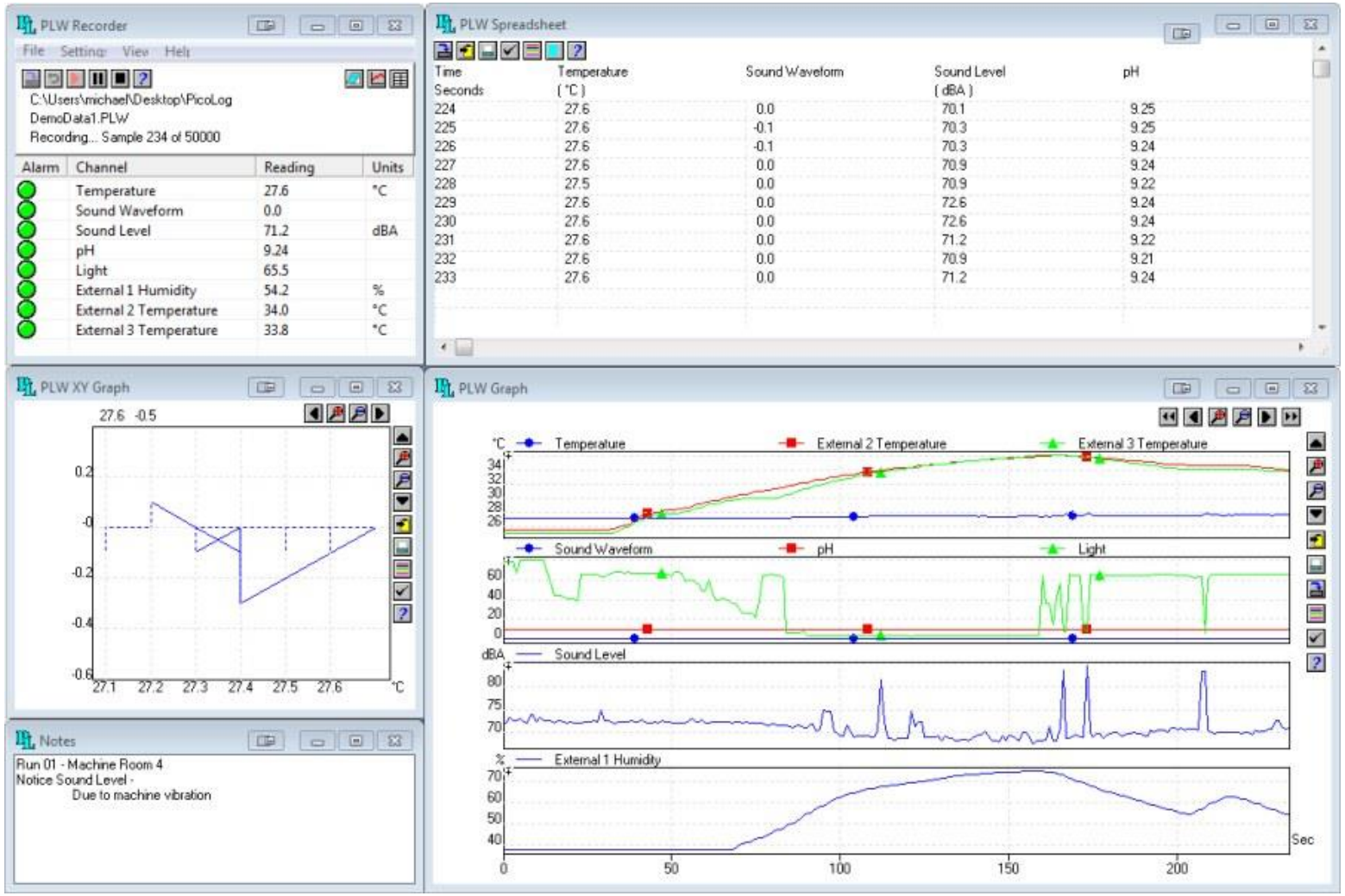

Figure 3.9 The GUI of the data logger for recording multi temperatures.

3.2 The pulse electromagnetic apparatus

The 2nd generation of the electromagnetic pulse device is re-designed and upgraded based on the 1st generation device designed by T. Manuwong.

Basically, this pulse apparatus is included three main components (a) the pulse box; (b) the discharging coil, and (c) the control panel. And this apparatus enables us to generate magnetic pulses with programmable amplitude, duration and frequency into the liquid/semi-liquid melt metal alloys during the solidification process. The reason for the development of the PMF apparatus is described in Chapter 2.

Comparing with 1st version, the improvements of this apparatus are: (1) much easier integrated with solidification apparatus, particular redesign the output part (induction coil); (2) more reliable power supply board and new cooling system by dual-fans; (3) add a hall sensor to measure the discharging electric current and real-time current data can be recorded and exported via an oscilloscope; (4) a newly built compact control panel for easy tuning;

3.2.1 The fundamentals and circuit design of the device

The pulse device converts a low current, relatively long time (tens of seconds) input into a high current, short time (milliseconds to microseconds) output. Hence, an energy shortage (multi-capacitors) is required for charging and discharging periods.

The conceptual design of an electromagnetic pulse device is shown in Figure 3.10. A regular AC power of 240 volts is used for charging. A Hall sensor is added

to measure the currents. When the switch 3 is connected to 1, the capacitors are being charged via the transformer where plugged into main. When shift switch 3 from left to right (2 and 3 are connected), there is current passing through the coil since the capacitors are discharging at this moment.

In order to measure the current in pulse coil, another two resistors (1 and 10 Ω) are individually used to insert into the red dash box in the circuit. The output of current is measured by oscilloscope. The details are described in Chapter 3.2.2 later.

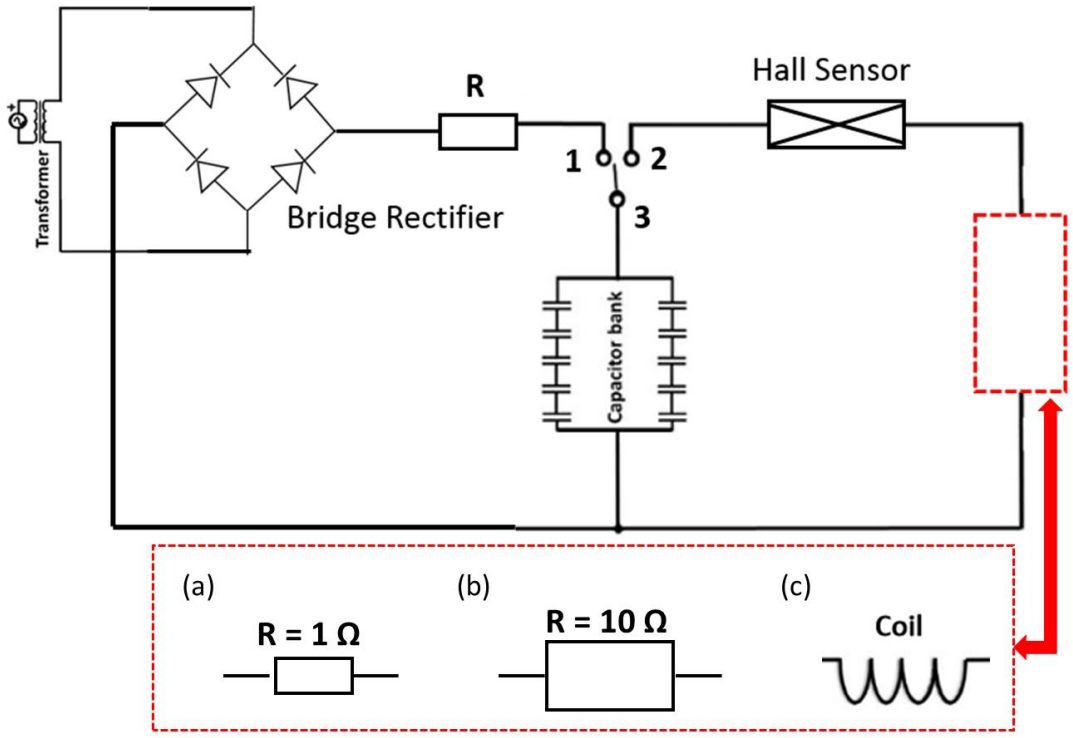

Figure 3.10 The conceptual electric circuit for the pulse electromagnetic device. The resistors of (a) 1 and (b) 10 Ω, and (c) pulse coils are separately connected into the circuit for current measurements.

3.2.2 Design of pulse generation device

Figure 3.11 shows the entire pulse generator device that is constituted by (1) the power input (green) and storage unit (black); (2) the controller board (red); (3) power output unit (yellow). The key module in a power storage unit is the power supply board (labelled in blue). The detailed circuit design of both controller board and power supply board are shown in Figure 3.12 and Figure 3.13, respectively. The power supply is used for converting AC current (frequency usually in between 50 and 60 Hz) from the transformer to DC current.

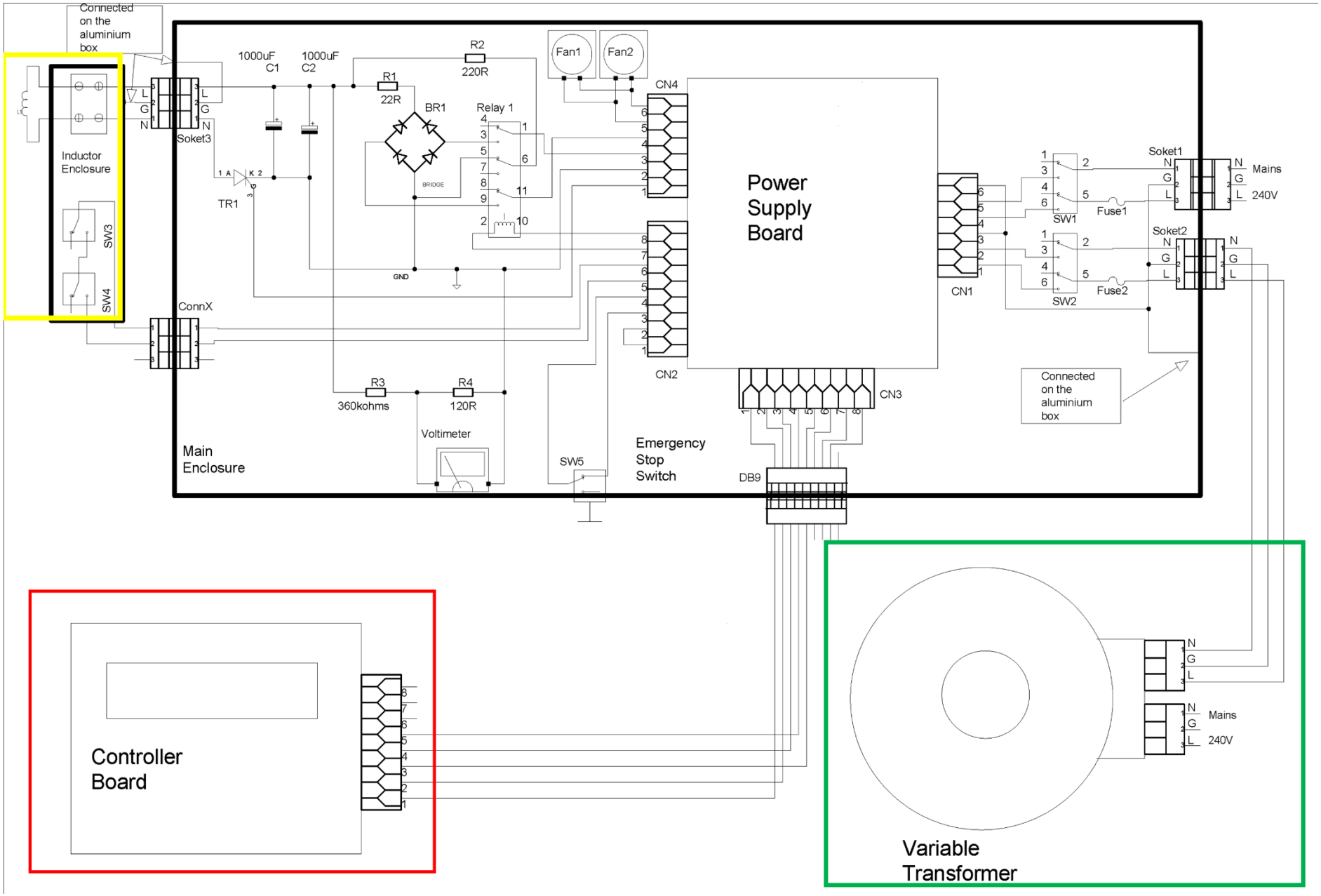

Figure 3.11 The detailed electronic circuit of the whole pulse electromagnetic box.

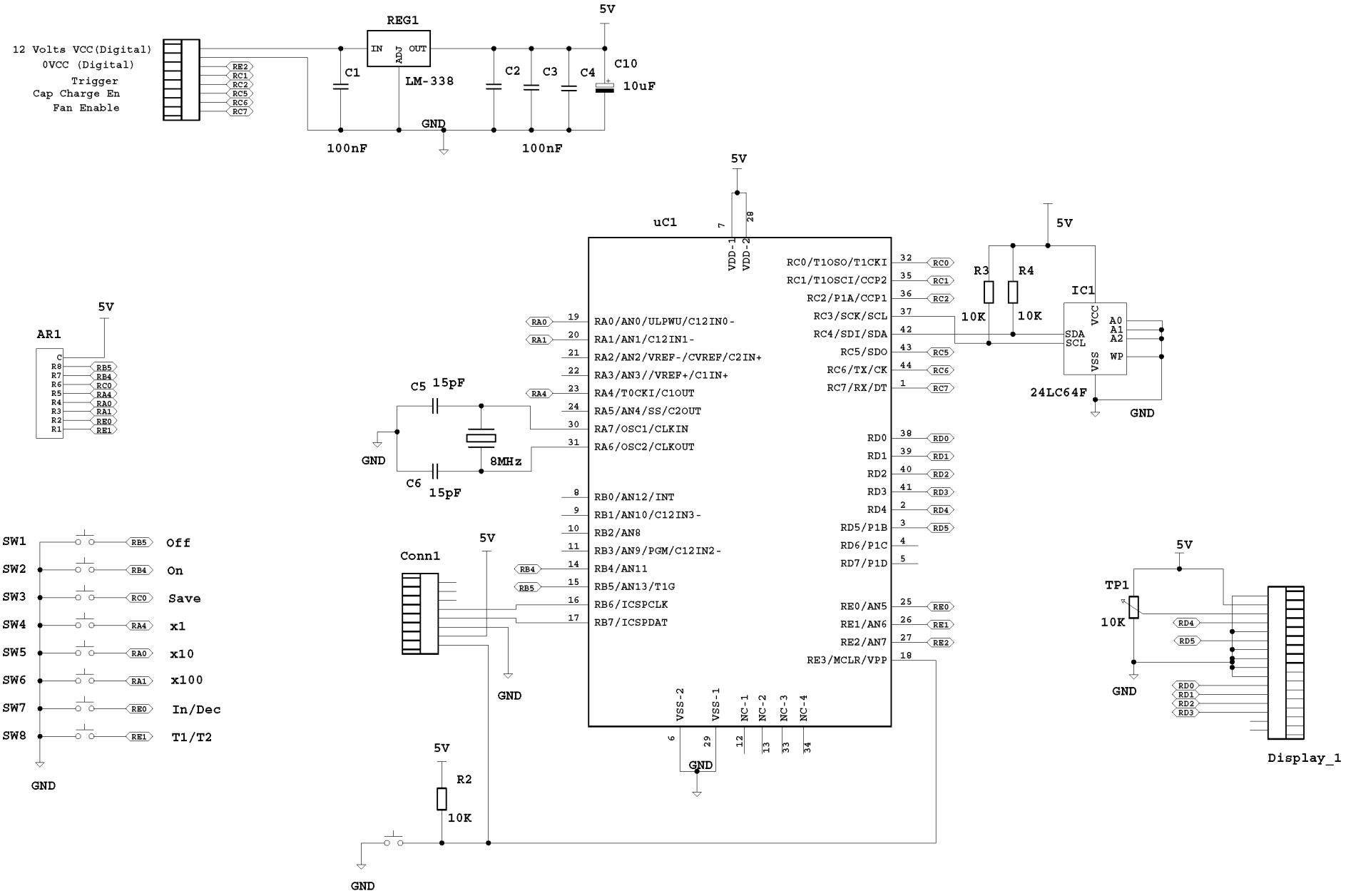

Figure 3.12 The detailed electronic circuit of the controller board

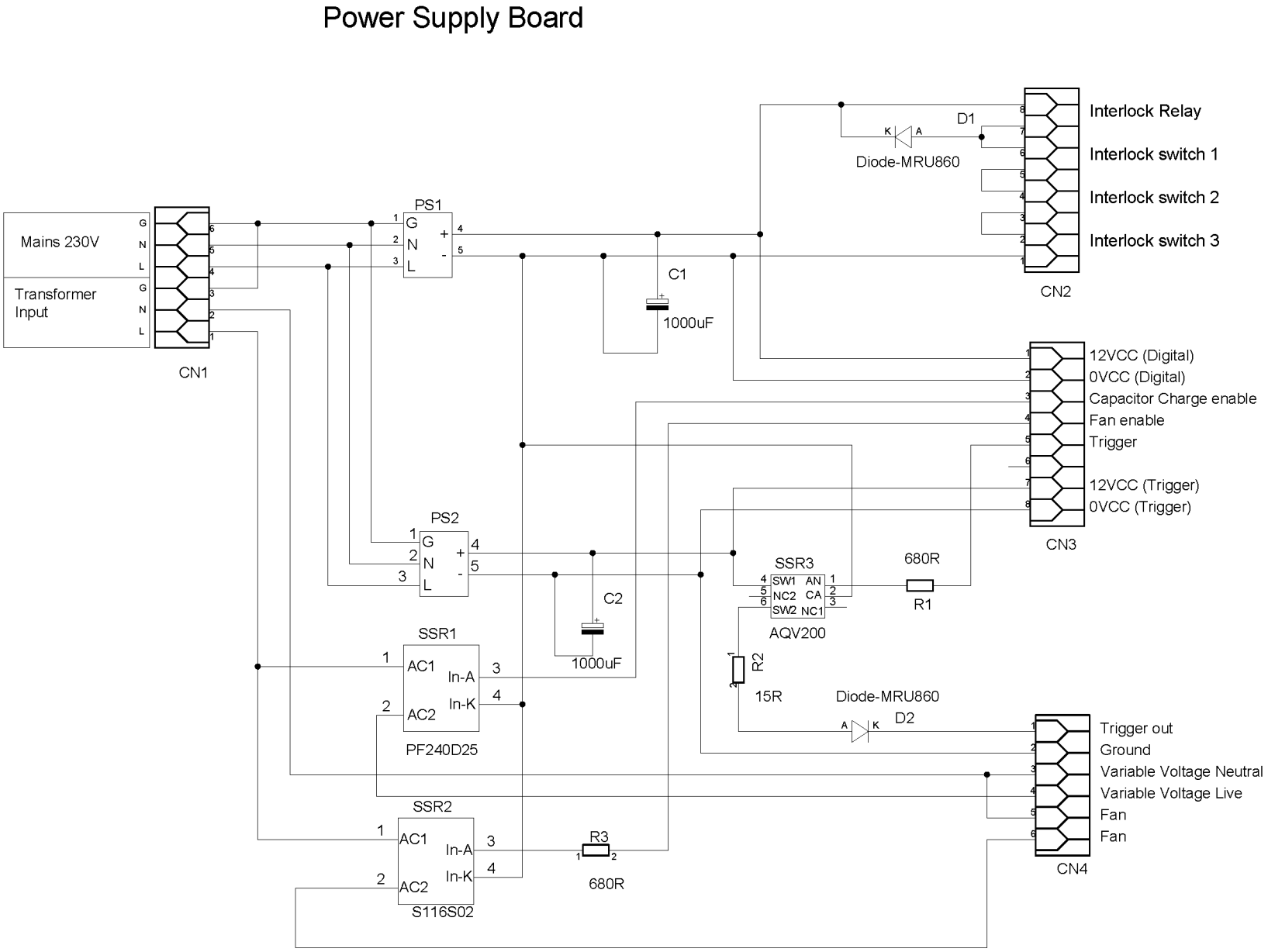

Figure 3.13 The detailed electronic circuit of the power supply board

Aluminium beam (22 x 22 mm, 5.6mm Groove, FlexLink), thickness of 2.5 mm pure Al sheets and a high strength polycarbonate sheet (4 mm thickness), and eight corner cube kits (strut profile 20 mm, Groove Size 6mm, Bosch Rexroth) are used to made the pulse box as a container.

Comparing with the 1st box, the 2nd is a compact with smaller volume for easy transportation. The 3D drawing of computer aid design (CAD) of pulse box is shown in Figure 3.14. In addition, a transparent cover is adapted to allow me to see any loosen links between cables and electrical components.

Figure 3.15 and Figure 3.16 show the top and side view of the actual circuit designed by Peter in the electronic workshop at University of Hull. The box included two chambers. A 220 Ω ceramic tube resistor (green) is inserted into the upper chamber as shown in Figure 3.15, because a cooling system is used to cool the resistor when higher charging voltages are used, e.g. above 180 V.

3.2.2.1 Cooling system

During the charging periods (particularly when relative high voltage is used to charge into the capacitor bank), a resistance is used to protect whole system. However, if the circuit keeps charging and discharging for a long period (e.g. up to a few hours), then the resistance will be overheating. Hence, a new cooling system was required to keep components within permissible operating temperature.

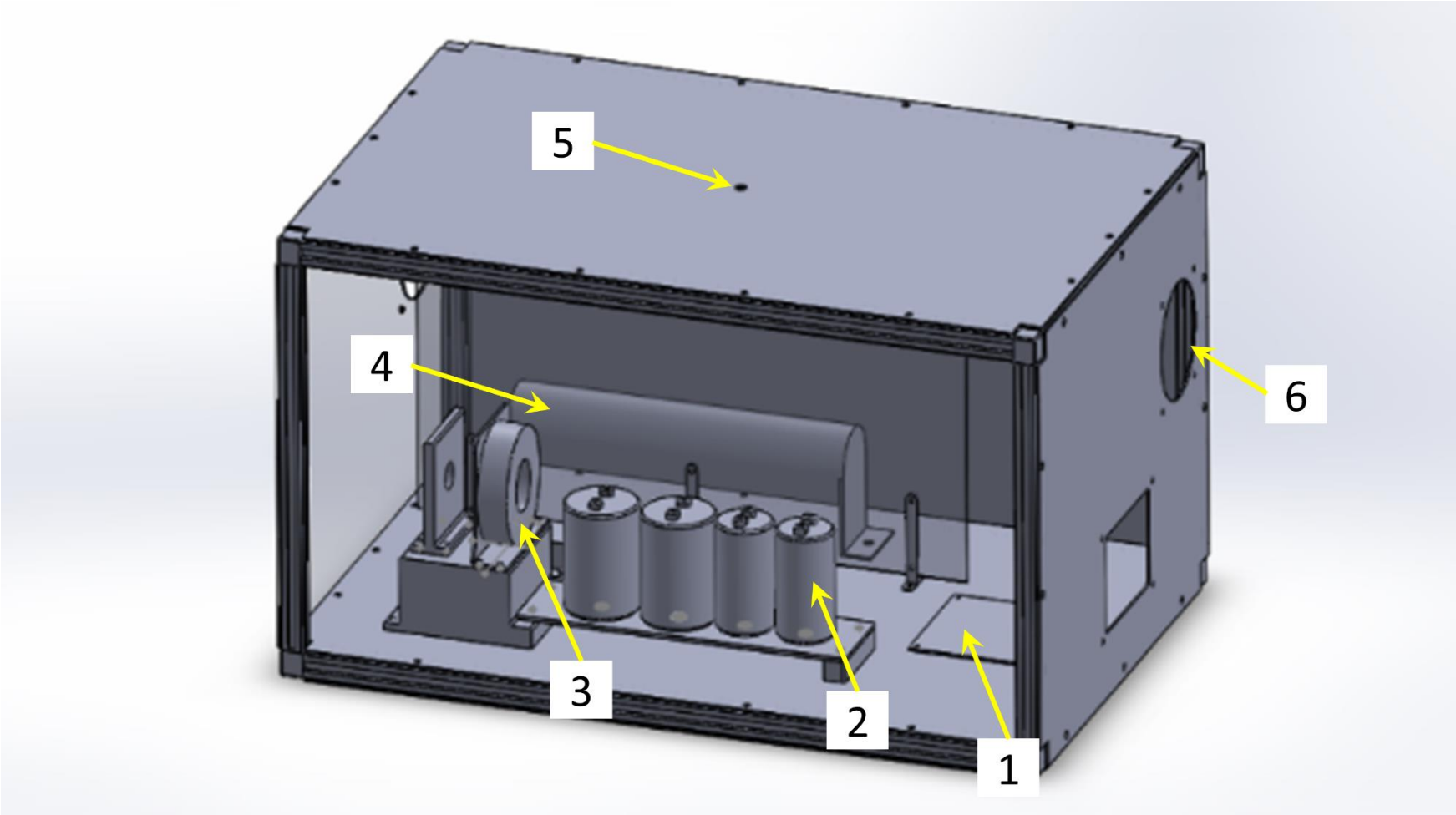

Figure 3.14 The 3D design of pulse generator by assembling all necessary components, including (1) power supply board; (2) capacitors; (3) Hall sensor; (4) resistor; (5) hole for emergency button; (6) hole for cooling fans.

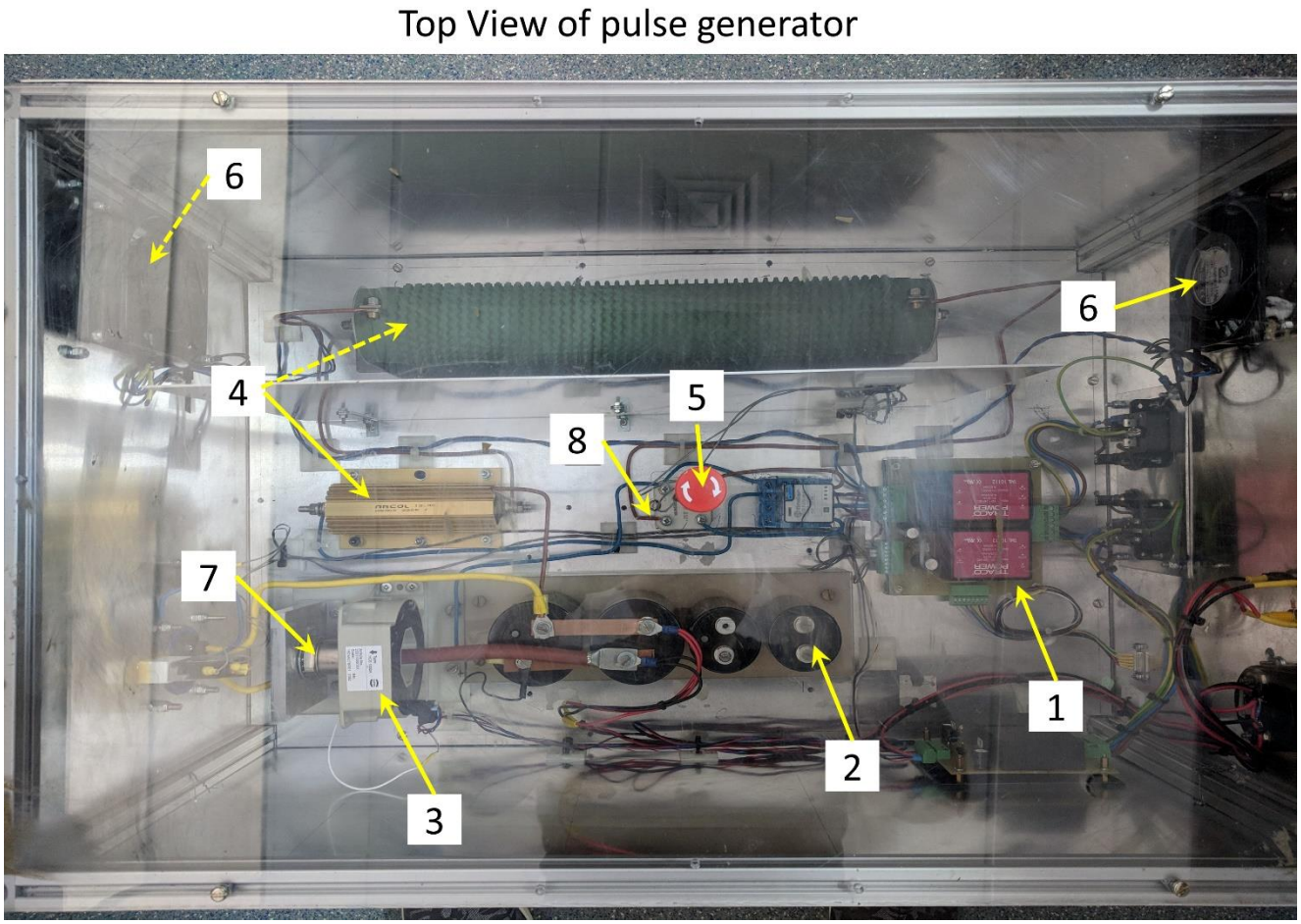

Figure 3.15 The top view of the pulse generator, highlighting some key components including: (1) power supply board; (2) capacitors; (3) Hall sensor; (4) resistors; (5) emergency button; (6) cooling fans; (7) Thyrister switch; (8) bridge rectifier.

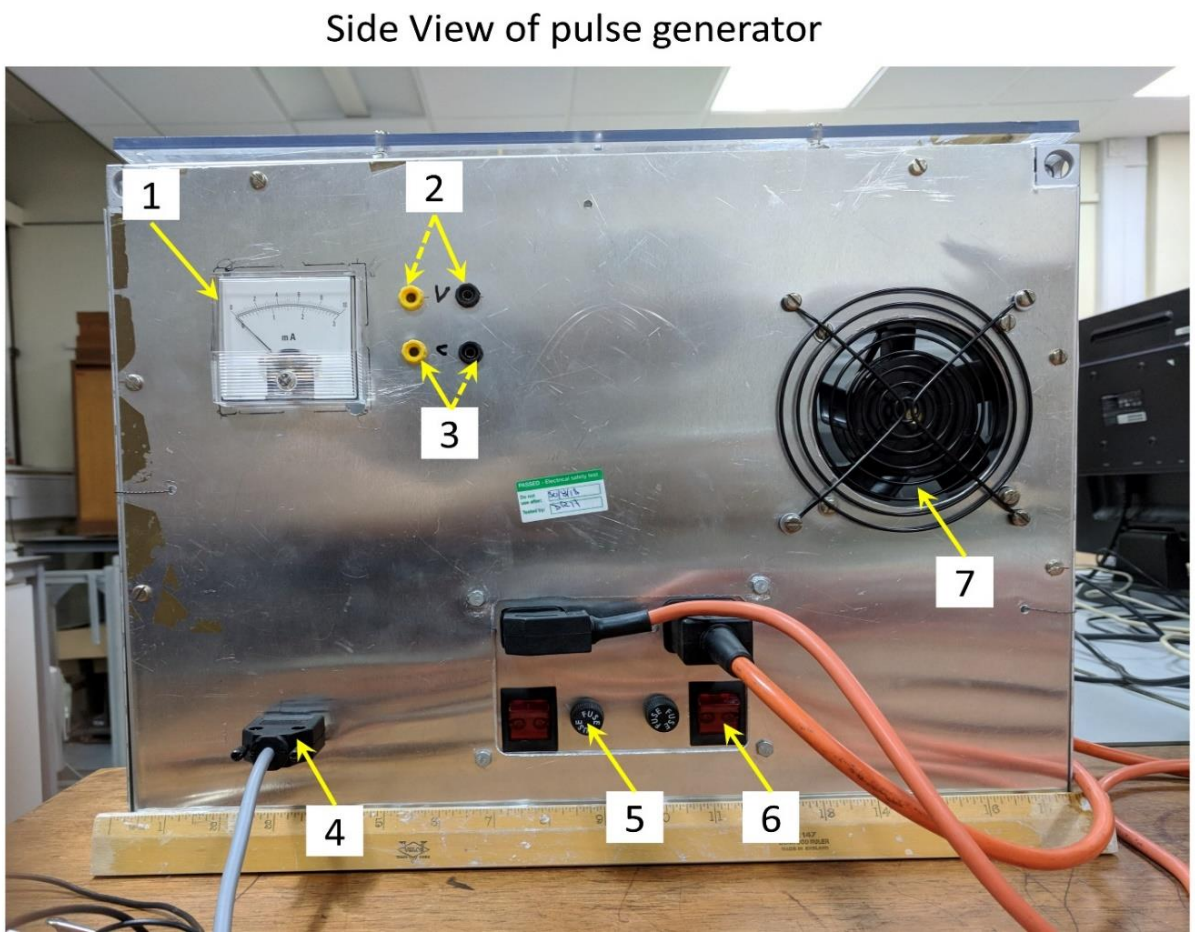

Figure 3.16 The side view of the pulse generator, highlighting key components including: (1) meter; (2) voltage ports for connecting oscilloscope; (3) current ports for connecting oscilloscope; (4) port for connecting pulse trigger; (5) fuses; (6) on-off button; (7) fan.

This new ventilation system has two axial fans (92 x 92 x 26 mm, 60m³/h, 13W, 230 V) and a dedicated, independent chamber is used for cooling the resistance shown in Figure 3.15.

Two fans play different roles in cooling procedure. One is used to suck the cooling air from outside, the other one is for propelling the hot air out of the box. Both fans are synchronized with the current signal. Therefore, once the current is circulating in the pulse box all fans keep working at the same time. In addition, the generating airflow from fans increases linearly with the inputting voltage. Hence, the dynamically adjustable working condition of fans provides an environmental solution with less energy consumption.

3.2.2.2 Hall sensor for current measurement

The voltmeter (PD72MIS500V/2/938-658, analogue panel meter, calibrated at 23°C, AC Voltage, 0 to 500 V) allows me to read the voltage from 1st and 2nd version box. When a periodic pulse is generated, the indicator in voltmeter will act as a pendulum, the amplitude of indicator depends on the magnitude of inputting volt. In addition, the indicator oscillation period is determined by the charging and discharging frequency.

Although this feature gives ‘virtual’ voltage information, more details e.g. current are needed for further understanding of the characteristic of 2nd generation box. Hence, a current sensor (HCM, 20310300101, HARTING) is accommodated next to the capacitor banks. The dimensional size and actual picture are shown in Figure 3.17. The discharging cable come out from the capacitor banks is strictly

required to pass through the centre of hall sensor, thus accuracy current measurement will be easier obtained through this setup.

A new ampere meter (another analogue panel meter) is replaced the 1st version voltmeter at same position on pulse generator. Unlike the voltmeter indicating the real output voltages, the ampere meter is acting as a virtual panel. This virtual current measurement design is very unique, functional and necessary. Because initial current is magnified at least several times after passing through the circuit in pulse box, it is not only unsafe to directly introduce the magnified current to the pulse box wall linked by the ampere meter, but also higher current will break the metre. Hence, a genius method is adopted to solve this problem.

Before the higher discharging current comes out, a 100 Ω resistor is used to link with the ampere meter. The value of final output current passing through the copper coils is unchanged, but the value indicated on ampere meter is reduced hundred times. For instance, a discharging current of 1000 A will pass the solenoid-shape copper coils, but only 10 A will display on the ampere meter. Hence, a safer, shock-protected ammeter fixed on pulse box wall is commissioned.

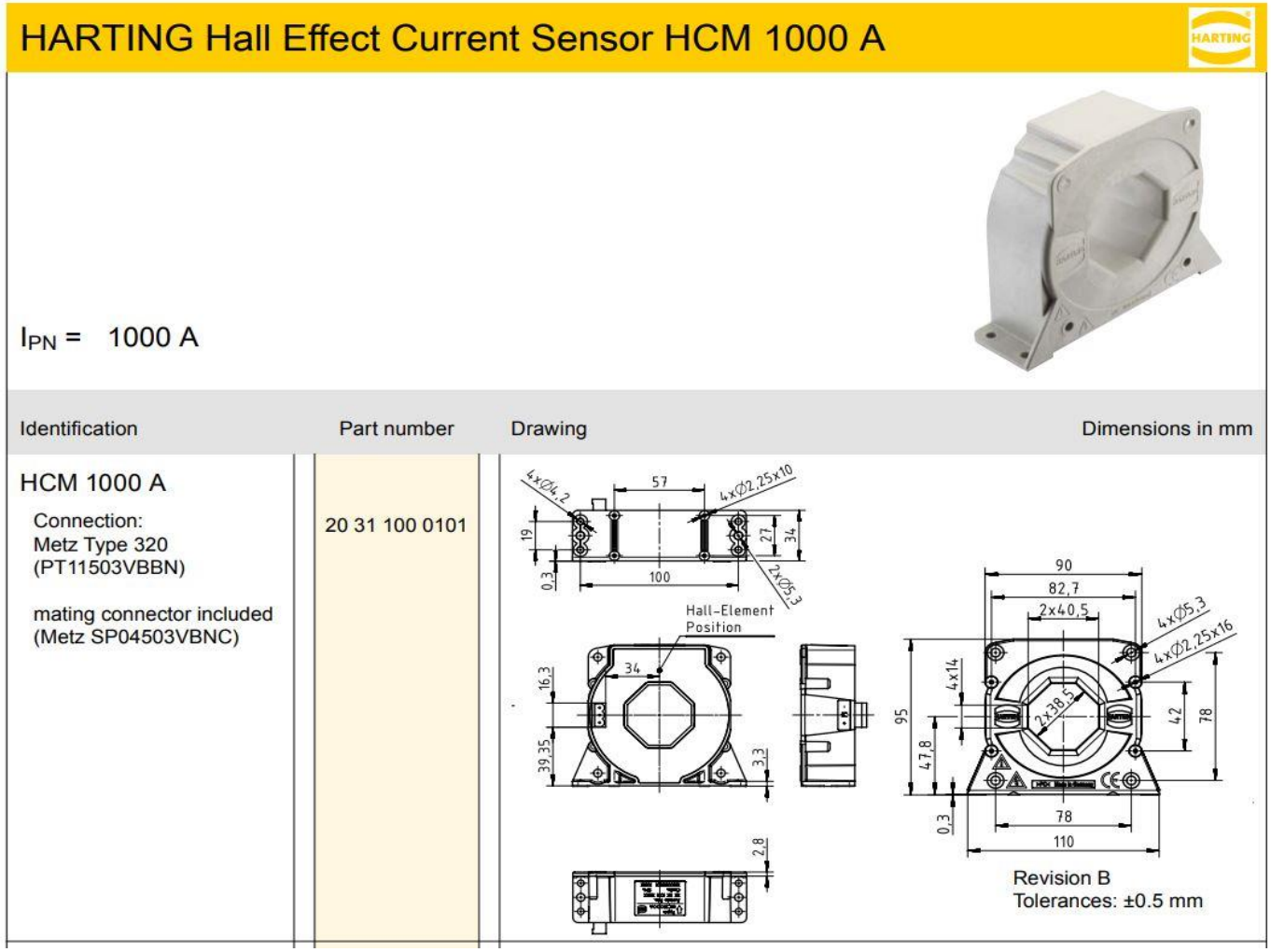

Figure 3.17 The dimensional and physical parameters of the current sensor (Hall sensor).

3.2.2.3 The development of pulse generating unit (solenoid induction coils)

The details of making the 1st version of pulse generating unit can be found in [47] and shown in Figure 3.18a. The generating magnetic intensity created by electromagnetic pulse device is determined by voltage (current amplitude), repetition frequency, average power, turns of induction coils, coil materials etc. The 3rd generation pulse generating unit is built for 2017 ESRF experiments shown in Figure 3.18c. An enamelled copper wire (2 mm, 14swg, Maplin, UK) was used to wind into a solenoid-shape coil with 30 turns, inner diameter (I.D) of 66 mm and a length of 100 mm. The improvement for 3rd version is significant included (1) more reliable and stable; (2) easier mount on sample stage (with Bridgeman furnace) to fit in beamline environment; (3) well insulation for safety purposes when comparing with 2nd edition for DLS experiment (Figure 3.18b).

For 3rd version, three machined Duratec 750 plates were geometric assembled together for firmly holding the copper coils creating a uniform gap between each turn. The gap between the coils is not always uniform for 1st and 2nd version which might affect the final structures.

The aluminium sheet and beams are machined to avoid any geometric blocking when all apparatus is assembled including furnace and ultrasonic generator etc. Firm holding is always required for synchrotron experiment. Because the entire units might shake when the strong current is passing through the coils. Hence, coils have to be fixed otherwise the shake of coil might block the X-ray illumination. The compact connection box is also used for saving spatial room.

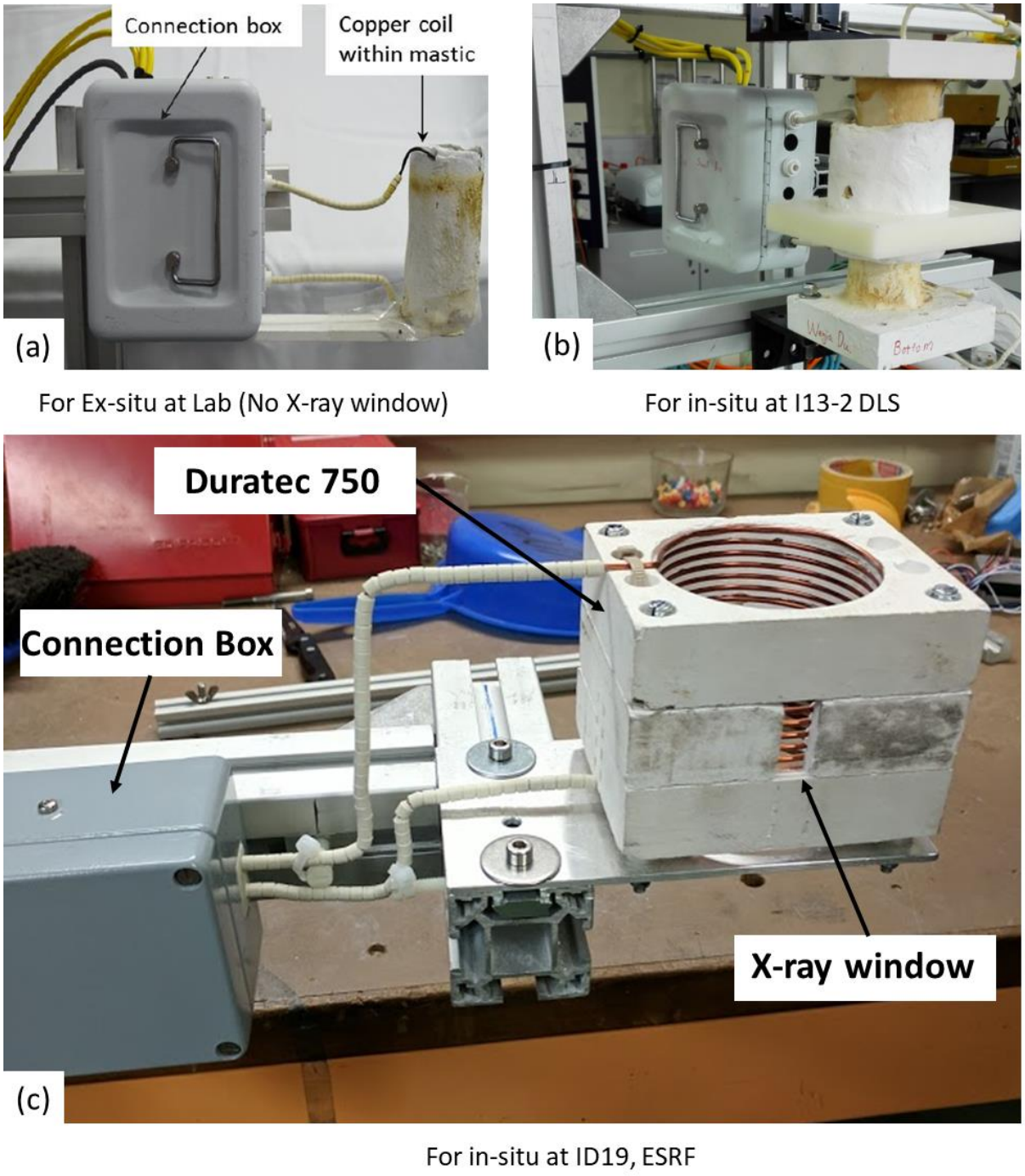

Figure 3.18 The different types of pulse generating units from 2015 to 2017, showing the improvement procedure of this unit.

3.3 Measurement of magnetic fluxes and discharging current

When low current is charged into the capacitor bank (two electrolytic capacitors 1000 μF, 550V) and then high current is discharged into the induction coil, generating an induced current *J* inside melt and induced magnetic flux (*B*). Thus, the interaction between *J* and *B* usually generates the Lorentz force. The magnitude of the force mainly dependents on the input voltage and charging time. In order to obtain an overview of Lorentz force against charging voltage, we must figure out how much current will pass through the induction coils.

3.3.1 Measurement of pulse magnetic flux densities

Gauss meter (model GM08 from Hirst Gauss Meter) is used to measure the pulse fluxes. It has ± 1% accuracy of the measured range. The GM08 is able to record fluxes and transfer into the computer. The GM08 specs is shown in Figure 3.19a. With 4 ranges the GM08 allows me to obtain signal frequency from 15 *Hz* to 10 *KHz*. It should be able to measure the high frequency magnetic pulse flux (1666 *Hz,* each pulse duration or pulse period is approximately 0.6 *ms* as shown in Figure 3.21, *f* is given by $\frac{1}{pulse\ duration} = \frac{1}{0.0006\ s} = 1666\ HZ$). However, in practice, the sampling rate is 3 reading per second (333 ms) where displays on the LCD screen. When GM08 is directly linked with PC for recording, the resolution of sampling rate will improve 100 ms (10 reading per second). Both methods of sampling rate are extremely low comparing the high frequency of pulse, because each pulse frequency leads at least two order of magnitude quicker than the sampling rate via standard method.

Hence, an advanced method is used by introducing a 100 *MHz* bandwidth of digital oscilloscope (TENMA, 72-8240, specs in Figure 3.19c) which is linked with GM08 for real-time monitoring and data recording. The GM08 has an analogue output port (Figure 3.19b1) to measure the continuous time-varying signals.

Figure 3.20 shows the schematic setup of the real-time pulse magnetic flux density measurements using (1) an Axial Hall probe, (2) discharging magnetic coils, (3) Gauss meter, and (4) a digital oscilloscope and its relevant software.

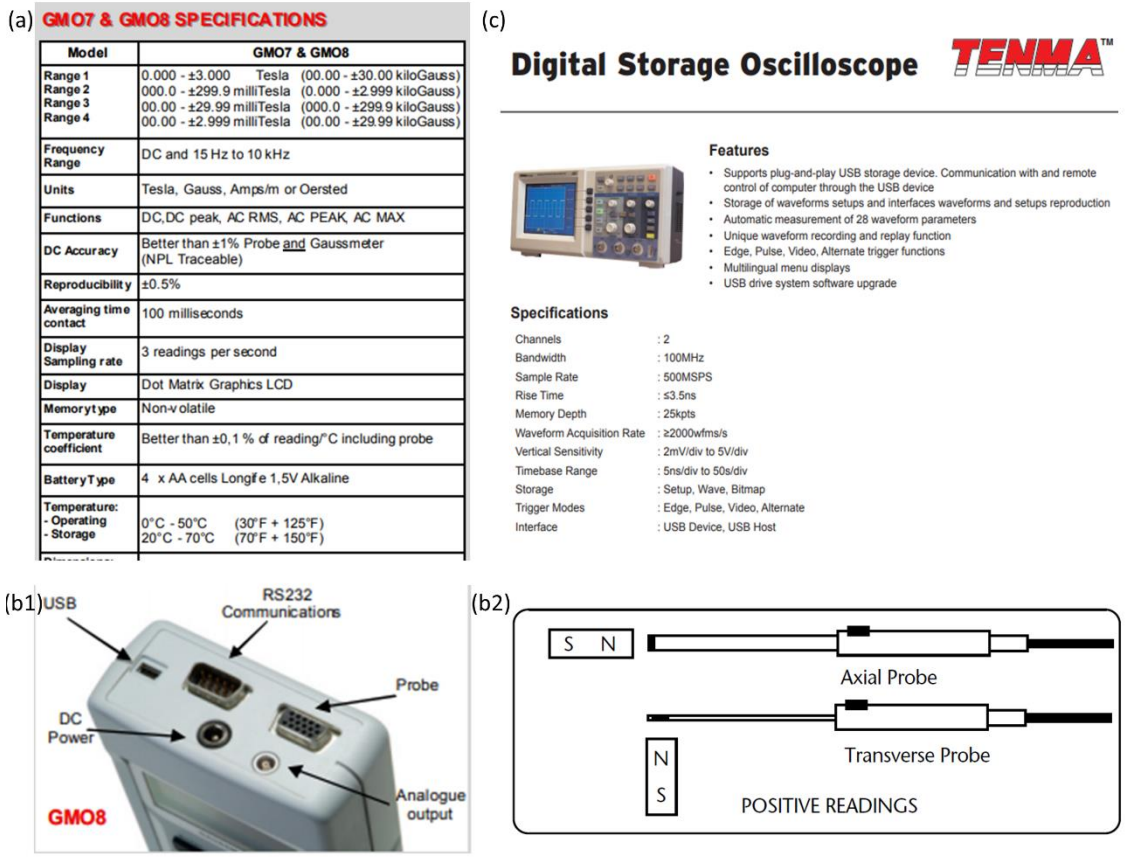

Figure 3.19 (a) the specification of GM08; (b1) the ports used to connect with Hall probe, PC and oscilloscope and (b2) the schematic of Axial probe and Transverse probe; (c) the specification of the TENMA 72-8240.

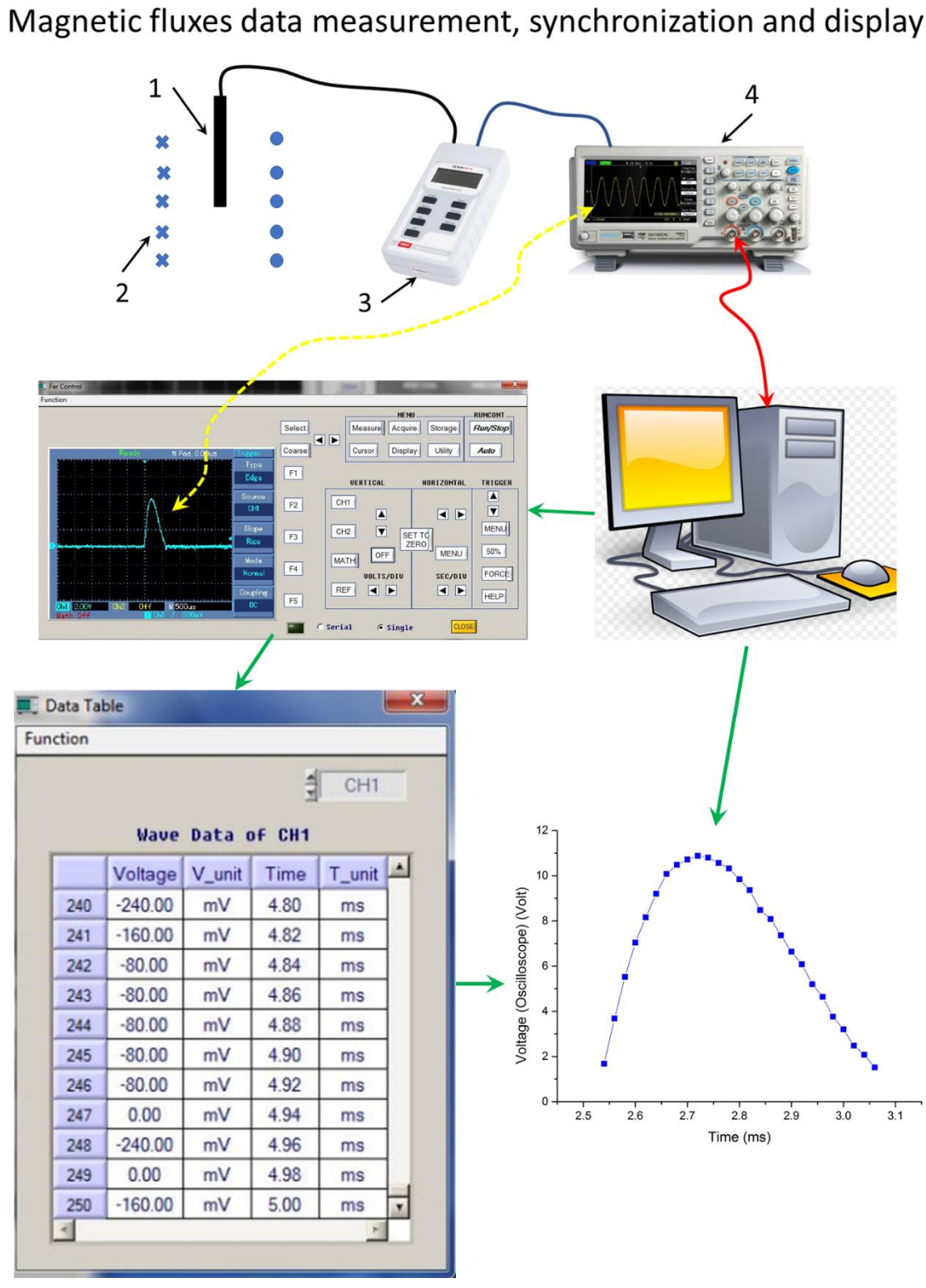

	Voltage	V_unit	Time	T_unit
240	-240.00	mV	4.80	ms
241	-160.00	mV	4.82	ms
242	-80.00	mV	4.84	ms
243	-80.00	mV	4.86	ms
244	-80.00	mV	4.88	ms
245	-80.00	mV	4.90	ms
246	-80.00	mV	4.92	ms
247	0.00	mV	4.94	ms
248	-240.00	mV	4.96	ms
249	0.00	mV	4.98	ms
250	-160.00	mV	5.00	ms

Figure 3.20 The schematic shows using 1. Axial Hall probe, 2. magnetic pulse coils, 3. Gaussmeter, and 4. Oscilloscope to measure the pulse magnetic flux densities that passing through the pulse coils, and its calibration.

In Figure 3.20, the Axial Hall probe is firstly connected with Gauss meter (GM08). A small connector pin is then inserted into the analogue output at the top of GM08 for later link with oscilloscope. Next, the oscilloscope probe is plugged to the oscilloscope port and the tip of this oscilloscope probe is connected to the previous connector pin. Finally, a USB cable is used to connect the PC and oscilloscope in order to provide GUI interface (DSO software) to acquire the peak profile of magnetic flux density.

Based on the setup of pulse electromagnetic field in Figure 2.5a, an Axial Hall probe (Figure 3.19b2) is selected to measure the real-time magnetic flux density with different voltage conditions positioned at the centre of be the coil without furnace. Data can be saved into the computer directly for further analyses as shown in Figure 3.21. Obviously, the magnetic flux density increased with higher input voltage. The real pulse profiles are not a genuine symmetric shape.

All entire pulse profiles are obtained by oscilloscope. The y-axis of Figure 3.21 is represent the analogue signal of magnetic intensity. The y-axis value needs to calibrate for the real magnetic flux value. For simplicity, only the peak value of pulse profile will be calibrated.

Firstly, DC peak function is selected in GM08. Next, the real peak value of magnetic flux density is able to displayed on the LCD screen in a relative long period (e.g. 60 ~ 120 s) under different voltages (e.g. 24, 48 V etc). Waiting a bit longer time is because the measured value of pulse will finally reach its peak by replacing the smaller one obtained before (higher value will eventually replace

the lower one). Finally, this peak value is assumed to be equal to the maximum value of a pulse profile which obtained by oscilloscope. By using this calibration method, the selective pulse profiles as a function of time with different voltage conditions are presented in Figure 3.22 for TOMCAT and I13-2 experiments.

In Figure 3.22, the peak values for each case have a linear relationship with input voltages, the time interval of flux density is almost same with the current results (Figure 3.24). Hence, I assume that the discharging current (*J*) and magnetic flux density (*B*) are synchronized with same frequency during the in-situ experiments. I also found that the magnetic fluxes generated in pulse coils are primarily dominated by the materials, numbers of turns, the diameter of the solenoid and the location of Axial Hall probe, etc.

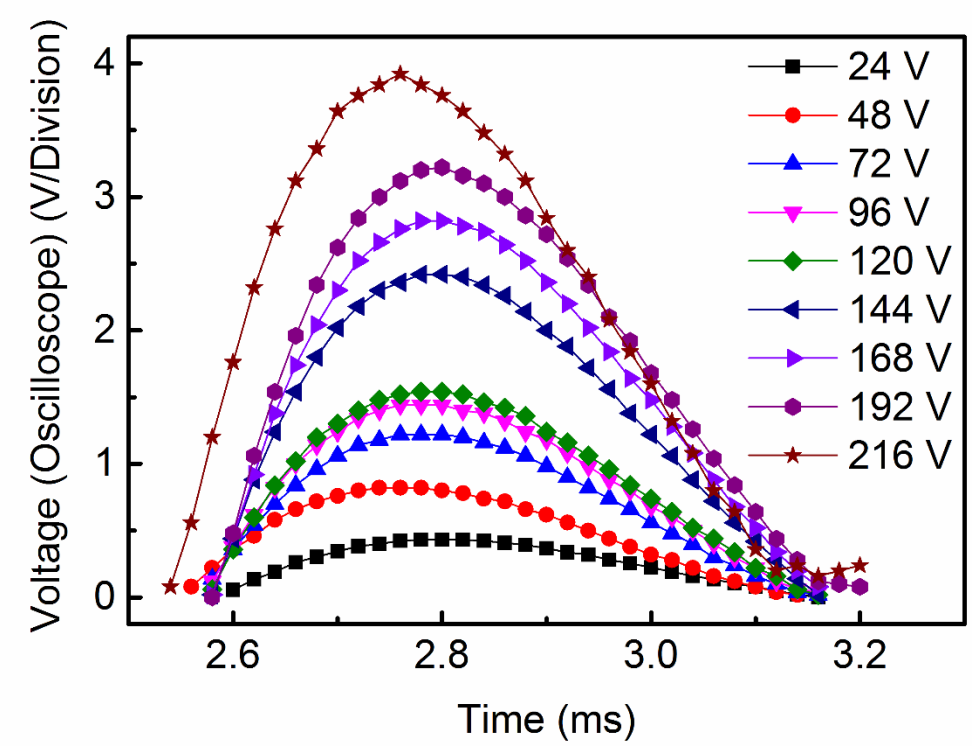

Figure 3.21 The real-time pulse magnetic flux densities measured by oscilloscope (Note: The results are used the 3rd version of pulse generator unit shown in Figure 3.18c).

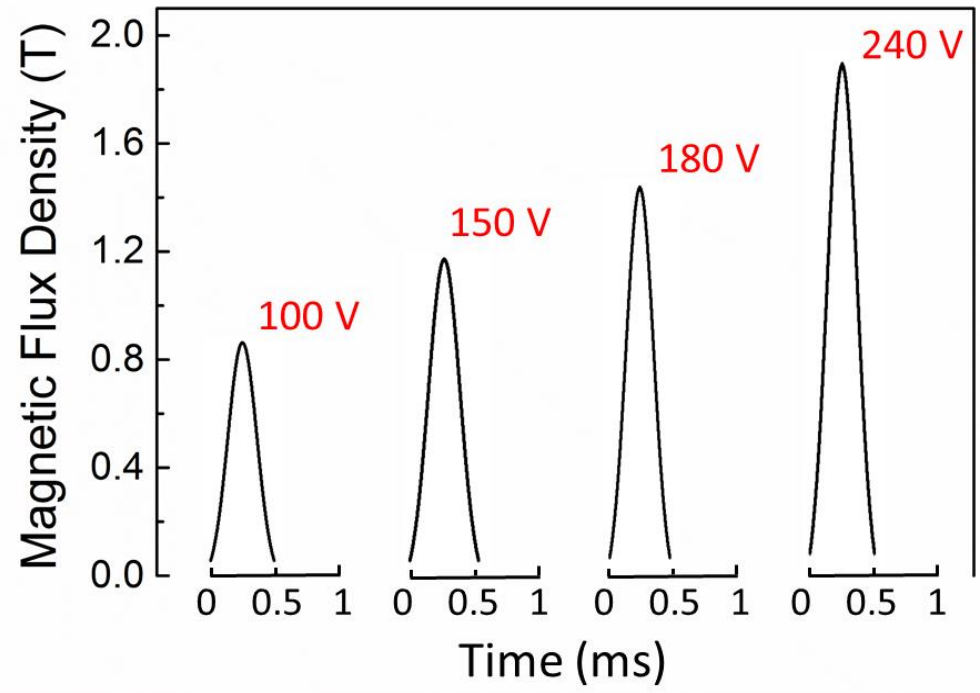

Figure 3.22 The measured pulse magnetic flux densities with different charging voltages.

3.3.2 Measurement of pulse current

In Figure 3.23, the schematic map shows using the oscilloscope to measure the current that passing through the pulse magnetic coils. Before measuring the current passing through the solenoid coil, another resistor (either 1 or 10 Ω) is individually used to insert into the red dash box in the circuit (Figure 3.10). The output of current signal is measured by Hall sensor (displayed by oscilloscope, the unit is volt per division). In other words, these two resistors (already known resistance values) are separately used to verify the relationship between the current signal and the input AC voltage. Moreover, the measured impendence coils by multi-metre is approximate 0.2 Ω while the resistance of coil is 0.1Ω.

According to measurement results shown in Figure 3.25 and Table 3.2, I found that there is a true relationship between the input AC voltage and the current signal when either 1 or 10 Ω is used. For example, when an AC voltage of 75 V is used, the output values are signal of 0.68 V for 1 Ω resistor and signal of 0.07 V for 10 Ω resistor respectively as shown in Table 3.2. The values of output current with 1 Ω resistor almost ten times higher than using 10 Ω resistor as the resistance are ten times difference, proving that there is a linear relationship for any resistor in the whole circuit.

Hence, an assumption is made that the linear relationship is also applied for the pulse coil when capacitors discharged the circuit. The measurement results also prove my assumption in Table 3.3 and Figure 3.26.

Figure 3.24 show measured output discharging current via oscilloscope (the unit is volt per division), demonstrating the pulse distribution for all cases when 40, 80, 120, 160, 200 and 240 Volts are inputted. During in-situ experiments magnetic pulses are continually generated into the melt, and time interval for each pulse is around 0.6 ms. Also, the intensity of discharging pulse current increases with increased charging volts into the capacitors.

Table 3.2 The calibration for pulse coils by using the 1 Ω and 10 Ω resistors.

Resistor	**1 Ω**		**10 Ω**	
Input AC Voltage (V)	Output in oscilloscope (V)	Current (A)	Output in oscilloscope (V)	Current (A)
25	0.2	35.25	0.02	3.525
50	0.44	70.5	0.044	7.05
75	0.68	105.75	0.07	10.575
100	1	141	0.096	14.1
125	1.2	176.25	0.12	17.625
150	1.4	211.5	0.15	21.15
175	1.7	246.75	0.175	24.675
200	2.15	282	0.2	28.2
225	2.4	317.25	0.235	31.725
250	2.7	352.5	0.26	35.25

Table 3.3 The measurement of output current (peak value) pass through the coils (pulse generating unit).

Input AC (Volt)	Output (peak value) in oscilloscope	DC current (A)
10	0.35	61.30434783
13	0.5	79.69565217
20	0.8	122.6086957
30	1.35	183.9130435
40	2	245.2173913
50	2.5	306.5217391
60	3	367.826087
70	3.5	429.1304348
80	4.1	490.4347826
90	4.7	551.7391304
100	5.2	613.0434783
110	5.85	674.3478261
120	6.4	735.6521739
130	7	796.9565217
140	7.6	858.2608696
160	9.2	980.8695652
180	9.9	1103.478261
200	10.8	1226.086957
250	13.6	1532.608696

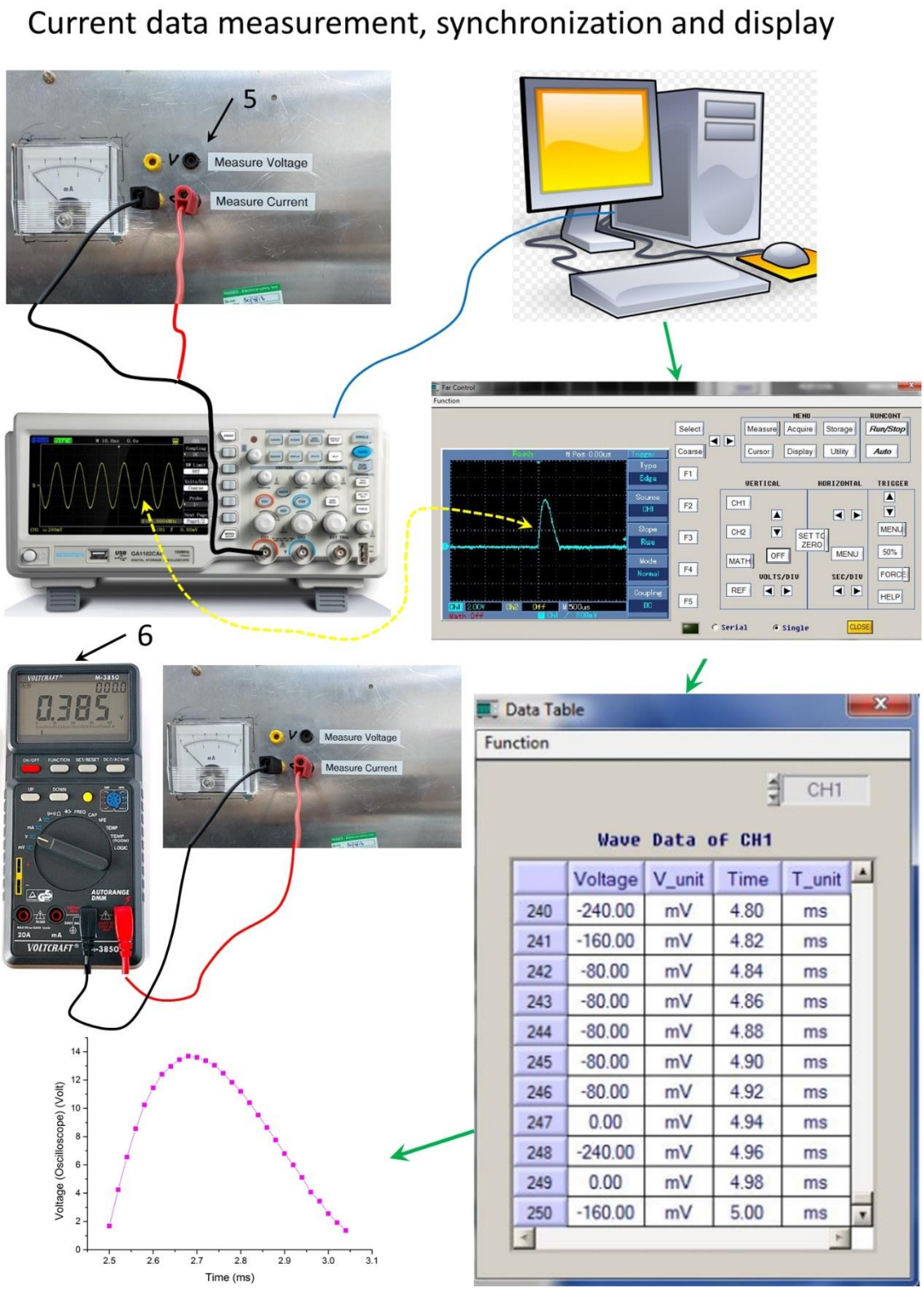

	Voltage	V_unit	Time	T_unit
240	-240.00	mV	4.80	ms
241	-160.00	mV	4.82	ms
242	-80.00	mV	4.84	ms
243	-80.00	mV	4.86	ms
244	-80.00	mV	4.88	ms
245	-80.00	mV	4.90	ms
246	-80.00	mV	4.92	ms
247	0.00	mV	4.94	ms
248	-240.00	mV	4.96	ms
249	0.00	mV	4.98	ms
250	-160.00	mV	5.00	ms

Figure 3.23 The schematic shows using the oscilloscope to measure the AC current (No. 5) that passing through the pulse magnetic coils, and using the multimeter (No. 6) and fixed resistors for calibration.

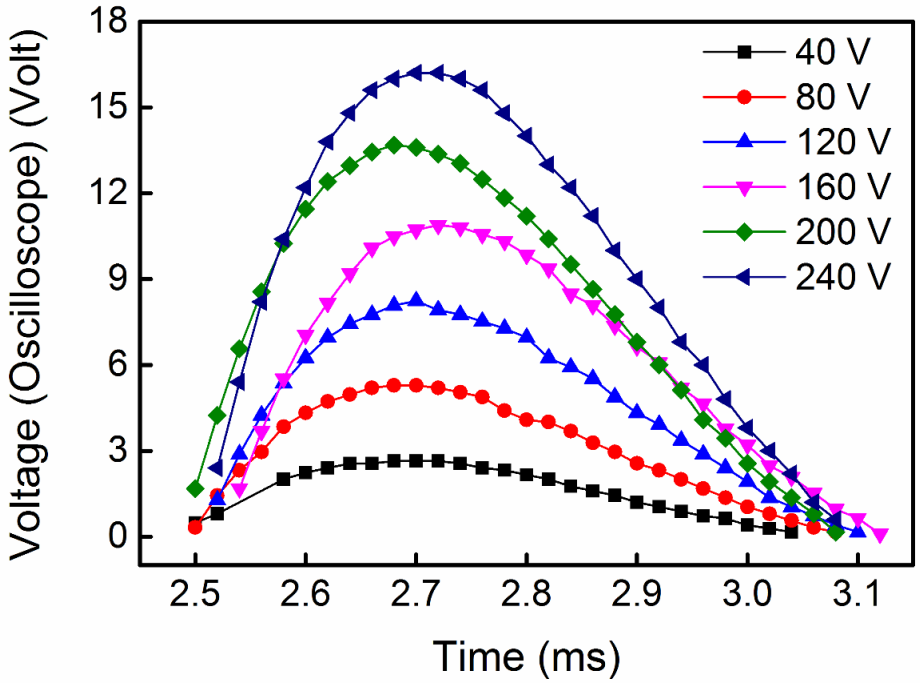

Figure 3.24 The measured output discharging current via oscilloscope, showing the pulse distribution when different input voltages are used.

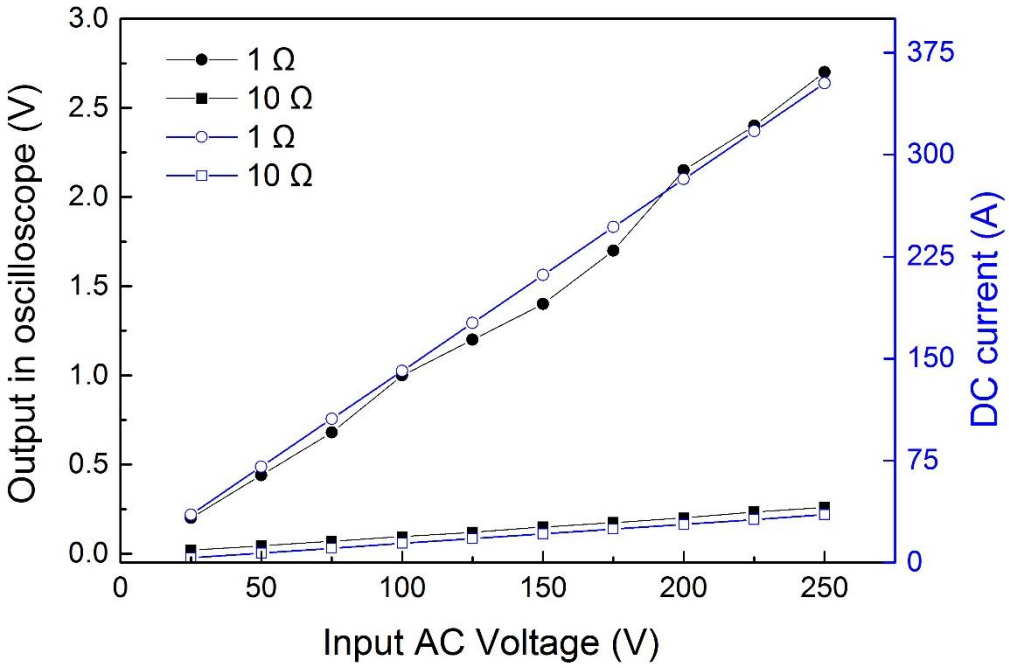

Figure 3.25 The input voltages against the voltage in oscilloscope and current measured by multi-meter by using the 1 Ω and 10 Ω resistors

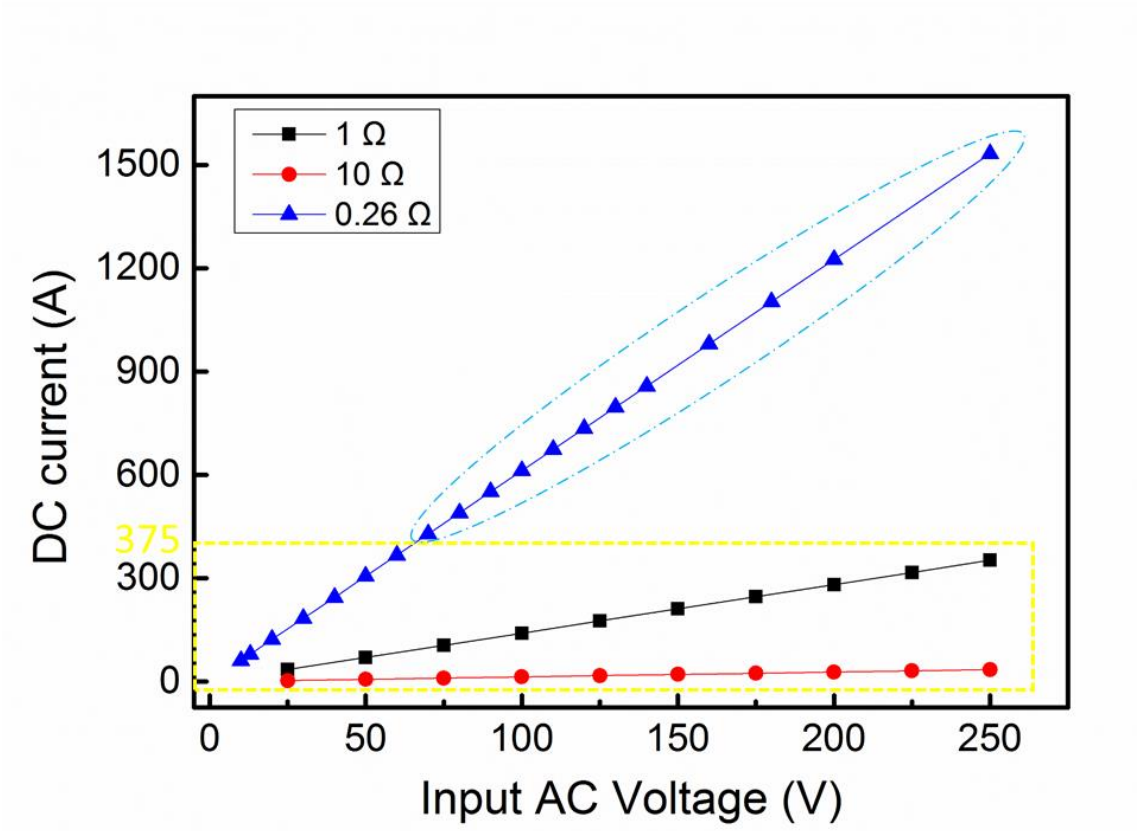

Figure 3.26 The relationship between the input (charging) voltage and the output (discharging) current of pulse coils from Table 3.3.

The relationships between various input voltages and output currents for different resistors (0.26, 1, and 10 Ω) are plotted in Figure 3.26. The linear relationships for two known resistors are proved in Figure 3.25 when the current is below 375 A, therefore this will also applied to pulse coil (0.26 Ω) when current is lower than 375 A based on measurement in Figure 3.26. Hence, all data in the yellow box is accurate and reliable. Based on my linear assumption, the current in coil follows the linear rule after 375 A with reasonable error (within the blue ellipse).

As can be seen from Figure 3.26, the output current reaches as high as approximate 1550 A when 240 V AC regular voltage is inputted into the PMF apparatus. Hence, a programmable PMF can be achieved with the magnetic pulse field is adjustable when various magnitudes of current are applied.

3.4 Contributions for the PMF equipment

The circuit diagram (Figure 3.11, Figure 3.12 and Figure 3.13) is designed and connected by electronic technician (Peter L. Kazinczi). The boxes of temperature controller (Figure 3.6) and pulse generator (Figure 3.15 & Figure 3.16) made by aluminium plates and beams are machining by mechanical workshop at University of Hull. The CAD scripts of furnaces (Figure 3.2, Figure 3.3 and Figure 3.4) and pulse generator (Figure 3.14) are designed by Wenjia Du. All necessary components are purchased and mechanical assembled by Wenjia Du. Measurements of magnetic fluxes and currents are performed by Wenjia for all various conditions after the demonstration by Peter.

3.5 Summary of components

As describe above, the entire pulse generator has three main parts: (1) pulse generator box, (2) power supply board and (3) controller board. All components included quantity, short description, supplier, manufacturer and order code are summarized in Appendix 2.

Chapter 4: **Experiment methods**

In my PhD study, synchrotron X-ray imaging and tomography techniques have been used primarily to study the highly dynamic microstructural evolution in solidification under pulse electromagnetic fields. This chapter describes sample preparation and experiments relevant to my PhD project, which have been conducted at three national synchrotron facilities (DLS, SLS, and ESRF).

4.1 Sample Preparation

Al-15%Cu, Al-35%Cu, Al-15%Ni and Al-5%Cu-1.5%Fe-1%Si (weight percentage see Table 1) were prepared at Advanced Materials Group, School of Engineering and Computer Science, University of Hull, UK.

Those alloys are chosen for the experiments since (1) there was sufficient X-ray absorption contrast between the liquid phase, primary dendritic phases and the solid intermetallic phase shown in Figure 4.2; (2) melting temperatures of those alloys are suitable for conducting synchrotron experiment without risky; (3) except Al-Cu alloy, other alloys have not been systematically studied yet.

Figure 4.1 shows the phase diagrams (weight percentage) of Al-Cu and Al-Ni alloys and the prediction of the solidification sequence for Al-5Cu-1.5Fe-1Si alloy. As can be seen from Figure 4.1a both the eutectic and liquidus temperature of Al-15wt%Cu alloy in phase diagram are 548.2 and 620 °*C*, respectively. And The liquidus and eutectic temperatures of Al-15%Ni alloy are 782 and 639.9 °C respectively as shown in Figure 4.1b.

Since quaternary phase diagram of Al-5Cu-1.5Fe-1Si alloy is very limited in open literatures. Hence, in Figure 4.1c, I used a Scheil approximation (equilibrium solidification) in Thermo–Calc (Thermo–Calc Software AB, Stockholm) to predict the solidification sequence and provide reference for in-situ study at ESRF. This simulation is supported by Dr Feng Wang in BCAST at Brunel University.

These alloys were made by melting the correct charge weights of pure aluminium ingots (99.97%), pure copper (99.97%) bar, pure nickel (99.0%) bars and pure iron (99.9%) bar inside an alumina crucible (internal diameter 92 mm × height 135 mm, Almath, UK) with its inner surface coated with a boron nitride spray. The crucible was then placed inside an electric resistance furnace which was heated over 100 degree than the melting temperatures (T_l) of each alloy. Each alloy is held at that temperature for 30 minutes to homogenise the liquid alloy. The details of these alloy are summarised in Table 4.1

Table 4.1 The melting and eutectic temperatures for different alloys.

Alloy (wt%)	**Melting Temp (ºC)**	**Eutectic Temp (ºC)**	**Hold time (min)**
Al-15Cu	620	548	30
Al-35Cu	554 [78]	548	30
Al-15Ni	782	639	30
Al-5Cu-1.5Fe-1Si	652 (Thermo-Calc)	N/A	30

In addition, I used counter–gravity casting apparatus because the thickness of samples has to be in 2 – 5 mm the minimum requirement as shown in Figure 4.2. It is almost impossible to directly pour these liquid metals into such thin tube.

Finally, these liquid metal were sucked into 100 mm quartz tubes (inner diameter of 10 or 2 mm) by using a custom-made counter-gravity casting apparatus [47] shown in Figure 4.3a. The liquid metal was drawn uphill under negative pressure (~0.5 atmospheric pressure) and flew quiescently into the quartz tube. Such operation can minimise any air bubble or oxide films entrained into the samples [62]. Thus, a clean alloy ingots were produced for subsequent in-situ and ex-situ experiments. The examples of casting sample for subsequent solidification experiment are shown in Figure 4.3b. The 10 mm samples are used for ex-situ experiments at laboratory, while the 2mm diameter samples are used for synchrotron experiments.

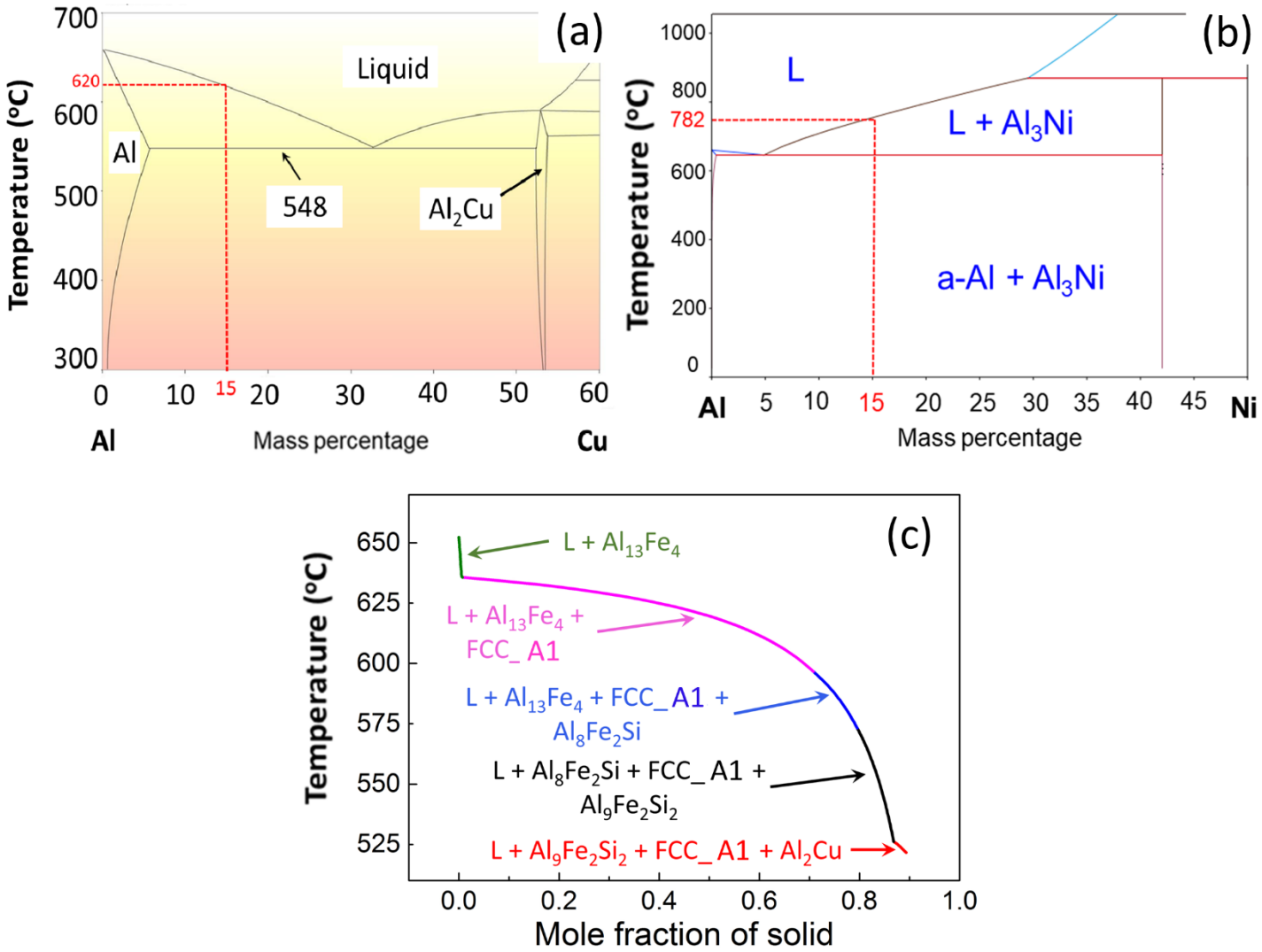

Figure 4.1 The phase diagram of (a) the Al-Cu alloy and (b) the Al-Ni alloy. (c) The mole fraction of the Fe-based intermetallic phases in an Al-5Cu-1.5Fe-1Si alloy calculated from the scheil solidification model.

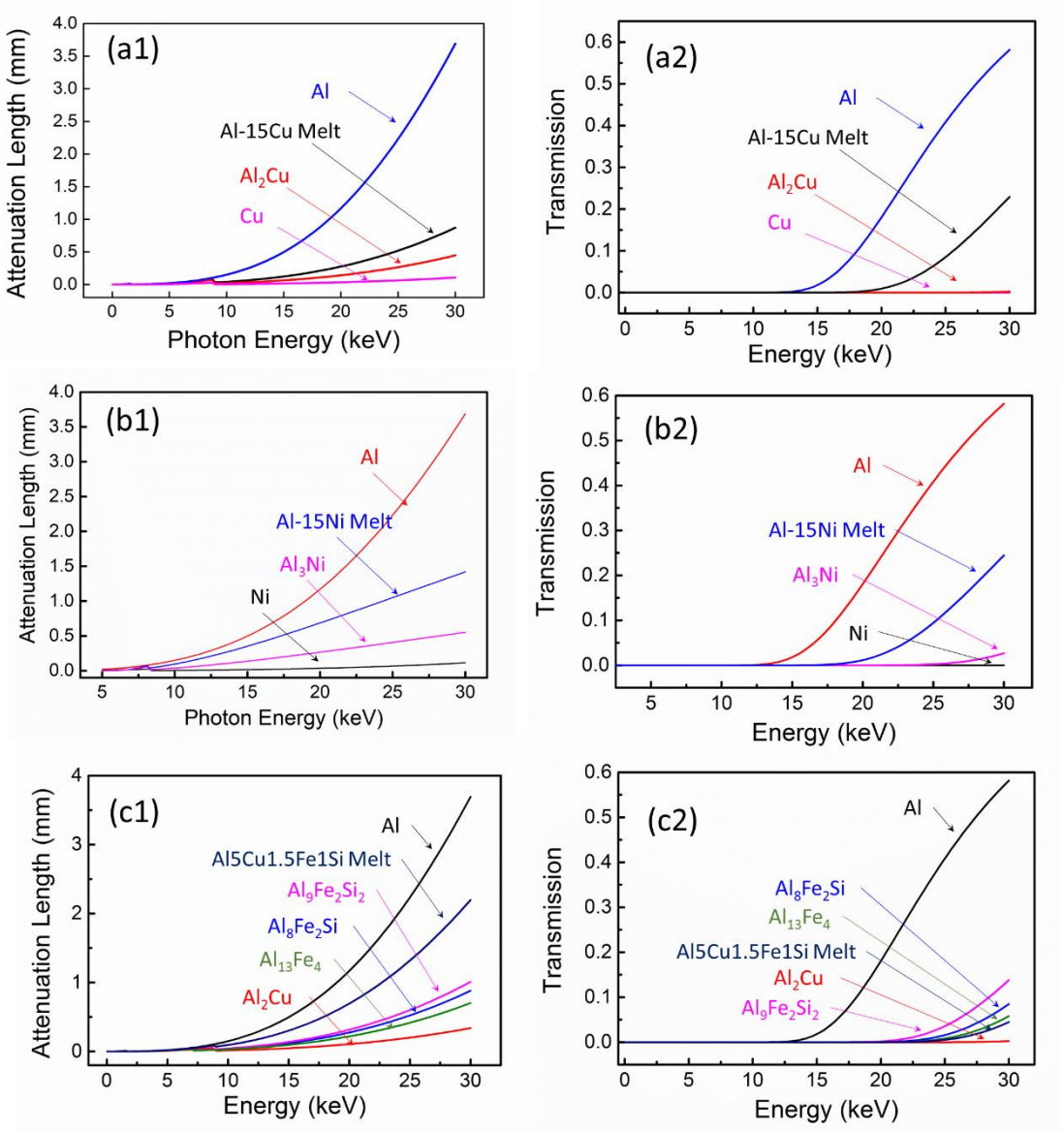

Figure 4.2 X-ray (a) attenuation length and (b) transmission of different phases in the experimental alloys in the X-ray energy range of 0 - 30 keV of (a) Al_2Cu, Al and Cu; (b) Al-15%Ni melt, Al_3Ni, Ni and Al; (c) Al, Al_2Cu, Al_8Fe_2Si, $Al_9Fe_2Si_2$, $Al_{13}Fe_4$ and Al-5Cu-1.5Fe-1Si Melt.

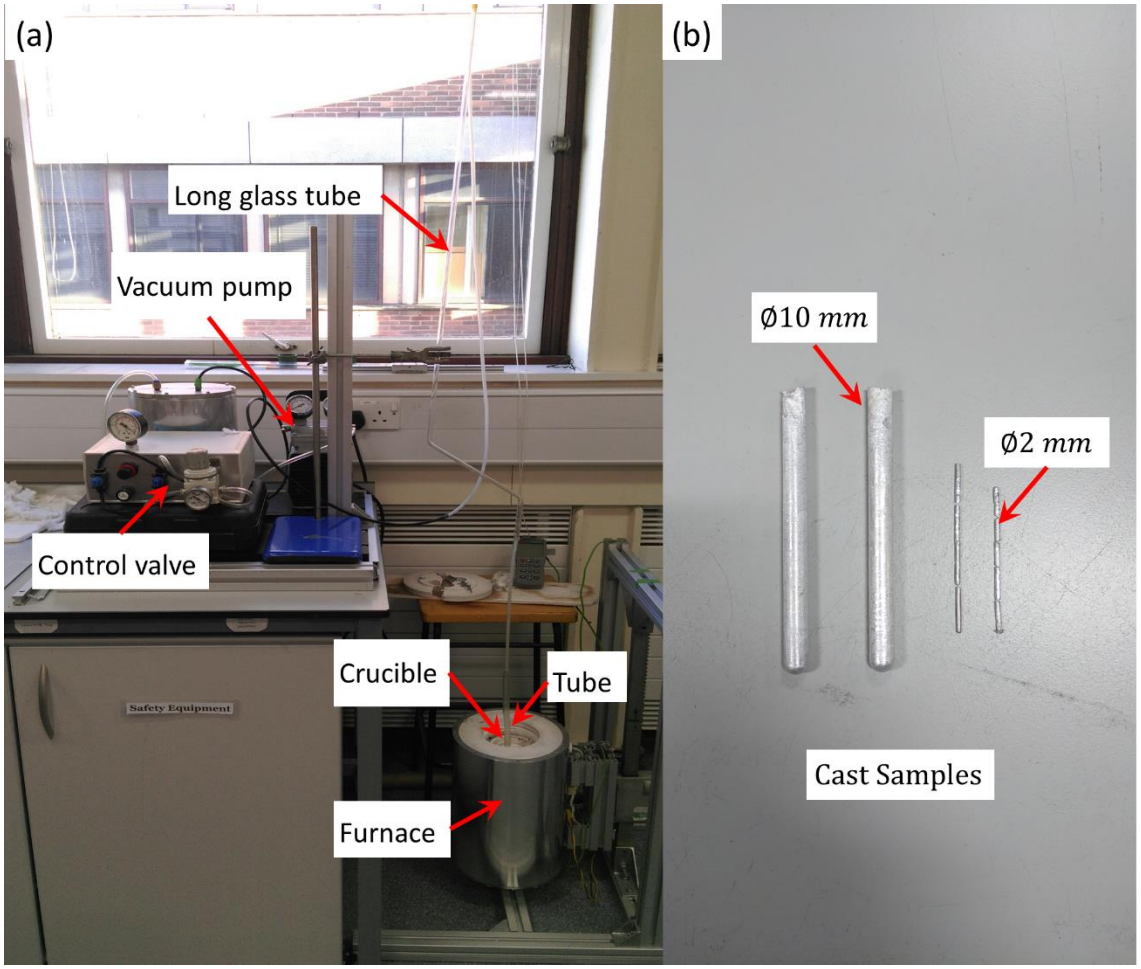

Figure 4.3 (a) The photo showing the counter–gravity casting apparatus used for casting samples; (b) The example of cast samples with different diameters.

Table 4.2 The in-situ synchrotron X-ray experiments that produce outputs for my research

Proposal number	Proposal title	Beamline & Facility	Experiment date	My responsibility
NT12131	In-situ, high speed radiography of the interactions between ultrasound bubbles and nucleating particles in solidifying metal alloys	I12, DLS	11-13Feb 2015	Participate
20141167	In situ tomography study of the evolution of solidification microstructures under magnetic pulses	TOMCAT, SLS	10-13June 2015	Lead
MT13488	In Situ Tomography Studies of the Solidification Microstructure of Al Alloys under Electromagnetic Pulses	I13-2, DLS	8-10July 2016	Lead
MA-3752	In-situ studies of the fundamental mechanisms of ultrasound treatment on the primary phases nucleation and growth in peritectic alloys	ID19, ESRF	20–24Sep 2017	Extensively participate

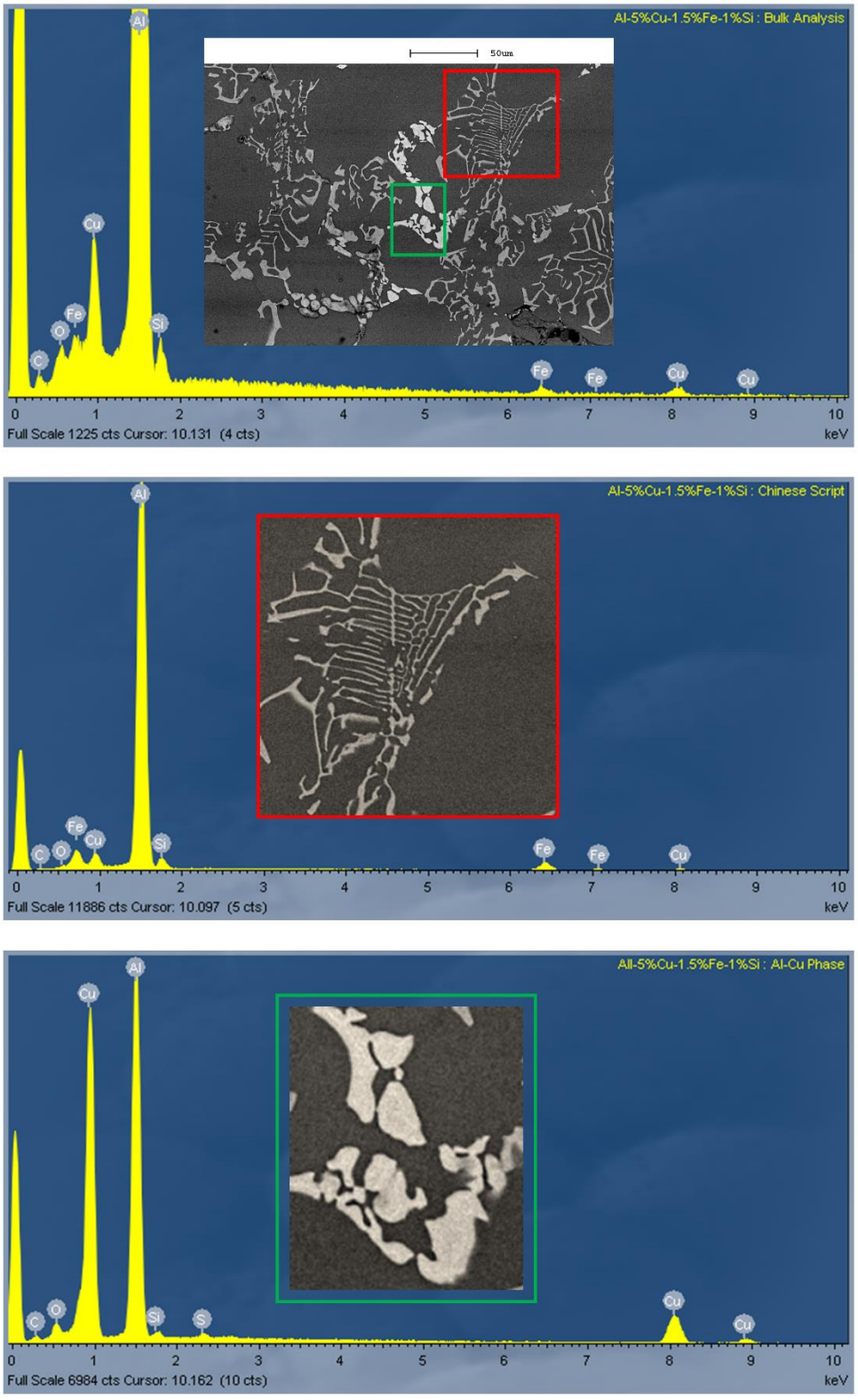

Figure 4.4 The EDS spectrums: (a) the entire region; (b) the Chinese-script region (red box); (c) the Al_2Cu region (green box).

Prior to the synchrotron tomography experiment, the Al-5%Cu-1.5%Fe-1%Si sample compositions were checked and analysed by energy dispersive X-ray spectroscopy (EDX) shown in Figure 4.4. This gives a general composition of the combined alloy and phases. The EDX analysis was carried out for the 0 T sample, an area close to the middle of the sample was chosen and the SEM images showed intermetallic phases.

Upon looking at bulk sample, it was decided that 400x magnification allowed a characteristic region for analysis which included all of the expected phases as well an unexpected solid phase as shown in Figure 4.4a. The EDS spectrum for the total area is as expected with large amounts of Al, a mediate peak for Cu and a small peak for Fe and Si when energy bellows 2 keV. The peak for O is quite small and indicates a small amount of contamination.

Then spot analysis was composed for each very distinct intermetallic region. A spot analysis for the very distinct region Chinese script was composed as shown in Figure 4.4b. It contains mainly Al with peaks of Cu and Fe, this phase is Al_8Fe_2Si based on Thermo–Calc estimation (Figure 4.1c). The peak for Cu is lower than that of the Fe in this intermetallic, therefore it concludes that the majority of Fe is present in this phase (since Cu is higher than Fe in bulk analysis). The spectrum of Figure 4.4c shows that the intermetallic phase is mainly constructed of Al and Cu with little amounts of Fe and O, this phase is identified as Al_2Cu.

Unfortunately, this EDS analysis cannot provide any further quantitative information than spectrums. Hence, from experimental view, the X-ray diffraction

(XRD) and an advanced EDS (with post analysis software) are required to determine the resolved phases.

4.2 In-situ synchrotron X-ray beamline conditions

I have participated a number of real-time and in-situ synchrotron X-ray experiments at different synchrotron facilities in year 2014 – 2018 as detailed in Table 4.2. I participated one beamline experiments and led three beamline experiments during my PhD study as described below:

For 2015 TOMCAT synchrotron μ-CT experiment, a polychromatic X-ray beam (with average energy of ~28 keV) was used since it significantly reduced the total scan time. The faster Ce scintillator (thickness of 100 μm) coupled pco.edge 5.5 detector (PCO AG, Germany) was used. The detector has maximum frame rate of 100 fps at all resolution which is suitable for 4D dynamic study. The sample-to-detector distance was set to 300 mm. A 10 × magnification objective lens was used, resulting in a pixel size of 0.65 μm per pixel with a field-of-view (FoV) of 2016 × 2016 pixels (equivalent to $\sim 1.31 \times 1.31$ mm^2). This allows sufficient number of dendrites to be obtained in the FoV for statistical analyses. In each tomogram, the sample rotated from 0 to 180 deg with an angular step of ~ 0.36 deg, and a total of 501 projections were taken (7.0 ms exposure time for each projection). Hence, one tomography scan was finished in ~3.5 s, and the skip time between two continuous scans was 10 s. To our knowledge, this is the fastest tomography solidification experiment with the PMF conducted at this resolution.

For 2016 Manchester branchline I13-2 imaging and tomography experiments, I only use a white X-ray beam (the average energy of beam using platinum coated mirror is 28.3 keV) generated by a undulator of 5mm gap was reflected from the platinum stripe of a grazing-incidence focusing mirror and high-pass filtered with 1.3 mm pyrolytic graphite, 3.2 mm aluminium and 20 µm steel. Both Al-35Cu and Al-15Ni Images were recorded by a CMOS (2560 × 2160 pixels) pco.edge 5.5 (PCO AG, Germany) detector which was coupled to a 500 µm-thick CdWO4 scintillator and a visual light microscope. The objective lens of 4 × was used, achieving an effective spatial resolution pixel size of 0.81 µm/pixel in a field of view of 2.1 mm × 1.8 mm. The exposure time was 0.1 s in order to obtain sufficient signal. For the tomography experiments, a total of 2001 equally-spaced projection images were acquired over 180 deg continuous rotation (‘fly scan’) for each sample.

For 2017 ID 19 European Synchrotron Radiation Facility (ESRF) experiments, white X-ray beam with average energy of ~26 keV were used to illuminated samples by recording 1000 projections covering an angular range of 180 deg. The sample-to-detector distance was set to 300 mm. The exposure time is approximate to 2 ms. Hence, the total time for a full 180deg scan was about 2 s. The readout area of the PCO Dimax CMOS camera was set to 1008 × 1008 pixels, and this camera was coupled to a 10 × magnifying optical lens resulting in a pixel size of 1 µm/pixel. Hence, a total volume of about 1 mm^3 recorded in each tomogram. In this experiment, all tomography scans were continues taken until the memory at ID19 is full. Without any gap (or skip time) between two

subsequence tomograms, therefore the ultrafast acquisition enables us to obtain the entire 4D information during cooling period. 50 tomograms were continuously captured.

All beamline parameters are summarized below in Table 4.3 and Table 4.4:

Table 4.3 The summarized different beamline parameters for each sample.

Sample name	Beamline	Beam energy	Sample – Detector distance	Pixel size	Camera
Al-15Cu	TOMCAT, SLS	Polychromatic radiation (Avg 28 keV)	300 mm	0.65	PCO.Edge 5.5
Al-35Cu	I13-2, DLS	Polychromatic radiation (Avg 28.3 keV)	200 mm	0.81	PCO.Edge 5.5
Al-15Ni	I13-2, DLS	Polychromatic radiation (Avg 28.3 keV)	200 mm	0.81	PCO.Edge 5.5
Al-5Cu-1.5Fe-1Si	ID19, ESRF	Polychromatic radiation (Avg 26 keV)	300 mm	1.1	pco.dimax

Table 4.4 The summarized of datasets dimensions for each alloy.

Sample name	Magnification	Projections per scan	Exposure time	Reconstruction Dimensions (pixel)
Al-15Cu	10 ×	501	7 ms	2016 × 2016 × 2016
Al-35Cu	4 ×	2000	100 ms	2560 × 2568 × 2158
Al-15Ni	4 ×	2000	100 ms	2560 × 2568 × 2158
Al-5Cu-1.5Fe-1Si	10 ×	1000	2 ms	1008 × 1008 × 1008

4.3 The in-situ solidification experiments

4.3.1 Experiment at TOMCAT of SLS

I propose using X-ray tomography to acquire 4D datasets for understanding how the PMF affect the growths and coarsening of the primary Al dendritic phases.

Two furnaces were used to heat the alloy sample which was inserted inside a 3 mm inner diameter quartz tube. Four K-type thermocouples were positioned at the locations inside the furnaces and marked by TC1, TC2, TC3 and TC4 in Figure 3.2. TC1 and TC2 are the temperature control points for the two furnaces. TC3 and TC4 are the points very close to the quartz tube and the distance between them was 10 mm. The two thermocouples were kept outside the quartz tube to avoid entangling the thermocouple wires during the sample rotation. A temperature calibration was performed with one thermocouple inserted inside the quartz tube at the location between TC3 and TC4.

For solidification experiments, the top and bottom furnaces were initially heated to ~715 and ~650 °C to melt the alloy and before X-rays were switched on. The upper furnace was maintained at ~710 °C, the temperature of the bottom furnace was ramped down from 610 to 575 °C in 4 minutes (an average cooling rate of 0.15 °C/s) using manual PID thermal controller. Figure 4.5a show that the repeatability of the temperature profiles during a number of heating-cooling cycles was very well maintained.

The input voltage was 80 V with the corresponding magnetic flux density of 0.75 T (the peak value) was immediately applied when the primary *α*-Al dendrite was once resolved at field of view. The pulse electromagnetic fields were applied into the melt continuously at a frequency of 1 Hz during solidification until 20 tomograms are obtained. Another solidification experiment was repeated except no pulses applied (obtained 20 tomograms). Solidification experiments carried out with the cooling rates 0.05 K/s and temperature gradient (*G*) 10 K/mm. The error of real specimen temperature is approximately 1~3 °C.

Another goal of this experiment is studying the growth and morphologies of equiaxed Al dendritic during coarsening. This experiment is performed with Z. Guo from Tsinghua University using the same solidification apparatus described in Chapter 3. The beamline parameters are maintained as described in 4.2.
Two furnaces were firstly heated up to ~700 ^{o}C to melt the alloy completely. The temperature of both upper and bottom furnaces was then simultaneously decreased until the sample temperature (showed by the readings from TC3 and TC4) reached ~610 ^{o}C. The beamline parameters at TOMCAT are described in 4.2.2. After the temperature was maintained, and tomography scans were started. The scans were taken continuously for about 6.7 minutes (398 seconds) as showed by the framed region in Figure 4.6. There are 60 tomo scans obtained for coarsening experiment. The real microstructures and phase fields modelling structures are compared but no quantitative analysis.

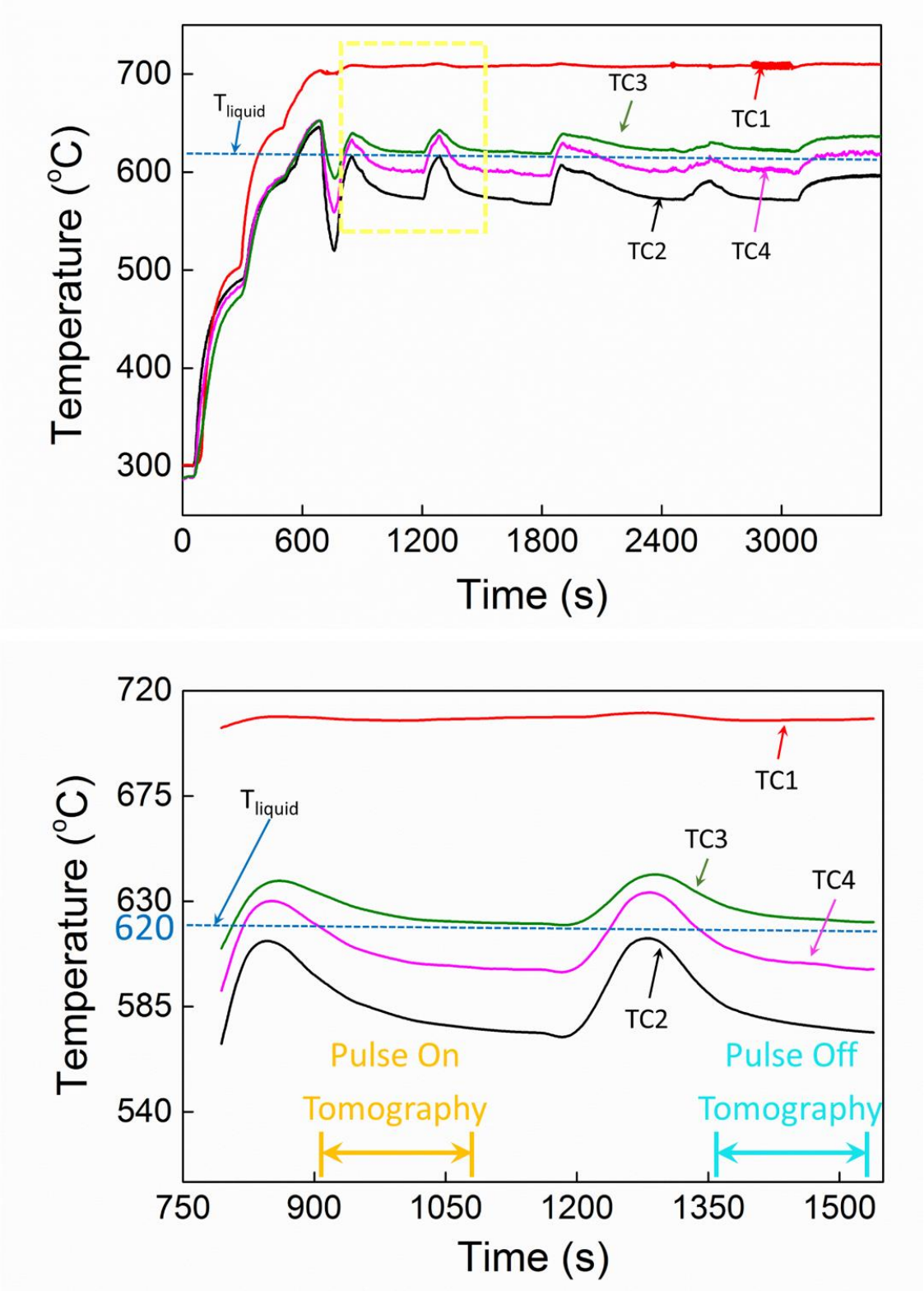

Figure 4.5 The control of the heating-cooling cycle of Al-15wt%Cu samples and the application of pulse electromagnetic field. Solidification experiments carried out with the cooling rates 0.05 K/s and temperature gradient (*G*) 10 K/mm.

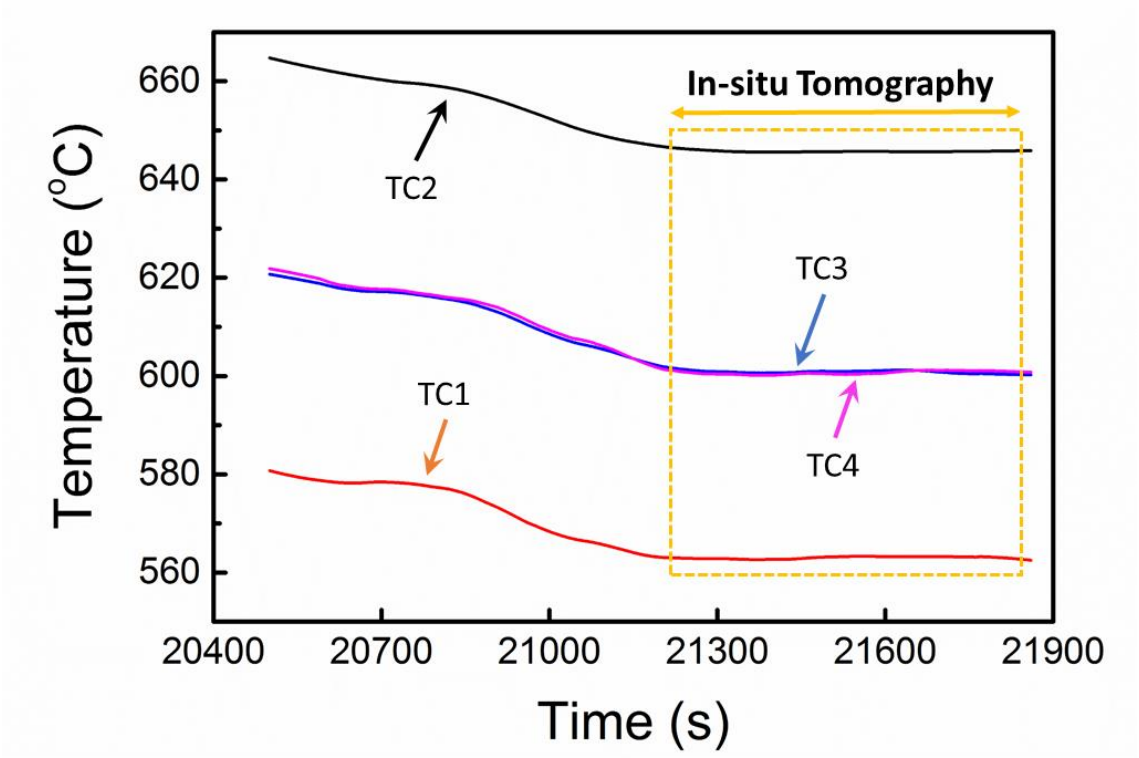

Figure 4.6 The measured temperature profiles of TC1, TC2, TC3, and TC4 during the tomography experiment. The framed area is the period for acquiring tomography scans.

4.3.2 Experiment at I13-2 of DLS

In this experiment, the top and bottom furnaces were initially heated to ~835 and ~925 °C to melt the alloy and then held for 30 minutes to homogenise the melt temperature (Figure 4.7a). After 30 minutes, while the temperature of the upper furnace was maintained at ~835 °C, the temperature of the bottom furnace was ramped down from 925 to 580 °C in 4 minutes (an average cooling rate of 1.44 °C/s) using a control program (PLATINUM) set by the Omega PID thermal controller. Both furnaces (TC1 and TC2) were then held at 835 and 580 °C,

respectively. Figure 4.7a show that the repeatability of the temperature profiles during a number of heating-cooling cycles was very well maintained.

When melt cooling started, pulse was applied into the melt at a frequency of 1 Hz. The pulse and X-ray radiography acquisition started at the same time and lasted for the period as indicated by the segment “pulse on” in Figure 4.7b. The input voltages used were 0, 100, 150, and 180 V respectively with their corresponding peak magnetic flux density at 0, 0.85, 1.2 and 1.5 T respectively. The studies were focusing on investigating the effects of different pulses on the evolution of primary Al_3Ni intermetallic phases. Radiography images were taken continuously during cooling until the measured temperatures at the locations TC 3 and TC 4 reached at 725 and 640 °C (the melt was in the semi-solid region), respectively and then the temperatures of both furnaces were maintained at this level (Figure 4.7b). Under this condition, solid phases were seen to appear in the field of view and recorded. The pulse and radiography acquisition were stopped at the same time, and then tomography acquisitions started (Figure 4.7b). The time for switching from radiography to tomography acquisition was 1 minute. To obtain sufficient image and tomography data for statistical analyses, for each PMF condition (different peak magnetic flux density), the same sample with the same heating-cooling profile was radiography and tomography scanned repeatedly for at least three times. Including the initial trial scans, a total of 39 tomography scans were obtained for the Al-15%Ni alloy samples.

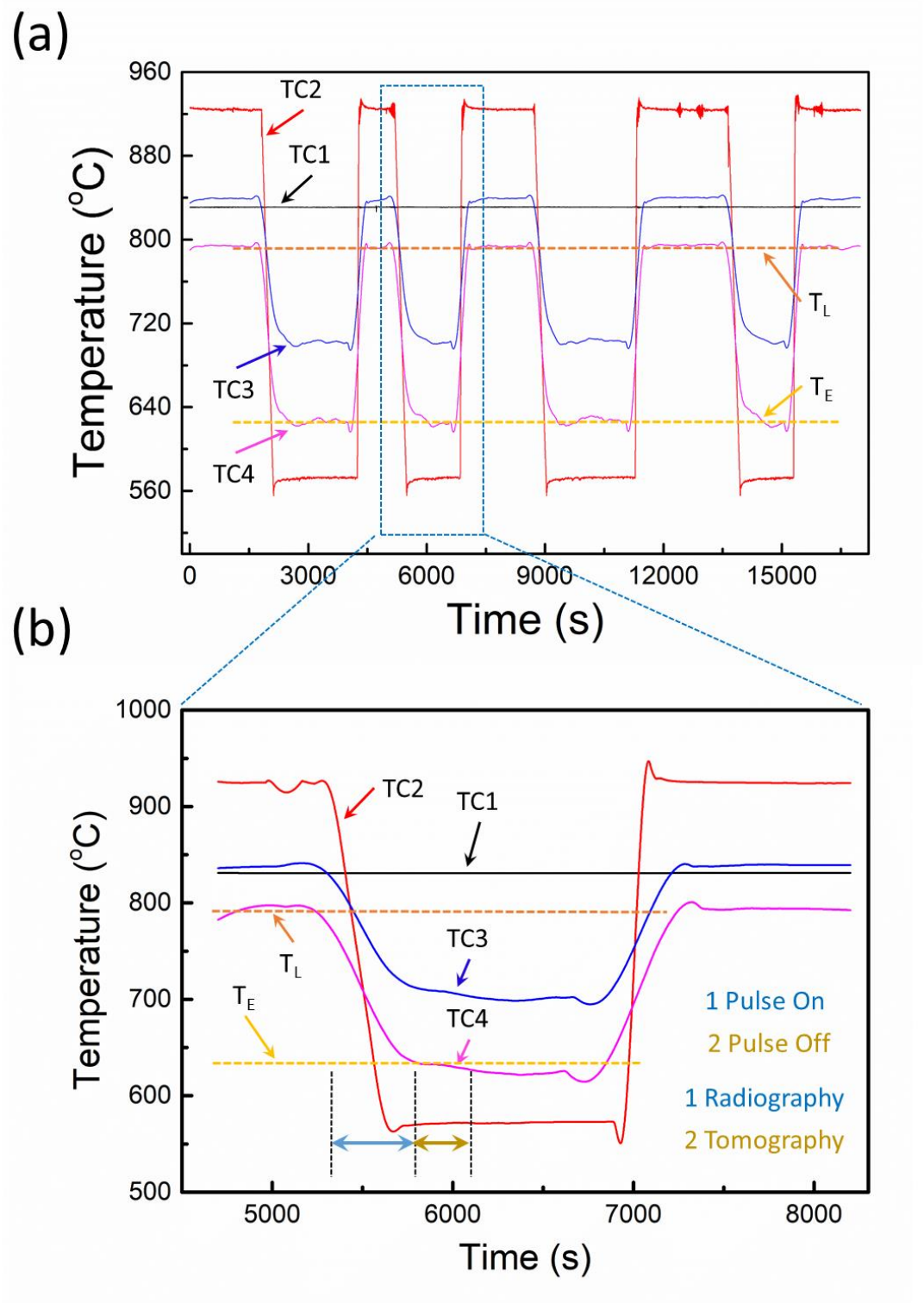

Figure 4.7 The control of the heating-cooling cycle of Al-15wt%Ni samples and the application of pulse electromagnetic field. Solidification experiments carried out with the cooling rates 1.44 K/s and temperature gradient (*G*) 30 K/mm.

4.3.3 Experiment at ID19 of ESRF

I proposed to study the Fe–based intermetallic phases evolution under the PMF to observe how the pulse affect the growth of α–Fe and β–Fe intermetallic phase.

Figure 4.1c reveals the different resolved phases with solidification advances (1) in range of 652 ─ 635 ^{o}C are: L + $Al_{13}Fe_4$; (2) then in range of 635 ─ 596 ^{o}C are L + $Al_{13}Fe_4$ + FCC_A1; (3) then in range of 596 ─ 573 ^{o}C are L + $Al_{13}Fe_4$ + FCC_A1 + Al_8Fe_2Si; (4) then in range of 573 ─ 526 ^{o}C are L + Al_8Fe_2Si + $Al_9Fe_2Si_2$ + FCC_A1; (5) then in range of 526 ─ 521 ^{o}C are L + $Al_9Fe_2Si_2$ + Al_2Cu + FCC_A1. Note: the A1 in Al-based alloy is FCC (ordered) aluminium from guide.

Based on the literature review and EDS analysis in Figure 4.4, Al_8Fe_2Si is α – Fe intermetallic phase and it demonstrated Chinese-script like phase. While the $Al_9Fe_2Si_2$, resolved after α-Fe intermetallic phase, is β-Fe intermetallic phase and a plant-like or needle-like phase is used to find in this alloy. The $Al_{13}Fe_4$ can occur only under equilibrium conditions. However, it suggests that for Al-5Cu-1.5Fe-1Si alloy the thermodynamics of the Fe-rich intermetallic formation in quaternary Al-Cu-Fe-Si systems are nearly identical to those in the ternary Al-Fe-Si alloys since the low Cu concentration (< 5.8 wt%Cu) [66].

The liquidus temperature of Al-5Cu-1.5Fe-1Si alloy is 652 °C shown in Table 4.1. Firstly, X-ray was used to examine the sample was fully melted. Secondly, before any tomography experiment a thermocouple was inserted into the melt. This

provides more information on temperature difference between furnace and sample. For example, when the top and bottom furnaces were initially heated to ~ 630 and ~ 560 °C, at this moment the sample temperature is 695 °C as shown in Figure 4.8a. Thirdly, I performed tomography experiment where the sample thermocouple was withdrawn, therefore the bottom furnace thermocouple reading was used as an indicator for the sample temperature reading. The time of 580 s was used for the bottom furnace during the 560 °C setting to 320 °C setting, after that the 300 s was used to decrease the top furnace setting from 630 °C to 490 °C as shown in Figure 4.8b.

The input voltage was 50 percentage of DC voltage (120 V) with the corresponding magnetic flux density of 0.2 T (the peak value) was immediately applied when the temperature of top furnace began to decrease. PMFs were applied into the melt continuously at a frequency of 1 Hz during solidification until around 40 tomograms are obtained (camera is out of space). The cooling rates is 0.4 K/s and temperature gradient (G) is 18 K/mm.

The same sample with the same heating-cooling path was tomography scanned repeatedly during directional solidification with 80 percentage of DC voltage (192 V). For ultrasonic melt processing, the 100 W ultrasound is triggered the melt for 7 seconds at sample temperature 635 °C. The ultrasound probe tip is 7 mm above the thermocouple measuring point.

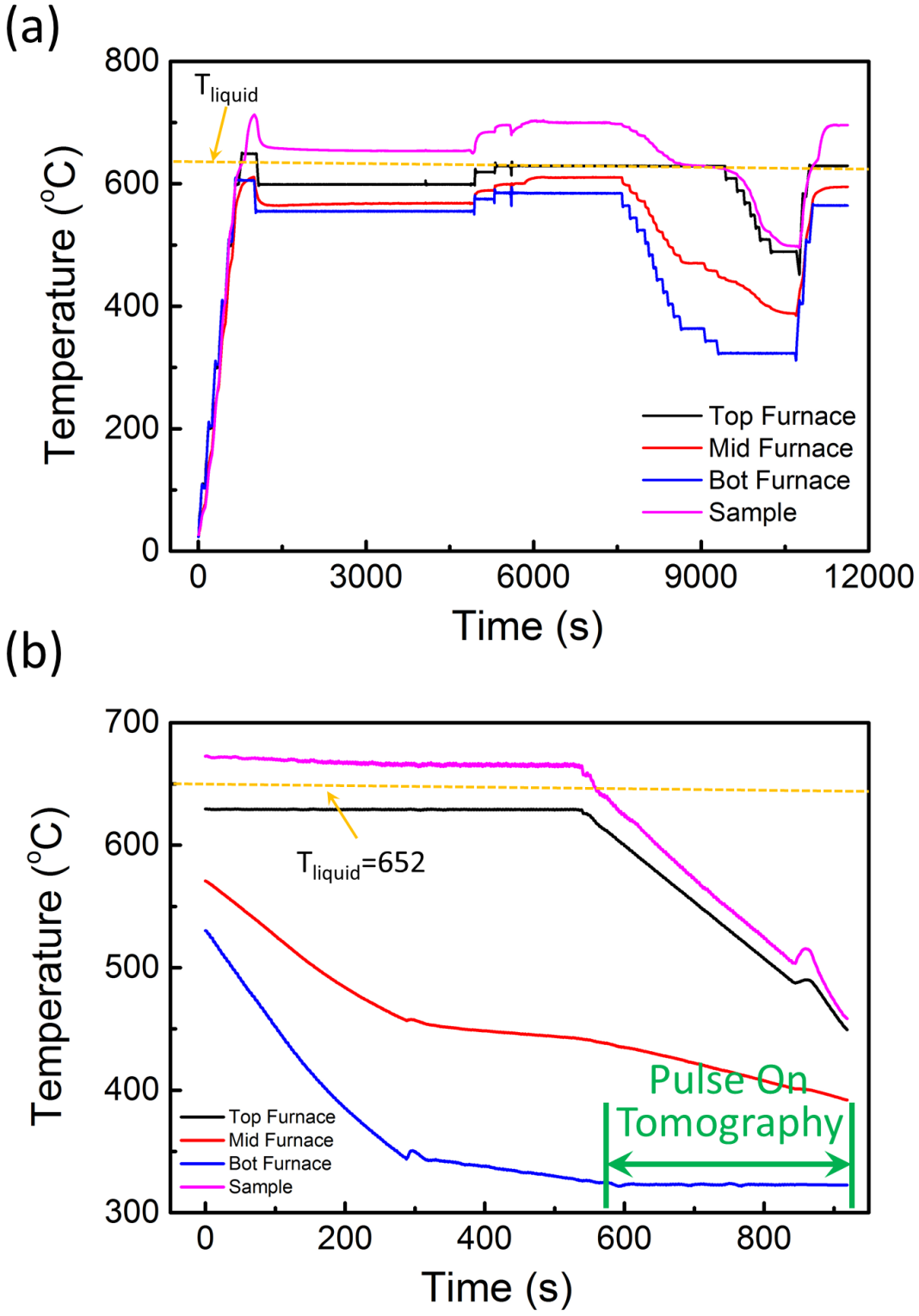

Figure 4.8 The control of the heating-cooling cycle of Al-5Cu-1.5Fe-1Si alloy samples and when the pulse electromagnetic field is introduced and when the tomography is taken. The cooling rates is 0.4 K/s and temperature gradient (G) is 18 K/mm.

4.4 Imaging processing

4.4.1 Noise reduction via filtering

Noise reduction is crucial for the final imaging visualization and accuracy of quantification. One of enhancements is image filtering. Filtering techniques are often useful to extract desired information from input data or simply to improve the appearance of the input data.

The common problem of filtering is to estimate a signal mixed with noise. Hence, a solution is the moving average, where the value of each pixel is replaced by the average of its neighbours as shown in Figure 4.9. The filtered output can then be viewed as the main trend of the function.

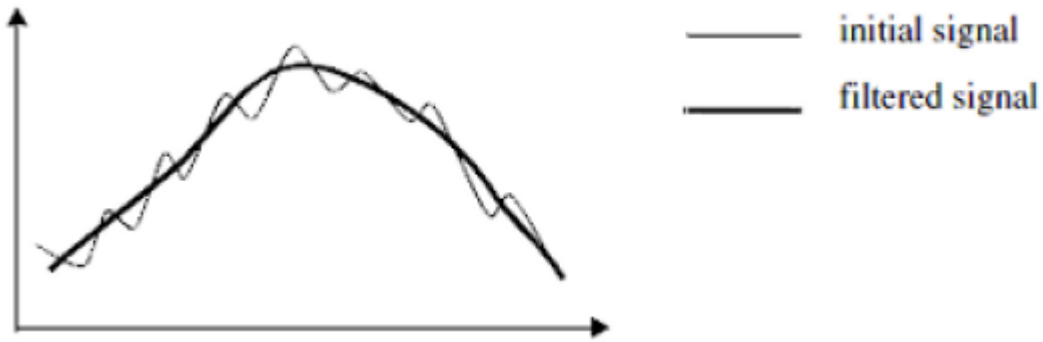

Figure 4.9 A moving average is used to estimate a signal mixed with noise.

The commonly used filter is the median filter which address each pixels, but median operator requires an ordering of the values in the pixel neighbourhood at every pixel location (significantly increase the computational resources).

It is replaced by the statistical median of its *N* x *M* neighbourhood. The median *m* of a set of numbers is that number for which half of the numbers are less than *m*

and half are greater; it is the midpoint of the sorted distribution of values. As the median is a pixel value drawn from the pixel neighbourhood itself, it is more robust to outliers and does not create a new unrealistic pixel value. To explain this, an example is demonstrated:

$$\begin{matrix} 12 & 17 & 15 \\ 20 & 14 & 16 \\ 18 & 19 & 14 \end{matrix} \rightarrow \begin{matrix} 12 & 17 & 15 \\ 20 & 16 & 16 \\ 18 & 19 & 14 \end{matrix}$$

The grey level values will be 12, 14, 14, 15, 16, 17, 18, 19 and 20. The median value is 16, therefore it will be the value of the out pixel at the middle of 3 × 3 kernel array.

This helps in preventing edge blurring and loss of image detail. The median filter is superior to the mean filter because it preserve sharp high-frequency detail (i.e. edges) whilst also eliminating noise, especially isolated noise spikes (such as 'salt and pepper' noise) [79].

The Gaussian filter is a very important one both for theoretical and practical reasons. The image is filtered using a discrete kernel derived from a radially symmetric form of the continuous 2-D Gaussian function defined as follow: $f(x,y) = \frac{1}{2\pi\sigma^2}\exp(-\frac{x^2+y^2}{2\sigma^2})$. Discrete approximations to this continuous function are specified using two free parameters: (1) the desired size of the kernel (as an *N* x *M* filter mask). Hence, *x* is the distance from the origin in the horizontal axis, *y* is the distance from the origin in the vertical axis; (2) the value of σ, the standard deviation of the Gaussian function.

As is always the case with linear convolution filters, there is a trade-off between the accurate sampling of the function and the computational time required to

implement it. First, the degree of smoothing is controlled by the choice of the standard deviation parameter s, not by the absolute value of the kernel size (which is the case with the mean filter). Second, the Gaussian function has a rather special property, namely that its Fourier transform is also a Gaussian function, which makes it very convenient for the frequency-domain analysis of filters [79]. Applying the Gaussian filter has the effect of smoothing the image. The smoothing use lowpass filters to reduce the contrast and soften the edges of objects in an image. A lowpass filter lets low frequencies go through but attenuates high frequencies and noise. It reduces contrast but tends also to defocus the image [79].

The anisotropic diffusion filter is used for denoising scalar volume data. It works effectively to preserve strong edges and enhance the contrast of edges.
In order to determine the new value for the current voxel, the algorithm compares the value of the current voxel with the value of its 6 neighbours. If the difference doesn't exceed the diffusion stop criterion, there is diffusion [80].

4.4.2 Tomographic reconstruction

The procedure of tomographic acquisition and reconstruction is summarised in Figure 4.10. The application of X-ray tomography during in-situ experiments generates a series of two-dimensional X-ray projections (radiographs) taken at different illumination angles θ. This full set of acquired data is used as an input to digitally reconstruct the 3D structure of the specimen. Firstly, the projections are transformed into a set of sinograms which allow efficient reconstruction artefact

removal. A sinograms represent the absorption intensities as a function of rotation angles θ. Finally, by performing an identical procedure on the entire set of sinograms, a full reconstructed 3D volume of the specimen is obtained.

There are many algorithms available for tomography reconstruction, with the Fourier transform method (FTM) and the filtered back projection method (FBP) being widely used due to their high accuracy and amenability for fast implementation [81].

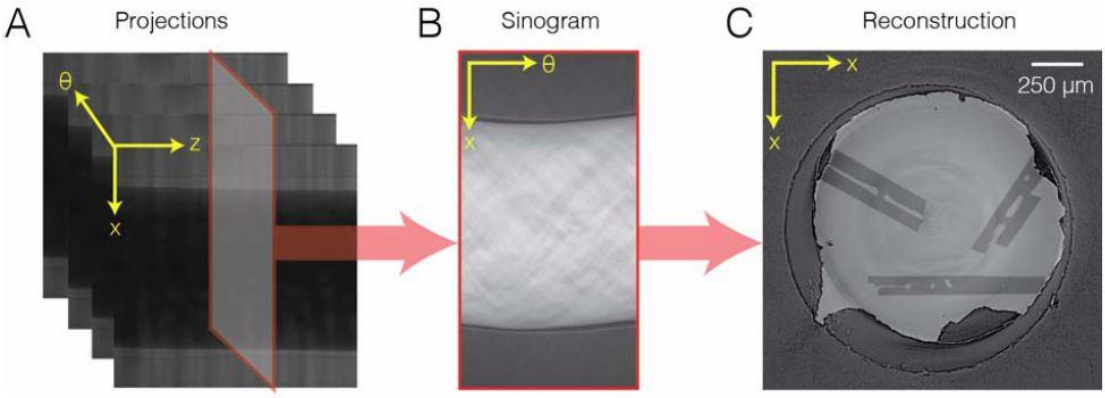

Figure 4.10 Schematic of the difference between (a) projections, (b) sinograms, and (c) reconstructions. Projections have the three dimensions (x, z, θ), while sinograms are (x, θ) slices of the dataset. To achieve the real space representation of the data, i.e., in moving from (b) to (c), one must solve the "inverse problem" of tomographic reconstruction [82].

The number of projections N_θ to collect per sample rotation (evenly spaced between 0◦ and 180◦) are determined the quality of reconstruction. When "fast" or "ultrafast" tomography experiments are performed, fewer projections has to be used in order to achieve fast data acquisition speed. The influence of N_θ on the quality of the FBP reconstruction. In Figure 4.11, with an increasing number of

projections, the microstructures become clearer and the artefacts are reduced. Thus, there is a compromise between speed of acquisition and spatial resolution requirements [83].

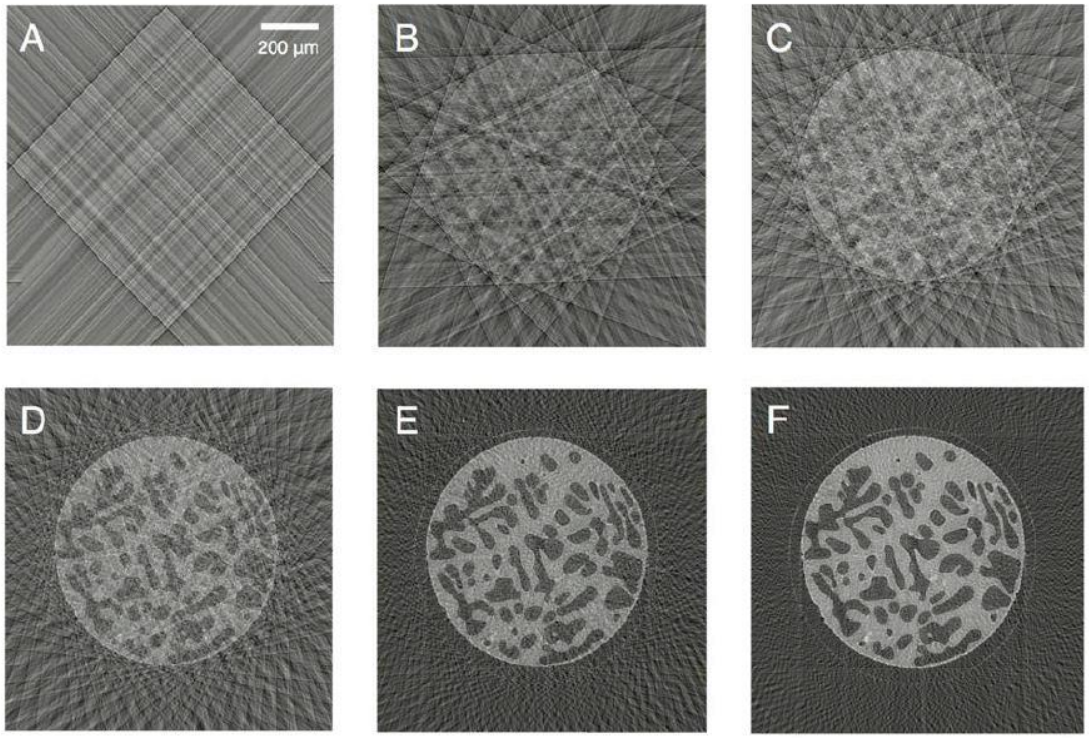

Figure 4.11 The effect of increasing the number of projections used in the reconstruction of a 512 × 512 domain: (a) 4, (b) 8, (c) 16, (d) 32, (e) 64, and (f) 90 projections. The microstructure becomes clearer and the artefacts are reduced with increasing number of projections [83].

4.5 Visualization by high performance computer (HPC)

A high-performance computer (Viper) housed at University of Hull provides me the best experience in terms of visualization. The very recently established supercomputer, Viper (5500 CPU cores) housed at University of Hull, including

two visualisation nodes (Nvidia GTX 980TI graphic visual cards) and four GPU nodes (Nvidia Tesla K40m) were used for processing the huge amount of 3D and 4D datasets. These computing and visualisation capability allowed us to directly process the 16bit datasets and reveal the high-fidelity solidification microstructures without any further cropping and binning.

I list the comparison using different hardware to process image stacks from either synchrotron X-ray radiography or tomography as shown in Table 4.5. Basically, the rendering of loads of tomography datasets depends on graphics cards performance. Avizo®, one of most popular software to analyse tomogram, could run on any graphics system (this includes GPU and its driver) that provides a complete implementation of OpenGL 2.1 or higher.

Users always need much more memory than the actual size of the data to load within Avizo®. Some processing may require several times the memory required by the original data set. For instance, a 4 GB dataset in memory and apply a non-local means filter to the original data and then compute a distance map, users may need up to 16 or 20 GB of additional memory for the intermediate results of processing. Commonly users will need 2 or 3 times the memory footprint of the data being processed for basic operations. For more complex workflows it may need up to 6 or 8 times amount of memory, so 32 GB may be required for a 4 GB dataset.

Table 4.5 The comparison of key specifications between the commercial PC and Viper.

	Commercial PC	**Workstation e.g. Dell T7610**	**Workstation e.g. Alienware**	**HPC e.g. Viper**
Graphics card	HD Graphics	Nvidia Quadro® K600	Nvidia GeForce®	Nvidia GTX 980TI
GPU	N/A	NVIDIA Tesla® K20C	Nvidia GeForce® GTX 1080 with 8GB	Nvidia Tesla® K40m with 12 GB
Image type	Only 8-bit	8-bit or cropped 16-bit	8-bit or cropped 16-bit	16-bit or 32-bit if needed
Import size	10 – 50 Mb	100 – 600 Mb	100 – 300 Mb	2 – 4 Gb
RAM	4 – 8 Gb	80 Gb	16 Gb	128 Gb

Also, hard drives are important, a standard hard drive (HDD) (e.g., 7200rpm SATA disk) can only stream data to your application at a sustained rate of about 40 MB/second. When users want to read a 1 GB file from the disk, you will likely have to wait 25 s. For a 10 GB file, the wait is 250 seconds, over 4 minutes.

The GPU memory needed depends on size of data, many modules are computationally intensive and their performance will be strongly affected by CPU performance. Some of the image processing algorithms rely on CUDA for computation, therefore high-end graphic cards are needed. Overall, fast CPU clock, number of cores, and memory cache are the three most important factors affecting Avizo® performance.

Generally, there are three high-end graphic cards series produced by Nvidia. One GTX 10 series is for gaming experience and the other two series (Quadro® or Tesla®) are both for design and professional applications. All provide powerful GPUs, large memory capacities, multiple 5K display outputs, advanced features etc. Particularly, Tesla series is dedicated for HPC. For instance, Nvidia Tesla® V100 is the world's most advanced data centre GPU ever built to accelerate AI, HPC, and graphics.

Chapter 5: **The formation of Al_3Ni intermetallic phase**

In this chapter, I present a systematic real-time synchrotron X-ray imaging and tomography study of the dynamic evolution of primary Al_3Ni intermetallic phases in an Al-15%wtNi alloy solidified under pulse electromagnetic fields.

The correlation between the Al_3Ni phase orientation, growth, fragmentation, 3D morphology and the applied pulse fields was analysed and quantified.

For the first time, I present clear and unambiguous real-time experimental evidence and theoretical calculation to elucidate how Al_3Ni phase fragmentation was caused by the shear stresses produced by the different pinch pressure acting on the melt and the phases during solidification. Such mechanism can be well exploited for enhancing grain refinement in alloy systems that contain intermetallic phases.

The 3D structures and morphologies of the Al_3Ni phases formed with different magnetic pulse peak fluxes were analysed and quantified using skeletonization function and reported for the first time as well.

5.1 Digital image and tomography data processing

5.1.1 Radiography

All radiography images were processed using the open source image processing software ImageJ [84], and Figure 5.1 shows the workflow. Firstly, all 32-bit datasets were transformed into 16-bit in order to reduce their size. Then a 3D median filter (radius = 1) was applied to these images to reduce noise. Secondly, all images were normalized, and a typical case is shown in Figure 5.1c. The normalized images (Figure 5.1c) were subtracted by an averaged image obtained from the fully liquid state (Figure 5.1b, the averaged first 100 images from the same dataset before any Al_3Ni phases appeared in the field of view). The normalization is made by using the following procedure with the purpose of removing any fixed-pattern noise:

$$\boldsymbol{Normalised\ image} = \frac{\boldsymbol{Raw\ image - Dark\ field}}{\boldsymbol{Flat\ field - Dark\ field}} \quad (5.1)$$

The final image is shown in Figure 5.1d. The projection images without sample are obtained with and without the X-ray beam switched on, which are referred to as flat fields and dark fields.

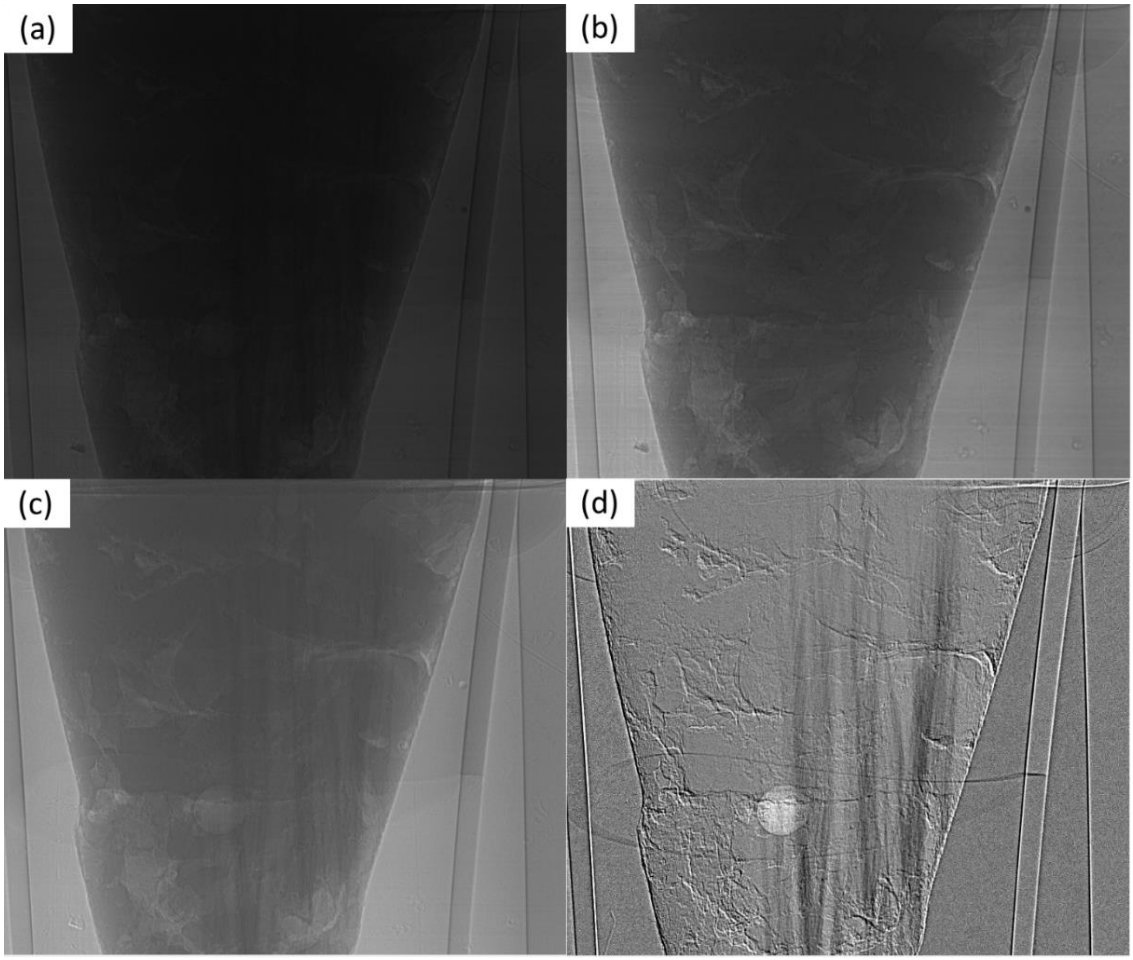

Figure 5.1 The imaging processing procedure: (a) a typical raw image; (b) the averaged frame obtained from the first 100 images when the alloy was in a fully liquid state; (c) a normalized image; (d) the final images by subtracting (b) from (c). Note: the projection images without sample are obtained with and without the X-ray beam switched on, which are referred to as flat fields and dark fields.

5.1.2 Tomography

Tomographic reconstruction was performed at DLS using the in-house software DAWN [85, 86]; the software incorporated flat- and dark-field correction, ring artefact suppression and filtered back projection. 3D data visualisation and segmentation were carried out using Avizo® 9.2 (VSG, France). The 3D median

filter with 1-pixel radius was used to reduce the noise of those images prior to visualization. The threshold for segmentation was carefully selected with all phases labelled. Constrained smoothing of the surface was also applied, and only objects larger than 36 voxels were included in measurements.

5.2 Three–dimensional skeleton analysis

The skeleton module in Avizo [87] is a powerful tool for extracting the centreline of complex structures from segmented images as well as grey value images. Figure 5.2 demonstrates a typical case of how to simultaneously “peel off” the Al_3Ni phases and use simple line sections to represent real phases for further quantification. A sub-volume of 400 × 100 × 500 voxels was selected from the 1.5 T tomogram dataset (Figure 5.7d1). Because the structures of 1.5 T are much more complicated than any other cases. The Al_3Ni is brighter compared to the matrix (a typical slice is showed in Figure 5.2d), and therefore the “bright on dark” approach was used.

Figure 5.2a shows the skeletons of Al_3Ni phases with estimated local thickness after application of auto skeleton module (both smooth coefficient and smooth iterations were tuned with the aim of removing noise signals). Almost all thicker skeletons (red and yellow lines) perfectly fitted the true Al_3Ni phases. However, after many attempts of optimisation, it is still difficult to eliminate the noisy skeletons (light and dark blue lines) and trace the true phases as shown in Figure 5.2b.

Hence, another semi-automatic method is used to increase the fidelity of tracking the true phases. The cylinder correlation module [87] in Avizo (XFiber Extension)

was used to detect the straight, curved, hollow cylinder fibres or tree-like structures. This procedure is time consuming for the big synchrotron X-ray tomography datasets. It depends on the graphic card (need CUDA computing). For example, on a GeForce 8800 GT with 1GB video memory the computing of an image of size 2000 x 2000 x 200 takes approximately 20 h. A crop of the initial input data for preliminary testing is often needed.

Generally, the work is a combination of creating a cylinder template first and then tracing the cylinder down to its centreline. It was often determined by giving an initial value first and then refined the value thorough several rounds of iterations. The minimum seed correlation and minimum continuation quality govern the possible seed and when the line tracing stop. Seeds value need to be large enough to make sure the relevant seeds are selected. Also, a larger value of min continuation quality will favour earlier termination of lines. Another data-specific parameter is the direction coefficient. Basically, if the target structures are more or less straight, a smaller value would be suitable. The minimum length is used to filter the shorter lines, and this is a threshold value to eliminate the noise length. In this work, I carefully measured the radius and length of the typical Al_3Ni phases in the chosen volume, and then created a unique template for that volume for the analyses. A longer cylinder template is more tolerant to noise, but more suitable for straight line structures rather than curved structures. Hence, a reasonable compromise is needed during the skeleton analyses, for example, more artefacts occurred at a region near a boundary. In our case, the outer cylinder radius and cylinder length were set at 20 μm and 300 μm for the chosen sub-volume, respectively, and the angular sampling was set at 10. After computing the

template, which included the correlation field and the orientation field, the trace correlation line module was implemented to track the centrelines of Al_3Ni phases. The main parameters used in this paper are summarized in Table 5.1.

Table 5.1 The parameters used for tracing Al_3Ni phases

Parameters	Values
Minimum Seed Correlation	117
Minimum Continuation Quality	70
Direction Coefficient	0.2
Minimum Length	100

Figure 5.2c shows the result of the traced correlation lines for the Al_3Ni phases (rendered in transparency). In order to validate the accuracy of the tracing algorithms, in Figure 5.2d, a slice of the raw tomogram data is presented together with the skeletons of the Al_3Ni phases tracked. Clearly, it shows that the characteristics of the straight or dendritic Al_3Ni phases were accurately tracked and well represented.

Building upon this 1.5 T case, such tracing method was applied to all other cases (0, 0.85 and 1.2 T). The Al_3Ni phases and their morphologies in those cases are similar or simpler as shown in Figure 5.7a3–d3. Hence, the template worked well for those cases. Based on the skeleton analyses, the statistical data for the length and orientation angle of each phase can be extracted and analysed, providing very rich information for quantifying the complex 3D structures.

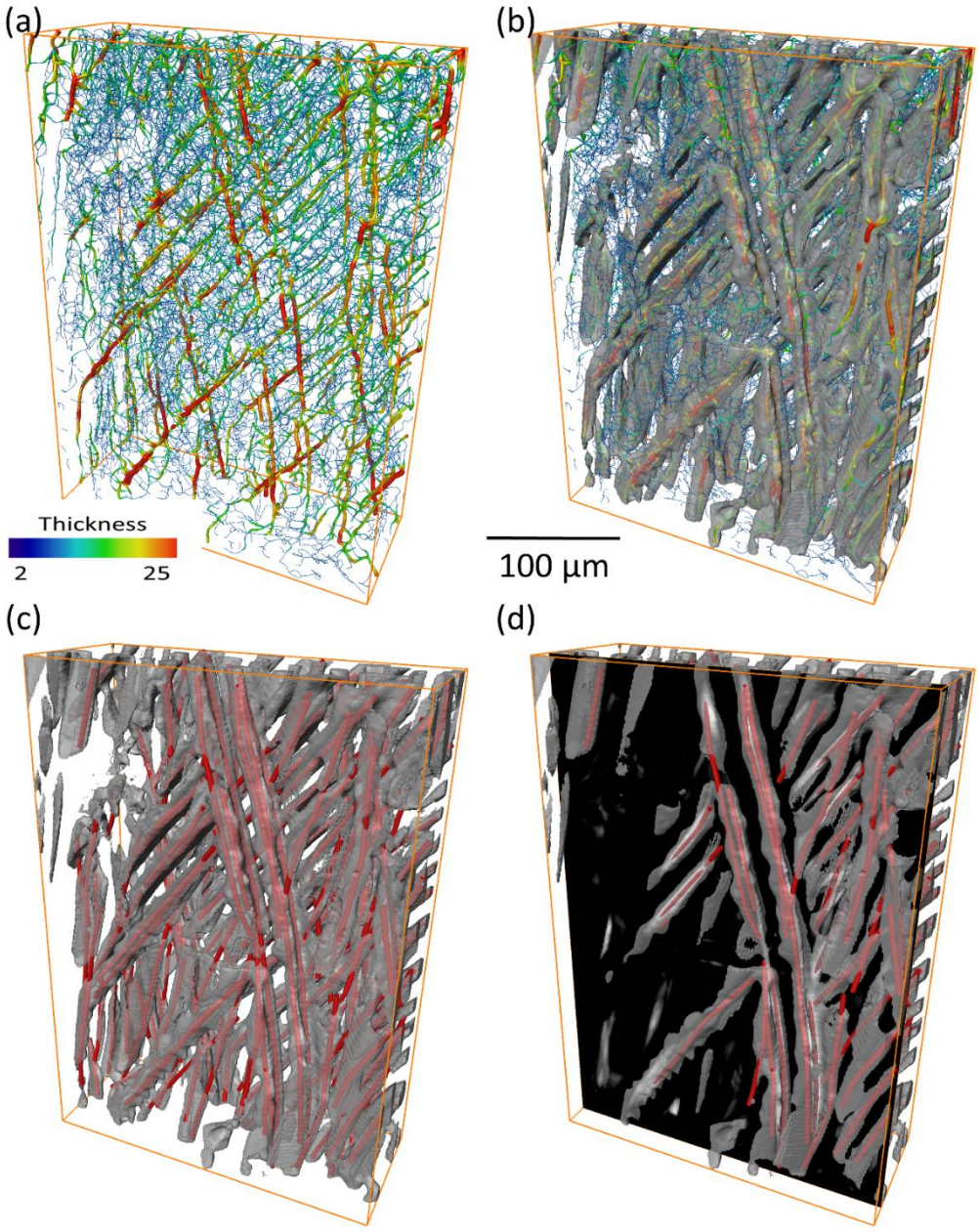

Figure 5.2 (a) The auto traced skeletons, showing the Al_3Ni thickness for the 1.5 T case; (b) the Al_3Ni phase is rendered as transparent with its skeleton inside, indicating the noise signal that may affect the true morphologies; (c) The same transparent Al_3Ni phases as showed in (b) with the noise masked out, and the shorter length phases removed. In addition, cylinder fibres were used to represent the phases, showing clearly the characteristics of the dendritic structures; (d) a typical slice taken from the auto skeleton process, showing the "bright on dark" approach used for tracking the Al_3Ni phases.

5.3 Phase growth, orientation and fragmentation revealed by radiography

5.3.1 Phase growth and orientation

Figure 5.3 shows the typical image sequences extracted from four X-ray image videos, revealing the growth of the primary Al_3Ni phases during solidification under four different magnetic flux densities (0, 0.85, 1.2 and 1.5 T, readers are highly recommended to view the accompany video for each case, i.e. Video 1, Video 2, Video 3 and Video 4). In the four images (Figure 5.3a1–d1) in the first row, Al3Ni phases (the solid black phases) were seen to appear in the liquid matrix. Subsequent images showed that the Al_3Ni phases exhibited different morphologies and different orientations when the pulses of different peak values were applied. In the case of 0 T (Video 1), Figure 5.3(a1–a4) show that an Al_3Ni phase of 500 μm length appeared at t =0 s. It floated freely in the liquid and rotated ~60° clockwise in 0.3 s and then went downwards to the location shown in Figure 5.3a2 (also see more clearly in the zoom-in enlarged Video 5). This is of course due to the difference in densities between the Al_3Ni phase ($\rho_{Al3Ni} = 3.817\ g/cm^3$) and the liquid melt ($\rho_{melt} = 3.014\ g/cm^3$). After 16 s in Figure 5.3a4, many more Al3Ni phases with almost random orientations were seen to appear in the field of view. One particular Al_3Ni phase marked by the black frame in Figure 5.3a5 was observed to grow from 7 to 120 μm until it met its neighbour. It slightly changed its direction of growth from Figure 5.3a5–a6. After a sufficient number of Al_3Ni phases appeared, growth and coarsening continued as clearly demonstrated in Figure 5.3a5–6.

In the cases of pulse peak values of 0.85 T (Video 2) and 1.2 T (Video 3), the Al3Ni phases appeared firstly at the bottom of the view field (Figure 5.3b1 and Figure 5.3c1). The majority of the subsequently nucleated Al_3Ni phases grew in the directions pointed out by white arrows in Figure 5.3b3 and Figure 5.3c3.
At the later stage of growth (Figure 5.3b5–6 and Figure 5.3c5–6), a number of the Al_3Ni phases were seen to grow branches, or to cross over or intercept each other. Such overlapping nature of the 2D projection images make it very difficult to resolve the true 3D characteristics of the phases, and it is absolutely necessary to use tomography to resolve such matters as discussed later.

In the 1.5 T case (Video 4), the first few Al_3Ni phases were seen on the right-hand side (Figure 5.3d1), aligning vertically and in parallel with the magnetic flux direction (the white arrow in Figure 5.3d3). Subsequently, more Al_3Ni phases appeared from the right to the left in the view field as shown in Figure 5.3d2-6 and maintained their vertical growth direction.

Those image sets can be summarized in a schematic of phase orientation as shown in Figure 5.4. The direction of solidification and magnetic field is along with the Z-axis, and each coloured bar represents a single phase under various magnetic fields. The rotation angle ($\boldsymbol{\theta}$) where the between the central line of one phase in the length direction and the horizontal direction (X-axis). The rotation angle is likely to increase and shift from low angle to high angle (purple arrow shows the direction) when the magnetic flux intensity goes up. The quantitative

information is systematically studied (four cases are shown in Figure 5.10a1-d1) and strength my experimental observation at Chapter 5.4.2.

Generally, two scenarios were often observed for the growth of the Al_3Ni phases. At the early stage, the Al_3Ni phases (for example, those labelled 1 to 8 in Figure 5.3) grew freely in the liquid matrix and a single phase could grow up to 2 mm long under PMF. At the later stage and when the number of Al_3Ni phases increased to a certain value, their growths were often affected by impingement with the neighbouring phases. Then the growth either stopped or changed direction.

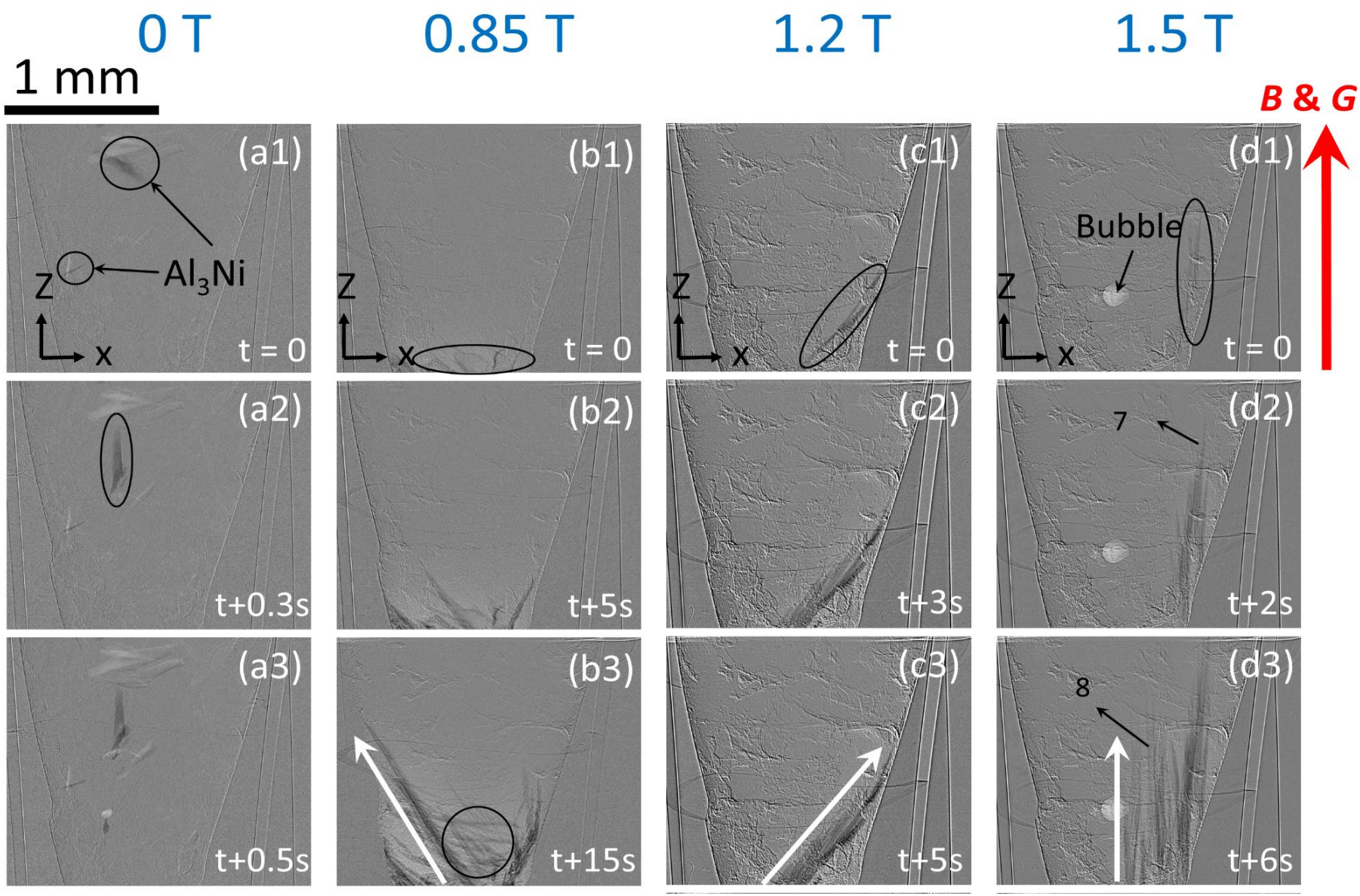
0 T
0.85 T
1.2 T
1.5 T
1 mm
B & G
(a1)
(b1)
(c1)
(d1)
Bubble
Al_3Ni
Z
x
t = 0
(a2)
(b2)
(c2)
(d2)
7
t+0.3s
t+5s
t+3s
t+2s
(a3)
(b3)
(c3)
(d3)
8
t+0.5s
t+15s
t+5s
t+6s

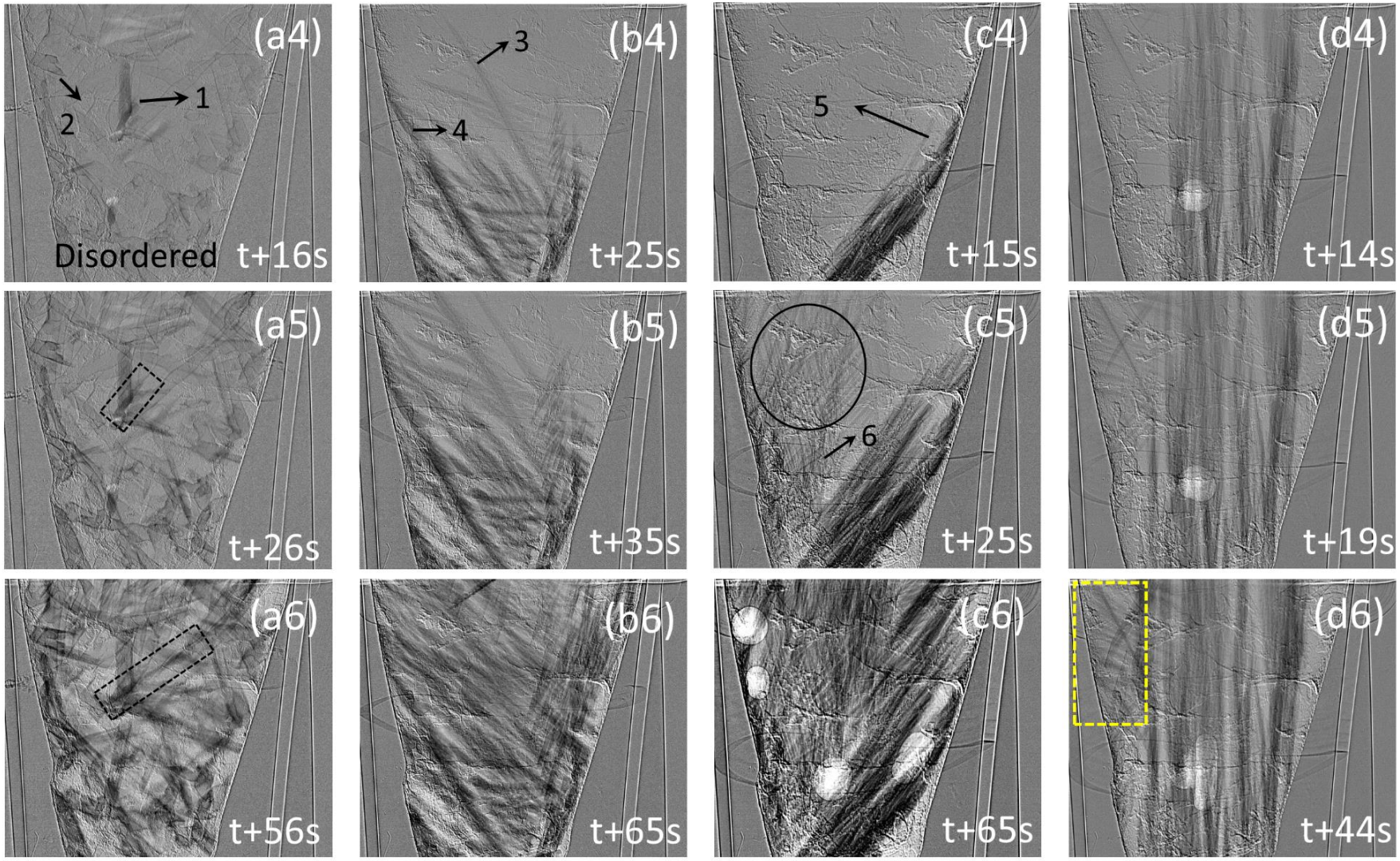
(a4)
2
1
Disordered t+16s
(b4)
3
4
t+25s
(c4)
5
t+15s
(d4)
t+14s
(a5)
t+26s
(b5)
t+35s
(c5)
6
t+25s
(d5)
t+19s
(a6)
t+56s
(b6)
t+65s
(c6)
t+65s
(d6)
t+44s

Figure 5.3 Four columns of Synchrotron X-ray radiographs, showing the growth dynamics of the primary Al_3Ni intermetallic phases of an Al–15%Ni alloy during the solidification of (a column) without magnetic pulse (0 T), and with magnetic pulse of the peak value of (b column) 0.85 T, (c column) 1.2 T and (d column) 1.5 T. For all cases, the measured average temperature gradient is G = 42.5 K/mm, the cooling rate is V = 0.35 °C/s, the pulse frequency is 1Hz.

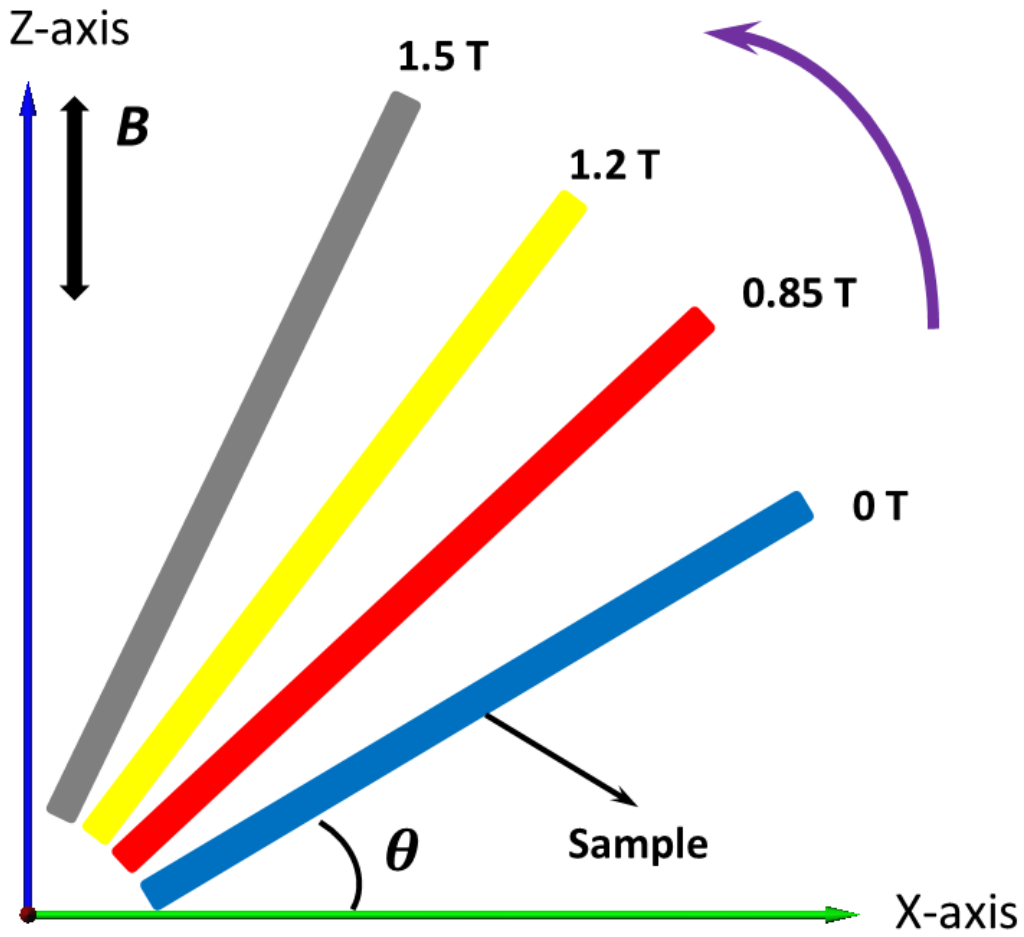

Figure 5.4 A schematic of phase orientation angles θ under various magnetic fields, showing the phase alignment mechanism.

To further quantify the growth dynamics of the Al_3Ni phases under different pulse conditions, the 8 labelled Al_3Ni phases (those have sufficient time to undergo free growth, and only impinge other phases at the later solidification stage) in Figure 5.3 were measured for their growing lengths ΔL ($\Delta L = L(n) - L(0)$, the length of the phase at time, *n*, minus the initial length when it first appeared in the view field) and growth rates.

Figure 5.5a shows that, without pulse (0 T), their growing lengths were in the range of 304 - 494 μm, much shorter than those with pulses (in the range of 1049

- 1849 μm). The cooling rates and thermal gradients are identical for all cases as indicated by the temperature profiles in Figure 4.7a. It indicates that applying a PMF into the molten melt can increase the growing length of the Al_3Ni phases for 2-3 times under the condition of free growth (when the growth is not blocked by other phases or the tube walls).

Figure 5.5b shows that, at the early stage of phase growth (less than 10 s), the free growth rates of the Al_3Ni phases in the three cases with magnetic pulses were approximately 10 - 40 times higher than in that in the 0 T case. Hence, the PMF can greatly increase the free growth rates of the primary Al_3Ni intermetallic phases.

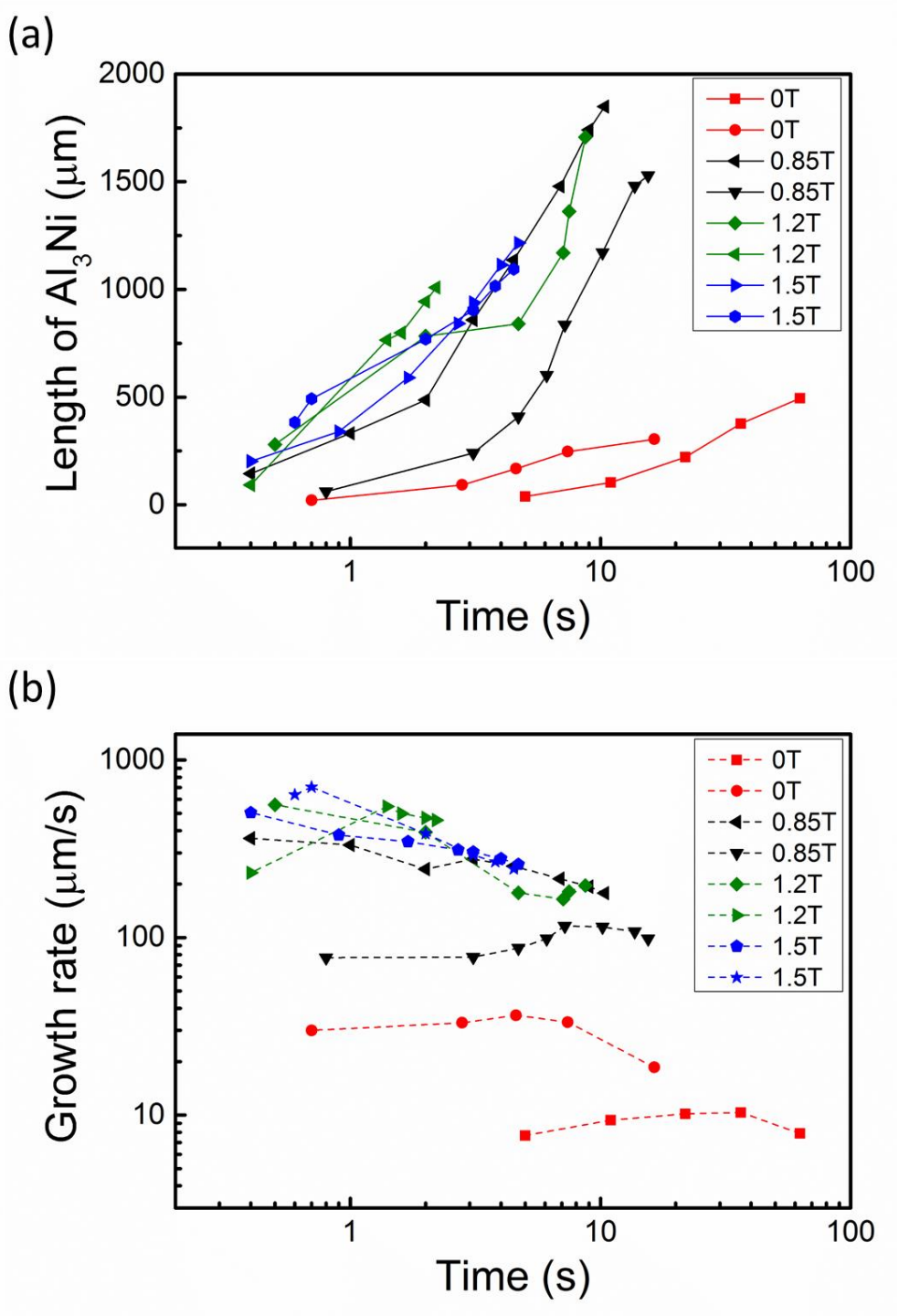

Figure 5.5 (a) The growing length of the primary Al_3Ni intermetallic phases at different solidification time; (b) growth rate of the primary Al_3Ni phases at different solidification time, without and with PMF. The measurements were made on the 8 phases labelled in Figure 5.3.

5.3.2 Phase fragmentation

Figure 5.6 (**readers are invited to view the video that is more instructive at Video 6**) show the extracted and enlarged frames from the bottom part of the 0.85T case (The circled area marked in Figure 5.3b3). Video 6 shows clearly and unambiguously the fragmentation of primary Al_3Ni phases and the raining down of the fragments under the action of the PMF of 0.85 T.

Figure 5.6a–b further highlights a few big fragments occurred in the inter-dendritic region between the bigger phases, and their subsequent downwards movement (due to the density difference) in a time scale of tens of seconds.

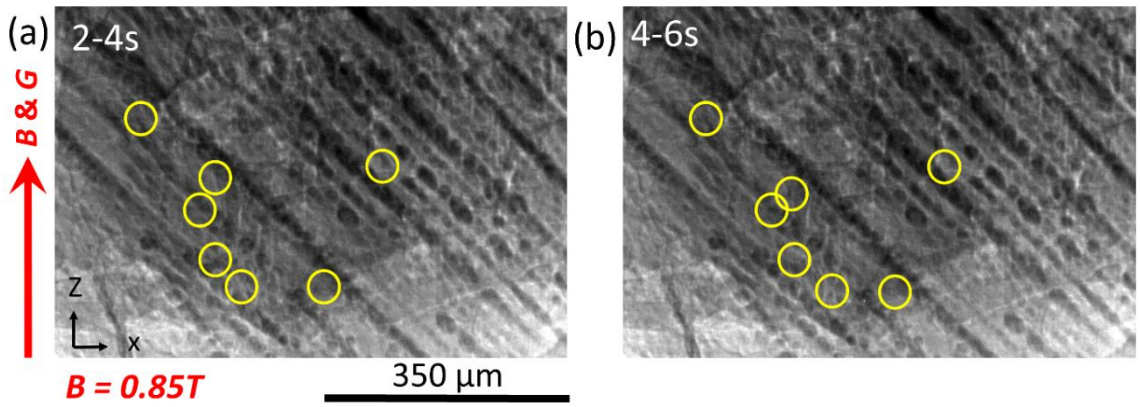

Figure 5.6 The images that are extracted from the middle–bottom region in Figure 5.3b, and then enlarged to show the typical fragmentation event (within the 2 s time frame) of Al_3Ni phases under PMF of 0.85 T and their movement. See video 6 for the very clear fragmentation events.

The fragmentation events were seen to occur clearly in the whole region of sample volume. Even at just a peak magnetic flux of 0.85T, the PMF appeared to be strong enough to fracture and detach the small phase particles off from the main branches. This is the first time that such real-time fragmentation of intermetallic phases was reported.

5.4 phase structure and morphology revealed by tomography

Although the radiography image videos provided rich dynamic information about the growth of the Al_3Ni phases, the overlapping nature of the 2D X-ray projection images makes it very difficult to distinguish individual phases and their 3D structure and morphology. Hence, at the end of each radiography acquisition, tomography was used to obtain the 3D information for the whole sample. The PMF was switched off during the tomography acquisition.

5.4.1 3D structure and morphology

Figure 5.7 shows the 3D renderings of the four cases (0, 0.85, 1.2 and 1.5 T). In the top row, Figure 5.7a1-d1 show the 3D structure and morphology of the Al_3Ni phases for the four cases. Different colors were used to render the Al_3Ni phases in each case with the liquid phases removed to highlight the Al_3Ni phases. The melt temperature during tomography scan was ~640 °C, slightly above the eutectic temperature, hence no eutectic phases were formed in this tomography scanned dataset.

The second row (Figure 5.7a2-d2) shows the same but transparent primary Al_3Ni phases from Figure 5.7a1-d1 with their skeletons; Figure 5.7a3-d3 show phases peeled down to only their skeletons, e.g. the central line of the tracked phases.
To reveal more clearly the 3D characteristics of the phases for the four cases, the typical phases in each case were manually selected and showed in Figure 5.7a4-

d4. Under 0 T, most of the primary Al_3Ni exhibit simple long block structure with flat surfaces (Figure 5.7a4, and more clearly seen in Video 1). Facet-type steps were often observed on the phase surfaces, indicating that facet-type growth with the planar surface is the main growth mechanism in the condition of no PMF. In the case of 0.85 T (Figure 5.7b4, and Video 2), more protrusions or irregularity was found in the phase surfaces, indicating the start of the transition away from facet growth towards dendrite growth. Such trend becomes more clearly in the case of 1.2 T (see Video 3) where a number of dendritically-structured phases were formed. At 1.5 T, the Al_3Ni phases grew into well-developed side branches (the secondary arms) as shown in Figure 5.7d4 and Video 4. In addition, the relatively shorter and rectangular-shaped blocky phases showed in the cases of 0 T and 0.85 T become elongated and relatively thin primary branches (arms) in the case of 1.2 T (Figure 5.7c4, d4, Video 3 and 4).

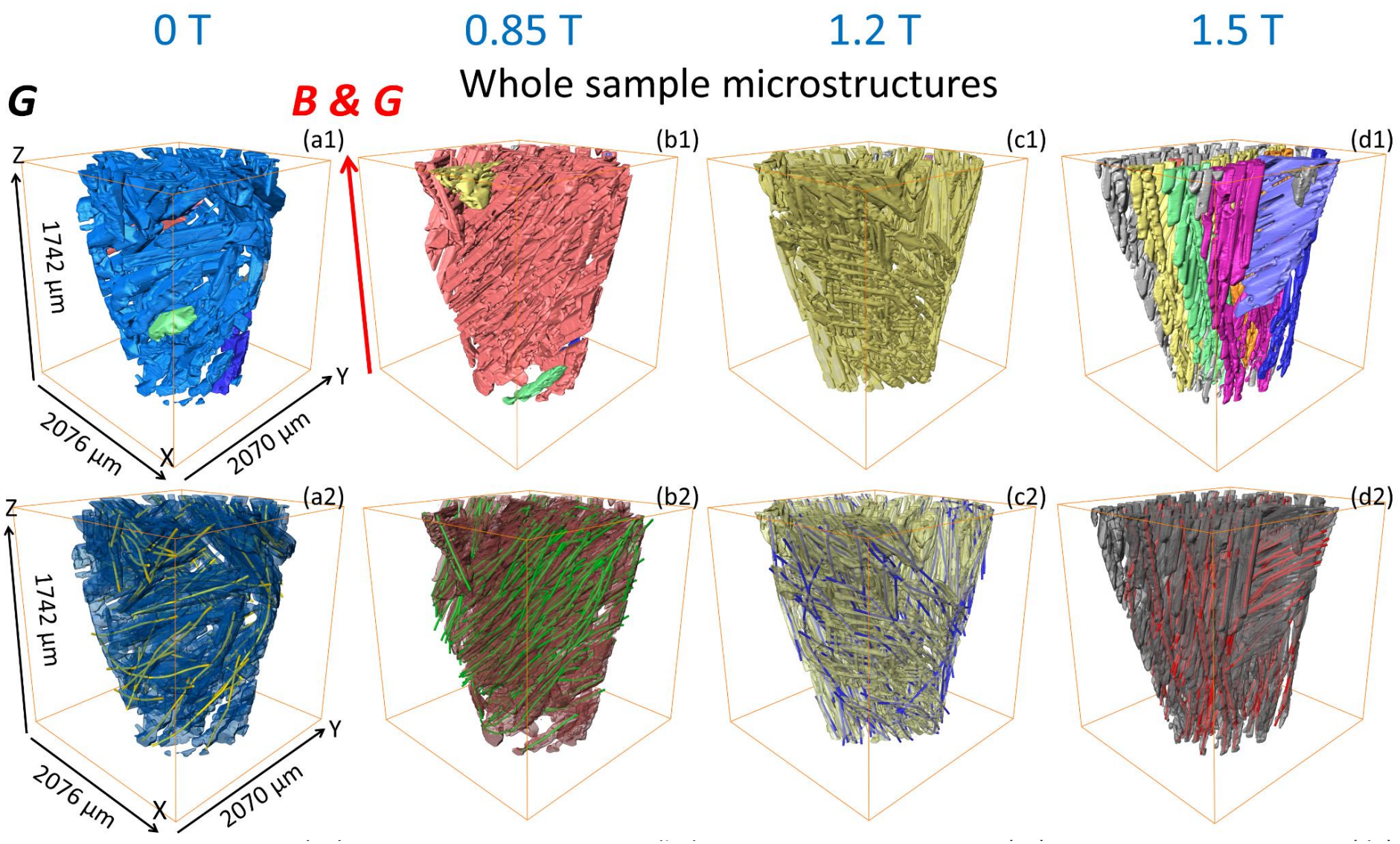
0 T
0.85 T
1.2 T
1.5 T
Whole sample microstructures
G
B & G
(a1)
(b1)
(c1)
(d1)
(a2)
(b2)
(c2)
(d2)
Z
Y
X
1742 µm
2076 µm
2070 µm

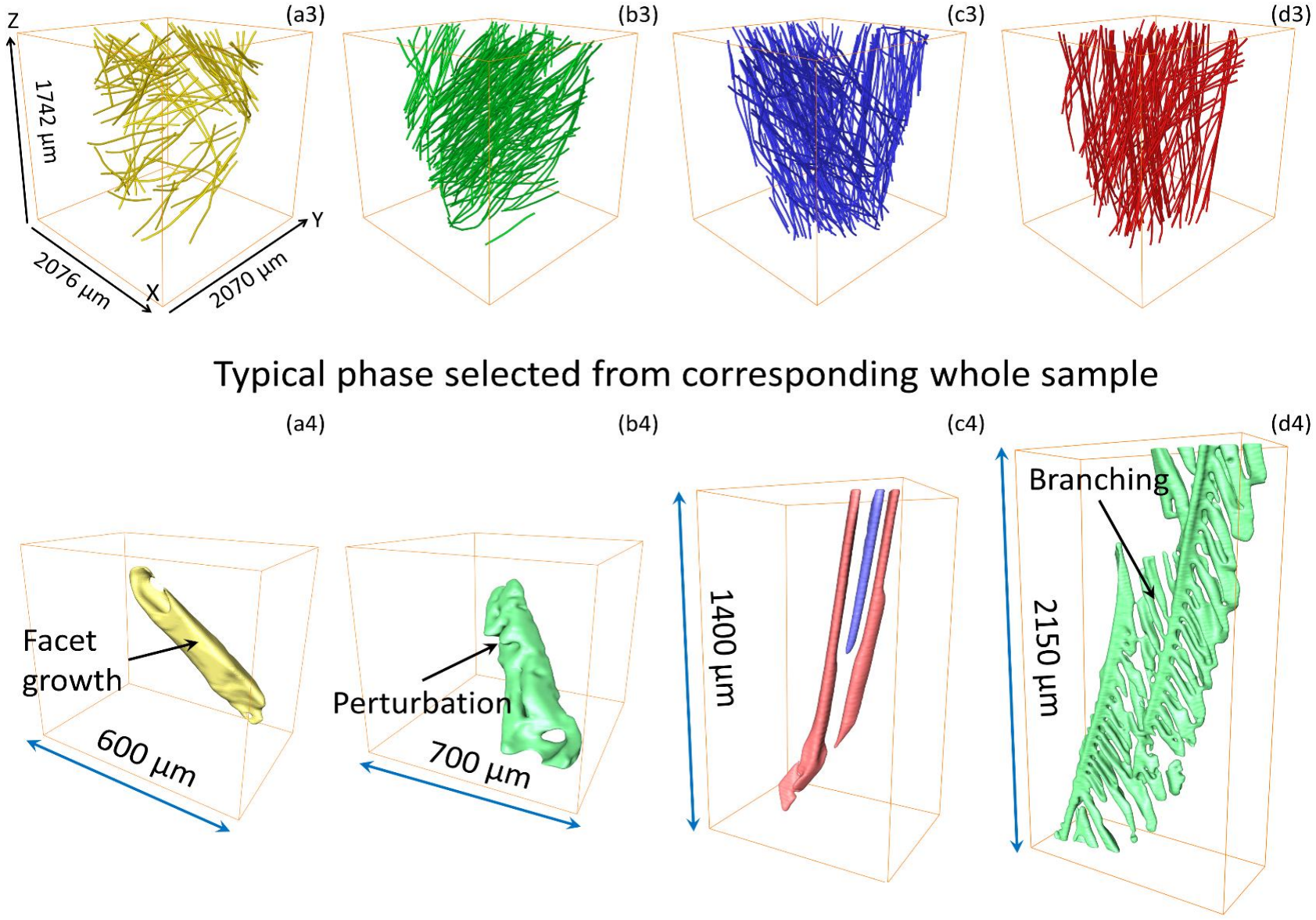
(a3)
(b3)
(c3)
(d3)
Z
1742 µm
Y
2076 µm
X
2070 µm
Typical phase selected from corresponding whole sample
(a4)
(b4)
(c4)
(d4)
Facet
growth
600 µm
Perturbation
700 µm
1400 µm
Branching
2150 µm

Figure 5.7 Four columns of tomography dataset renderings, (the liquid was removed for showing clearly the Al_3Ni phases), showing the 3D structure and morphology of the Al_3Ni phases of an Al–15%Ni alloy, corresponding to the four cases in Fig. 4, i.e. (a column) 0 T, (b column) 0.85 T, (c column) 1.2 T and (d column) 1.5 T. Skeletonisation analysis (details are described in supplemental materials) was also used to obtain the skeletons for the phases in each dataset. Typical Al_3Ni phases were also extracted and selected from the entire sample to show the transition from facet growth to dendritic growth as the pulse density increase.

In order to fully characterize the phase growth, the curvature has to be measured. A general surface can be described locally by a patch as shown in Figure 5.8. The curvature at surface point *p* at the center of the patch can be completely characterized by two principal radii of curvature, R_1 and R_2. Each radius corresponds to an imaginary circle that is tangent to the surface patch at *p*. These circles are perpendicular to each other and represent the maximum and minimum radii of curvatures for the patch. The inverse of the principal radii of curvature are the principal curvatures and are given by $k_1 = \frac{1}{R_1}$ and$k_2 = \frac{1}{R_2}$.

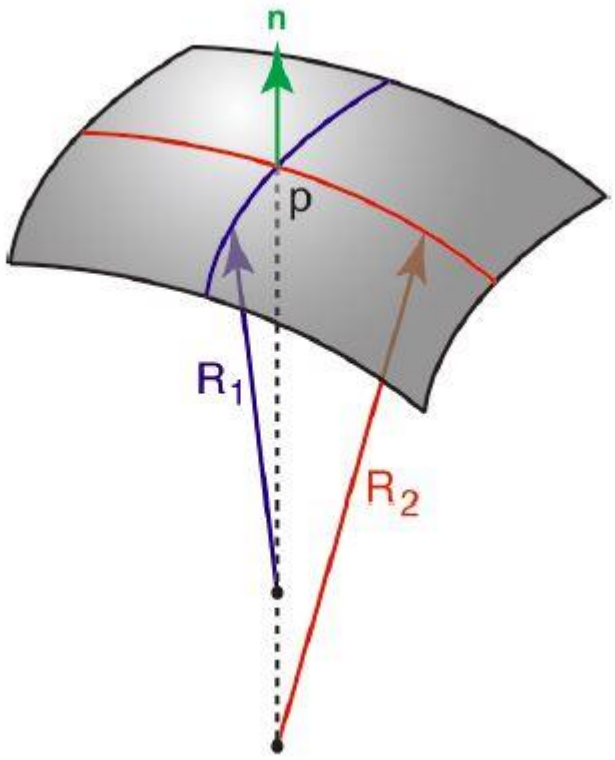

Figure 5.8 Surface patch with its corresponding radii of curvature, R1 and R2, at a point of interest p. n is a unit vector that is perpendicular to the patch at p.

Equivalently, two other parameters may be used to characterize the the mean curvature, H, and the Gaussian curvature, K can be written as $H = \frac{1}{2}\left(\frac{1}{R_1} + \frac{1}{R_2}\right)$ and $K = \left(\frac{1}{R_1} \times \frac{1}{R_2}\right)$ [88]. The mean curvature (*H*), determines the solute concentration at the interface according to the Gibbs-Thomson equation, leading to the flux of solute from areas of high interfacial curvature to areas of low interfacial curvature and the evolution of the morphological structures. As material is deposited or removed, the mean curvature will change. This change also depends on the Gaussian curvature, because the evolution of the Gaussian and mean curvatures are coupled [89].

Clearly, the transition from facet growth (structures with planar surfaces) to dendritic growth (tree-like) occurred at approximately at 0.85 T, because the temperature conditions were identical. The difference in the phase morphologies is the results the changes of growth modes at the liquid-solid interface due to the application of PMF as discussed later in the discussion session. The phase morphology changes can be further characterized by analyzing their curvatures (the important parameters for describing phase morphologies). Figure 5.9 shows the mean curvatures and Gaussian curvatures of the Al_3Ni phases in two cases (0 T and 1.5 T). Each phase is colored according to the local values, i.e. from -0.1 (blue) to 0.1 (red) for the mean curvature, and from -0.005 (blue) to 0.005 (red) for Gaussian curvature. Figure 5.9a1 shows that, under 0 T, most Al_3Ni phases have flat surfaces due to facet growth mode. In addition, Figure 5.9c shows that, in the 0.85 and 1.2 T cases, the mean curvature peaks shift to the right, indicating that more phases have positive mean curvature. While, for the

1.5T case, Figure 5.9a2 shows that much more positive curvatures (red, convex) appeared at the phase tips regions while more negative curvatures (blue, concave) occurred at the branch roots. Figure 5.9c shows that the peak of 1.5 T mean curvature shifts to the left, indicating that a higher percentage of branches occur in the PMF of 1.5 T.

Voorhees, *et al* [49] proposed that mean curvature may not be sufficient to fully characterize the surface evolution because the saddle-shaped interfaces (in which $R_1 = -R_2$. In this case $H = 0$; thus, the interfacial solute concentration is equal to that of a planar interface, even though the interface is clearly not planar) could have zero mean curvatures. Therefore, it is necessary to measure both the mean and the Gaussian curvatures (Figure 5.9d) in order to characterize the coarsening process, or equivalently both radii of curvatures. Clearly, the Gaussian curvature peaks of all four cases were located in the center at zero, but the curves become broader with the increase of PMF fluxes, especially for the 1.5 T case, once again indicating that much more groove regions between the neighboring phase branches or dendritic arms were generated due to the higher PMF flux. These results demonstrate that the phase growth mechanism and morphology are significantly altered by the PMF.

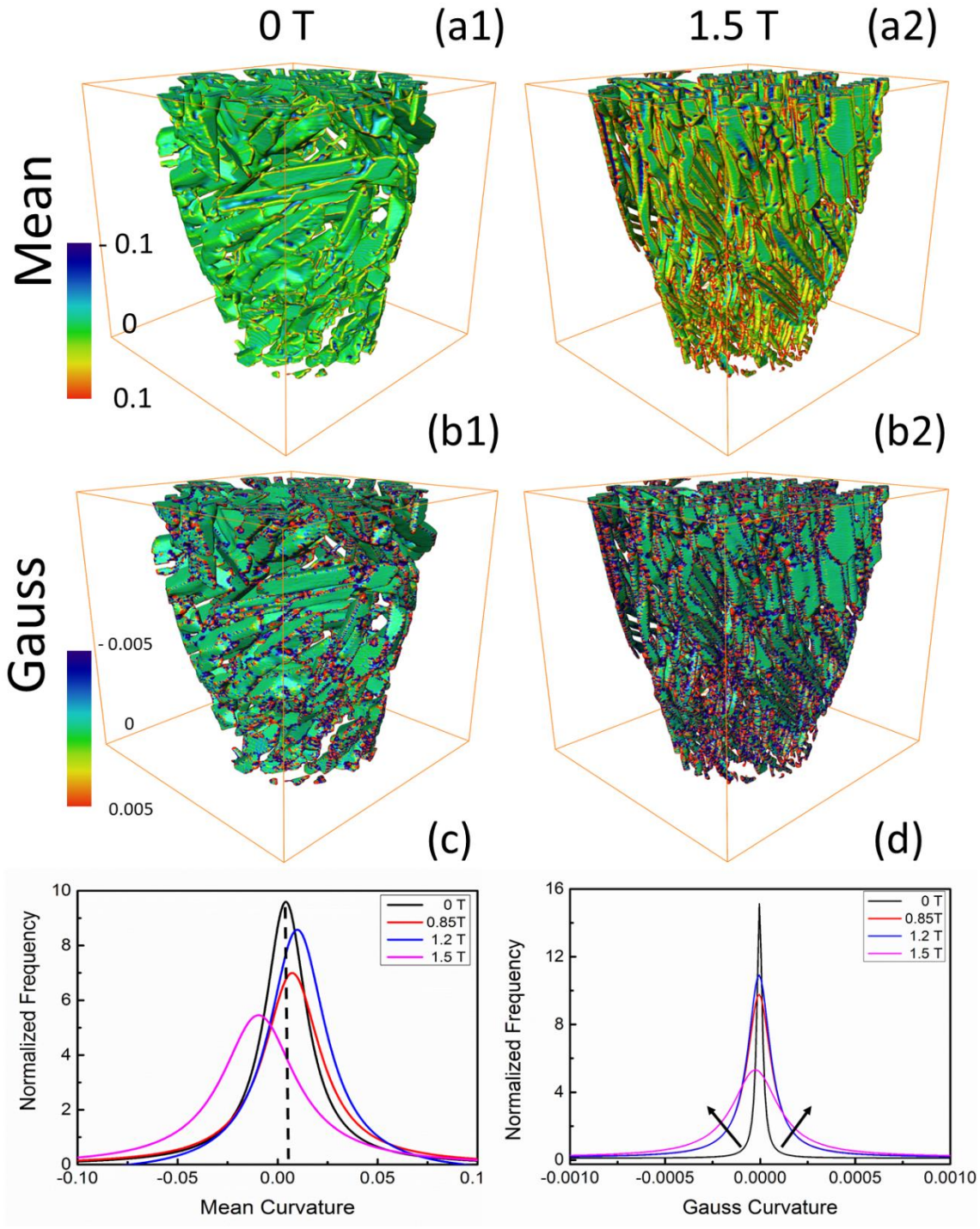

Figure 5.9 The (a) mean and (b) Gaussian curvatures of the Al_3Ni phases in the 0 T and 1.5 T cases. (c) and (d) are the curvature distributions for the four cases

5.4.2 Skeletonization of the Al_3Ni intermetallic phases

Skeleton analyses of the tomography datasets generate very rich 3D datasets which are not obtainable by conventional 2D image analyses. The statistical information concerning the phase angles, number and length of the Al_3Ni phases are summarised in Table 5.2 and Figure 5.10.

Figure 5.10a1–d1 shows the phase angle distributions (the angle between the central line of an individual phase in the length direction and the horizontal x-axis). The distributions are fitted by the Gaussian distribution function, and the majority (95%) of angles are within $\mu \pm 2\sigma$ range. For example, 31.6 to 55.84 degree for 0.85 T and 36.66 to 70.86 degree for the 1.2 T case. Nearly 60% of Al_3Ni phases are less than 45 degree for 0 T. At 1.5 T case, nearly 60% of Al_3Ni phases are aligned over 70 degree and 75% are over 50 degree. Hence, the peaks shift from an angle of ~35 degree to an angle of ~ 70 degree, indicating that the Al_3Ni phases rotated and aligned more towards the magnetic flux direction as the increasing of the magnetic flux densities.

The phase length distributions are shown in Figure 5.10a2–d2. For the 0 T case, over 55% of the phases are shorter than 1 mm (Figure 5.10a2) and the maximum length is shorter than 2 mm. However, for all cases with pulses, the phase length grew, even up to 2.7 mm. For the 0.85 T case, in Figure 5.10b2, the percentage of a single phase with lengths higher than 1.2 mm is over 70%. While Figure 5.10d2 shows that, for the case of 1.5T, over 70% of Al_3Ni phases are longer than 1.5 mm.

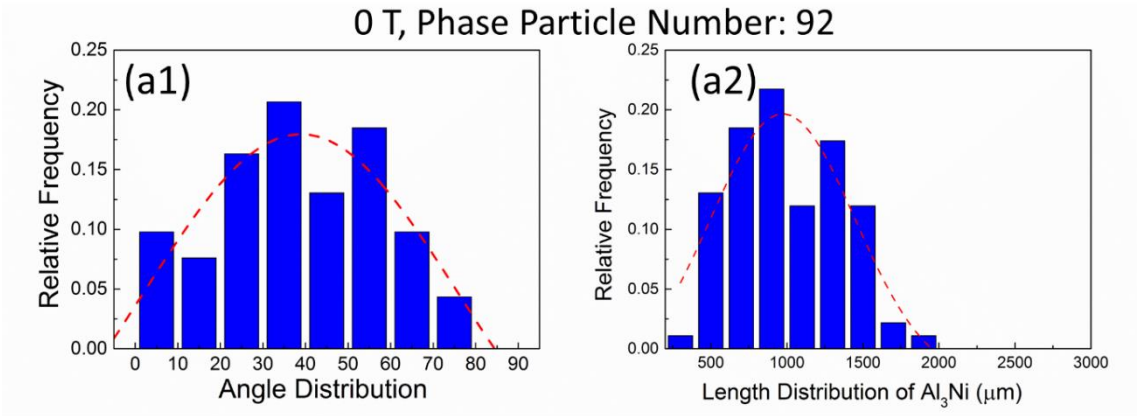
0 T, Phase Particle Number: 92
(a1)
Relative Frequency
Angle Distribution
(a2)
Relative Frequency
Length Distribution of Al3Ni (μm)

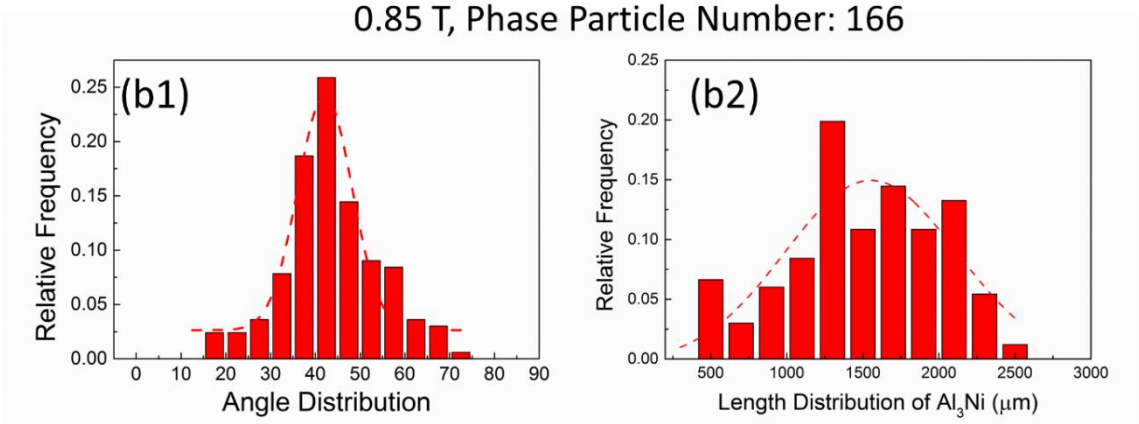
0.85 T, Phase Particle Number: 166
(b1)
Relative Frequency
Angle Distribution
(b2)
Relative Frequency
Length Distribution of Al3Ni (μm)

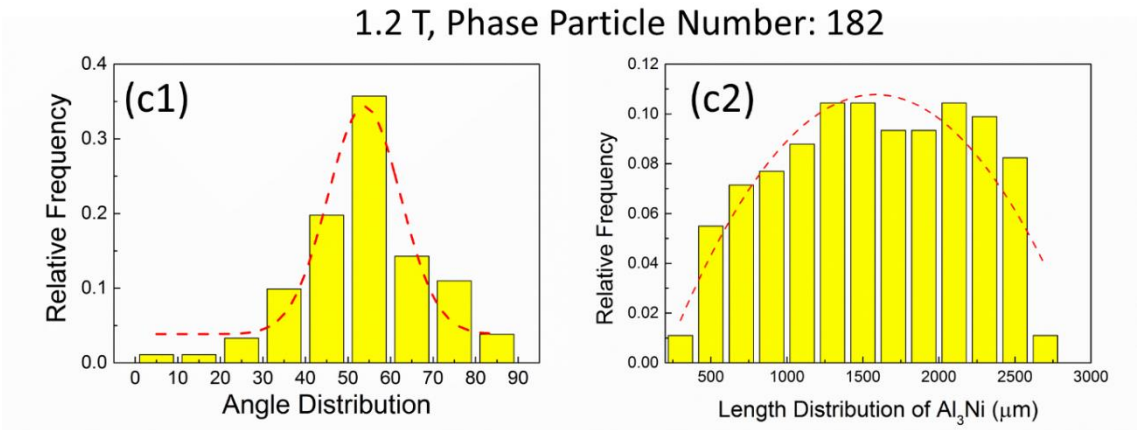
1.2 T, Phase Particle Number: 182
(c1)
Relative Frequency
Angle Distribution
(c2)
Relative Frequency
Length Distribution of Al3Ni (μm)

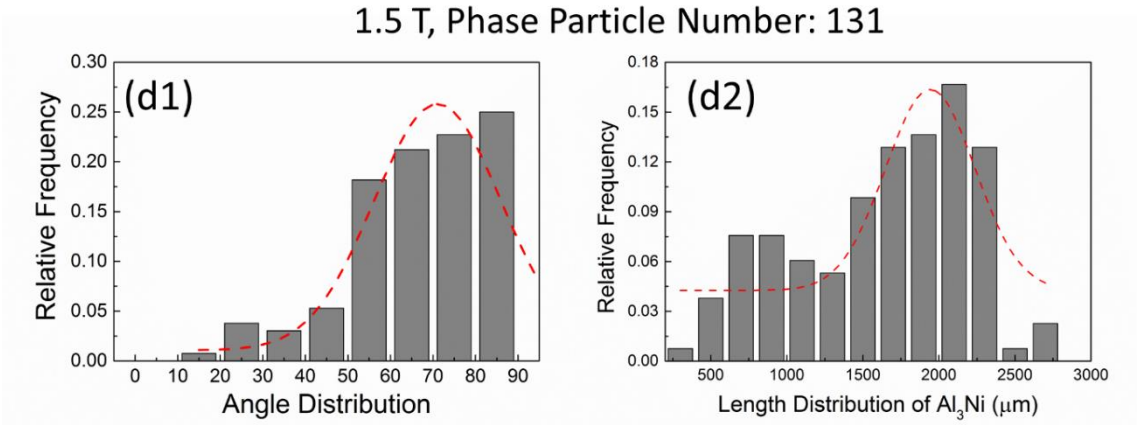
1.5 T, Phase Particle Number: 131
(d1)
Relative Frequency
Angle Distribution
(d2)
Relative Frequency
Length Distribution of Al3Ni (μm)

Figure 5.10 The phase angle distributions (left column: the angles between the central line of the phase in the length direction and the horizontal direction) and the phase length distributions (right column) of the primary Al_3Ni phases for the four cases: (a) 0 T; (b) 0.85 T; (c) 1.2 T; (d) 1.5 T.

Generally, the phase length increased with the increasing of the magnetic flux densities. The results of phase lengths with PMFs are likely two times longer than those without PMF shown in Figure 5.5a and Figure 5.10a2–d2. The phase lengths obtained from tomography are usually longer than those from radiography, because the images of curved Al_3Ni phases which normal to beamline direction cannot be revealed.

In summary, the statistical analyses as shown in Figure 5.10 clearly indicate that the applications of PMFs lead to the increase of the phase angle and phase length, especially increasing the percentage of large angles and long phases.

5.4.3 Al_3Ni phase growth and branching under 1.5 T

Figure 5.11a-c shows the same 3D microstructures as that in Figure 5.7d1, but viewed from different angles, and Figure 5.11b actually shows the 3D structures in the X–Z plane, which is corresponding to the 2D radiography images showed in Figure 5.3d6. The supplementary video 4 (including radiography and tomography together) demonstrates clearly that the primary Al_3Ni dendritic phases are elongated and parallel multi-layers are gradually formed in presence of 1.5 T pulse. Those phases shown in grey (h 0 0), yellow (h_1 0 0), green (h_2 0 0), purple (h_3 0 0) crystal planes etc are almost parallel with each other in Figure

5.11b due to the fact that Al_3Ni phases have different anisotropic properties and magnetic susceptibilities.

The real-time data revealed that the primary dendritic Al_3Ni stems were formed in parallel under a 1.5 T axial pulse magnetic field and these phases were reoriented toward and grew along the magnetic flux direction (Z-axis). The 1.5 T magnetic pulse is sufficient to cause phase side-branching. More interestingly, video 6 shows that most of the fragmentation events occurred at the initial growing stage of the secondary arms. The application of PMF plays the vital role in the phase fragmentation. While no fragmentation event we observed at all in the 0 T case as again clearly illustrated in Video 5. In this article, the EBSD could not be performed which provide more crystallography information, because the sample was partial re-melted.

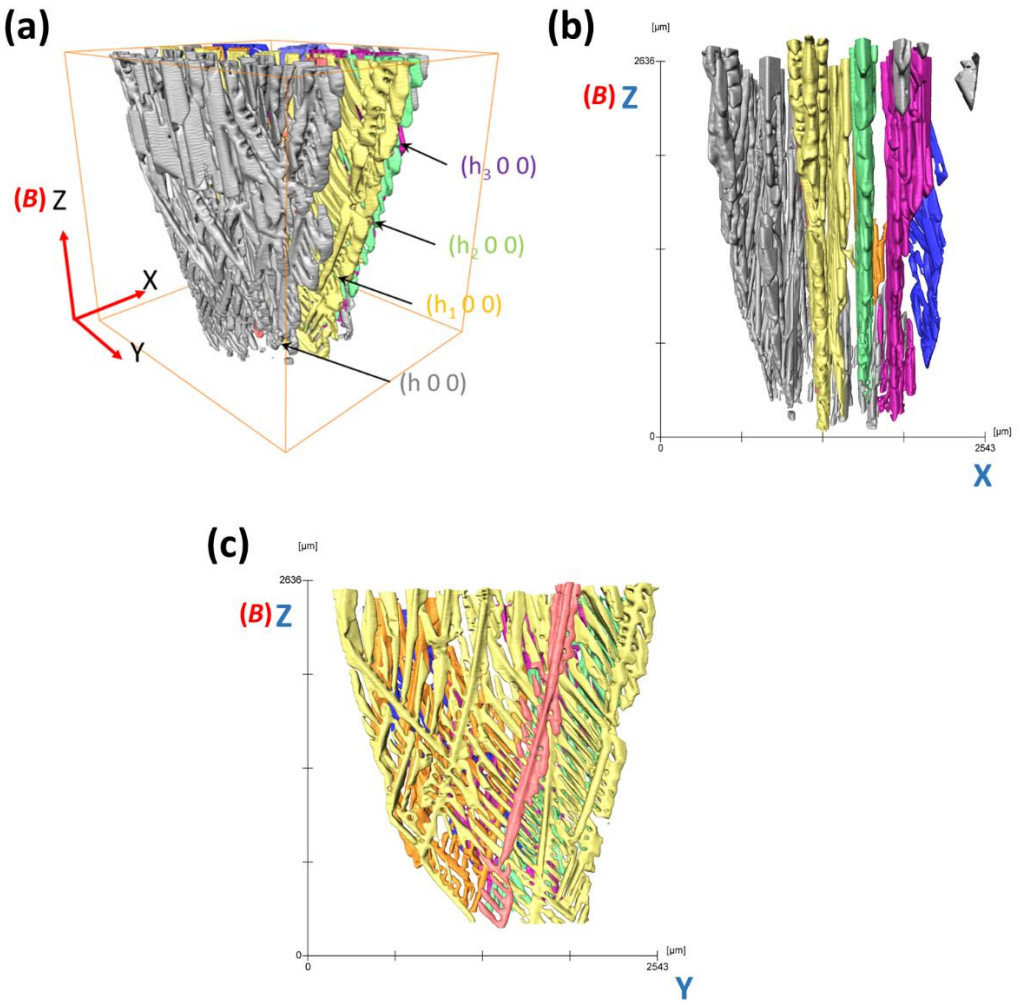

Figure 5.11 The mechanism of primary Al_3Ni phase growth under 1.5 T PMF during solidification, showing the initial phase orientation and its subsequent growth direction of primary Al_3Ni columns are aligned with the Z-axis direction (the magnetic flux direction), resulting in parallel multi-layers formed.

5.5 Discussion

5.5.1 Effects of PMFs on phase orientation

The solid Al_3Ni phases grew out of the solidifying melt are paramagnetic and both magneto-hydrodynamic and magnetization effects are acting on the Al_3Ni phases. The Hartmann number (Ha) [90] is one of the most important parameters to characterize the flow in a magnetic field, and it is defined as:

$$Ha = 2\boldsymbol{B}r\sqrt{\frac{\sigma}{\eta_0}} \tag{5.2}$$

r is the length of the Al_3Ni phase that appeared in the first frame of the video, η_0 is the viscosity without magnetic fields, $\boldsymbol{\sigma}$ is the electrical conductivity of the melt. Thus, in the melt, the increased effective viscosity, $\eta_{(e)}$, is due to the enhanced magnetic flux density based on the following equation [91]:

$$\eta_{(e)} \approx \frac{1}{3}\eta_0 Ha \approx \frac{2}{3}\boldsymbol{B}r\sqrt{\sigma\eta_0} \tag{5.3}$$

For the Al-15%Ni, we used the data reported in [52], and the melt viscosity is $\eta_{(0)} = 10^{-3}\ Pa \cdot s$, while the electrical conductivity of the melt is $\sigma = 10^9\ \Omega^{-1} \cdot m^{-1}$ [92]. The calculated Ha and $\eta_{(e)}$ for the four cases are summarised in Table 5.2.

In Video 5, it shows clearly that, at 0 T, the rotation of the relative bigger Al_3Ni phases is caused by the different densities between the phase and the melt, and the driving force is gravity. Such phase rotation phenomena driven by gravity were not observed in all cases with PMFs. However, Figure 5.3b–d show clearly the end results of phase alignment under PMFs. Indicating that the PMFs played a dominant role than gravity in the phase alignment. More importantly, Video 2-4

show clearly that phase alignment under PMF has completed at the very early stage of phase growth (before we are able to see the phases in the radiography videos). It has been well-accepted that magnetic field only has the influence on the phases that are larger than a certain size, often called the critical size r_{cri}. Wang, *et al* [92] calculated the minimum radius of a spherical Al_3Ni crystal on which magnetic fields have an effect on, and it was ~70 nm. Hence with the current synchrotron X-ray imaging spatial resolution, it is impossible to resolve the rotating movements of the initial critical Al_3Ni crystals under the action of the PMFs.

In general, the rotating angle θ as a function of time t for small electric conductive particles under magnetic fields can be calculated as [93]:

$$8\pi\eta_{(e)}r^3\frac{d\theta}{dt} + \frac{4\pi r^5\sigma B^2}{15}\frac{d\theta}{dt} + \frac{2\pi r^3}{3\mu_0}\Delta\chi B^2 sin2\theta = 0 \quad (5.4)$$

Only viscous (1st term), the rotational torque of a particle (2nd term) caused by Lorenz force and magnetic fields (3rd term) are taking into account in Eq 5.4. Hence the rotating time of a single Al_3Ni crystal under PMFs can be calculated as [93]:

$$\tan\theta = \tan\theta_0 \exp\left(\frac{-t}{\tau}\right),\ \tau = \mu_0\frac{30\eta_{(e)} + r^2\sigma B^2}{5\Delta\chi B^2} \quad (5.5)$$

μ_0 is the permeability in a vacuum ($\mu_0 = 4\pi \times 10^{-7}\ H\cdot m^{-1}$), $\Delta\chi$ is the difference of magnetic susceptibility between the Al_3Ni and liquid melt (here the $\Delta\chi = 10^{-5}\sim10^{-6}$). Eq. 5.5 indicates that higher magnetic fluxes *B*, smaller characteristic length *r* results in a shorter rotation time *t* for the alignment of the Al_3Ni phases.

For the three cases with PMFs, if the characteristic length *r* is taken as the initial length of the Al_3Ni phases firstly appeared in the radiography image sequences (the first resolvable phase from the melt), the calculation based on Eq. 5.5 indicated that the rotation time is in the order of 10^{-2} s for all pulse cases. Therefore, for all cases with PMFs, the magnetic field induced phase orientation occurred and completed in the time scale of 10^{-2} s. This is at least one order of magnitude quicker than the image acquisition speed (10^{-1} s in our case). Thus, from the temporal resolution point of view, we cannot resolve the rotational movement of the Al_3Ni phases either. This analysis confirms that, before the first resolvable Al_3Ni phases appeared in the field of view, phase alignment has already completed.

5.5.2 Effects of PMFs on Al_3Ni fragmentation

The magnetic permeability μ (as a function of magnetic susceptibility χ_m) is the inherent property for measuring the degree of magnetization for a material. I used the mixing rule to calculate the permeability of the Al-15%Ni, i.e. $\mu_{Al3Ni\ or\ Melt} = C_{Al}\mu_{Al} + C_{Ni}\mu_{Ni}$, where μ_{Al} and μ_{Ni} are the magnetic permeability for pure Al and Ni; C_{Al} and C_{Ni} are the atomic percent for pure Al and Ni, respectively. Hence, the calculated permeability of Al_3Ni is $\mu_{Al3Ni} = 1.89 \times 10^{-4}$, and the molten melt is $\mu_{melt} = 5.77 \times 10^{-5}$ H/m. For simplicity, I used consistently 15%wtNi, i.e. 7.5%atNi for the melt.

A magnetic field can produce an induced current inside a conductive sample with the current often concentrated near the sample surface region, and this is often called skin effect. The skin depth δ [18] can be calculated as:

$$\delta = \sqrt{\frac{\omega}{\pi f \mu_{melt}}} \tag{5.6}$$

where μ_{melt} is the permeability, *f* is the frequency of pulse (1666 *Hz*), and ω is the electric resistivity of the sample (we used 2.65×10^{-8} Ω*m for the melt as did in [94]). *f* is given by $\frac{1}{pulse\ duration} = \frac{1}{0.0006} = 1666\ HZ$. From Eq. 5.6, the skin depth is calculated as 0.3 mm. This suggests that the PMFs mainly applied up to 30% depth of sample (the maximum diameter of the sample is 2 mm).

While the induced pulse current generated inside the melt will produce a pinch pressure inside the melt. In this study, it is radial compressive stresses, and can be calculated as [18, 95]:

$$P = \frac{1}{4} \cdot \mu \cdot J^2 \cdot (r^2 - a^2) \tag{5.7}$$

where *μ* is permeability, *J* is the current density, *r* the radius of sample and *a* is the distance from the centre of sample. The sample is a cylinder type geometry with a radius of ~1 mm (the sample geometry is draw in yellow in Figure 5.13a), and the induced current density is $J = 10^3$ A/mm^2 in the Al melt for the 1.5 T case [47] (The induced current is almost impossible to measure during in-situ experiment. Hence the modelling value simulated by T. Manuwong is used for calculating the pinch force). Of course, there are differences in the electric conductivity of the Al_3Ni phase and the melt. It would affect the induced current since *J* is a function of *σ*. Because the difference of *J* for the Al_3Ni phase and the melt is small compared to the difference of *μ* for the two (the result of $\sigma_{Melt}/\sigma_{Al3Ni}$ = 1.13 is almost 30 times smaller than the μ_{Melt}/μ_{Al3Ni} = 32). Hence, I use a constant *J* for both Al_3Ni phase and the melt. In this way, the calculated pinch

pressures for Al_3Ni (P_{Al3Ni}) and melt (P_{Melt}) were plotted in Figure 5.13a. The difference in the pinch pressures between the solid phase and liquid phase ($P_{Shear} = \Delta P = P_{Al3Ni} - P_{Melt}$) results in a shear stress acting on the Al_3Ni phases at L–S interface. Such shear stress, of course, varies with the profile of the pulse applied, and Figure 5.13a shows the shear stress is in range of 0.65 ~ 33 MPa. In other words, the pinch force gradually decreases from 33 to 0.65 MPa when the position moves from sample wall to the sample centre.

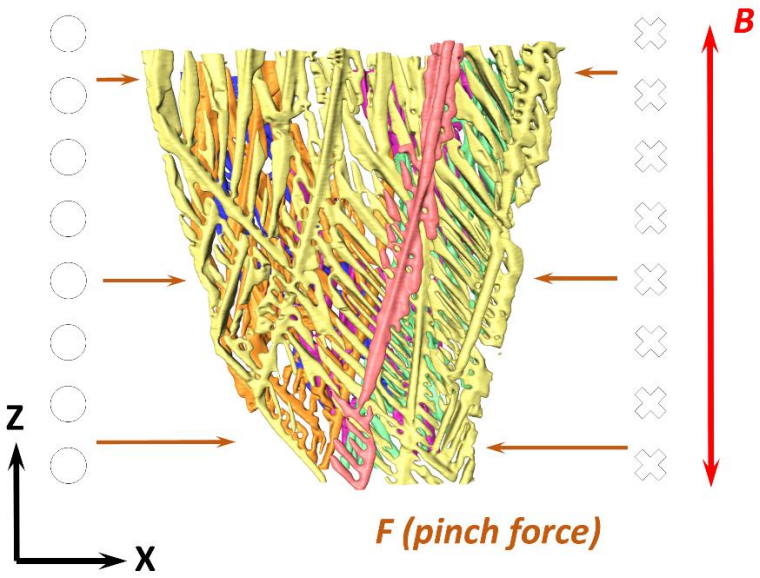

Figure 5.12 The schematic of pinch force radially acting on the sample (cross-section of 3D microstructure from Figure 5.7d) in presence of the 1.5 T PMF.

The schematic of pinch pressure acting on the Al_3Ni sample is demonstrated in Figure 5.12. Based on electromagnetic pulse setup shown in Figure 2.5a, the magnetic direction is along with the Z-axis, paralleling with gravity direction. Correspondingly, the radial electromagnetic forces (pinch force) are generated from outside sample toward to the sample centre and these forces are parallel each other. According to skin effect (Eq. 5.6), the pinch force gradually decreases

when the position is closer to the sample centre, the estimated pinch force with geometry shows in Figure 5.13a.

The yield strength σ_y of Al_3Ni intermetallics is a function with absolute temperature T and can be calculated as [52]:

$$\sigma_y = 10^{-3} \cdot E(T) \tag{5.8}$$

$$E(T) = E_{300} \left\{1 + B \cdot \left(\frac{T-300}{T_m}\right)\right\} \tag{5.9}$$

where *E(T)* is Young's modulus at *T*; E_{300} is the modulus at 300 K and T_m is the absolute melting temperature. The E_{300} of Al_3Ni intermetallic is measured as 140 GPa [96] while the constant *B* is taken as -1.33 [97]. Hence, the estimated yield strength by Frost and Ashby method [98] is in range of 5 ~ 30 MPa when the temperature between 640 and 782 ◦C (Figure 5.13b).

By comparing the shear stress acting onto the Al_3Ni and the estimated yield strength of the Al_3Ni phases, the shear stress ΔP is sufficiently enough to shear off the small Al_3Ni dendritic arms from their primary arms as clearly demonstrated in Video 6. Another interesting phenomenon is that no fragmentation events were found in the main primary arms at all (Video 6), indicating that those arms have developed sufficient strength to withstand the shear action from the pinch pressure. Furthermore, without PMF (0 T case, see Video 5), no fragmentation events were observed at all for any small or big Al_3Ni phases, apart from the bigger phase rotation under gravity.

The very frequently occurred fragmentation events shown in video 6 further confirm that fragmentation is the dominant mechanism for phase multiplication. The small fragments showered downwards into the field of view and might act as

nuclei for the new phases in the subsequent solidification process. The increase in the Al_3Ni phase number was confirmed in the cases of 0.85 T and 1.2 T, where the number of Al_3Ni phases increased to 166 and 182 respectively (Figure 5.10). Fragmentation of dendritic structures during solidification of metal alloys has been studied extensively in the past. Generally, it has been well accepted that the mechanism of dendrite fragmentation can be attributed to (1) solute concentration difference [72] or (2) shear or bend stresses leading to fracture due to enhanced interdendritic flow [97] or (3) shock wave induced by cavitation bubble collapse [99].

Elotti, *et al.* [72] had argued that the magnetic field enhanced interdendritic convection is the main cause for creating enhanced solute redistribution at the necking area of the Al-15%Cu dendrites, that cause the remelting of the dendritic root arms, hence fragmentation. While in our case, the Al_3Ni phase is an intermetallic compound with the fixed composition (Figure 4.1b). With a relatively slow cooling rate, i.e. ~1.44 °C/s in our experiments, the Al_3Ni phase growth occurred in a quasi-static manner and the diffusion of Al and Ni atoms across the liquid-solid interface is the dominant control mechanism. However, solute diffusion occurs in a time scale of 1–10 s as calculated by Liotti, *et al.* [72]. While the PMF applied to the solidifying alloys occurred in 80~100 ms. Almost 2 orders of magnitude quicker than the time required to achieve any meaningful solute movement. Hence, any convection related solute redistribution inside the melt and any solute induced phase remelting would be impossible to occur in the time scale when the PMF was applied. Video 6 shows clearly a large number of smaller Al_3Ni fragments (size in dozens of micros or so) rained down in the field

of view. Such phenomena is again different to what observed by Liotti, et al [72] (Figure 5.3 to Figure 5.13), where fragmentation just occurred locally in the interdendritic regions. Figure 5.13b shows that the yield strength of the Al_3Ni phases decrease linearly with the increase of temperature, and in the temperature range of the experiments, the yield strength is in the range of 5-30 MPa. Hence the shear stresses showed in Figure 5.13a is sufficiently enough to cause the fracture of the Al_3Ni phases, especially at the early stage of the solidification where the strength of the Al_3Ni phases are generally below 15 MPa, where at the central location of the sample, the shear stresses are generally above 25 MPa.

Hence, the combined very rich real-time images and theoretical calculation provide unambiguous evidence and robust argument that the Al_3Ni phase fragmentation is due to the shear effect from the pinch pressure, and it is the dominant mechanism for enhancing phase multiplication. Such mechanism can be well exploited for enhancing grain refinement in alloy systems that contain intermetallic phases.

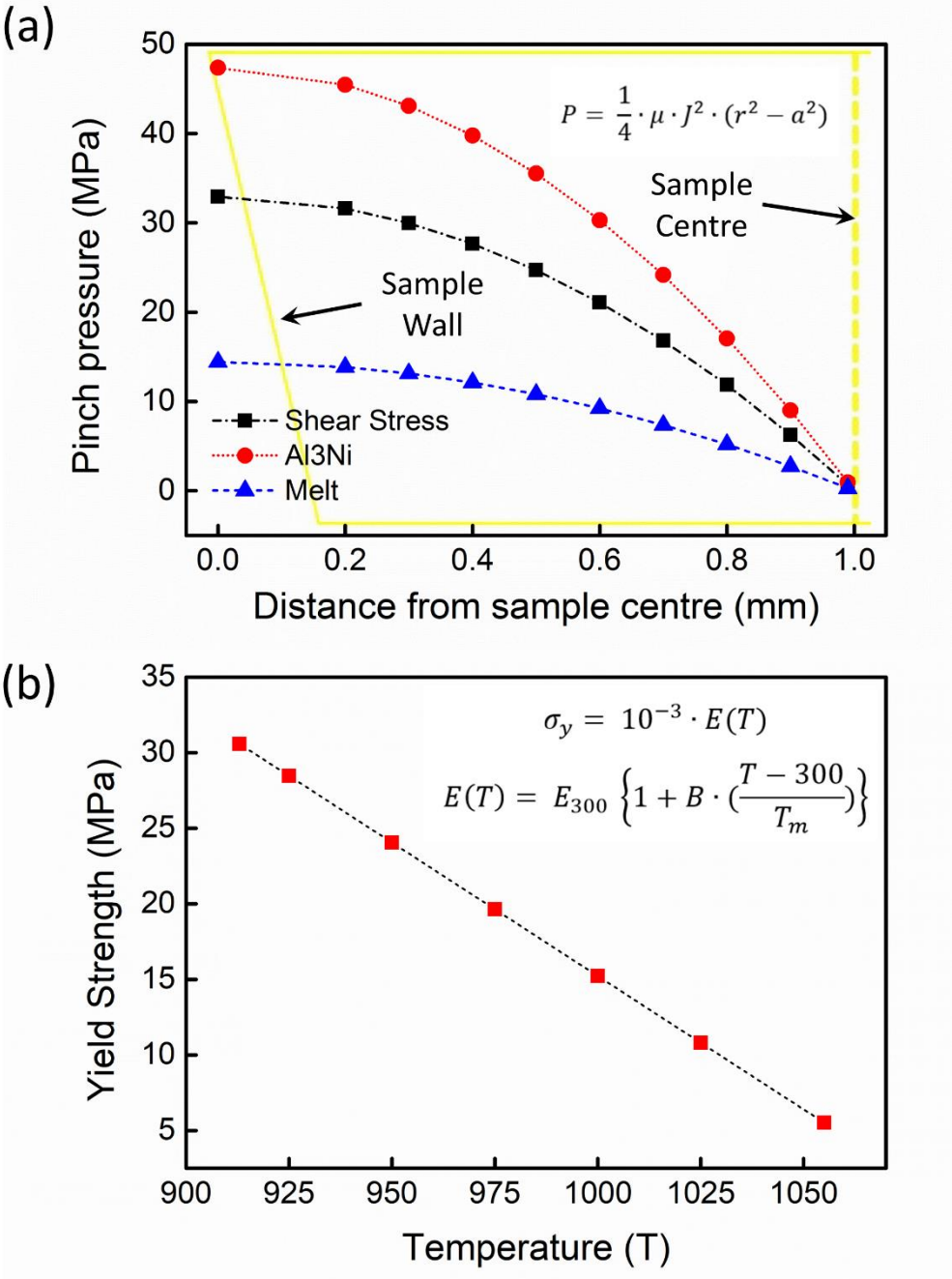

Figure 5.13 (a) The estimation of shear force acting on the Al_3Ni phases as a function of the distance from the sample centre (the difference pinch pressure induced by the magnetic pulses on the primary Al_3Ni intermetallic phases and Al-Ni melt); (b) The σ yield strength as a function of the absolute temperature in the range from the melting point 1055 K (782 ˚C) to eutectic point 912 K (639 ˚C).

Table 5.2 Summary of the data for the Al3Ni phases subject to different magnetic pulses

Parameters	Unit	Case1	Case2	Case3	Case4
Discharge voltage	**V**	0	100	150	180
Magnetic flux pulse peak value	**T**	0	0.85	1.2	1.5
Magnetic flux pulse of full width at half maximum (FWHM) value	**T**	0	0.475	0.6	0.75
Firstly resolved characteristic length of Al_3Ni	**μm**	176	48	50	47
Solid fraction (f_s)	**N/A**	0.216	N/A	0.253	0.246
Liquid fraction (f_l)	**N/A**	0.784	N/A	0.747	0.754
Number of Al_3Ni phases	**N/A**	92	166	182	131
Mean length of Al_3Ni	**μm**	1015.49	1508.21	1576.49	1624.16
Mean radius of Al_3Ni	**μm**	90	70	30	20
Mean Al_3Ni Orientation (θ)	**Degree**	38.63	43.72	53.76	66.61
Ha	**N/A**	0	81.6	120	141

Electrical conductivity	$\boldsymbol{\Omega^{-1} \cdot m^{-1}}$	10^9			
Effective viscosity	**Pa * s**	0.001	0.0272	0.04	0.05
The rotation time	**s**	N/A	8.62×10^{-2}	8.37×10^{-2}	7.12×10^{-2}
The permeability of pure Ni	**H/m**	7.54×10^{-4}			
The permeability of pure Al	**H/m**	1.26×10^{-6}			
The permeability of Al-15%wtNi melt	**H/m**	5.77×10^{-5}			
The permeability of Al_3Ni	**H/m**	1.89×10^{-4}			
Thermal Gradient (∇T)	**K * m^{-1}**	3×10^4			

5.6 Conclusion

Systematic real-time synchrotron X-ray imaging and tomography experiments have been carried out to study in-situ the dynamic evolutions of primary Al_3Ni intermetallic phases in an Al-15%wtNi alloy solidified under pulse electromagnetic fields of different magnetic flux densities. For the first time, clear and unambiguous real-time evidences have been presented to show how Al_3Ni phase orientation, growth and fragmentation were affected and controlled by the applied pulse magnetic fields. The 3D structures and morphological changes of the primary Al_3Ni phases were systematically analysed and quantified using skeletons function and reported for the first time. Through the combined experimental data analyses and theoretical calculations, the following conclusions have been reached:

Under a pulse magnetic field, the Al_3Ni phase orientation occurs at the very early stage after nucleation, and completes in a time scale of 10^{-2} s, approximately 2 or 3 order of magnitude quicker than the phase orientation caused by gravity. The phases tend to align more and more parallel towards the magnetic flux direction as the flux density increases. In addition, the free growth rate of the Al_3Ni phases is 10–40 times higher than in that without the field, and the growing length of the Al_3Ni phases is 2–3 times longer than those without the field;

When the peak pulse magnetic flux applied is larger than 0.85 T, the growth of Al_3Ni phases was observed to progressively change from a facet growth to a dendritic growth mode, resulting in side branching, secondary arms and finally dendritic structures;

Phase fragmentation was also observed for the first time in situ and presented. The unambiguous experimental evidence and theoretical calculation indicates that the shear stresses produced by the different pinch pressure acting on the melt and the phases are sufficient to shear off the smaller Al_3Ni phase branches from their primary branches. Such mechanism can be well exploited for enhancing grain refinement in alloy systems that contain intermetallic phases.

Chapter 6: **The formation of α-Al dendritic phases**

In this chapter, I present systematic real-time studies of the highly dynamic evolution of primary *α*-Al dendritic phases in an Al-15%Cu alloy followed by the coarsening results using pulse electromagnetic field solidification device and 4D synchrotron X-ray tomography at TOMCAT beamline, Swiss Light Source.

The 4D datasets reveal how pulse magnetic fields affect the nucleation and subsequent growth and fragmentation of *α*-Al dendrites during solidification. The structures and morphologies of the Al dendrites with/without 0.75 Tesla were analysed and quantified using skeletonization function.

For the first time, the combination of unambiguous real-time experimental evidences and theoretical calculation are used to elucidate how dendrites fragmentation was caused by the shear stresses produced by the Lorentz force acting on the melt and the phases during solidification, clarifying a first fresh insight into the fragmentation induced by PMF.

6.1 Image processing and 3D skeleton function

The raw projections were automatically performed on the TOMCAT cluster [100] using the GridRec algorithm [101] coupled with the Parzen filter [102]. The supercomputer, Viper (technical specs are presented in Chapter 4) housed at University of Hull were used for processing the huge amount of 3D datasets. These computing and visualisation capability enable us to process directly the 16 bit datasets and produce the high fidelity solidified microstructures without cropping and binning of the original datasets.

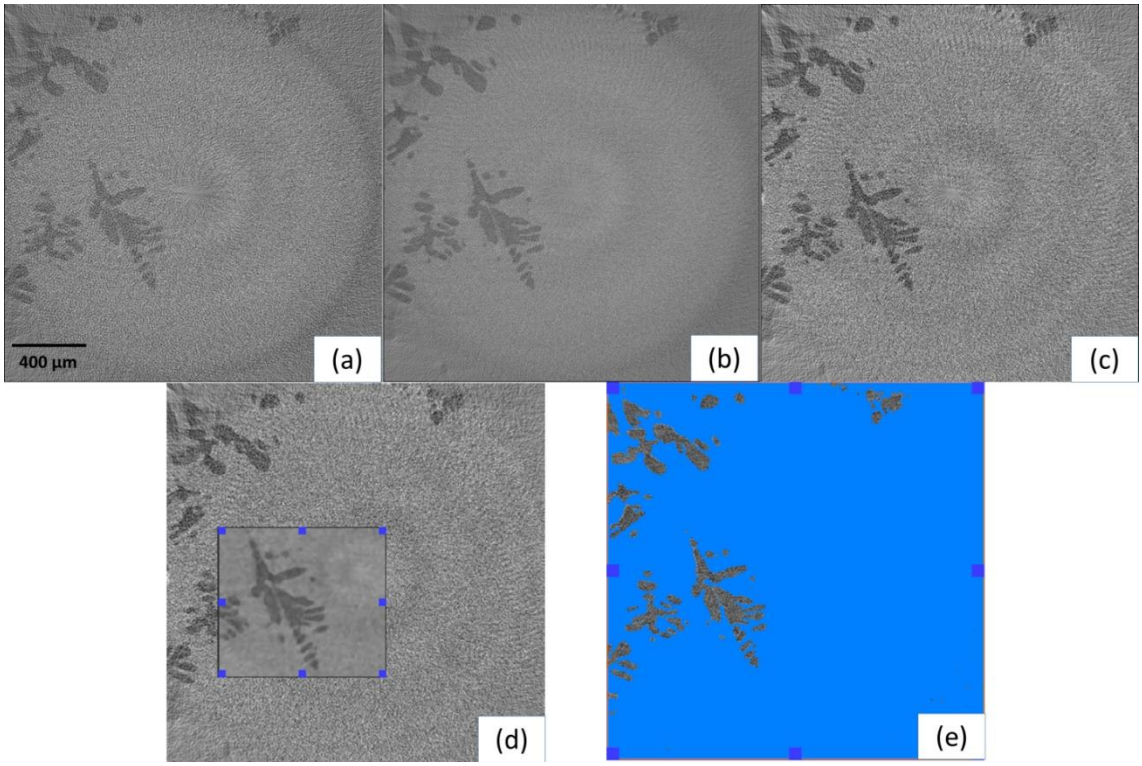

Figure 6.1 The image processing workflow after reconstruction (a) a typical raw synchrotron X-ray image; (b) removing the noise from (a); (c) subtracting the flat field image from (the image taken without the sample on the beam path) from (b); (d) applying the 3D anisotropic diffusion filter to (c); (f) adding threshold to (d).

All 16-bit datasets were denoised, segmented and rendered using an open source platform (Fiji) [103] and Avizo® 9 to reveal the 3D dendrites. Methods including 3D anisotropic diffusion filtering, thresholding, segmentation and smoothing were used to improve the image quality and achieve a better microstructure rendering. All raw tomography scans went through semi-automatic processing. The pro-processing for de-noising before segmentation is demonstrated in Figure 6.1.

3D auto skeleton, cylinder correlation and detecting fibres modules [104, 105] were used and peeled the original structures off while preserving the original

topology features. These feature tracing modules significantly reduce the manual labour for evaluating 3D microstructural evolution over time. This 3D skeleton process performed in Avizo®, and the 3D complex tree-like structures were simplified by implementing an algorithm of successive thinning, removing voxels at the surface and transforming remain voxels into linear sections. Hence, statistical information can be acquired. More details are described in Chapter 5.

6.2 4D morphological evolution and Al dendritic fragmentation

4D In-situ tomography study offers an opportunity to capture the dynamic structures in 3D format. The rendered 3D tree-like structures are demonstrating the classical four-fold dendritic patterns from 0 to 266 *s*. Generally, liquid melt are deliberately removed to highlight the solid phases. During tomography acquisition, the temperature is set above the eutectic temperature (T_e=542 °C), therefore no eutectic phases were resolved to affect primary Al dendrite study. The porosity in both cases was not obviously observed since the datasets were obtained at earlier solidification stage with less solid fraction (< 25%).

6.2.1 Entire sample observation – Fragmentation

The formation of dendritic patterns in solidifying Al alloys shown in Figure 6.2 and Figure 6.3. The multi-colours were used to render the different Al branches, and to present the entire 3D morphologies of the primary *α*-Al dendrite without and with the PMF during solidification. Five successive sequence of images show the 3D time-resolved *α*-Al dendritic morphologies and with one final skeletons.

Figure 6.2a capture the typical Al dendritic growth of primary, secondary and tertiary arms, demonstrating the strong anisotropy on the horizontal plane (X-Y direction) during solidification without the PMF. Initially, solidification begins with the nucleation of dendrites on the tube surface shown in Figure 6.2a1. Then, in Figure 6.2a2–5, secondary dendrites (SD) rapidly grow into the free space (melt) before any impingements. The secondary dendrites grow on a plane which has an angle with X–Y plane. Small tertiary perturbations already formed vertically after 13.3 *s* and most tertiary arms grow parallel to the Z–axis. Figure 6.2a6 shows the skeletons (estimated thickness) of structures with transparent microstructures outside in Figure 6.2a5. All skeletons could fit irregular dendritic features well, and red lines outline the main branches, while the blue and green lines represent the small dendrites.

There are a few open reports on dendritic fragmentation induced either by natural convection or by ultrasound or both [106, 107]. Grain refinement and multiplication are often considered as result of fragmentation. One well-known fragmentation mechanism is the pinch-off driven by capillary [108, 109]. The detachment of dendritic side-branches at the narrow neck with their parent stem. However, a new fragmentation scenario induced by the PMF is observed in this experiment. It is the first time to capture such massive fragmented particles in an entire sample volume. Figure 6.3b and animated for both cases in Movie 2 clearly illustrates lots of resolved small particles, two-fold irregular flakes and four-fold flakes floated in view field with even 0.75 *T* pulse condition, strongly demonstrating the ongoing of fragmentation at 26.6 *s*. The Lorentz force

generated by the PMF is strong enough to break the grain structure permanently and will be discuss later.

The skip time between two successive tomograms is 10 *s* (camera off due to data transfer) and the fragmentation event remains in very short period. Hence, the detachment of *α*-Al dendrites at local root area (pinch–off effect) was not obviously and easily captured due to the temporal resolution. These *α*-Al flakes were floating upwards captured at 39.9 *s* due to the density difference between the Cu-riched melt (ρ_{melt} = 3.0 g/cm^3) and primary *α*-Al (ρ_{Al} = 2.7 g/cm^3). These flake-like structures is earlier pattern shape before they evolve to dendritic shape. These small size fragments (comparing with the Al branches) are likely to (1) re-melt or (2) join together and then become bigger clusters which will be survive during upward movements. At 66.5 s, only few irregular *α*-Al dendritic fragments remain at the right top of view field. Finally, these connecting fragmented clusters disappeared after 79.8 s. There is a possibility that bigger fragments might keep floating up and finally out of view field since bigger clusters are unlikely re-melted again.

Generally, in Figure 6.3b, the entire 3D microstructures with the PMF present a symmetric shape and its symmetry plane is close to 45 deg of X–Y axis, exhibiting a transition of growth orientation from strong anisotropy (without the PMF) to weak anisotropy (with the PMF). It might be achieving the isotropy when higher magnitude of magnetic flues is inputted. With the PMF, the primary main dendritic branch grows upwards along the Z-axis until filled the FoV. In is interesting to notice that almost all ternary arms grow upward due to the interaction between thermal gradient and magnetic fluxes. Moreover, the 0.75 *T* of PMF significantly

increases formation rate of the secondary, ternary and even higher-order dendritic growth at L-S interface. The characteristic of individual dendritic growth with the PMF will be discussed later.

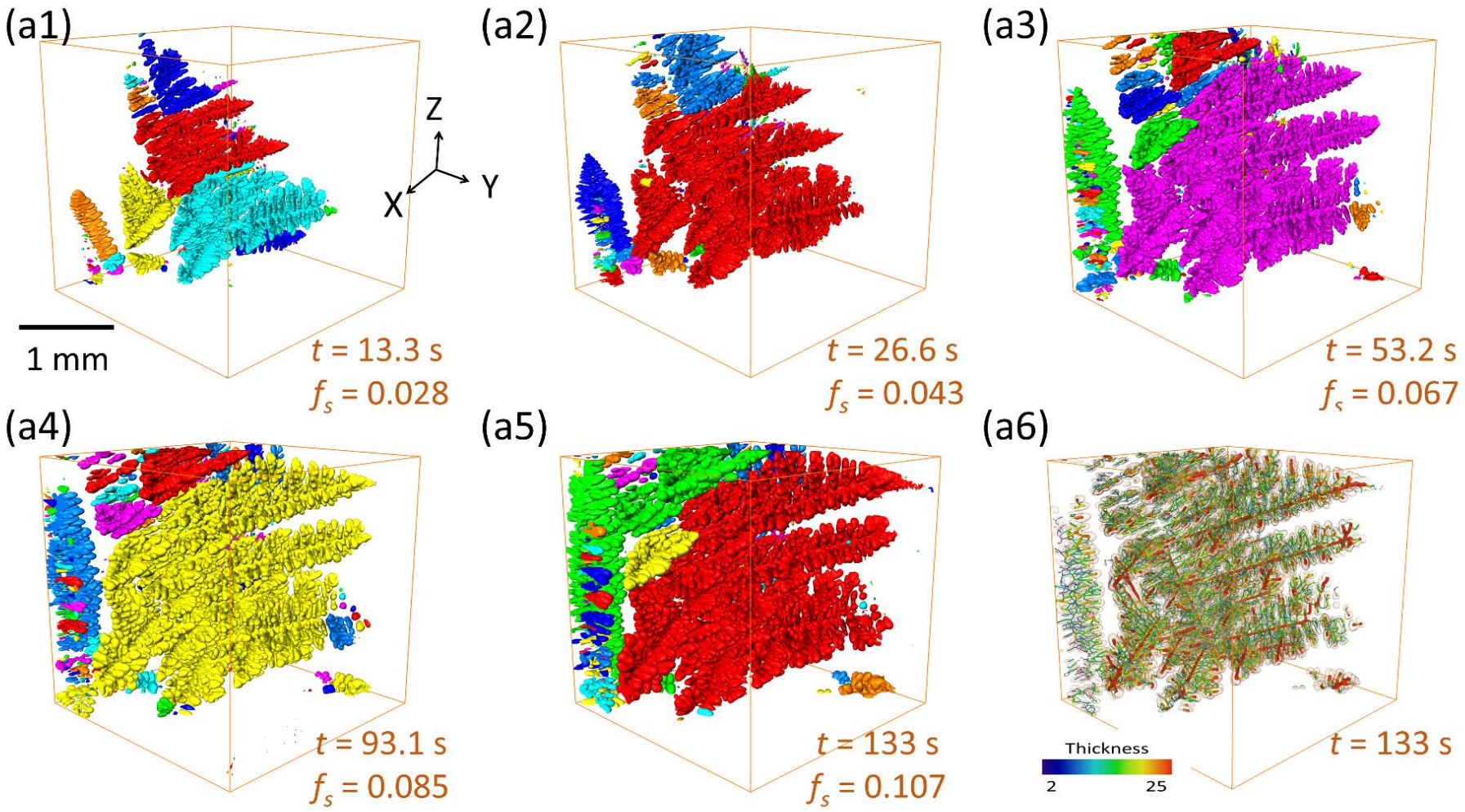

Figure 6.2 Full 4D (three dimensional plus time) primary α–Al dendritic morphologies characterization via synchrotron X-ray tomography during solidification without the PMF

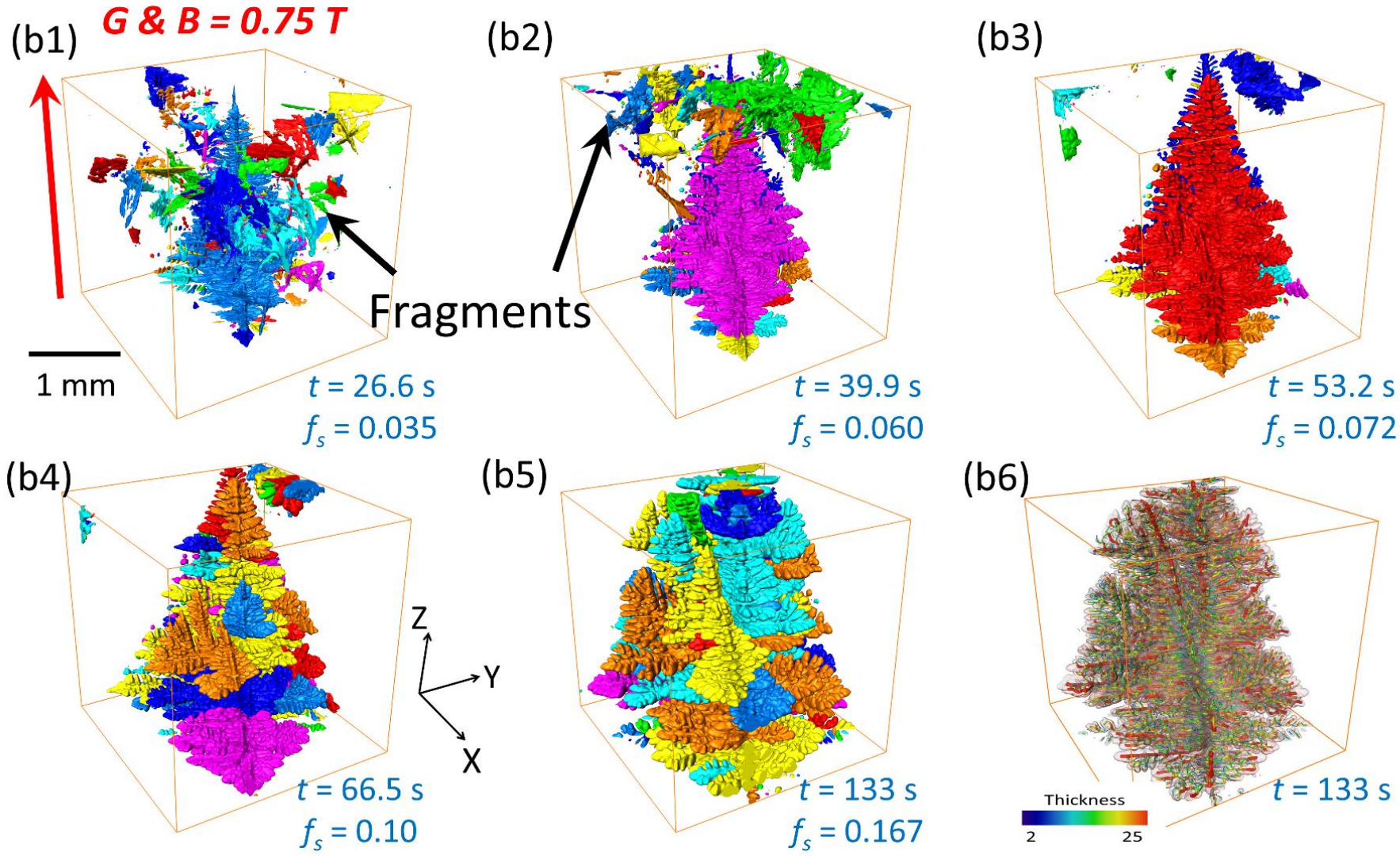

Figure 6.3 Full 4D (three dimensional plus time) primary α–Al dendritic morphologies characterization via synchrotron X-ray tomography during solidification with 0.75 T (Tesla) magnetic pulse. The massive fragments were observed when pulses were applied.

6.2.2 Individual dendritic scale observation – hyper branching

In order to easily and in-depth visualize the dendritic phases. For no PMF case, the images are manually selected to represent a sub-volume 276 × 227 × 130 μm^3 in size and taken from same volume in Figure 6.2a. While for the PMF case, a sub-volume 130 × 162 × 260 μm^3 was extracted from Figure 6.3b.

Basically, the dendritic tips grew quicker than the root bases resulting in a droplet-like shape. With the PMF, morphologies demonstrate flat-like dendrites with thinner thickness, while for regular case the developing of dendrites exhibit round-shaped arms. For both case, the growth mechanism of secondary dendrite in terms of (1) re-melting small dendrites to benefit the bigger adjacent arm; (2) coalescence of arms are also verified the previous study [65] are also confirmed. However, we report the scenario of dendrite growth characteristic when the PMF is induced.

For no PMF case, almost all secondary dendritic arms are not growing perpendicularly to the main primary dendritic branch but with a slight angle. Figure 6.4a shows that the growth of SD has different rates on the left and right sides. Because the left side is counter-gravity direction while right side towards to the gravity direction, the density gradient and gravity plays a major role in leading this difference. Initially, dendrites exhibit a symmetric shape in X–Z plane as shown in Figure 6.4a1. But after 26.6 *s*, the right-side arms have quick growth rates creating an asymmetric four-fold shape in Figure 6.4a2–5. Moreover, doublone-like dendrite (blue arrow) is observed along the Y–axis after 39.9 *s*. Of

course, dendritic tips split after 26.6 *s* and the tip splitting is responsible for the formation of the seaweed-like structure. Moreover, both seaweed-like structure and doublone-like structure co-exist and grow perpendicular to main branch.

While with the PMF, two small dendrites (1) and (2) evolved with time to become two main branches and the growth direction is almost perpendicular with each other shown in Figure 6.5b. The preferential growth direction for *α*-Al dendrites is <1 0 0> according to the previous research. Dendrite 1 (D1) grow rapidly due to there is no restriction and interaction with other dendrites during earlier cooling period. Although it has a slightly angle with the heat flow and magnetic direction, it almost grow parallel to the heat flow (Z) direction. At 39.9 *s* in Figure 6.5b1, the length of dendrite (3) and (4) are similar. However, with solidification advance, D4 loses growth competition to D2 in 13.3 *s* and D4 almost stops growing after 53.2 *s* as shown in Figure 6.5(1-2). This might attribute to the growth of D4. Because the length of D4 evolves rapidly and become a barrier for solute transport and then decrease the diffusion rate at the interface. Between main branch D1 and D2, there are a few secondary and ternary dendrites are observed at very beginning in Figure 6.5(2–3). These well developing split tips demonstrate the significant interfacial instability e.g. Mullins–Sekerka instabilities [110] of phase growth with pulse condition.

I observed that several small protrusions come out from stem of D1 and generate an asymmetric coralline-like pattern in 66.5~266 *s*, creating a surface with large curvatures. In Figure 6.5(5), black arrows show that tips splitting are dominating

at 79.8 *s*. Side-branching and splitting phenomena are more frequently observed when performing with the PMF, leading to the hyper-branched structures if one compares the Figure 6.4 and Figure 6.5. The hyper-branched morphology is attributed to modification of local solute distribution. All evidences demonstrate that the PMF has strong correlation with growth types during solidification. Because any phase growth direction is governed by three factors e.g. the preferential crystal orientation, the magnetic direction, the thermal gradient direction.

Formation of seaweed-like and coralline-like structures, were unambiguously observed due to side-branching and tip-splitting from tomography datasets in Figure 6.5. The characteristic of primary Al dendritic growth driven by the PMF is the foremost tips repeatedly split into two or more tips. Obviously, the presence of magnetic pulse has strong influence on side-branching. Haxhimali *et al*. [111] proposed that seaweed structures are formulated by tip splitting due to modification of surface tension anisotropy. Here, the Lorentz force (as an extra energy) will created by interaction of induced current (*J*) and magnetic field (*B*). The deformation at tip of D1 in Figure 6.5(6) laid a strong evidence that the PMF is strong enough to affect the interfacial anisotropy.

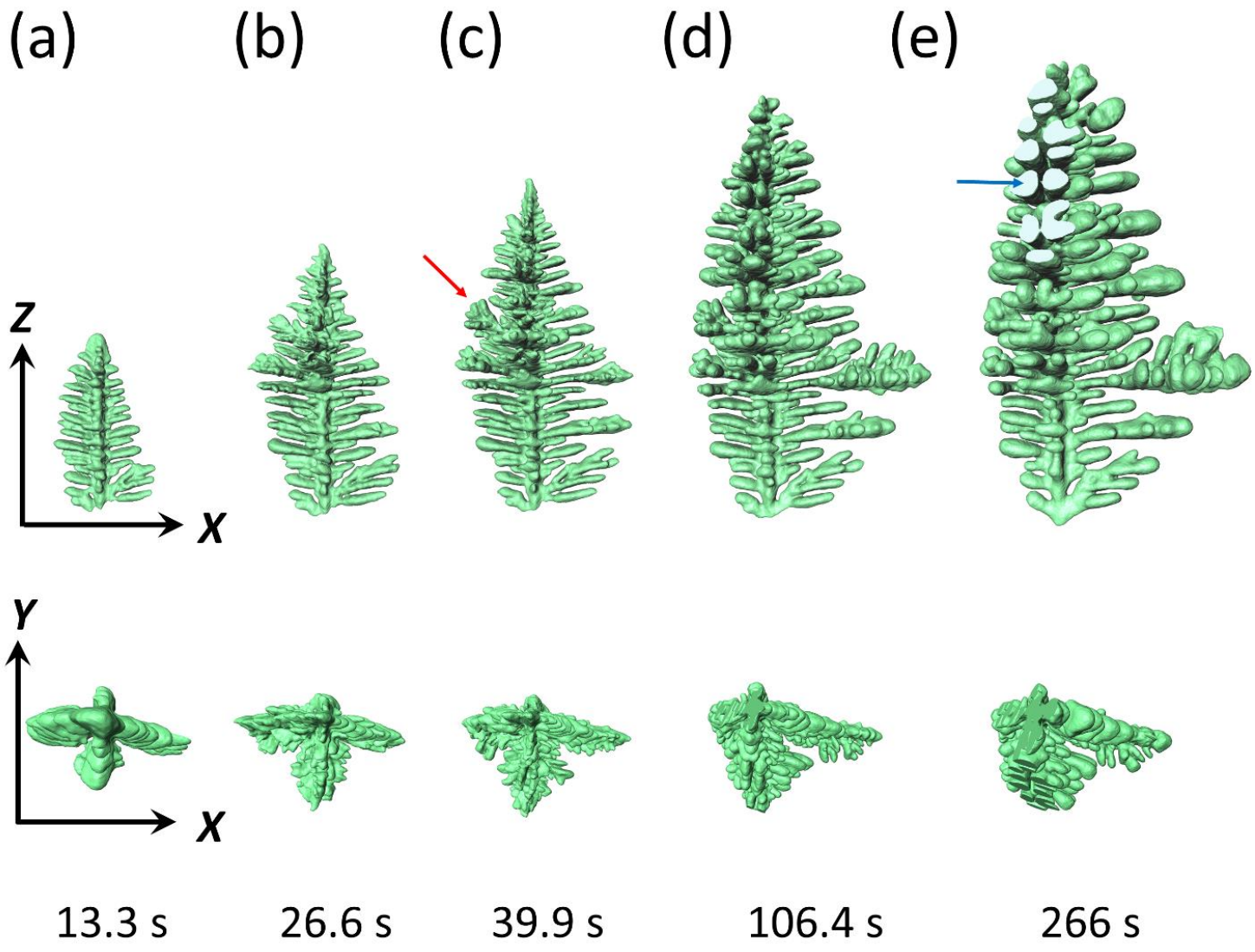

Figure 6.4 The typical 3-D morphological evolution of primary α-Al dendrites manually selected from Figure 6.2 during solidification process

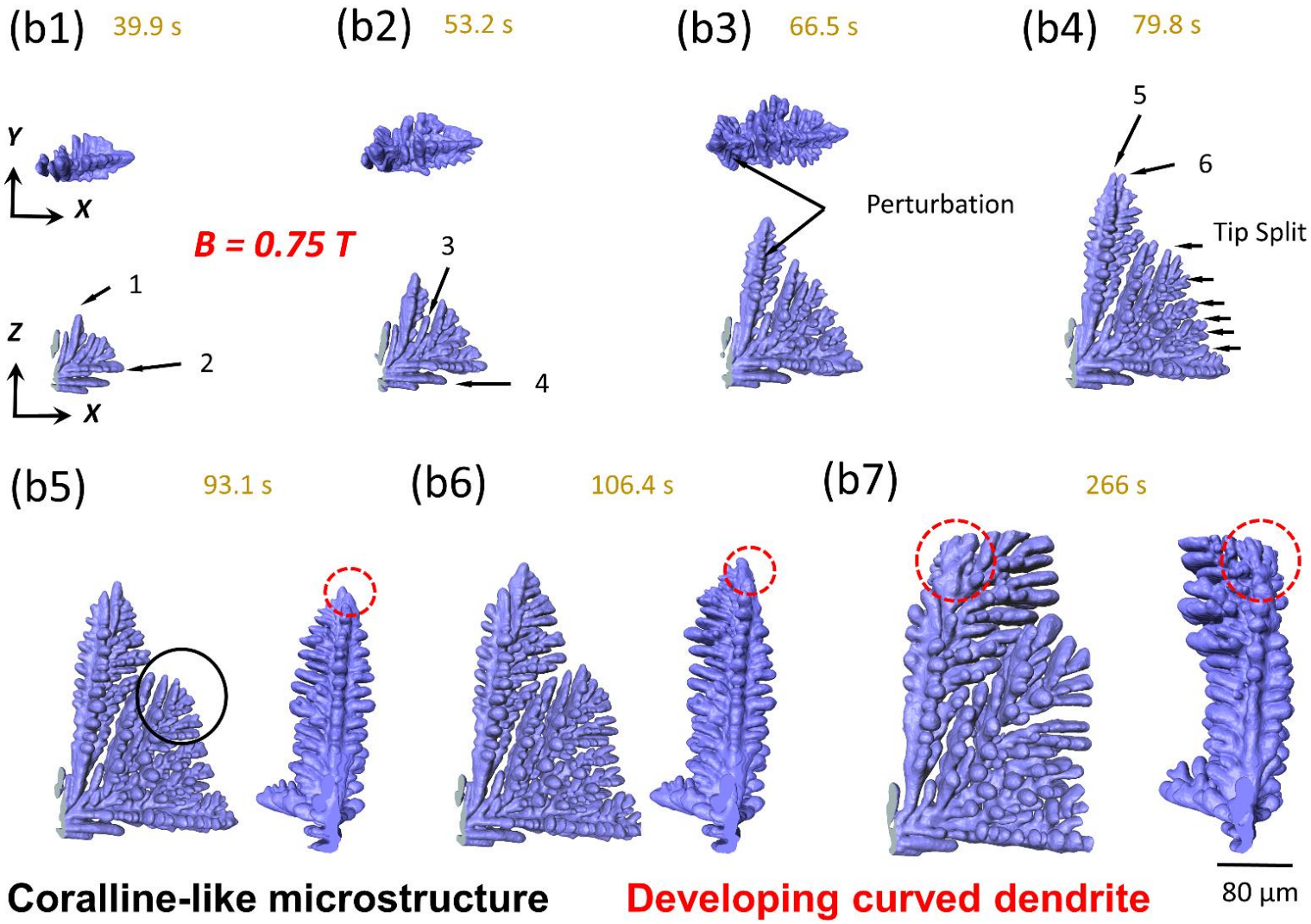

Figure 6.5 The typical three-dimensional morphological evolution of primary α-Al dendrites manually selected from Figure 6.3 during solidification process with 0.75 T magnetic pulses.

6.3 Quantification of solidifying structural evolution

6.3.1 Evolution of solid fraction and surface area

The solid fraction (f_s) calculated from the 3D datasets for both cases as shown in Figure 6.2 and Figure 6.3. According to Gibbs *et al*. [112] study, the driving force of f_s evolution is the undercooling at very early period solidification (before the f_s over 20%). After that the cooling rate dominates the Al dendritic growth in subsequent solidification process. I focus the evolution of Al dendrites at the early stage of solidification and all obtained f_s values are beyond 25% for both cases as mentioned above, therefore undercooling is identical.

The S_v quantifies the average grain size in certain domain. The decreasing of S_v leads to the increasing of the average feature size. The normalized surface area of the solid–liquid per unit volume of solid phase (S_v) in Al-15%wtCu alloy is shown in Figure 6.6.

The evolution of S_v on multi-scale of the zoomed individual dendrite (276 × 227 × 130 for no PMF case, and 130 × 162 × 260 μm^3 for the PMF case) and the entire sample (1.3 mm^3) for are plotted. Guo *et al*. [51] suggested that the Cahn model is more accurate at later solidification stage when f_s is higher than 50% which cannot be applied to our study. However, the Poirier model originated from Lifshitz-Slyozov-Wagner (LSW) model is employed here to quantify the evolution of dendritic growth. The law of Poirier model [113, 114] is written as:

$$\frac{S_v}{S_{v0}} = [1 + k \times (S_{v0})^n \times t]^{\frac{-1}{n}} \quad (6.1)$$

S_{v0} is the initial value of S_v, S_v is variable with different datasets, k and n are fitting number parameters.

For no PMF case, the evolution of S_v on the individual dendritic scale and on the entire sample scale were fitted with n = 2.66 and n = 2.72, respectively. Our results are comparable with results obtained by Terzi *et al*. (n = 2.1) study [115] for Al-10%wtCu alloys. There is little difference of S_v between the individual scale and the whole sample scale during 100~200 *s*. Hence, the mechanisms of S_v evolution that act on dendritic scale are likely to be representative of overall volume for solidification without any PMF.

For no PMF, S_v deviation between these two scales (red stars and black squares) can be observed after 200 *s*, because we have to crop the same volume (region of interest) for visualization, comparison and quantification of the individual dendritic branch. Moreover, this rule also applies to the PMF case. The fitting values for individual dendritic scale and the whole sample scale were n = 4.52 and n = 2.78 respectively, demonstrating the PMF significantly affect the dendrites evolve at local area. Initially, the values are similar before 66.5 *s* for individual dendrite and sample scale. However, the increasing S_v deviation (blue and orange triangular) shows that the whole sample evolves quicker than the single dendrite. Interestingly, the tip-splitting are frequently observed in 66.5~79.8 *s* shown in Figure 6.5(3–4). This side-branching events happens in the same time at different sub-region resulted the extensively change of S_v in whole region. Hence, the degree of dendritic evolution need to pay attention when evaluating the large RoI volume during solidification under the PMF.

Also, the fitting *n* is 2.78 for the PMF case is closer to 3 than the no PMF case (*n*=2.72), presenting the dendrites are likely exhibited the globular shape when the PMF is applied (Because the Poirier model ($S_v/S_{v0} \propto t^{-\frac{1}{n}}$) explains that

formation of globular structures when *n* is close to 3). Hence, the strong anisotropy is degenerated as observed from Figure 6.2 to Figure 6.5.

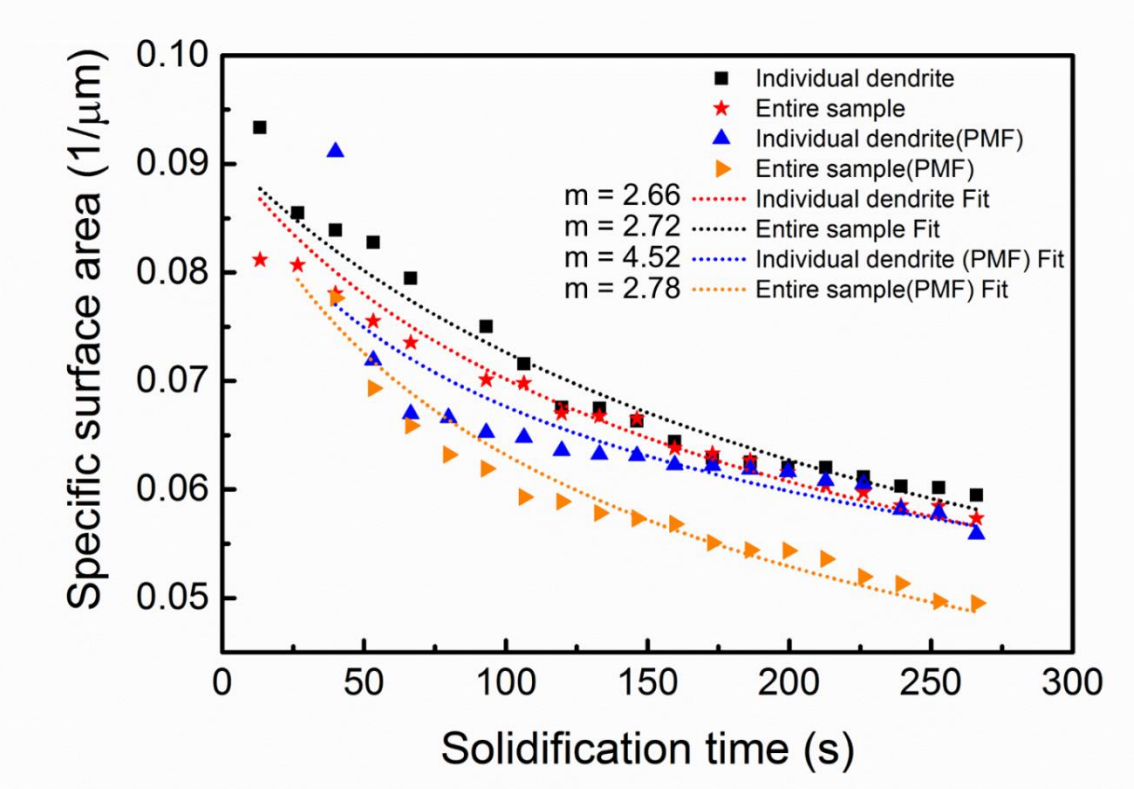

Figure 6.6 The α-Al dendritic specific surface area (S_v) (normalized entire sample scale and individual dendritic scale) evolution with time during solidification with and without the PMF, and the corresponding fitting curves by using Poirier's model.

6.3.2 Competitive growth mechanism and curvature

The growth competition with the PMF has not been reported via 4D in-situ. In Figure 6.7a, three dendritic branches (DB) are selected from Figure 6.3, demonstrating a more complicated mechanism of growth competition during solidification with the PMF. Obviously, this mechanism validates and compensate

the model proposed by M. Azeem *et al.* [58], because the magnetic pulse factor is introduced in this experiment.

Firstly, the DB2 and DB3 able to freely grow out in the melt and their lengths on X–Y plane are almost same at 106.4 *s*. DB3 lost the competition to DB2 in the following time. As can be seen, DB2 rapidly grow in horizontal direction and almost filled the view field at 252.7 *s*. The length of DB3 hardly increased except coarsening process, because the significant growth of DB3 blocks the subsequent solute transform and liquid might be trapped at the interdendritic between DB2 and DB3. Later, at 133 *s*, DB1 and DB2 grow in close proximity to each other shown in Figure 6.7a2. Suddenly, DB1 stopped growing up along Z-axis and give its way to DB2 before impingement shown in Figure 6.7a3–4. DB1 tips have to grow horizontally due to suppression and restriction by DB2 growth. Interestingly, I found that the higher-order dendritic arms on DBs grow upwardly and these arms are rarely resolved at bottom of DBs. This phenomenon is attribute to the interaction of thermal gradient and magnetic alignment.

Moreover, the curvature (red and blue colours correspond to large and negative curvatures respectively) evolution with PMF is present in Figure 6.7a. As solidification advances, both higher positive value at tips and lower negative values at root are reduced and dominated by zero curvature (green colour), indicating the coarsening also happens even at early stage as I already observed in Figure 6.4.

To further quantify the degree of curvature, the evolution of distribution of mean curvature for entire sample scale and individual dendritic scale during solidification for both cases are calculated in Figure 6.7b. Generally, the distribution becomes narrower with increased time and toward to zero value.

The all initial mean curvature shows a normal distribution with a negative peak. The distributions become narrow and with a peak shifts towards zero for both cases as solidification advances. When peak shifts from either negative side or positive side to zero, suggesting that the curved surface of dendrites becomes flatter. The distributions with the PMF (dot lines) shift more distance to zero than the no PMF case (solid lines) shown in Figure 6.7b. Correspondingly, 4D observation unambiguously demonstrates that the flat-shape dendrites are frequently observed during solidification with the PMF in Figure 6.5.

In Figure 6.7b1, the normalized frequency are significantly different with the PMF for entire sample scale. At t =39.9 s, the peak value of distribution has slight difference (0.2). But the peak value increases dramatically with application of the PMF. At t =266 s, the peak value is 0.13 for the PMF case and is almost 1.5 times higher than the no PMF case (0.075). However, the PMF has less impact on normalized frequency for the individual dendritic scale shown in Figure 6.7b2. For example, at t =212.8 s, the peak value (0.065) with the PMF is just slightly higher than the no PMF case (0.055).

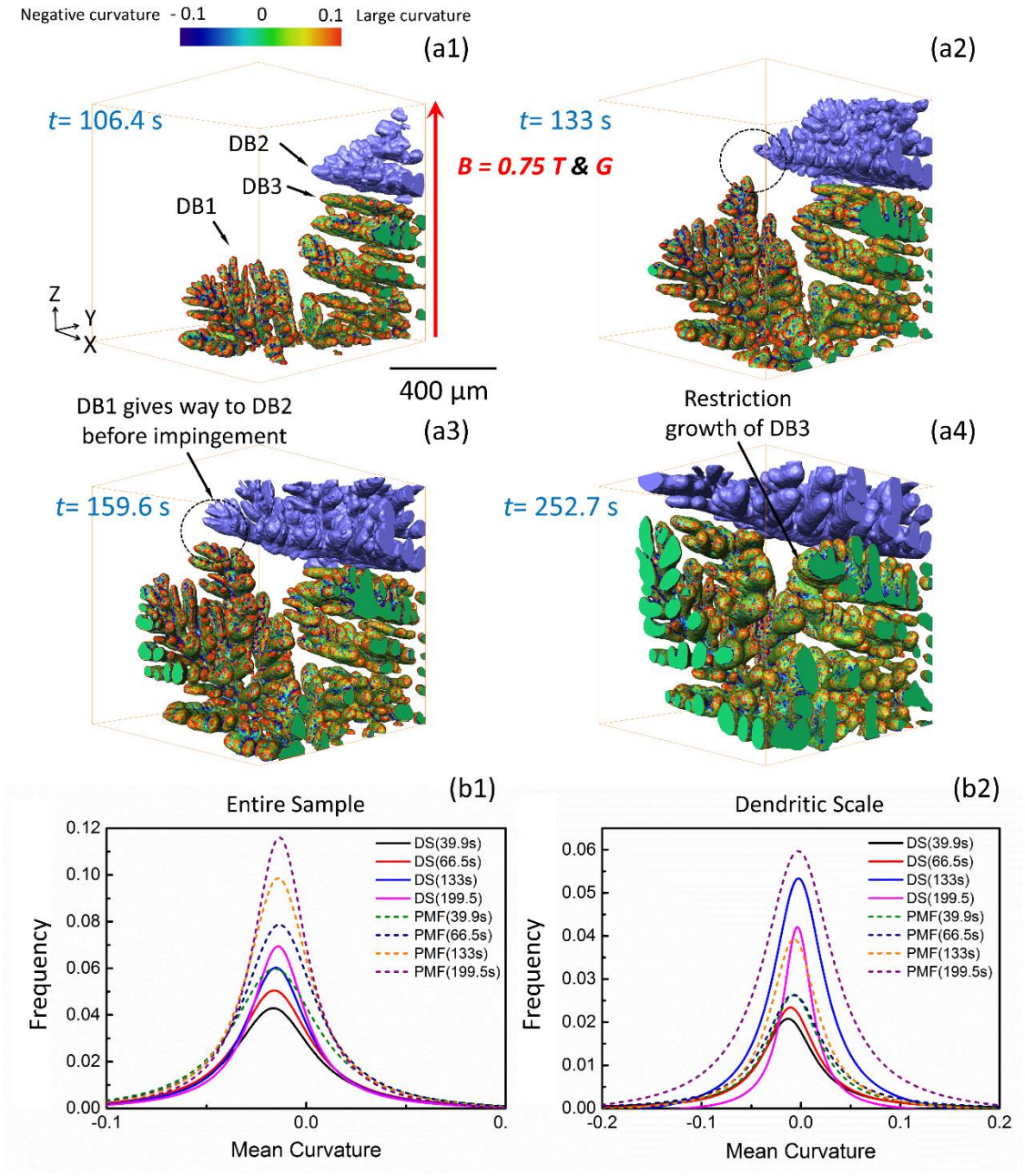

Figure 6.7 (a) Dendritic growth competition with the PMF. Two main dendritic clusters were rendered (One is labelled by purple, the other is rendered for demonstrate the mean curvature evolution); (b) the evolution of mean curvature (characterized in entire sample and individual dendrite scales) at the L–S surface with and without the PMF.

6.3.3 Dendritic growth

4D sequence of tomograms enables to predict of the α-Al dendrite growth kinetic with time. Four secondary dendrites (D1P – D4P) are carefully selected from the PMF case in Figure 6.3 and another four SD arms (D1S – D4S) are also selected from no PMF case from Figure 6.2. In Figure 6.8a–b shows the evolution of normalized dendritic length ($\Delta L = L - L_0$, where L presents the dendrite tip position at certain time and L_0 is the initial tip position) during solidification for with/without the PMF. The corresponding dendritic arm tip growth velocities are shown in Figure 6.8c.

The dendrites in growing included two stages: the initial free growth driven by undercooling and reach an asymptotic value driven by cooling rate (physical impingement may occur at high f_s).

In Figure 6.8a, the SD lengths and their growth velocities vary from arm to arm, measurement shows four dendritic arms have different initial slopes (before 100 *s*) and the respective plateaus values. The range of ΔL is from 386~1093 *μm* for no PMF case. The impingement hinders the subsequent growth for dendrite arm D1S and D4S after 133 *s*.

However, by adding the PMF during solidification, dendritic arm lengths and their tip speeds demonstrate the similar kinetic behaviour as shown in Figure 6.8b, and the range of ΔL is from 947~1149 *μm* with pulse, e.g. at t=26.6 *s*, dendritic D4P has highest growth rate, but after 199.5 *s*, the longest length of dendrites is D1P and continually gradually grows until out of view region.

The curves of dendritic length are fitted by using a Kolmogorov-Johnson-Mehl-Avrami (KJMA) model [116, 117], which describes the kinetics of phase

transformation involving nucleation and growth. This model is valid for general non-isothermal solidification and can be written as below:

$$L\,(t) = L_0\,\{1 - \exp[-\alpha(t - t_0)^n]\} \tag{6.2}$$

Where L_0 represents the asymptotic length value of dendrites, t_0 is initial period of nucleation, n is known as Avrami's exponent and α is reaction constant. A. Bogno [118] quantified n as 2 or 3 based on X-ray radiography experiment. In this article, there is good agreement between theoretical KJMA model and our experimental data shown in Figure 6.8a-b. The Avrami's exponent n for the PMF case (0.85~2.02) is considerable higher than no PMF case (0.38~0.82).

Results show the tip velocity has no consistency over time and has different growth manners of tip velocity with/without the PMF. The foremost tip velocity is in range of 0~25 *μm/s* and there is slight difference in growth rate between with the PMF and without case. Only a decelerating tendency is found for no PMF case. However, dendritic tips D1P & D2P curves illustrate an accelerating and a decelerating regime together for the PMF case. The heat flow at local area governs the acceleration or deceleration of tip velocity. The tip velocity increase (an accelerating stage) with the PMF is attributed to the modification of thermal property induced by the PMF. The PMF not only provides an extra energy into the system but also enhance the fluid flows. Finally, all dendrite tip velocity towards zero at last. The slowdown of tip velocity due to the interaction of neighbour dendrites, adjacent dendrites reject the Cu-rich solute at interface and the restriction of diffusion (the solute pile-ups) [119].

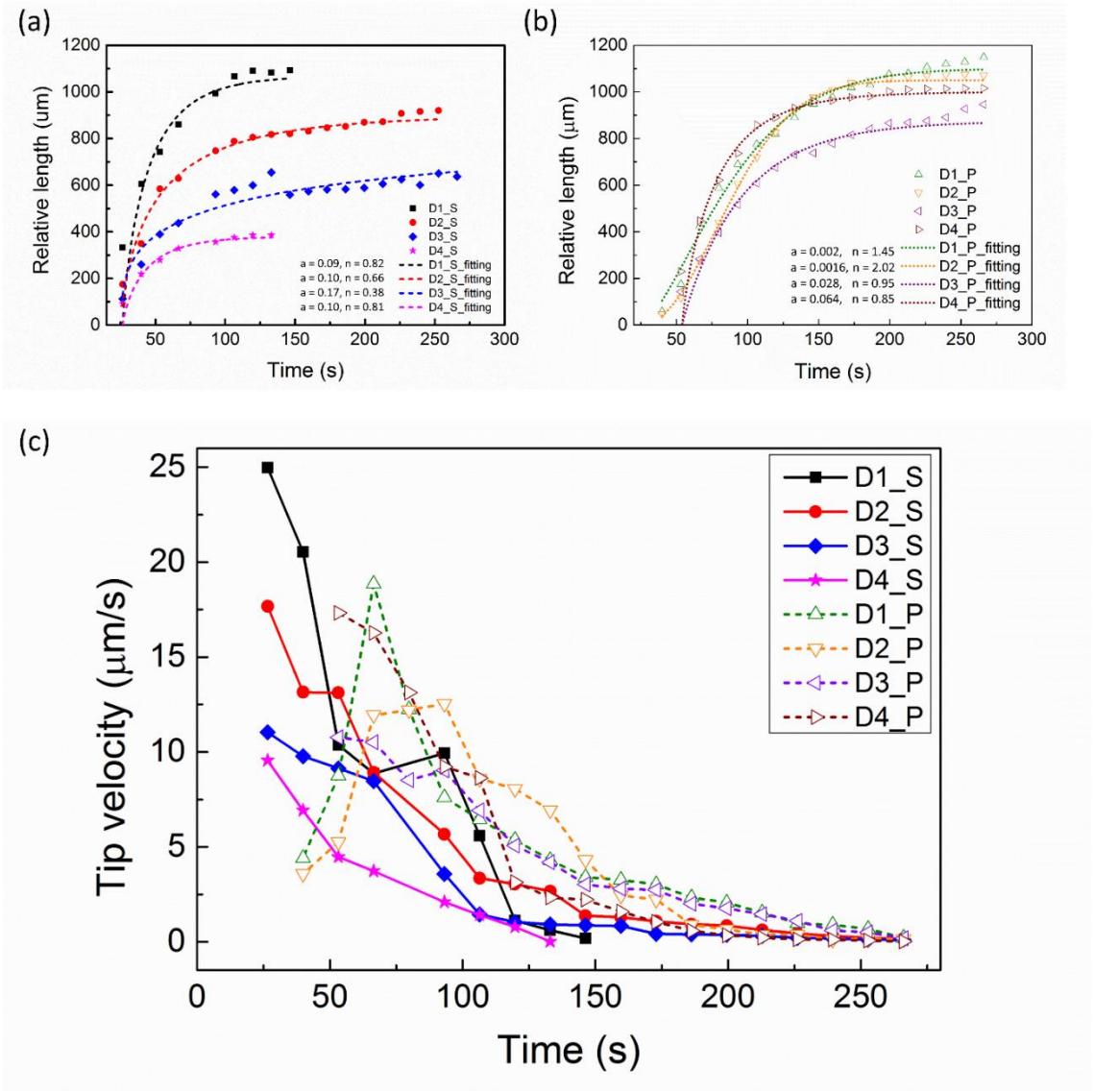

Figure 6.8 The measurements of relative length (dash line fitting with KJMA model) of primary α-Al dendritic arm evolution in Al-15%wtCu alloys (a) without and (b) with the PMF; and (c) corresponding tips' growth rate without (solid line) and with the PMF (dash line).

6.3.4 Fluid flow – Permeability models

The rate of viscous fluid flow through a porous medium is proportional to the pressure gradient and the permeability *K* (called Darcy's constant). The Kozeny–

Carman relationship could be expressed in different ways depending on which grain structure. Hence, the grain size is the major factor for estimating the permeability in a domain, and microstructures with the PMF are unique from observation in Figure 6.5.

For simplicity, the permeability of the interdendritic flow parallel to the primary dendrite arms in no PMF case can be calculated using the modified Kozeny–Carman relationship as follows [120]:

$$K_1 = \frac{\lambda_2^2 (1- f_s)^3}{180\, f_s^2} \tag{6.3}$$

where f_s is solid fraction, λ_2 is the secondary dendrite arm spacing measured in datasets. As described above, the globular microstructures (degeneration of strong anisotropic grains) are likely seen for the PMF case since the quantification of S_v (n=2.78 is close to 3) in Figure 6.6. Therefore, the modified Kozeny–Carman relationship for the PMF should slightly different with Eq. 6.3 and can be written as follow [120]:

$$K_2 = \frac{d^2 (1- f_s)^3}{180\, f_s^2} \tag{6.4}$$

where d is the grain size of the equiaxed grains measured in datasets.

For both cases, the values of λ_2 and d are measured at least three times to make sure the accuracy. In Figure 6.9, the permeability against the solid fraction was plotted to demonstrate the interdendritic flow inside the whole sample volume. Overall, the permeability of K_2 is higher than K_1 value after f_s reaches to 6%, providing a strong evidence that the PMF increase the flow during solidification. Value of K_2 ($4261 \times 10^{-12} m^2$) is almost two times higher K_1($2161 \times 10^{-12} m^2$) when f_s reaches to 10%. The improved permeability might improve the diffusion

and reduce the solute pile-ups at L-S interface, and reduce final porosity fraction during subsequent solidification. The transition from columnar dendrites to fined globular dendritic in grains is strongly attributed to enhanced permeability induced by the PMF.

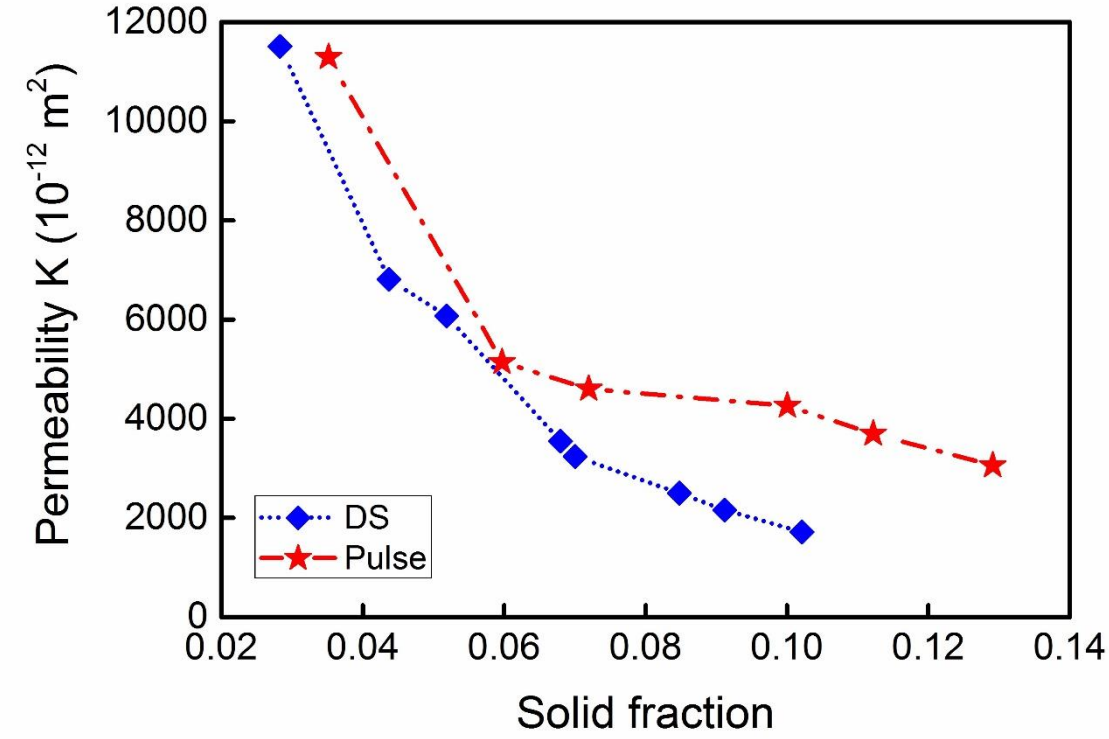

Figure 6.9 The estimated permeability K_1 and K_2 without/with the PMF based on modified Kozeny–Carman relationship with different grain morphologies, demstrating the increased flow at the interdendritic areas when the PMF is applied.

6.3.5 Skeletonization – A new insight to quantify complex structures

The skeletonisation available in Avizo® to peel off the 3D network of the irregular dendritic phases (same features from Figure 6.2 but transparent with theirs' skeletons inside shown in Figure 6.10a1) down to skeletons (Figure 6.10a2).

These skeletons also represent the estimated thickness (2~25) with connecting nodes. The results after thinning process is quite credible and can be used for further statistical analysis.

As discuss above in Figure 6.3, the loads of fragmentation are observed between 39.9 and 53.2 *s* with the PMF. In Figure 6.10b, the quantification of the number of branching nodes evolvement verify the observation. Statistical dendritic branching nodes are firstly used for in-depth directly quantifying and understanding fragmentation events. For instance, with 0 T, the number of nodes stops increasing after reaching at the maximum value (~3000) before 53.2 s, and coarsening might be responsible for the decreasing node number. While, with 0.75 T, node number keeps increasing until 226.1 s. Finally, the node number with PMF (~4500) is almost double than no PMF case (~2200). The promotion of nodes is attributed to fragmentation and side-branching induced by the PMF between 26.6 and 226.1 s since cooling condition is identical.

Figure 6.10c&d show the relative frequency distribution of primary α-Al dendritic length and phase orientation at 133 s (randomly selected). I quantified hundreds of dendrites. The Al dendrites are oriented to higher (75~90 deg, red columns) or lower angle (0~25 deg) under the PMF, showing the alignment of dendrites. Interestingly, the statistical result of length distribution in Figure 6.10c is consistent with manual measurements in Figure 6.8a–b. The length distribution in Figure 6.10c shows that the range of length is between 600 and 1350 μm with the PMF and over 50 percentage of dendritic lengths are longer than 750 μm, while length range is 200~1050 μm without the PMF and almost 80% dendrites

are shorter than 450 μm. The length results demonstrate that the PMF is responsible for length elongation.

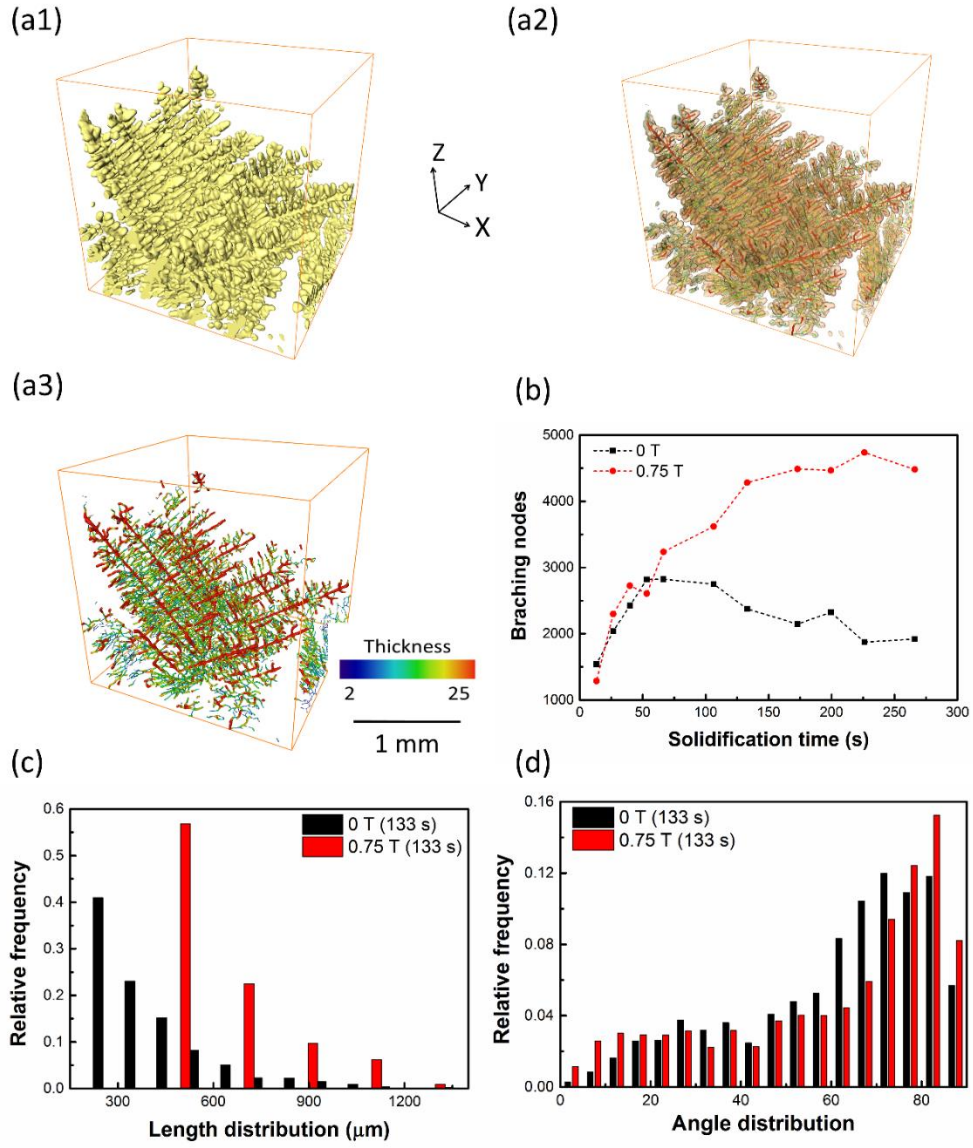

Figure 6.10 A typical example shown (a1) the original microstructures; (a2) the transparent microstructures with theirs' skeletons inside and (a3) the dendrites were peeled down and only keep their skeletons. The statistical results of Al dendrites tomography with and without PMF show: (b) the branching nodes with solidification time generated from skeleton function, and primary α-Al dendritic (c) angle and (d) length distribution at 133 s.

6.4 The coarsening of α-Al dendritic phases

The dynamics of multi-dendrites concurrent growth and coarsening of an Al-15wt%Cu alloy during solidification were studied using a highly computationally efficient 3D phase field model (PF) and real-time synchrotron X-ray micro-tomography.

The PF modelling was performed by Dr Z. Guo from Tsinghua University. A block structure adaptive mesh refinement algorithm coupled with a parallel computing scheme was implemented to solve the equations. Using his model, high fidelity 3D phase field simulations of the evolutions of multi-dendrites were achieved in a realistic computing time. The modelling detailed were described elsewhere [121, 122].

Direct comparisons with the time-evolved tomography datasets were made for the first time to quantify the relative importance of dendrite growth and coarsening mechanisms.

6.4.1 4D synchrotron tomography of dendritic morphology evolution

Figure 6.11 shows the time-evolved 3D multi-dendrites of subvolume1 with size of approximately 715×715×715 μm^3. A total of 30 dendrites were identified and found to nucleate initially at the bottom area of the domain, most likely due to a relative lower temperature near the quartz tube wall.

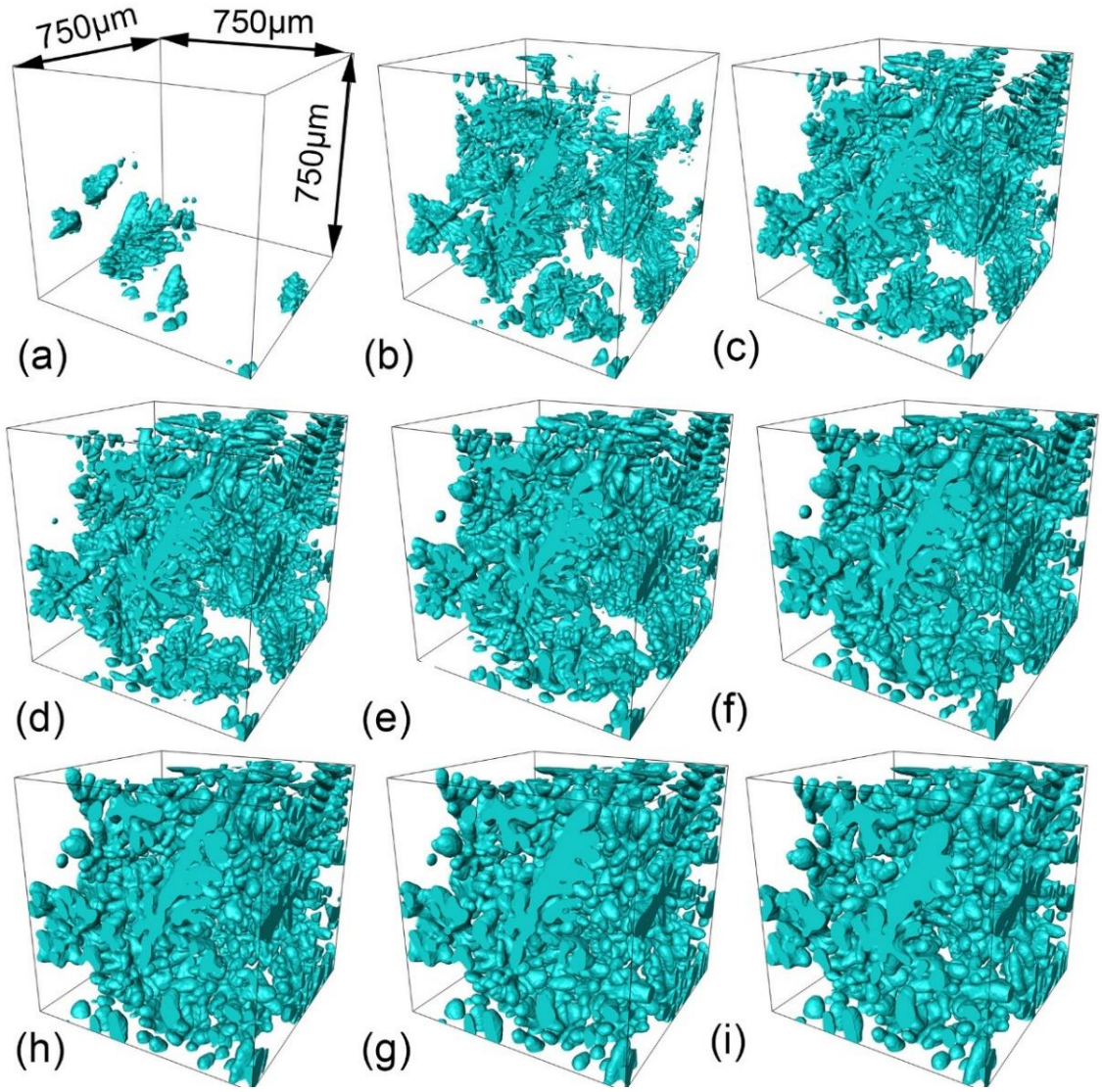

Figure 6.11 Multiple equiaxed dendrites growth and coarsening of an Al-15wt% Cu alloy at the solidification time of (a) 10 s, (b) 20 s, (c) 30 s, (d) 40 s, (e) 60 s, (f) 110 s, (g) 160s, (h) 210 s, (i) 300 s.

After nucleation, the dendrites grew relatively fast and filled the whole sub-volume domain in less than 30 s, as shown in Figure 6.11. Also, dendrites coarsened simultaneously as the dendrites grew but it was much faster at the beginning (comparing the coarsening from Figure 6.11b to Figure 6.11e to that from Figure

6.11e to Figure 6.11i). Actually, the morphology of the dendrites hardly changed after 210 seconds, i.e. from Figure 6.11h to Figure 6.11i.

6.4.2 The phase fields simulations comparing with experiment

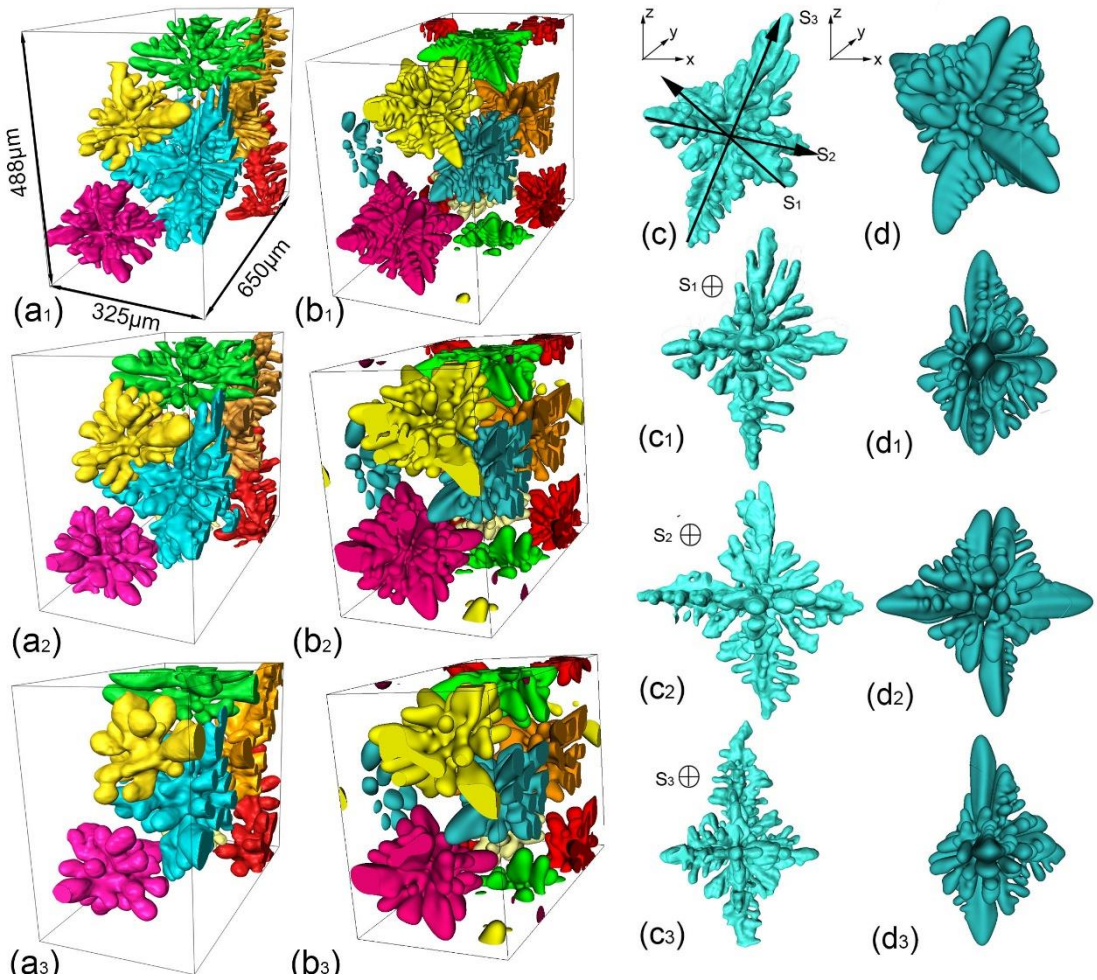

Figure 6.12 Comparison of the multi-dendritic morphology during growth and coarsening and one typical single dendrite morphology (c-d) (at growth time of 30s) between the X-tomography experiment (a1-a3) and phase field simulations (b1-b3) corresponded to the growth time of 30 s, 60 s, and 110 s respectively.

Figure 6.12a-b compares the multi-dendrites between the simulated ones and those from the X-ray tomography. It shows that the dendrites simulated by the phase field model are very similar to those obtained from tomography in terms of morphology and coarsening. Although in the simulation, I did not consider the effect of the nucleation order, i.e. some dendrites were nucleated earlier than the others. One typical dendrite was extracted from simulation and X-ray tomography respectively. Orientation and the morphology of some based slices S_1-S_3 were also compared as showed in Figure 6.12c-d, they all showed highly similarity, which proved the reliability of the phase field simulation in this work.

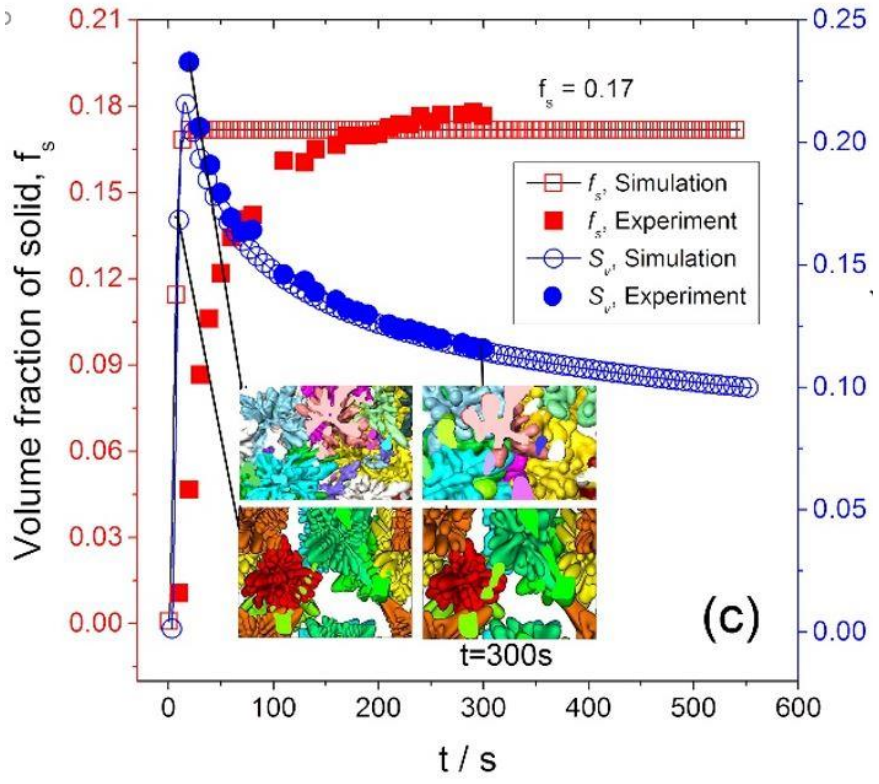

Figure 6.13 The comparison of solid fraction and specific surface area evolutions between X-ray tomography and phase field modelling.

To further quantify the coarsening behavior, the solid volume fraction (f_s) normalized solid/liquid interface area S_v ($S_v = S / V_0$, where V_0 is the total volume of the domain) were retrieved from both tomography and simulated datasets, the comparison of the f_s and the S_v evolutions between experiment and modelling were calculated and shown in Figure 6.13.

The f_s in experiment grew abruptly at the initial stage of solidification and approached maximum value after t = 250 s, However, in the simulation, it took much shorter time for the solid fraction to reach its equilibrium value, i.e. 0.17. Despite the initial difference, the simulated and experimental curves of f_s reached approximately the same value at around t = 150 s, and then maintained the same trends. The reason for the difference was that, in the experiment, the temperature was decreased gradually and the dendrites were nucleated at different times. More importantly, the driving force for dendrite growth was small because the gradual decrease of temperature. Whereas in simulation, the whole domain was set to be isothermal at once and all dendrites grew simultaneously from the beginning of the simulation. Hence, more driving force to grow multi-dendrites from the very beginning of nucleating dendrites. It is important to see that such initial difference does not affect the results after 100 s, i.e. when the whole domain was filled with dendrites, or when the normalized surface area approached its maximum. This gives us a solid confidence that, although no tomography scan was acquired after 300 s due to the storage issue, I can use the simulated data to study the coarsening behaviours in much longer time scale.

6.5 Discussion

6.5.1 Effect of PMFs on Al dendritic fragmentation

With the PMF, the pull and pressure electromagnetic forces coexist simultaneously in a short period. However, the pressure force is dominated. The pressure force can be substituted by a radial direction force and an axial direction force. The radial direction force leads to pinch effect and produces electromagnetic compressive vibration (The vibration will diffuse and superpose to produce the pressure wave), and convection is attributed to axial direction force according to A. Kelesnichenko [123]. The sample volume is relative small, therefore the forced convection might be ignorable in this article.

Generally, mechanisms of dendritic fragmentation have been studied extensively in the past. For example: (1) remelting model driven by thermal instability; (2) pinch-off (Gibbs–Thompson) model; (3) mechanical fracture induced by shear stresses.

I examined all the possibilities. Firstly, there is no strong thermal fluctuation leading to structure remelting. Secondly, in Figure 6.7b, the large negative curvature was minimized and lead to reduce the root area of dendrite arm. However, this mechanism requires longer times to happen. Hence, pinch-off [108, 109] is not main the driving factor in this study. Thirdly, when the radial pressure forces periodically generated, the periodical pinch effect simultaneously occurs and stir the melt. The pinch pressure [95] created by the electromagnetic force is demonstrated in Eq. 5.7. The sample radius of 1 mm, the aluminium permeability is close to $1.25 \times 10^{-6}\ \mathrm{H/m}$ and the induced current density in the Al molten melt is 10^3 A/mm^2 [47]. Hence, the pinch pressure is in range of 0.025~0.32 MPa from

620 to 600 ^{o}C as shown in Figure 6.14. (1) Pilling [97] proposed the yield stress is 0.6 MPa for Al alloy at 540 ^{o}C and (2) D. Eskin [124] found the ultimate tensile strength (UTS) of Al-5%wtCu alloy in the temperature range of 587~617 ^{o}C is 0.15~0.25 MPa. By comparing the pinch pressure and above referenced values, it is highly possible that pinch stress could shear off the small Al dendritic arm at low f_s stage and therefore lead to the fragmentation. The real-time observation in Figure 6.3 confirms my proposed mechanism.

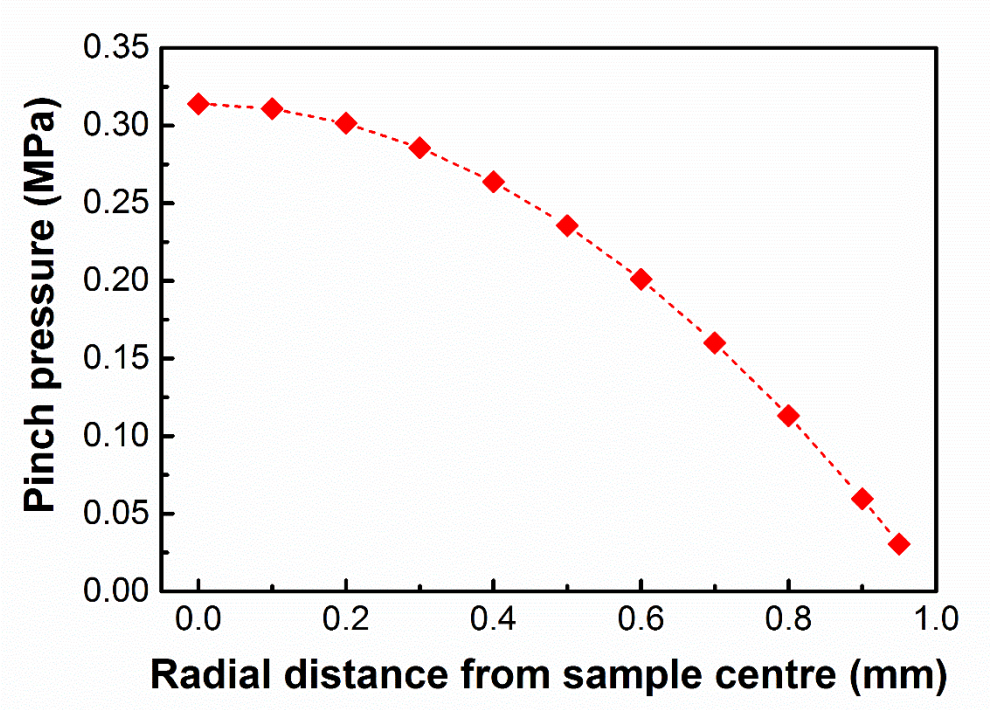

Figure 6.14 The variation of pinch pressure stress induced by the 0.75 T PMF on the Al dendrites with geometric parameter (radial distance from sample centre).

6.5.2 Effect of TEMHD on crystal growth

The experimental observation (Figure 6.3) of low anisotropy structures and formation of seaweed-like structures (Figure 6.5) in the presence of a 0.75 PMF might be attributed to convective transport of solute by thermoelectric magneto hydrodynamics (TEMHD). The TEMHD is briefly introduced in Chapter 2.4.

According to A. Kao *et al.* [75] study, the thermoelectric field $S\Delta T$ is in the direction of the thermal gradient causing current to pass along the inside of the dendrite emanate by the tip and pass through the liquid back down into the mushy zone forming a closed loop. This is highlighted in Figure 6.15a, which shows contours of J_z in planes parallel and normal to the growth direction.

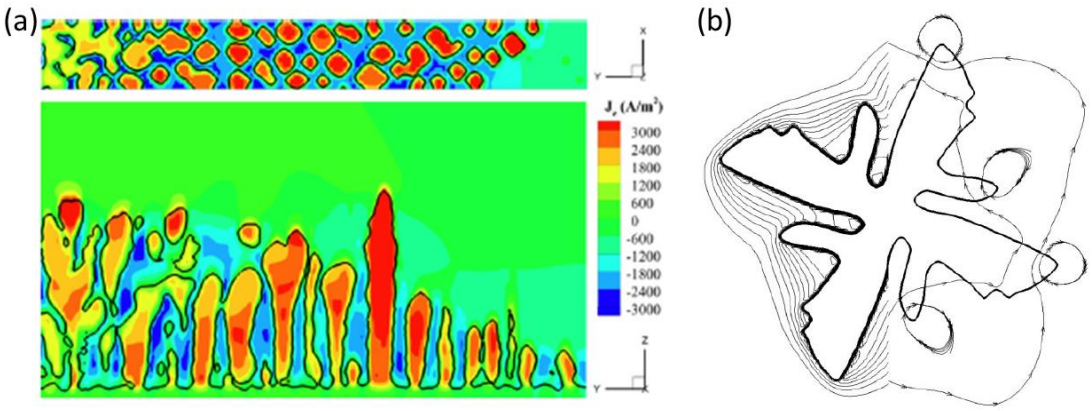

Figure 6.15 (a) J_z. Top: x, y plane. Bottom: y, z plane; (b) Left: solute concentration of dendrite growing in high magnetic field. Right: velocity streamlines using approximation of flow entering z-direction and going around crystal.

The current is localised to the mushy zone and does not extend into the bulk liquid. In the presence of the magnetic field this current generates a Lorentz force. The solid dendrites are considered to be rigid and the Lorentz force is essentially

balanced by structural forces. In the interdendritic liquid, the Lorentz force drives fluid flow and this force is balanced by viscous drag pressure gradient and electromagnetic damping.

A. Kao [125] also found the tip velocity is increased with magnetic field compared to the case of stagnant growth without magnetic field via a numerical model. Same conclusions have been obtained via my in-situ experiments (especially for Al_3Ni intermetallic in Figure 5.5b).

The TEMHD is strongly dependent on the orientation of the magnetic field relative to growth direction. He proposed that original growth orientation is changed in presence of magnetic field since one dendrite would experience the movement which is due to the transport of the solute and thermal fields as Newtonian forces have not been considered. The movement is caused by a high velocity recirculation at the tip as shown in Figure 6.15b, causing the colder fluid not to be directed normal to the preferred direction of growth. This flow, on the side of the dendrite tip, will cause the local free energy to be higher on this side and as the flow passes over the dendrite, hotter fluid is deposited which lowers the free energy, stunting growth. This leads to a clockwise rotation in an anticlockwise flow [125].

Although his simple model only consider single dendrite in 2D shape, it would be helpful to explain my experimental findings for primary dendritic phases and intermetallic phases which demonstrated that growth orientation is significantly changed. The circulating flow by TEMHD (i.e. shown in Figure 2.30b) influences

the evolution of structural patterns during the solidification process. For future research, the time-resolved 3D microstructures are needed for simulation, because it will give geometric and actual situation. Hence, my real-time semi-solid datasets obtained from synchrotron is crucial for modelling validation.

Chapter 7: **The formation of Fe-rich intermetallics**

This chapter is present the preliminary investigation of the effects of pulse electromagnetic field processing on the microstructure of an Al-5%Cu-1.5%Fe-1Si alloy. Fe-rich intermetallic phases are usually reducing the homogeneity of cast alloy and the properties e.g. toughness, strength and corrosion, etc.

The evolution of solidification structures is characterized by scanning electron microscopy (SEM) and ultrafast synchrotron X-ray tomography at ID19 beamline of ESRF. The effects of PMF of different magnetic fluxes on the microstructure refinement and dispersion of the Fe-rich α- and β- intermetallic phases are in-situ observed.

7.1 2D microstructures via electron microscopy

Effects of PMFs on primary phase & Fe-rich intermetallics

Backscattered electron microscopy (BSE) was used to reveal better imaging of the composition of the alloys. In this thesis, images are taken from the bottom of each cast samples with magnification of 100 x and 400 x since the Fe intermetallic has higher density than melt during solidification.

In Figure 7.1, the left column shows a better comparison of dendritic growth at low magnification (100 x). The grain refinement of primary Al phases is achieved since there is a structure transition from big dendritic columns with no pulse to globular microstructures with 0.2 T pulse which particularly distributed in the

middle of sample. The PMF not only can affect the growth of primary phases but also has significant impact on the microstructure of Fe intermetallic phases.

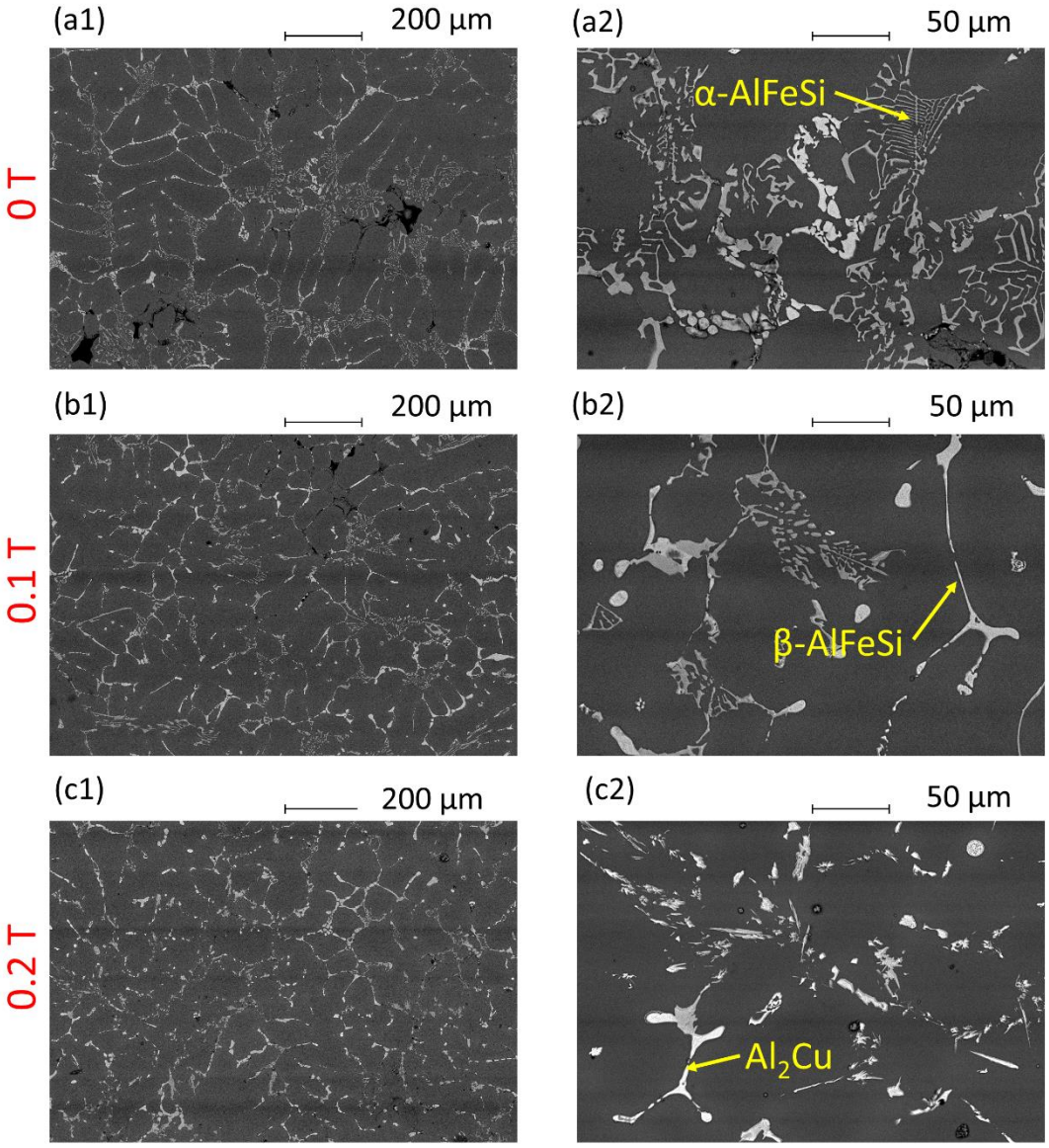

Figure 7.1 The 2D SEM images of Fe-rich phases with low (100 x) and high (400 x) magnification under different intensities of pulse magnetic fluxes: (a) 0 T; (b) 0.1 T and (c) 0.2 T.

At higher magnification of 400 x, the right column shows that the 2D size distribution of Chinese script-like of α-Al_8Fe_2Si is significantly reduced when a 0.2 T pulse was applied. The input magnetic pulses can degenerate the Chinese script-like features, demonstrating that how Fe-rich phases are increasingly broken as the intensity of the pulse is increased. For example, in Figure 7.1c2 the 0.2 T case shows large amounts of dispersion and decrease in density of the α-Al_8Fe_2Si intermetallics.

7.2 3D microstructures via synchrotron tomography

7.2.1 Fe-rich intermetallics under external physical fields

Two-dimensional Chinese script-like and needle-like Fe-rich intermetallic phases have been reported using advanced electron microscopes [126, 127]. However, very limited reports of the 3D/4D genuine microstructures of Fe-rich phases under external fields. In this study, ultrafast synchrotron tomography (down to 2s per tomogram) scans are performed to provide in-situ experimental evidence of how PMF affect the growth of Fe-rich phases. The experiment details can be found in Chapter 4.

Generally, it is first time, the real-time Fe-rich intermetallics in semi-liquid melt with PMF are presented as shown in Figure 7.2. The three slices are demonstrated that external physical fields (either pulse electromagnetic or ultrasound processing) obviously decrease the formation size of Fe-rich

intermetallics which are considered deleterious to properties, especially toughness.

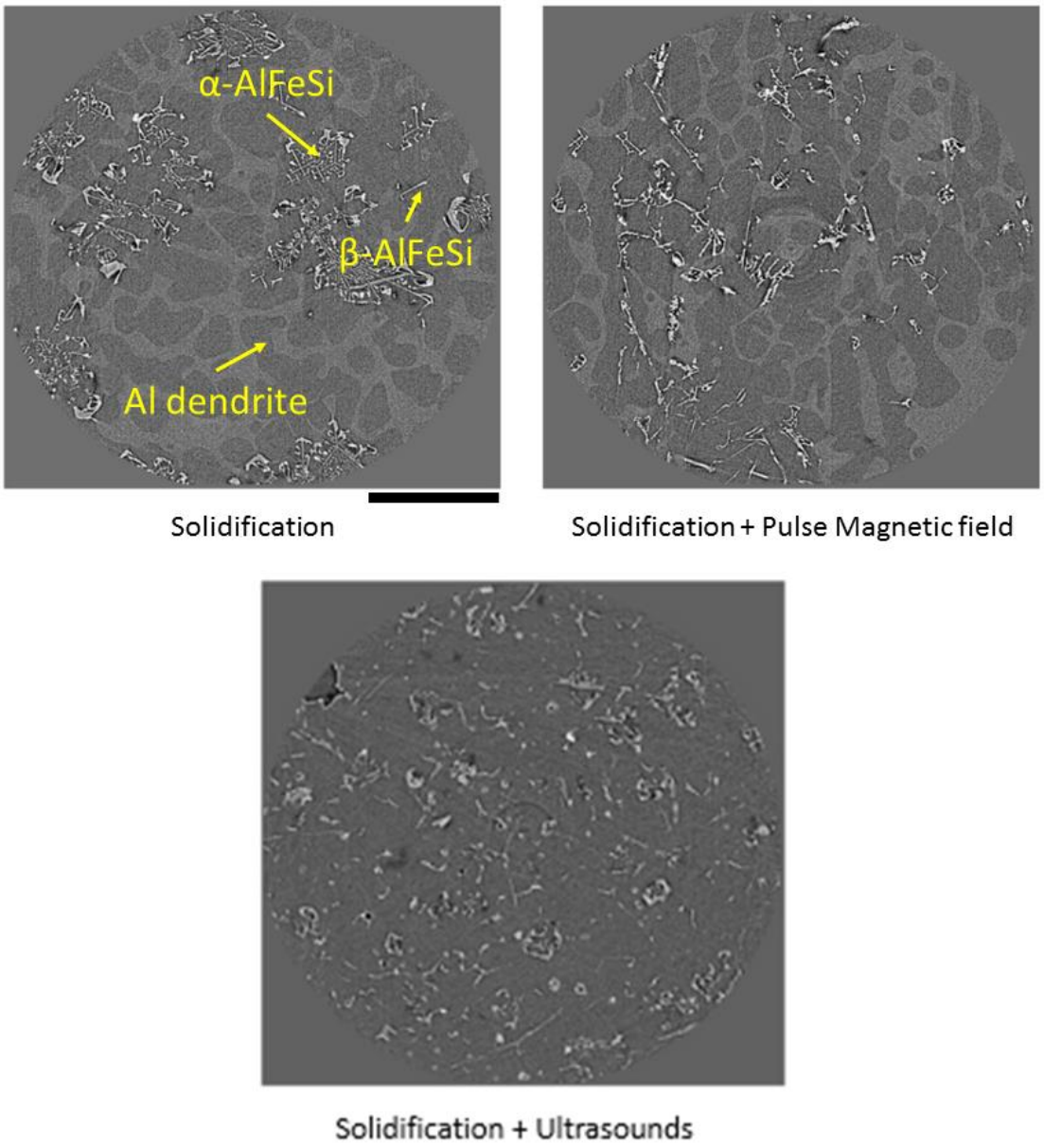

Figure 7.2 2D slices selected from three synchrotron tomograms show that microstructure of Fe-rich intermetallics under different external fields during solidification. Note: the scale bar is 0.25 mm for all slices.

7.2.2 3D morphologies of α-Al_8Fe_2Si and β-$Al_9Fe_2Si_2$ phases

In the Al-Cu-Fe-Si system, final crystal structures of Fe-rich intermetallics have been identified and classified, including α, β, π, δ, γ and θ phases [66]. Among these phases, α- and β- intermetallics have been considerably studied in Al-Cu-Fe-Si alloys [128, 129].

Figure 7.3 shows an example of 3D morphologies of Fe-rich intermetallics during solidification at 0.4 K/s. More time-resolved datasets need to be analysed in near future to reveal the mechanism of nucleation and subsequent growth.

Figure 7.3a is a slice of the 3D raw tomogram. The dark region represents the primary Al dendrites, while the Fe-rich α- and β- AlFeSi phases appear to be lighter since the difference of attenuation coefficient in the photon energy range from 15~30keV (Figure 4.2c).

Figure 7.3 b&d show that α-Al_8Fe_2Si intermetallic has either a complex morphology of a Chinese script (purple) or a simple structure of a petal (orange), while a plate-like (red) of β-intermetallic (Figure 7.3c). The plate like shape often regards as needle-like phase when only 2D section is characterized. The β-$Al_9Fe_2Si_2$ intermetallics are often nucleated either on the tube wall or on the pores in our experiment. The α-AlFeSi phases are less harmful to the mechanical properties than β-AlFeSi intermetallics.

.

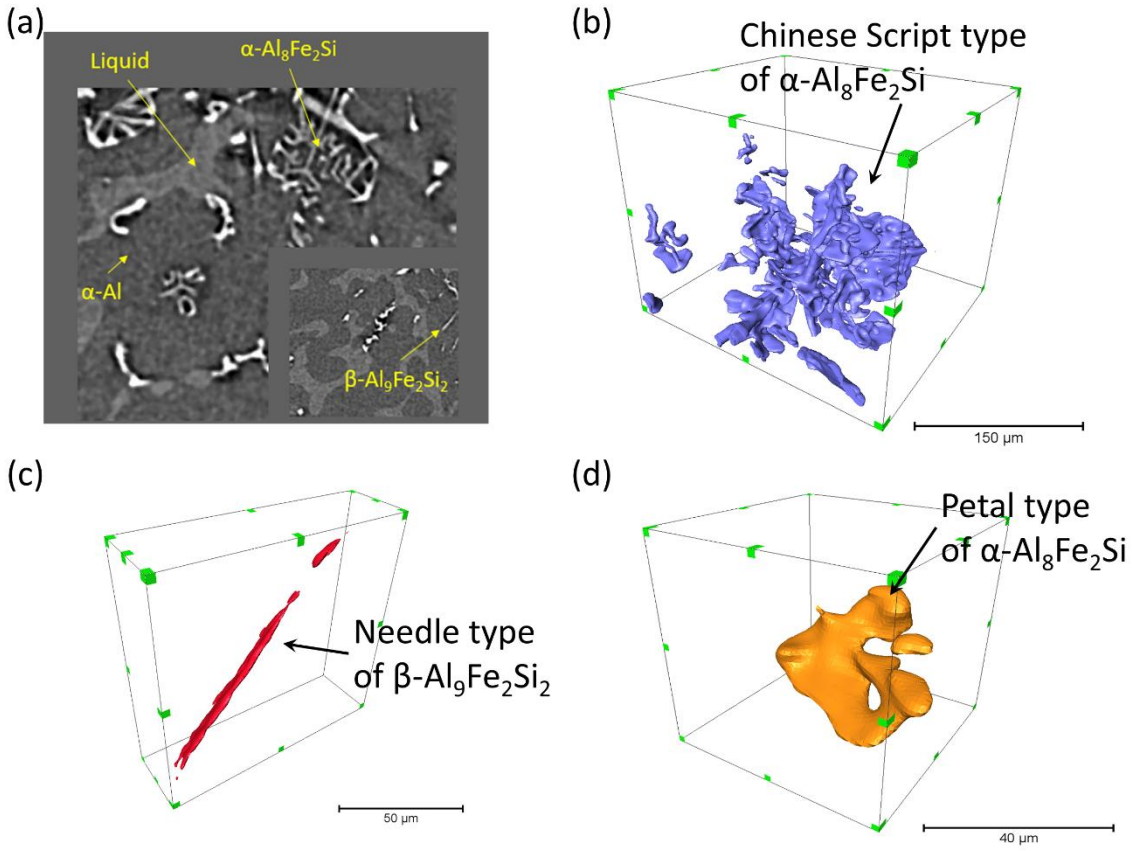

Figure 7.3 (a) 2D slices show the clear phase contrast and microstructures. Typical 3D Fe-rich intermetallic morphologies of (b) Chinese script-like of α-Al_8Fe_2Si; (c) needle type of β-$Al_9Fe_2Si_2$ and (d) petal type of α-Al_8Fe_2Si obtained from synchrotron tomography without PMF.

Figure 7.4 shows two 3D morphologies of α-Al_8Fe_2Si intermetallics (one is purple, the other is dark pink) under 0.2 Tesla of magnetic pulse are demonstrated in same view field. This view field has similar volume with the one has no pulse shown in Figure 7.3b. It is obvious to see that size of Fe-rich phase decrease and the microstructures are consolidating since the length of branching arms is reduced.

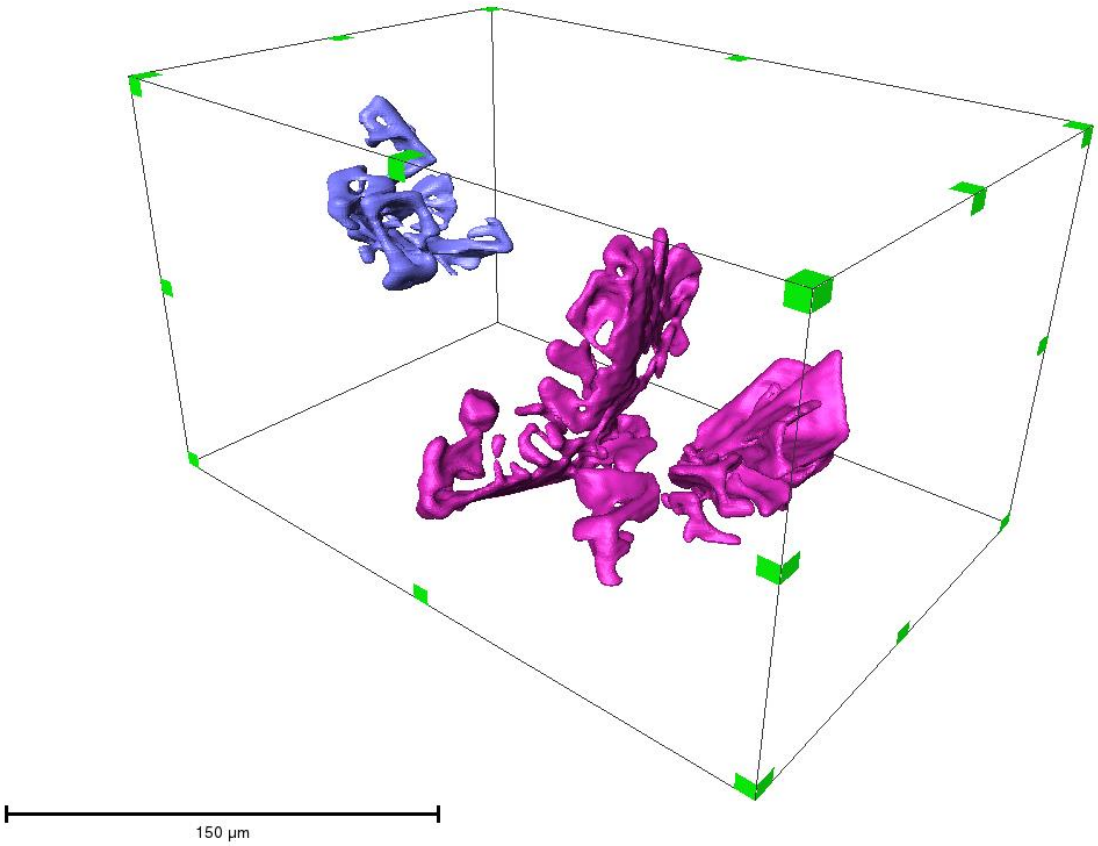

Figure 7.4 The 3D Fe-rich intermetallic morphologies of Chinese script-like of α-Al_8Fe_2Si obtained from synchrotron tomography under 0.2 T of PMF with same cooling conditions shown in Figure 7.3

7.3 Discussion

The evolution of solidification structures is characterized by scanning electron microscopy (SEM) and ultrafast synchrotron X-ray tomography.

Here, few limited datasets have been analysed to illustrate complexity 3D morphology of Fe-rich phases. However, more than 150 datasets under various conditions collected at ESRF have not been revealed. Hence, the 4D observation of microstructures and subsequent quantification were not able to present.

The temperature for resolved phases via modelling (Figure 4.1c) are verified by experiment (Figure 4.8). Characterization results shows the PMFs modify the primary Al dendritic phases and the Fe-rich intermetallic phases. The grain refinement of primary Al phases is achieved since there is a structure transition from big dendritic columns with no pulse to globular microstructures with 0.2 T pulse which particularly distributed as shown in Figure 7.1 and growth of α-Al_8Fe_2Si phases were obviously restricted (Figure 7.4). Quantification of solid volume and length of β-$Al_9Fe_2Si_2$ intermetallic will be presented in journal paper soon. Last, the true 3D morphologies of three different types of Fe-rich intermetallic phases in this alloy were clarified, for the first time, in this research.

Chapter 8: **Suggestions for Future Research**

Following and extending T. Manuwong's research (develop the PMF apparatus and ex-situ tomography characterization), my thesis is a continuing work (upgrade the PMF apparatus and develop an in-situ observation approach) to contribute the EPSRC project (EP/L019965/1).

The in-situ approach is already being used within Prof. Mi's group to study multi-phase materials during solidification under external fields, ranging from eutectic to intermetallic, demonstrating the applicability to the semi-solid conditions.

However, there are also suggestions for future:

(1) The relationship between magnetic flux density and different geometrical of a specific coil. Using an experimental measurement and modelling to establish an intrinsic of this physical fields;

(2) In order to observe highly dynamic events, e.g. the alignment, fragmentation dynamic or even early period of nucleation, a fast-temporal resolution of synchrotron X-ray is needed for further studies;

(3) The larger field of view might need for tomography experiment to reveal the effect of the PMF on semi-solid structures in bulk sample;

(4) Limited solidification and the PMF conditions were in-situ studied. Further synchrotron experiments are highly recommended to yields a processing–structure map which could provide solutions for industry application.

Reference:

[1] E. Hall, The deformation and ageing of mild steel: III discussion of results, Proceedings of the Physical Society. Section B 64(9) (1951) 747.

[2] P. Mohanty, J. Gruzleski, Mechanism of grain refinement in aluminium, Acta Metallurgica et Materialia 43(5) (1995) 2001-2012.

[3] D. McCartney, Grain refining of aluminium and its alloys using inoculants, International Materials Reviews 34(1) (1989) 247-260.

[4] G.I. Eskin, Ultrasonic treatment of light alloy melts, CRC Press1998.

[5] M.A. Easton, M. Qian, A. Prasad, D.H. StJohn, Recent advances in grain refinement of light metals and alloys, Current Opinion in Solid State and Materials Science 20(1) (2016) 13-24.

[6] X. Liao, Q. Zhai, J. Luo, W. Chen, Y. Gong, Refining mechanism of the electric current pulse on the solidification structure of pure aluminum, Acta Materialia 55(9) (2007) 3103-3109.

[7] Z.H.I. Sun, M. Guo, J. Vleugels, O. Van der Biest, B. Blanpain, Strong static magnetic field processing of metallic materials: A review, Current Opinion in Solid State and Materials Science 16(5) (2012) 254-267.

[8] C. Li, Z. Ren, Y. Shen, Q. Wang, Y. Dai, H. Wang, Faceted growth of primary Al2Cu crystals during directional solidification in high magnetic field, Journal of Applied Physics 114(15) (2013) 154903.

[9] X. Li, Y. Fautrelle, A. Gagnoud, D. Du, J. Wang, Z. Ren, H. Nguyen-Thi, N. Mangelinck-Noel, Effect of a weak transverse magnetic field on solidification structure during directional solidification, Acta Materialia 64 (2014) 367-381.

[10] X. Li, Y. Fautrelle, Z. Ren, R. Moreau, Formation mechanism of axial macrosegregation of primary phases induced by a static magnetic field during directional solidification, Sci Rep 7 (2017) 45834.

[11] T. Liu, Q. Wang, A. Gao, C. Zhang, D. Li, J. He, Crystal orientation and grain alignment in a hypoeutectic Mn–Sb alloy under high magnetic field conditions, Journal of Alloys and Compounds 481(1-2) (2009) 755-760.

[12] X. Li, Z. Ren, Y. Fautrelle, Alignment behavior of the primary Al3Ni phase in Al–Ni alloy under a high magnetic field, Journal of Crystal Growth 310(15) (2008) 3488-3497.

[13] X. Li, Y. Fautrelle, A. Gagnoud, R. Moreau, D. Du, Z. Ren, X. Lu, EBSD Study on the Effect of a Strong Axial Magnetic Field on the Microstructure and Crystallography of Al-Ni Alloys During Solidification, Metallurgical and Materials Transactions A 47(3) (2016) 1180-1197.

[14] K. Takahashi, S. Taniguchi, Electromagnetic separation of nonmetallic inclusion from liquid metal by imposition of high frequency magnetic field, ISIJ international 43(6) (2003) 820-827.

[15] B. Thidé, Electromagnetic field theory, Upsilon Books2017.

[16] C. Vives, Effects of forced electromagnetic vibrations during the solidification of aluminum alloys: Part I. Solidification in the presence of crossed alternating electric fields and stationary magnetic fields, Metallurgical and Materials Transactions B 27(3) (1996) 445-455.

[17] J. Li, J. Ma, Y. Gao, Q. Zhai, Research on solidification structure refinement of pure aluminum by electric current pulse with parallel electrodes, Materials Science and Engineering: A 490(1-2) (2008) 452-456.

[18] J. Barnak, A. Sprecher, H. Conrad, Colony (grain) size reduction in eutectic Pb-Sn castings by electroplusing, Scripta metallurgica et materialia 32(6) (1995) 879-884.

[19] S. Eckert, B. Willers, P.A. Nikrityuk, K. Eckert, U. Michel, G. Zouhar, Application of a rotating magnetic field during directional solidification of Pb–Sn alloys: Consequences on the CET, Materials Science and Engineering: A 413-414 (2005) 211-216.

[20] S. Steinbach, L. Ratke, The effect of rotating magnetic fields on the microstructure of directionally solidified Al–Si–Mg alloys, Materials Science and Engineering: A 413-414 (2005) 200-204.

[21] A.F. Kolesnichenko, Electromagnetic processes in liquid material in the USSR and East European countries, ISIJ international 30(1) (1990) 8-26.

[22] M. Garnier, Electromagnetic processing of liquid materials in Europe, ISIJ international 30(1) (1990) 1-7.

[23] S. Asai, Birth and recent activities of electromagnetic processing of materials, ISIJ international 29(12) (1989) 981-992.

[24] S. Asai, Recent development and prospect of electromagnetic processing of materials, Science and Technology of Advanced Materials 1(4) (2000) 191-200.

[25] A. Nishimura, Y. Kawano, Effect of Direct Vibration in an Alternating Electromagnetic Field on Grain Refinement of Al Alloys, Journal of Japan Institute of Light Metals 25(6) (1975) 193-199.

[26] Y. Mizutani, K. Miwa, T. Tamura, Y. Nakai, Y. Otsuka, Grain refinement of tough pitch copper by electromagnetic vibrations during solidification, Materials transactions 47(7) (2006) 1793-1797.

[27] C. Vivès, Grain refinement in aluminum alloys by means of electromagnetic vibrations including cavitation phenomena, JOM-e 50(2) (1998) 1-9.

[28] M. Nakada, Y. Shiohara, M.C. Flemings, Modification of solidification structures by pulse electric discharging, ISIJ international 30(1) (1990) 27-33.

[29] K. Vashchenko, D. Chernega, S. Vorobev, N. Lysenko, Y.E. Yakovchuk, Effect of electric current on the solidification of cast iron, Metal Science and Heat Treatment 16(3) (1974) 261-265.

[30] A.K. Misra, A novel solidification technique of metals and alloys: under the influence of applied potential, Metallurgical and Materials Transactions A 16(7) (1985) 1354-1355.

[31] A.K. Misra, Misra technique 1 applied to solidification of cast iron, Metallurgical Transactions A 17(2) (1986) 358-360.

[32] M. Nakada, Modification of solidification structures by pulse electric discharging, Massachusetts Institute of Technology, 1985.

[33] X. Li, Y. Fautrelle, Z. Ren, Influence of an axial high magnetic field on the liquid–solid transformation in Al–Cu hypoeutectic alloys and on the microstructure of the solid, Acta Materialia 55(4) (2007) 1377-1386.

[34] Z.-x. Yin, D. Liang, Y.-e. Chen, Y.-f. Cheng, Q.-j. Zhai, Effect of electrodes and thermal insulators on grain refinement by electric current pulse, Transactions of Nonferrous Metals Society of China 23(1) (2013) 92-97.

[35] S. Yesilyurt, S. Motakef, R. Grugel, K. Mazuruk, The effect of the traveling magnetic field (TMF) on the buoyancy-induced convection in the vertical Bridgman growth of semiconductors, Journal of Crystal Growth 263(1-4) (2004) 80-89.

[36] V. Metan, K. Eigenfeld, D. Räbiger, M. Leonhardt, S. Eckert, Grain size control in Al–Si alloys by grain refinement and electromagnetic stirring, Journal of alloys and compounds 487(1-2) (2009) 163-172.

[37] K. Zaïdat, N. Mangelinck-Noël, R. Moreau, Control of melt convection by a travelling magnetic field during the directional solidification of Al–Ni alloys, Comptes Rendus Mecanique 335(5-6) (2007) 330-335.

[38] Y.-Y. Gong, J. Luo, J.-X. Jing, Z.-Q. Xia, Q.-J. Zhai, Structure refinement of pure aluminum by pulse magneto-oscillation, Materials Science and Engineering: A 497(1-2) (2008) 147-152.

[39] Z.-X. Yin, Y.-Y. Gong, B. Li, Y.-F. Cheng, D. Liang, Q.-J. Zhai, Refining of pure aluminum cast structure by surface pulsed magneto-oscillation, Journal of Materials Processing Technology 212(12) (2012) 2629-2634.

[40] D. Liang, Z. Liang, Q. Zhai, G. Wang, D.H. StJohn, Nucleation and grain formation of pure Al under Pulsed Magneto-Oscillation treatment, Materials Letters 130 (2014) 48-50.

[41] G.I. Eskin, D.G. Eskin, Ultrasonic treatment of light alloy melts, CRC Press2014.

[42] Mi. J, Eskin. D, Solidification processing of metallic alloys under external fields, Springer2018.

[43] J. Als-Nielsen, D. McMorrow, Elements of modern X-ray physics, John Wiley & Sons2011.

[44] J. Stöhr, Two-photon x-ray diffraction, Physical review letters 118(2) (2017) 024801.

[45] D. Tan, In situ ultrafast synchrotron X-ray imaging studies of the dynamics of ultrasonic bubbles in liquids, University of Hull, 2015.

[46] D.H. Bilderback, P. Elleaume, E. Weckert, Review of third and next generation synchrotron light sources, Journal of Physics B: Atomic, molecular and optical physics 38(9) (2005) S773.

[47] T. Manuwong, Solidification of metal alloys in pulse electromagnetic fields, University of Hull, 2015.

[48] F. Fusseis, X. Xiao, C. Schrank, F. De Carlo, A brief guide to synchrotron radiation-based microtomography in (structural) geology and rock mechanics, Journal of Structural Geology 65 (2014) 1-16.

[49] G.T. Herman, Image Reconstruction from Projections: The Fundamentals of Computerized Tomography (Computer Science Applied Mathematics), image 10 (1980) 03.

[50] E. Maire, P.J. Withers, Quantitative X-ray tomography, International materials reviews 59(1) (2014) 1-43.

[51] E. Guo, A.B. Phillion, B. Cai, S. Shuai, D. Kazantsev, T. Jing, P.D. Lee, Dendritic evolution during coarsening of Mg-Zn alloys via 4D synchrotron tomography, Acta Materialia 123 (2017) 373-382.

[52] S. Shuai, E. Guo, A.B. Phillion, M.D. Callaghan, T. Jing, P.D. Lee, Fast synchrotron X-ray tomographic quantification of dendrite evolution during the solidification of Mg Sn alloys, Acta Materialia 118 (2016) 260-269.

[53] D. Tolnai, P. Townsend, G. Requena, L. Salvo, J. Lendvai, H.P. Degischer, In situ synchrotron tomographic investigation of the solidification of an AlMg4.7Si8 alloy, Acta Mater 60(6-7) (2012) 2568-2577.

[54] J.M. Yu, N. Wanderka, A. Rack, R. Daudin, E. Boller, H. Markötter, A. Manzoni, F. Vogel, T. Arlt, I. Manke, J. Banhart, Formation of intermetallic δ phase in Al-10Si-0.3Fe alloy investigated by in-situ 4D X-ray synchrotron tomography, Acta Materialia 129 (2017) 194-202.

[55] N. Limodin, L. Salvo, M. Suéry, M. DiMichiel, In situ investigation by X-ray tomography of the overall and local microstructural changes occurring during partial remelting of an Al–15.8wt.% Cu alloy, Acta Materialia 55(9) (2007) 3177-3191.

[56] J. Banhart, Advanced tomographic methods in materials research and engineering, Oxford University Press2008.

[57] B. Cai, B. Liu, S. Kabra, Y. Wang, K. Yan, P.D. Lee, Y. Liu, Deformation mechanisms of Mo alloyed FeCoCrNi high entropy alloy: In situ neutron diffraction, Acta Materialia 127 (2017) 471-480.

[58] M.A. Azeem, P.D. Lee, A.B. Phillion, S. Karagadde, P. Rockett, R.C. Atwood, L. Courtois, K.M. Rahman, D. Dye, Revealing dendritic pattern formation in Ni, Fe and Co alloys using synchrotron tomography, Acta Materialia 128 (2017) 241-248.

[59] P.J. Withers, X-ray nanotomography, Materials Today 10(12) (2007) 26-34.

[60] T.L. Burnett, N.J.H. Holroyd, J.J. Lewandowski, M. Ogurreck, C. Rau, R. Kelley, E.J. Pickering, M. Daly, A.H. Sherry, S. Pawar, T.J.A. Slater, P.J. Withers, Degradation of metallic materials studied by correlative tomography, IOP Conference Series: Materials Science and Engineering 219 (2017) 012001.

[61] J.Y. Buffiere, E. Maire, J. Adrien, J.P. Masse, E. Boller, In Situ Experiments with X ray Tomography: an Attractive Tool for Experimental Mechanics, Experimental Mechanics 50(3) (2010) 289-305.

[62] J. Mi, R. Harding, J. Campbell, Effects of the entrained surface film on the reliability of castings, Metallurgical and Materials Transactions A 35(9) (2004) 2893-2902.

[63] J. Mi, R. Harding, J. Campbell, The tilt casting process, International Journal of Cast Metals Research 14(6) (2002) 325-334.

[64] R.H. Mathiesen, L. Arnberg, F. Mo, T. Weitkamp, A. Snigirev, Time resolved x-ray imaging of dendritic growth in binary alloys, Physical Review Letters 83(24) (1999) 5062.

[65] N. Limodin, L. Salvo, E. Boller, M. Suéry, M. Felberbaum, S. Gailliègue, K. Madi, In situ and real-time 3-D microtomography investigation of dendritic solidification in an Al–10wt.% Cu alloy, Acta Materialia 57(7) (2009) 2300-2310.

[66] C. Puncreobutr, In situ synchrotron characterisation of Fe-rich intermetallic formation during the solidification of Al-Si-Cu-Fe alloys, Imperial College London, 2013.

[67] S. Kumar, K. O'Reilly, Influence of Al grain structure on Fe bearing intermetallics during DC casting of an Al-Mg-Si alloy, Materials Characterization 120 (2016) 311-322.

[68] Y. Zhao, W. Du, B. Koe, T. Connolley, S. Irvine, P.K. Allan, C.M. Schlepütz, W. Zhang, F. Wang, D.G. Eskin, J. Mi, 3D characterisation of the Fe-rich intermetallic phases in recycled Al alloys by synchrotron X-ray microtomography and skeletonisation, Scripta Materialia 146 (2018) 321-326.

[69] S. Terzi, J.A. Taylor, Y.H. Cho, L. Salvo, M. Suéry, E. Boller, A.K. Dahle, In situ study of nucleation and growth of the irregular α-Al/β-Al5FeSi eutectic by 3-D synchrotron X-ray microtomography, Acta Materialia 58(16) (2010) 5370-5380.

[70] B. Cai, J. Wang, A. Kao, K. Pericleous, A.B. Phillion, R.C. Atwood, P.D. Lee, 4D synchrotron X-ray tomographic quantification of the transition from cellular to dendrite growth during directional solidification, Acta Materialia 117 (2016) 160-169.

[71] A.J. Shahani, X. Xiao, P.W. Voorhees, The mechanism of eutectic growth in highly anisotropic materials, Nat Commun 7 (2016) 12953.

[72] E. Liotti, A. Lui, R. Vincent, S. Kumar, Z. Guo, T. Connolley, I.P. Dolbnya, M. Hart, L. Arnberg, R.H. Mathiesen, P.S. Grant, A synchrotron X-ray radiography study of dendrite fragmentation induced by a pulsed electromagnetic field in an Al–15Cu alloy, Acta Materialia 70 (2014) 228-239.

[73] E. Liotti, A. Lui, S. Kumar, Z. Guo, C. Bi, T. Connolley, P.S. Grant, The spatial and temporal distribution of dendrite fragmentation in solidifying Al-Cu alloys under different conditions, Acta Materialia 121 (2016) 384-395.

[74] J. Shercliff, Thermoelectric magnetohydrodynamics, Journal of fluid mechanics 91(2) (1979) 231-251.

[75] A. Kao, B. Cai, P.D. Lee, K. Pericleous, The effects of Thermoelectric Magnetohydrodynamics in directional solidification under a transverse magnetic field, Journal of Crystal Growth 457 (2017) 270-274.

[76] M. Araki, PID control, Control Systems, Robotics and Automation: System Analysis and Control: Classical Approaches II, Unbehauen, H.(Ed.). EOLSS Publishers Co. Ltd., Oxford, UK., ISBN-13: 9781848265912 (2009) 58-79.

[77] A. Savitzky, M.J. Golay, Smoothing and differentiation of data by simplified least squares procedures, Analytical chemistry 36(8) (1964) 1627-1639.

[78] J.-O. Andersson, T. Helander, L. Höglund, P. Shi, B. Sundman, Thermo-Calc & DICTRA, computational tools for materials science, Calphad 26(2) (2002) 273-312.

[79] C. Solomon, T. Breckon, Fundamentals of Digital Image Processing: A practical approach with examples in Matlab, John Wiley & Sons2011.

[80] D. Bernard, O. Guillon, N. Combaret, E. Plougonven, Constrained sintering of glass films: Microstructure evolution assessed through synchrotron computed microtomography, Acta Materialia 59(16) (2011) 6228-6238.

[81] A.C. Kak, M. Slaney, Principles of computerized tomographic imaging, IEEE press New York1988.

[82] A. Mohamad-Djafari, Inverse problems in vision and 3D tomography, John Wiley & Sons2013.

[83] A.J. Shahani, Interfacial Evolution in Four Dimensions: Growth and Coarsening in Highly Anisotropic Systems, Northwestern University, 2016.

[84] C.A. Schneider, W.S. Rasband, K.W. Eliceiri, NIH Image to ImageJ: 25 years of image analysis, Nature methods 9(7) (2012) 671-675.

[85] M. Basham, J. Filik, M.T. Wharmby, P.C. Chang, B. El Kassaby, M. Gerring, J. Aishima, K. Levik, B.C. Pulford, I. Sikharulidze, Data Analysis WorkbeNch (DAWN), Journal of synchrotron radiation 22(3) (2015) 853-858.

[86] V. Titarenko, R. Bradley, C. Martin, P.J. Withers, S. Titarenko, Regularization methods for inverse problems in X-ray tomography, Proc. SPIE, 2010, pp. 78040Z-1.

[87] T.F. Scientific, Avizo Software User's Guide. https://www.fei.com/software/avizo-user-guide/, 2018).

[88] D. Kammer, P. Voorhees, The morphological evolution of dendritic microstructures during coarsening, Acta Materialia 54(6) (2006) 1549-1558.

[89] R. Mendoza, Morphological and topological characterization of coarsened dendritic microstructures, 2004.

[90] S. Cappello, D. Escande, Bifurcation in viscoresistive MHD: The Hartmann number and the reversed field pinch, Physical review letters 85(18) (2000) 3838.

[91] H. Yasuda, I. Ohnaka, O. Kawakami, K. Ueno, K. Kishio, Effect of magnetic field on solidification in Cu-Pb monotectic alloys, ISIJ international 43(6) (2003) 942-949.

[92] C. Wang, Q. Wang, Z. Wang, H. Li, K. Nakajima, J. He, Phase alignment and crystal orientation of Al3Ni in Al–Ni alloy by imposition of a uniform high magnetic field, Journal of Crystal Growth 310(6) (2008) 1256-1263.

[93] J. Akiyama, H. Asano, K. Iwai, S. Asai, Analysis of Uniaxial Alignment Behavior of Nonmagnetic Materials under Static Magnetic Field with Sample Rotation, Materials Transactions 49(4) (2008) 787-791.

[94] R.A. Serway, J.W. Jewett, Principles of physics, Saunders College Pub. Fort Worth, TX1998.

[95] K. Okazaki, M. Kagawa, H. Conrad, An evaluation of the contributions of skin, pinch and heating effects to the electroplastic effect in titatnium, Materials Science and Engineering 45(2) (1980) 109-116.

[96] Y. Fukui, K. Takashima, C. Ponton, Measurement of Young's modulus and internal friction of an in situ Al-Al3Ni functionally gradient material, Journal of Materials Science 29(9) (1994) 2281-2288.

[97] J. Pilling, A. Hellawell, Mechanical deformation of dendrites by fluid flow, Metallurgical and Materials Transactions A 27(1) (1996) 229-232.

[98] H.J. Frost, M.F. Ashby, Deformation mechanism maps: the plasticity and creep of metals and ceramics, Pergamon press1982.

[99] D. Tan, T.L. Lee, J.C. Khong, T. Connolley, K. Fezzaa, J. Mi, High-Speed Synchrotron X-ray Imaging Studies of the Ultrasound Shockwave and Enhanced Flow during Metal Solidification Processes, Metallurgical and Materials Transactions A 46(7) (2015) 2851-2861.

[100] C. Hintermüller, F. Marone, A. Isenegger, M. Stampanoni, Image processing pipeline for synchrotron-radiation-based tomographic microscopy, Journal of synchrotron radiation 17(4) (2010) 550-559.

[101] F. Marone, M. Stampanoni, Regridding reconstruction algorithm for real-time tomographic imaging, Journal of synchrotron radiation 19(6) (2012) 1029-1037.

[102] R. Huesman, G. Gullberg, W. Greenberg, T. Budinger, Users manual: Donner algorithms for reconstruction tomography, (1977).

[103] J. Schindelin, I. Arganda-Carreras, E. Frise, V. Kaynig, M. Longair, T. Pietzsch, S. Preibisch, C. Rueden, S. Saalfeld, B. Schmid, Fiji: an open-source platform for biological-image analysis, Nature methods 9(7) (2012) 676.

[104] R.S. Bradley, P.J. Withers, Post-processing techniques for making reliable measurements from curve-skeletons, Computers in biology and medicine 72 (2016) 120-131.

[105] A. Rigort, D. Günther, R. Hegerl, D. Baum, B. Weber, S. Prohaska, O. Medalia, W. Baumeister, H.-C. Hege, Automated segmentation of electron tomograms for a quantitative description of actin filament networks, Journal of structural biology 177(1) (2012) 135-144.

[106] F. Wang, D. Eskin, J. Mi, C. Wang, B. Koe, A. King, C. Reinhard, T. Connolley, A synchrotron X-radiography study of the fragmentation and refinement of primary intermetallic particles in an Al-35 Cu alloy induced by ultrasonic melt processing, Acta Materialia 141 (2017) 142-153.

[107] B. Wang, D. Tan, T.L. Lee, J.C. Khong, F. Wang, D. Eskin, T. Connolley, K. Fezzaa, J. Mi, Ultrafast synchrotron X-ray imaging studies of microstructure fragmentation in solidification under ultrasound, Acta Materialia 144 (2018) 505-515.

[108] D. Ruvalcaba, R. Mathiesen, D. Eskin, L. Arnberg, L. Katgerman, In situ observations of dendritic fragmentation due to local solute-enrichment during directional solidification of an aluminum alloy, Acta Materialia 55(13) (2007) 4287-4292.

[109] H. Neumann-Heyme, K. Eckert, C. Beckermann, Dendrite fragmentation in alloy solidification due to sidearm pinch-off, Physical Review E 92(6) (2015) 060401.

[110] W.W. Mullins, R. Sekerka, Stability of a planar interface during solidification of a dilute binary alloy, Dynamics of Curved Fronts, Elsevier1988, pp. 345-352.

[111] T. Haxhimali, A. Karma, F. Gonzales, M. Rappaz, Orientation selection in dendritic evolution, Nat Mater 5(8) (2006) 660-4.

[112] J.W. Gibbs, K.A. Mohan, E.B. Gulsoy, A.J. Shahani, X. Xiao, C.A. Bouman, M. De Graef, P.W. Voorhees, The Three-Dimensional Morphology of Growing Dendrites, Sci Rep 5 (2015) 11824.

[113] P. Voorhees, M. Glicksman, Ostwald ripening during liquid phase sintering—Effect of volume fraction on coarsening kinetics, Metallurgical and Materials Transactions A 15(6) (1984) 1081-1088.

[114] D. Poirier, S. Ganesan, M. Andrews, P. Ocansey, Isothermal coarsening of dendritic equiaxial grains in Al 15.6 wt.% Cu alloy, Materials Science and Engineering: A 148(2) (1991) 289-297.

[115] S. Terzi, E. Boller, L. Salvo, M. Suéry, In situ X-ray microtomography study of the solidification and remelted microstructures of Al–Cu alloys, International Journal of Cast Metals Research 22(1-4) (2009) 275-278.

[116] M. Avrami, Granulation, Phase Change, and Microstructure Kinetics of Phase Change. III, The Journal of Chemical Physics 9(2) (1941) 177-184.

[117] J. Farjas, P. Roura, Modification of the Kolmogorov–Johnson–Mehl–Avrami rate equation for non-isothermal experiments and its analytical solution, Acta Materialia 54(20) (2006) 5573-5579.

[118] A. Bogno, H. Nguyen-Thi, B. Billia, N. Bergeon, N. Mangelinck-Noël, E. Boller, T. Schenk, J. Baruchel, In situ analysis of dendritic equiaxed microstructure formation in Al-Cu alloys by synchrotron X-ray radiography, Transactions of the Indian Institute of Metals 62(4-5) (2010) 427-431.

[119] J. Sekhar, R. Trivedi, Solidification microstructure evolution in the presence of inert particles, Materials Science and Engineering: A 147(1) (1991) 9-21.

[120] H.-T. Li, P. Zhao, R. Yang, J.B. Patel, X. Chen, Z. Fan, Grain Refinement and Improvement of Solidification Defects in Direct-Chill Cast Billets of A4032 Alloy by Melt Conditioning, Metallurgical and Materials Transactions B 48(5) (2017) 2481-2492.

[121] M. Yang, S.-M. Xiong, Z. Guo, Characterisation of the 3-D dendrite morphology of magnesium alloys using synchrotron X-ray tomography and 3-D phase-field modelling, Acta Materialia 92 (2015) 8-17.

[122] Z. Guo, J. Mi, S. Xiong, P.S. Grant, Phase field study of the tip operating state of a freely growing dendrite against convection using a novel parallel multigrid approach, Journal of Computational Physics 257 (2014) 278-297.

[123] A.F. Kolesnichenko, A.D. Podoltsev, I.N. Kucheryavaya, Action of pulse magnetic field on molten metal, ISIJ international 34(9) (1994) 715-721.

[124] D.G. Eskin, Suyitno, L. Katgerman, Mechanical properties in the semi-solid state and hot tearing of aluminium alloys, Progress in Materials Science 49(5) (2004) 629-711.

[125] A. Kao, K. Pericleous, M. Patel, V. Voller, Effects of magnetic fields on crystal growth, International Journal of Cast Metals Research 22(1-4) (2009) 147-150.

[126] A. Verma, S. Kumar, P.S. Grant, K.A.Q. O'Reilly, Influence of cooling rate on the Fe intermetallic formation in an AA6063 Al alloy, Journal of Alloys and Compounds 555 (2013) 274-282.

[127] K. Liu, X. Cao, X.G. Chen, Solidification of Iron-Rich Intermetallic Phases in Al-4.5Cu-0.3Fe Cast Alloy, Metallurgical and Materials Transactions A 42(7) (2010) 2004-2016.

[128] I. Bacaicoa, M. Wicke, M. Luetje, F. Zeismann, A. Brueckner-Foit, A. Geisert, M. Fehlbier, Characterization of casting defects in a Fe-rich Al-Si-Cu alloy by microtomography and finite element analysis, Engineering Fracture Mechanics 183 (2017) 159-169.

[129] C. Puncreobutr, A.B. Phillion, J.L. Fife, P. Rockett, A.P. Horsfield, P.D. Lee, In situ quantification of the nucleation and growth of Fe-rich intermetallics during Al alloy solidification, Acta Materialia 79 (2014) 292-303.

Appendices

Appendix 1. Manufacturing and calculating for Furnace

To manufacture the furnace, there are 4 steps as follows:

Step 1: to find out the total power of the furnace

$$Area_{in} = \pi h_h d_h$$

Where $Area_{in}$ the surface area of inner furnace, h_h is height of heating zone, d_h is diameter of heating zone. Thus, total power for the heating needs is

$$P_{total} = P' \times Area_{in}$$

Step 2: calculate the diameter of heating element: D_{em}

$$D_{em} = 34.4 \times \sqrt[3]{\frac{P^2 \times \rho_t}{V_h^2 \times v_{Per}}}$$

Where *P* is power of heating element (kW), v_h is voltage of heating element, v_{Per} is permitted power load on surface (Watt/cm^2) and ρ_t is resistivity of heating element at designed temperature.

Length of heating element: L_{em}

$$L_{em} = \frac{V_h^2 \times area_{cross}}{10^3 \times P \times \rho_t}$$

Where $area_{cross}$ is the area cross section of heating element

Step 3: length of the helical coil

L_{he} is total length of helical coil, D_{he} is diameter of helical coil

Step 4: verify the dimension of heating element

$$v_{effective} = \frac{10^3 \times P}{\pi \times D_{em} \times L_{em}} \leq v_{Per}$$

Appendix 2. The list of components for PMF device

Quantity	Description	Order Code	Supplier	Manufacturer
For pulse generator box				
2	Capacitior 1000uF 550V	2456327	Farnell	ALS61A102ME550
1	Resistor 22R 1.0KW	1760850	Farnell	TE1000B22RJ
1	Resistor 220R 100W	1174297	Farnell	HSC100220RJ
1	BRIDGE RECTIFIER	1761329	Farnell	SKB 30/16 A1
1	THYRISTOR	9104623	Farnell	VS-181RKI100PBF
1	Relay 3 poles 12V	1169199	Farnell	60.13.9.012.0040
1	SOCKET, DIN/SURFACE, 11 PIN	1169212	Farnell	90.27SMA
2	Fan	789-7889	RS	OA92AP-22-1WB
1	Power soket	2080425	Farnell	GSP1.8101.1
1	Power plug	1125810	Farnell	4782.0000
1	Power soket	1713277	Farnell	6163.0018
1	Power plug	1170114	Farnell	4795.0000
2	Fuse Holder	1154860	Farnell	BK/HTB-24I-R
1	Fuse pack 10A (10 fuses)	1871081	Farnell	CF06332F/10/10
1	Fuse pack 2A (10 fuses)	534950	Farnell	TDC10 2A
1	Panic switch	1082379	Farnell	A01ES+A0154B
2	Rocker Switch 15A	1752637	Farnell	2500R11E
1	Power Socket	821-2028	RS	555388
1	Power Plug	821-2009	RS	555328
2	Micro switch Generic	2505954	Farnell	ASQ11510
1	Voltmeter Generic	1015960	Farnell	PD72MIS500V/2/938-658
1	DB9 Connector			
1	Generic connector			
For power supply board				
1	Reistor 680R -smd	2057832	Farnell	ERJ8GEYJ681V
1	Resistor 15 R	2101728	Farnell	PWR220T-35-15R0J

1	Solid State Relay AQV101A	185-4172	Farnell	AQV101A
1	SSR 3A	2302216	Farnell	AQV252G2SX
1	SS relay 16A zero crossing	1618480	Farnell	S216S02F
1	SS relay 280v 25A	1533357	Farnell	PF240D25
2	Power supply 12V 1.25A	2464697	Farnell	VTX-214-015-112
2	Diodes MRU860	1625180	Farnell	MUR860
2	Terminal Block	707-5054	RS	20020004-C081B01LF
2	Terminal block socket	707-5111	RS	20020110-C081A01LF
2	Terminal Block	707-5402	RS	20020006-H061B01LF
2	Terminal block socket	707-5468	RS	20020110-H061A01LF
2	Capacitir 1000uF	9692878	Farnell	ECA1VHG102
For controller board				
1	PIC16F887-I/PT	1439542	Farnell	PIC16F887-I/PT
1	24LC64-I/SN	9758070	Farnell	24LC64-I/SN
2	Capacitor-20pF	184-4172	Farnell	C0603C200J5GACTU
4	Capacitor-100nF	882-0023	Farnell	GRM188R71H104KA93D
1	Capacitor-10uF	1657928	Farnell	06034D106MAT2A
3	Resistor 10K	923-8603	Farnell	RC0603FR-0710KL
1	Crystal 8mhz	9712844	Farnell	LFXTAL003156
9	Push button-switch	479-1508	RS	4-1437565-1
1	5V Regulator	2383023	Farnell	LM1084IT-5.0/NOPB
1	Display	2063159	Farnell	MC21605C6W-BNMLW
1	Resistor array 10k	9356819	Farnell	4609X-101-103LF
1	Pins	1248150	Farnell	826936-3
1	Trimpot	2328493	Farnell	3314J-1-223E

List of Tables

List of Figures